HELLEN COSTENARO GUADAGNIN

Corrosion resistance study of AA2524 anodized in sulphuric-tartaric acid and sealed with hybrid coatings

São Paulo
(2017)

HELLEN COSTENARO GUADAGNIN

Corrosion resistance study of AA2524 anodized in sulphuric-tartaric acid and sealed with hybrid coatings

A thesis presented to the Polytechnic School of the University of São Paulo for the degree of Doctor of Science.

A thesis presented to the Faculty of Engineering of the University of Mons for the degree of Doctor in Applied Sciences.

São Paulo

(2017)

HELLEN COSTENARO GUADAGNIN

Corrosion resistance study of AA2524 anodized in sulphuric-tartaric acid and sealed with hybrid coatings

A thesis presented to the Polytechnic School of the University of São Paulo for the degree of Doctor of Science

A thesis presented to the Faculty of Engineering of the University of Mons for the degree of Doctor in Applied Sciences

Area: Chemical Engineering

Supervisors: Prof. Dr. Hercílio Gomes de Melo and Prof. Dr. Marie-Georges Olivier

São Paulo

(2017)

Este exemplar foi revisado e corrigido em relação à versão original, sob responsabilidade única do autor e com a anuência de seu orientador.

São Paulo, _____ de _____ de _____

Assinatura do autor: _____

Assinatura do orientador: _____

Catalogação-na-publicação

Costenaro Guadagnin, Hellen
Corrosion resistance study of AA2524 anodized in sulphuric-tartaric acid and sealed with hybrid coatings / H. Costenaro Guadagnin -- versão corr. – São Paulo, 2017.
237 p.

Tese (Doutorado) - Escola Politécnica da Universidade de São Paulo. Departamento de Engenharia Química.

1.AA2524 2.TSA anodizing 3.Hybrid sol-gel 4.Corrosion 5.EIS I.Universidade de São Paulo. Escola Politécnica. Departamento de Engenharia Química II.t.

ACKNOWLEDGMENTS

My heartiest thanks go to my supervisors Hercílio and Marjorie for the support, the excellent supervision and the opportunity to develop my PhD work here in Brazil and in Belgium.

To my parents and family that allowed me and encouraged me to fly away and follow my dreams. Thank you for giving me love to be here and anywhere that I want.

To my husband, Rafael, that stimulates me in my academic life, understanding and supporting my choices. Thank you for everything.

I am so grateful to Maysa and Fernanda. They supported me all the time I needed and they were always available to discuss, explain and help me with my doubts. They both have an important part in my background.

I want to thank Dr. Isolda and her research group for receiving me so well in the Electrochemical and Protective Coatings laboratory at IPEN.

To my friends at USP: Rocio, Bruna, Adriana, Diego, Teresa and especially Marina, who was the responsible for corrosion being my favourite subject and for introducing me to Hercílio.

To my friends from UMONS: Alexis, Hamid, Marc P., Arnaud N., Arnaud K., Eya, Emeline, Tangui, Julien, Driss, Anne-Laure, Lilya, Eric. A very special thanks to Luiza and Leonardo, there is no word to demonstrate how thankful I am and how important was to have them as my friends in Mons.

To my friends: Tânia, Talita, Ilka, Lea, Ju, Mi, Sandra Mara, for supporting me especially when I was working at the Navy; Polly, Fabi, Ana, Martha, Gustavo, Bruna, André and the childhood friends from Alegrete.

To CNPq for the financial support and to the FLYCOAT project financed by the Region Wallonne (Belgium).

ABSTRACT

Aluminium alloys are widely used in the aerospace industry due to their lightweight and high specific strength. However, these alloys are particularly sensitive to localized corrosion in chloride environments and need to be protected by a robust system. One of the protection methodologies consists in anodizing. The produced layer increases the corrosion resistance and also serves as anchoring site for organic coatings application. Chromium-based anodizing has been usually employed, nevertheless, as chromate compounds are toxic for health and the environment, chromium-based surface treatments will be prohibited in the aerospace industry in a near future. Tartaric-sulphuric acid (TSA) anodizing is a promising environment compliant alternative, which is already being used at industrial level with appropriate corrosion protection and paint adhesion properties. This study aims at proposing a hybrid sol-gel treatment after TSA anodizing of AA2524 specimens in order to improve the corrosion resistance of the anodized layer while maintaining its compatibility with organic coatings. For this, anodic aluminium oxides (AAO) were produced at different anodizing voltages and protected by dip-coating with a hybrid sol-gel layer obtained from a tetraethoxysilane (TEOS) and 3-glycidoxypropyltrimethoxysilane (GPTMS) hydrolysis solution with high water content. Corrosion resistance evaluation was carried out by means of electrochemical impedance spectroscopy (EIS) in NaCl 0.1 mol L^{-1} and salt-spray chamber exposure (ASTM B117-11 standard). The morphology of the anodic porous layer was investigated by means of FE-SEM, whereas glow discharge optical emission spectroscopy (GDOES) was employed to evaluate the distribution of the sol-gel layer within the porous AAO. FE-SEM characterization confirmed that the layer properties (pore distribution, porosity and thickness) were strongly dependent on the anodizing conditions, whereas GDOES depth profile showed penetration of the hybrid coating within the pores of the anodized layer. The two characterization techniques showed inefficient surface sol-gel coverage for the samples anodized at higher voltage, likely due to insufficient sol-gel deposition. The results of the EIS characterization tests up to 1008 h (42 days) showed that, irrespectively to the anodizing voltage, the hybrid sol-gel protected AAO was stable with only slight evolution of the diagrams with immersion time. Moreover, the hybrid coating protected samples presented higher low frequency impedance modulus than hydrothermally sealed (HTSed) reference TSA anodized samples, which was confirmed by electrical equivalent circuit (EEC) fitting of the EIS data. EEC fitting also revealed that the resistance of the pores to electrolyte penetration was increased by the application of the sol-gel

coating when compared to the resistance of the HTSed reference samples and indicated better anticorrosion performance for the sample anodized at 16 V. These results were confirmed by the salt-spray tests. Investigation on the ageing of the hybrid sol-gel hydrolysis solution showed that its viscosity hardly changed up to two weeks of test and that hybrid coatings applied from these solutions were stable and afforded good corrosion protection to the TSA anodized substrate, an improvement of the anticorrosion properties of the hybrid coating was verified for an ageing time of 168 h. Preliminary tests performed with a solvent-free organic coating (epoxy) indicated good compatibility with the hybrid TEOS-GPTMS coating characterized by very high impedance and good stability upon exposure to the salt-spray chamber.

Key words: AA2524; anodizing; TSA; hybrid sol-gel; corrosion; EIS.

RESUMO

Ligas de alumínio são muito utilizadas na indústria aeronáutica por serem materiais leves e altamente resistentes. Porém, essas ligas são particularmente sensíveis à corrosão localizada em meios que contêm cloretos, e precisam de sistemas robustos de proteção. Uma das metodologias de proteção consiste em anodização. A camada produzida aumenta a resistência à corrosão e também serve como sítio de ancoragem para aplicação de revestimentos orgânicos. A anodização crômica tem sido usualmente empregada na indústria aeronáutica. No entanto, como compostos contendo íons cromato são tóxicos para a saúde e para o meio-ambiente, tratamentos de superfície à base de cromo serão proibidos na indústria espacial em um futuro próximo. Anodização em banho de ácido sulfúrico-tartárico (TSA) é uma alternativa promissora e ambientalmente compatível, a qual já está sendo usada industrialmente com apropriada proteção à corrosão e adesão para pintura. Este estudo tem como objetivo propor um tratamento utilizando um revestimento híbrido sol-gel para melhorar a resistência à corrosão da liga AA2524 anodizada em TSA e que mantenha sua compatibilidade com revestimentos orgânicos. Para isso, camadas anodizadas de alumínio (CAA) foram produzidas em diferentes voltagens e protegidas por camada de híbrido sol-gel obtida pela hidrólise de tetraetilortosilano (TEOS) e glicidóxipropiltrimetóxisilano (GPTMS) em solução com alto teor de água e aplicada pela técnica de dip-coating.

A avaliação da resistência à corrosão foi realizada através de espectroscopia de impedância eletroquímica (EIS) em NaCl 0,1 mol.L^{-1} e por exposição à câmara de névoa salina (norma ASTM B117-11). A morfologia da camada porosa foi investigada por MEV e a espectroscopia de emissão óptica por descarga luminescente (GDOES) foi empregada para avaliar a distribuição do híbrido sol-gel no interior dos poros da camada porosa. As caracterizações por MEV confirmaram que as propriedades da camada (distribuição dos poros, porosidade e espessura) são fortemente dependentes das condições de anodização, e a composição em profundidade obtida por GDOES mostrou que o revestimento híbrido penetrou nos poros da camada anodizada. As duas técnicas de caracterização mostraram uma cobertura ineficiente da camada sol-gel para as amostras anodizadas nas voltagens mais elevadas, provavelmente devido à deposição insuficiente do híbrido. Os testes de EIS com duração de até 1008 h (42 dias) mostraram que, independentemente da voltagem de anodização empregada, a camada anódica coberta com sol-gel ficou estável ocorrendo apenas pequenas evoluções dos diagramas com o tempo de imersão. Além do mais, as amostras protegidas com o revestimento

híbrido apresentaram maiores valores de módulo de impedância em baixa frequência do que as amostras anodizadas em TSA e hidrotermicamente seladas (HTsed) usadas como referências. Essa tendência foi confirmada pelo ajuste com circuitos elétricos equivalentes (EEC) dos resultados de EIS que também mostrou que a aplicação do sol-gel híbrido torna mais difícil a penetração do eletrólito agressivo nos poros da camada anodizada quando comparada com as amostras HTSed, e indicou melhor desempenho anticorrosivo para a amostra anodizada em 16 V. Esses resultados foram confirmados pelos testes de névoa salina. A investigação do envelhecimento da solução de sol-gel mostrou pouca mudança na viscosidade da solução de hidrólise em duas semanas de testes e que os revestimentos híbridos aplicados a partir dessas soluções foram estáveis e promoveram boa proteção à corrosão para as amostras anodizadas em TSA, com melhora das propriedades anticorrosivas após 168 h de envelhecimento. Testes preliminares realizados com revestimento orgânico livre de solvente (epóxi) indicaram boa compatibilidade deste com o revestimento híbrido TEOS-GPTMS. O revestimento epóxi propiciou valores de módulo de impedância elevados e estáveis e também boa estabilidade após exposição à câmara de névoa salina quando aplicado sobre o revestimento híbrido aplicado sobre a liga 2524.

Palavras-chave: AA2524; anodização; TSA; sol-gel híbrido; corrosão; EIS.

RÉSUMÉ

Les alliages d'aluminium sont largement utilisés dans l'industrie aérospatiale en raison de leur légèreté et de leur haute résistance spécifique. Cependant, ces alliages sont particulièrement sensibles à la corrosion localisée dans les milieux chlorurés et doivent être protégés par un système de protection robuste. L'une des méthodes de protection consiste à anodiser le matériau. L'anodisation à base de chrome hexavalent est généralement employée. Cependant, comme les composés à base de chromates sont toxiques pour la santé et l'environnement, les traitements de surface les contenant seront interdits dans l'industrie aérospatiale dans un proche avenir. L'anodisation sulfo-tartrique (TSA) est une alternative prometteuse pour l'environnement qui est déjà utilisée au niveau industriel et qui permet une protection appropriée contre la corrosion et bonne adhérence à la peinture. Cette étude vise à proposer un traitement à base de sol-gel hybride appliqué après anodisation d'échantillons AA2524 en bain sulfo-tartrique. Ce traitement permet d'améliorer la résistance à la corrosion de la couche anodisée tout en maintenant sa compatibilité avec les revêtements organiques. Pour cela, des couches anodiques d'oxyde d'aluminium (AAO) ont été produites à différentes tensions et ensuite protégées avec un sol-gel hybride appliqué par dip-coating. Les précurseurs utilisés lors de la synthèse du sol-gel sont le tétraéthoxysilane (TEOS) et de 3-glycidoxypropyltriméthoxysilane (GPTMS). Ils ont été hydrolysés dans une solution acide contenant une teneur élevée en eau. L'évaluation de la résistance à la corrosion a été réalisée par spectroscopie d'impédance électrochimique (EIS) dans une solution de NaCl 0,1 mol.L^{-1} et lors de l'exposition au brouillard salin (norme ASTM B117-11). La morphologie de la couche poreuse anodique a été analysée au moyen de MEB, tandis que la spectroscopie d'émission optique à décharge luminescente (GDOES) a été utilisée pour évaluer la distribution du sol-gel à l'intérieur de la couche poreuse. La caractérisation au MEB a confirmé que les propriétés de la couche (distribution des pores, porosité et épaisseur) étaient fortement dépendantes des conditions d'anodisation, tandis que le profil en profondeur obtenu par GDOES indiquait une imprégnation du revêtement hybride dans les pores de la couche anodisée. Les deux techniques de caractérisation ont montré que le sol-gel ne recouvrait pas la totalité de la surface pour les échantillons anodisés aux tensions les plus élevées, probablement en raison d'un entrainement insuffisant de la quantité de sol-gel lors du dip-coating. Les résultats des essais de caractérisation EIS jusqu'à 1008 h (42 jours) ont montré que, indépendamment de la tension d'anodisation, le sol-hel hybride protégeait efficacement

le AAO et que les performances des couches étaient maintenues lors de l'immersion malgré une légère évolution des diagrammes d'impédance. De plus, les échantillons protégés par le revêtement hybride présentaient un module d'impédance à basse fréquence plus élevé que les échantillons anodisés et hydrothermiquement colmatés (HTSed) utilisés comme référence. Les diagrammes obtenus par spectroscopie d'impédance électrochimique ont été modélisés en utilisant des circuits électriques équivalents (EEC). L'analyse des EEC a confirmé que la résistance des pores à la pénétration de l'électrolyte est augmentée par l'application du revêtement sol-gel et qu'elle est supérieure à celle déterminée pour les échantillons de référence HTSed. Les performances au brouillard salin sont également améliorées pour l'échantillon anodisé à 16 V et colmaté au sol-gel. L'étude du vieillissement de la solution d'hydrolyse sol-gel hybride a montré que sa viscosité ne change pas significativement jusqu'à deux semaines. Les revêtements hybrides appliqués à partir de ces solutions étaient stables et donnaient une bonne protection contre la corrosion du substrat anodisé. Une légère amélioration des propriétés anticorrosion du revêtement hybride a été vérifiée pour un temps de vieillissement de la solution de 168 h. Les essais préliminaires réalisés avec un revêtement organique exempt de solvant (époxy) indiquent une bonne compatibilité avec le revêtement hybride TEOS-GPTMS caractérisée par une impédance très élevée et une bonne stabilité lors de l'exposition à la chambre brouillard salin.

Mots clés: AA2524; Anodisation; TSA; Sol-gel hybride; corrosion; EIS

LIST OF FIGURES

LIST OF TABLES

CONTENTS

1 INTRODUCTION

Aluminium alloys from the 2xxx series are widely used in the aerospace industry due to their lightweight, high specific strength and durability from which the most important brand is the 2024-T3 (STALEY; LEGE, 1993; GARCÍA-RUBIO et al., 2009b). However, in the last years, efforts to improve mechanical and corrosion resistances of these alloys have led to the launch of the 2*x*24 (*x* = 1-5) series with stricter control of the main alloying elements and lower limits of Fe and Si impurities levels (WANG; STARINK, 2006).

Aluminium alloy 2524 is a new kind of aerospace material with high damage-tolerance and excellent fatigue properties (CHEN et al., 2013). It has been considered as a potential substitute for commercial Al 2024 alloy (CERVANTES et al., 2001) and is currently used on the Boeing 777 aircraft as fuselage and lower wing skin materials (CHEN et al., 2013).

Irrespectively to the brand, 2xxx Al alloys are particularly sensitive to localized corrosion in chloride containing environments. Therefore, in order to maintain their integrity, minimize maintenance needs and repairs, as well as to maximize component life, protective treatments are required (THOMPSON et al., 1999). One of the protection methodologies consists on thickening the Al oxide film by anodizing in acidic baths. The particular structure of the anodized layer, composed of a thin barrier layer and a thick porous layer (GARCIA-VERGARA et al., 2006a; LE COZ; ARURAULT; DATAS, 2010; OKA; TAKAHASHI, 1979), provides both corrosion resistance and a base for applying protective organic coatings (DIGGLE; DOWNIE; GOULDING, 1969).

In the aircraft industry, chromic acid anodizing (CAA) is widely used for Al alloys, providing outstanding corrosion protection, paint adhesion and preserving the fatigue properties of the substrate (GARCÍA-RUBIO et al., 2009a; GARCÍA-RUBIO et al., 2010). However, environmental concerns and legal restrictions associated with the use of Cr (VI) in industrial processes have led to the replacement of CAA and the implementation of alternative anodizing electrolytes (ARENAS; CONDE; DAMBORENEA, 2010; CURIONI et al., 2009) based on the use of inorganic or organic acids or a mixture of them. For instance, the anodizing process licensed by Boeing uses a mixture of boric and sulphuric acids, while the European aircraft industry employs an anodizing process involving the addition of tartaric acid in dilute sulphuric acid electrolyte, called tartaric–sulphuric acid (TSA) anodizing (ARENAS; CONDE; DAMBORENEA, 2010). This latter bath is considered environmentally

compliant and provides corrosion resistance properties compatible with the requirements of the aerospace industry with appropriate paint adhesion (GARCÍA-RUBIO et al., 2010; FENG et al., 2010). In addition, it has been proved that it can produce oxide layers with comparable corrosion protection to those formed in chromic acid baths (GARCÍA-RUBIO et al., 2009a).

For industrial use, the anodized layer must be painted or sealed to prevent aggressive species to reach the base metal (DIGGLE; DOWNIE; GOULDING, 1969; GARCÍA-RUBIO et al., 2009a; CAPELOSSI et al., 2014). The sealing procedure is frequently performed by immersion in a hot aqueous potassium dichromate solution (ZUO; ZHAO; ZHAO, 2003), but, as previously mentioned, Cr (VI) is toxic for health and the environment and these baths will be prohibited in a near future in the aerospace industry. In order to avoid chromium specimen, the sealing can be done by immersion in boiling deionized water (ZEMANOVÁ et al., 1998). However, even though improving the corrosion resistance, this procedure strongly reduces painting adhesion, as the pores of the anodized layer are plugged by boehmite precipitation. Therefore, boiling water hydrothermal sealing cannot be used when an organic coating must protect the anodized substrate.

One very promising approach is the use of hybrid sol-gel coatings obtained by the sol-gel methodology, which have demonstrated to be an efficient alternative for the replacement of the chromate technology (FIGUEIRA; SILVA; PEREIRA, 2015). Their chemistry is based on the formation of an oxide network by hydrolysis and condensation reactions of alkoxysilane precursors, where alcohol and water are formed as by-products (DONLEY et al., 2003; BALBYSHEV et al., 2003). Due to their particular configuration, they can provide both an inorganic functionality for bonding to the metal substrate and an organic functional group, which can be very dense, adherent and protective, for interaction with subsequent polymeric layers (BALBYSHEV et al., 2003). Moreover, their preparation and application can be performed at room temperature, they are chemically inert and have proved good corrosion protection ability for different metals with commercially demonstrated scale-up potential (DONLEY et al., 2003; DRUART et al., 2011).

2 OBJECTIVE

2.1 General objective

This study aims at proposing a hybrid sol-gel coating as a post-treatment for TSA anodized AA2524 specimens in order to improve their corrosion resistance while maintaining the compatibility with organic coatings.

2.2 Specific objectives

- Investigate the effects of the anodizing voltage on the physical properties of the anodized layer: thickness and pore distribution;

- Investigate by Field Emission Scanning Electron Microscopy (FE-SEM) analysis and Glow Discharge Optical Emission Spectroscopy (GDOES) the sol-gel surface distribution and its penetration within the pores of the anodized layer produced at different anodizing voltages;

- Evaluate by Electrochemical Impedance Spectroscopy (EIS) and salt-spray tests the corrosion resistance of samples anodized in TSA at different voltages and coated with the hybrid (TEOS-GPTMS) sol-gel layer. For comparison, samples anodized in TSA and hydrothermally sealed in boiling deionized water were also tested;

- Use electrical equivalent circuits (EEC) to fit the impedance data in order to determine the more relevant parameters for improving the corrosion resistance of the samples anodized and coated with the hybrid sol-gel layer or hydrothermally sealed;

- Evaluate by rheological characterization the effects of ageing on the stability of the sol-gel hydrolysis solution and by EIS the corrosion protection provided by hybrid sol-gel coatings applied from solutions aged for different times to AA2524 samples anodized in TSA at 14 V;

- Investigate by EIS and salt-spray the compatibility with an epoxy-based coating of the hybrid sol-gel coating applied on AA2524 non-anodized or anodized in TSA at 14 V.

The novelty of the proposed study is because, to the authors' knowledge, in the literature, there is no work available where the corrosion resistance of a hybrid sol-gel coated TSA

anodized AA2524 was evaluated. This original contribution concerns the optimization of the anodizing parameters in order to evaluate the influence of the anodic layer morphology and structure on its sealing by boiling water or sol-gel hybrid coating.

3 LITERATURE REVIEW

3.1 Aluminium alloy 2524

Aluminium alloys from the 2000 series, Al–Cu–Mg, are widely used for aerospace structural components owing to their high strength and low density (ZHENG et al., 2011; SHEN et al., 2016). The most employed brand is the 2024, which is used in parts where toughness, fatigue resistance and mechanical strength are major requirements like in fuselages and shear webs (WANG; STARINK, 2006). However, aircraft designers have required materials with better performance and enhanced corrosion resistance properties than the conventional AA2024 alloy (ZHENG et al., 2011; GRIESHOP; BUCHHEIT, 2014; YANG; ZHAN; LI, 2015). In this way, in the 1990s the Aluminum Company of American (AlCOA) developed the AA2524 alloy, a "cleaner" version of AA2024 alloy with lower and more controlled amounts of alloying elements (DEBARTOLO; HILLBERRY, 2001; ZHENG et al., 2011) as well as decreased amounts of impurities. Nowadays, AA2524 sheets are used as skin sheets in Boeing and Airbus aircrafts (SHEN et al., 2016; SRIVATSAN; KOLAR; MAGNUSEN, 2002).

Table 3.1 shows the comparison between the nominal chemical compositions of the AA2024 and AA2524[1]. In the latter alloy there is a stricter control in the amounts of the two main alloying elements (Cu and Mg) and lower quantities of the Fe and Si contents, which are impurities frequently found in the composition of the 2000 series aluminium alloys. For both alloys, Cr, Mn and Cu are added to control grain structure, weldability and corrosion resistance (BARBUCCI et al., 1998), and specifically Cu is added to improve mechanical resistance (QUEIROZ et al.; 2008). According to Chen et al. (2013), by controlling the impurity contents and the process parameters, AA2524-T3 can exhibit approximately 15–20 % increase in fracture toughness, twice the fatigue crack growth resistance and 30–40 % longer lifetime before failure when compared to AA2024-T3, without loss of strength or corrosion resistance. Additionally, DeBartolo and Hillberry (2001) report significant

[1]International Alloy Designations and Chemical Composition Limits for Wrought Aluminum and Wrought Aluminum Alloys. Available in: <www.aluminum.org/tealsheets>. Access: April 04th 2015.

reduction in the amount of the *S*–type (Al_2CuMg) intermetallic particles in the microstructure of AA2524 when compared to AA2024, as well as a diminution in the quantity of β-type intermetallics, those containing iron, even though in a lesser extent than that verified for the *S* -type ones.

Table 3.1- Nominal chemical compositions (wt %) of the AA2024 and AA2524[1]

	Elements								
Alloy	Cu	Mg	Mn	Zn	Fe	Ti	Si	Cr	Al
2024	3.8-4.9	1.2-1.8	0.9	0.3	0.5	-	0.5	0.1	balance
2524	4.0-4.5	1.2-1.6	0.45-0.9	0.15	0.12	0.1	0.06	0.05	balance

Source: International Alloy Designations and Chemical Composition Limits for Wrought Aluminum and Wrought Aluminum Alloys[1]

Microstructural characterization of the 2024 alloy has been largely studied and much information is available in the literature (BOAG et al., 2009; BUCHHEIT et al., 1997; HUGHES et al., 2010; WANG; STARINK, 2007; QUEIROZ et al., 2008; PALOMINO, 2007) whereas for the alloy 2524 this feature is very limited and the results conflicting. Queiroz et al. (2015) reported the comparison between the AA2024-T3 and AA2524-T3 shown in Figure 3.1. The first alloy is characterized by a fewer number of intermetallics (IMs), which, however, are generally larger than those found in the latter. Two main types of coarse IMs particles (Al-Cu-Mg and Al-Cu-Mn-Fe-(Si)) were identified by energy dispersive X-ray spectrometry (EDS) analysis. In the AA2024-T3, the Al-Cu-Mn-Fe-(Si) particles are present in higher amounts and with different morphologies from those found in the AA2524-T3, whereas the Al-Cu-Mg are more numerous, smaller and more uniformly distributed in the AA2524.

Figure 3.1 - Microstructures of the AA2024-T3 (a) and AA2524-T3 (b) alloys

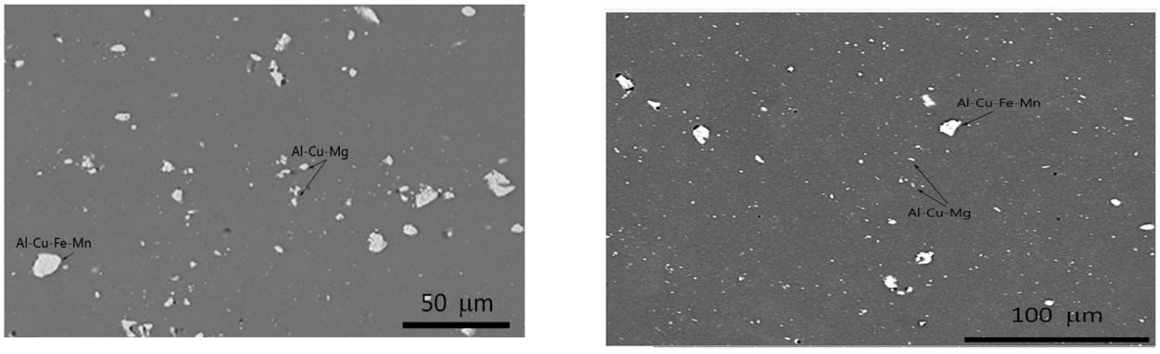

AA2024-T3 AA2524-T3

Source: Queiroz et al., 2015.

Cervantes et al. (2001), Zheng et al. (2011) and Chen et al. (2013) did not identified Mg in the IMs of the 2524 alloy. Cervantes et al. (2001) report that in contrast with the 2024 alloy, the 2524 presents a "relatively uniform second-phase regime with only a few large inclusions having significant Cu" and that the Al-Cu-Mn-Fe precipitates are the dominant IMs with relatively small size (≤ 0.5 μm). Chen et al. (2013) report that the common IMs present in the 2524 alloy are θ phase (Al_2Cu) and Al_7Cu_2(Fe, Mn) phase. In the other hand, Moreto et al. (2011) detected two types of precipitates rich in Cu: $Al_{20}Cu_2(Fe, Mn)_3$ and Al_2CuMg. None of these works presented a detailed microstructure characterization of the AA2524. Regarding the presence of Mg, it must be emphasized that the high reactivity of this element can lead to its removal from the composition of the IMs during the polishing procedure, which could be a possible reason for its absence in some of the results presented in the literature.

Figure 3.2 shows the microstructure of the AA2524 alloy presented by Zheng et al. (2011). The composition analysed by Scanning Electron Microscopy (SEM) shows a large number of IMs containing Al-Cu-Fe-Mn elements, considered as Al_7Cu_2(Fe, Mn) phase, and small IMs containing Al-Cu-Mn considered as $Al_{20}Cu_2Mn_3$ phase. For the AA2024 alloy this latter phase is always present as dispersoids with dimensions in the range of few hundred nanometres (MOLENA DE ASSIS, 2017) and, to the best of our knowledge, it is not classified as an IM particle. In addition, in works with this alloy brand (2024) these dispersoids are hardly identified by SEM analysis (ZHAO et al., 2013; SHEN et al., 2014; QUEIROZ, 2008).

Figure 3.2 - Micrographs showing the distribution and composition of constituent particles in the AA2524 alloy

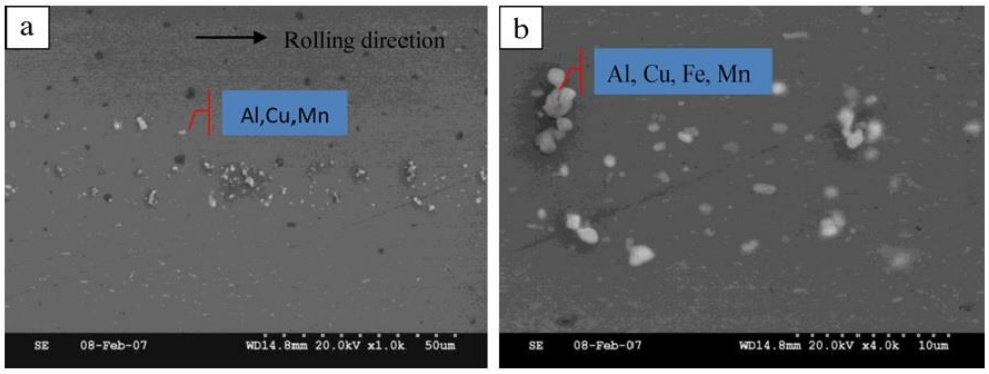

Source: Zheng et. al., 2011.

3.2 Corrosion of aluminium alloys

Although having a low equilibrium potential, aluminium is considered resistant to corrosion in neutral media. This behaviour is due to the formation of a thin aluminium oxide layer (Al_2O_3) on the metal surface, which is protective and inert (TROMPETTE et al., 2010). The thickness of the oxide formed in air at room temperature ranges between 2 and 3 nm (SHIMIZU et al., 1991), however it is adherent and compact, establishing a protective barrier between the metal and the surrounding medium. According to Pourbaix diagram (POURBAIX, 1974) for pure Al, the thermodynamic stability of the aluminium oxide in aqueous systems lies in the pH range between 4 and 8. Above or below these pH values the oxide can be dissolved exposing the base metal to aggressive media, leading to corrosion, which, in most practical cases, occurs locally, giving rise to pitting corrosion (TROMPETE et al., 2010). Nevertheless, the stability domain of the oxide layer is greatly affected by the presence of aggressive ions, especially chlorides, which locally destabilize the oxide layer. In the presence of such ions, aluminium is susceptible to localized corrosion even in neutral media.

Aluminium alloys can corrode in many forms: general, intergranular, exfoliation, filiform, stress-corrosion cracking, corrosion fatigue (THOMPSON et al., 2009), but pitting is the main form, which, in passive metals, consists in the local breakdown of the passive layer (WOLYNEC, 2003). Pitting corrosion of high strength aluminium alloys is an important issue because their structural integrity can be greatly reduced due to fatigue cracks that are easily nucleated at corrosion pits and can rapidly propagate under dynamic or cyclic loads (XU; WANG, 2015).

During pitting formation the zones of attack are determined by the microscopic and submicroscopic characteristics of the passive layer; however, pitting can also occur in metal/environments system apparently free from heterogeneities, but containing aggressive anions, such as chloride ions in the solution (RAMANATHAN, 1988).

The general electrochemical reactions occurring during aluminium corrosion can be represented as follows (TWITE; BIERWAGEN, 1998):

$$Al \rightarrow Al^{3+} + 3e^- \quad (3.1)$$

$$O_2 + 2H_2O + 4e^- \rightarrow 4OH^- \text{ (alkaline or neutral media)} \quad (3.2)$$

$$2H^+ + 2e^- \rightarrow H_2 \text{ (acid, deaerated media)} \quad (3.3)$$

The occurrence of the cathodic reactions (equations 3.2 and 3.3) on the metal surface is extremely enhanced by galvanic coupling effects related to the presence of heterogeneities in the alloys microstructure. These areas present different electrochemical potential in relation to the matrix feeding the corrosion activity. Moreover, in the vicinity of these zones, the passive film is generally less resistant, further increasing the probability of the onset of localized corrosion.

As widely documented in the literature, high strength aluminium alloys have heterogeneous microstructure due to the complex composition and thermomechanical treatments that they are submitted to optimize their mechanical properties. According to Bousquet (2011), the following microstructural features are found in such alloys:

IM particles (from 1 μm to 50 μm) – they are enriched in different alloying elements and are formed during the rapid cooling (quenching) process to which the alloys are submitted after the solution annealing;

Dispersoid particles (from 0.02 to 0.5 μm) – they are formed by the precipitation of transition elements (Cr, Mn or Zr) which are insoluble in the Al matrix. Their role is to control the grain structure, delay the recrystallization process and increase the grain size. They do not contribute to hardening;

Strengthening precipitates (with dimensions between few nanometers and 0.1 μm) – composed of clusters of solute atoms or metastable phases coherent or semi-coherent with the matrix. They precipitate inside the grains and contribute to matrix hardening by blocking the movement of dislocations. They can enlarge due to an overaging process, causing a reduction in the hardness of the material.

Intergranular precipitates (between 0.1 and 0.4 μm) – they precipitate at the grain boundaries or at the subgrains by diffusion of solute atoms found near these regions. When this process is significant it can lead to the formation of regions depleted in alloying elements (Precipitate-Free Zones-PFZ) near the grain boundaries, which can reach few hundred nanometres.

Several investigations show that the IMs are the main responsible for the initiation of the localized corrosion process in high strength aluminium alloys (BIRBILIS; BUCHHEIT, 2005; QUEIROZ et al., 2008; HUGHES et al., 2011; ZHOU et al., 2012). For the 2024-T3 alloy, the more studied brand of the 2XXX series, localized corrosion is initiated by dealloying of S-

phase IMs (Al-Cu-Mg) and ulterior trenching of the Al matrix in their vicinity (BUCHHEIT et al., 1997). With increasing immersion time, Al-Cu-Fe-Mn (QUEIROZ et al., 2008; BOAG et al., 2011) and Al-Cu-Fe-Mn-Si (BOAG et al., 2011) particles are sequentially activated. Due to the similarities between the composition of the IMs found in the microstructure of this alloy and those present in the 2524, the initiation mechanism of local corrosion activity should be the same, even though it can be expected that the process intensity will be lowered in this latter alloy due to the lower number of IMs (DEBARTOLO; HILLBERRY, 2001; ZHENG et al., 2011). Therefore, as high corrosion resistance is required for structural metallic materials employed in an aircraft, the high strength aluminium alloys used in the aerospace industry are protected by a multilayer system.

3.3 Anodizing process

One of the most used methodologies to improve the corrosion resistance of aluminium and its alloys is anodizing, which consists in thickening the naturally formed aluminium oxide layer by applying an anodic potential in baths with appropriate compositions. The process was first reported by Buff, in 1857, who observed that aluminium became covered with an oxide layer when placed in the anodic side of an electrolytic cell (VARGEL, 2004). Afterwards, in the beginning of the 20th century (1911), Frenchman de Saint Martin proposed a first patent for a process where aluminium was anodized in a sulphuric medium containing iron sulphate. This was followed by several developments like those proposed by Bengough and Stewart, for protection of aeroplanes in Duraluminum (1923), the sulphuric anodising process proposed by Gower and O'Brien (1937) and the oxalic anodizing developed during the 1930s in Japan and in Europe (VARGEL, 2004).

During anodizing the structure of the aluminium anodized oxide (AAO) is mainly dependent on the electrolyte composition. Two types of AAO can be produced: the barrier and the porous types (DIGGLE, DOWNIE; GOULDING, 1969; LEE; PARK, 2014). On the one hand, barrier types AAO are produced in electrolytes where the oxide film is almost insoluble. This comprises boric acid solution, ammonium borate or tartrate aqueous solutions (pH 5-7), ammonium tetraborate in ethylene glycol, and several organic electrolytes including citric, malic and glycolic acids. On the other hand, porous AAO are produced in electrolytes where the aluminium oxide is slightly soluble. Those are typically acidic electrolytes, which the

most commercially important are: sulphuric, phosphoric, chromic and oxalic acids at almost any concentration. A basic difference between these two types of AAO is that, at a given temperature, the thickness of the barrier oxide type is solely controlled by the applied voltage, whereas for porous oxide type, the final thickness is determined by the passed charge, i.e., current density and time (DIGGLE, DOWNIE; GOULDING, 1969). Due to the capacity of producing oxide films with desirable engineering properties, like hardness, corrosion and abrasion resistance, the technology for producing porous AAO has received great attention from industry (LEE; PARK, 2014) and has been widely used to protect high strength aluminium alloys in the aerospace industry (GARCÍA-RUBIO et al., 2010).

Porous AAO consists of a close-packed array of columnar hexagonal cells, each consisting of a central pore surrounded by an oxide wall perpendicular to the substrate surface and separated from this latter by a thin compact barrier layer (THOMPSON et al., 1999; LEE; PARK, 2014; WHELAN; CASSIDY; DUFFY, 2013). This process has received interest in the industry due to its almost unique ability to develop this regular porous morphology, which desirable properties such as hardness, corrosion and abrasion resistances can be achieved by adequately controlling the anodizing conditions (DIGGLE, DOWNIE; GOULDING, 1969). The porous layer also provides excellent adhesion base for painting and decorative coloration. Anodized materials can be found in electronic devices, cookware, plasma equipment, vehicles, architectural materials, etc (LEE; PARK, 2014).

The film morphology is shown in Figure 3.3 (LE COZ; ARURAULT; DATAS, 2010). The barrier layer at the pores bottom avoids the direct contact of the aggressive medium with the substrate, providing superior corrosion protection. Due to its opened structure, the porous layer does not contribute to the anticorrosion properties of the system and, in the corrosion protection domain, serves, basically, as an anchoring layer for applying protective organic coatings (GARCIA-RUBIO et al., 2010). For the aeronautic industry, the thickness of the barrier layer is approximately 20 nm and the porous layer is close to 3 μm (GARCIA-RUBIO et al., 2009a; CAPELOSSI et al., 2014).

Figure 3.3 - Cross section view showing the barrier and porous layer

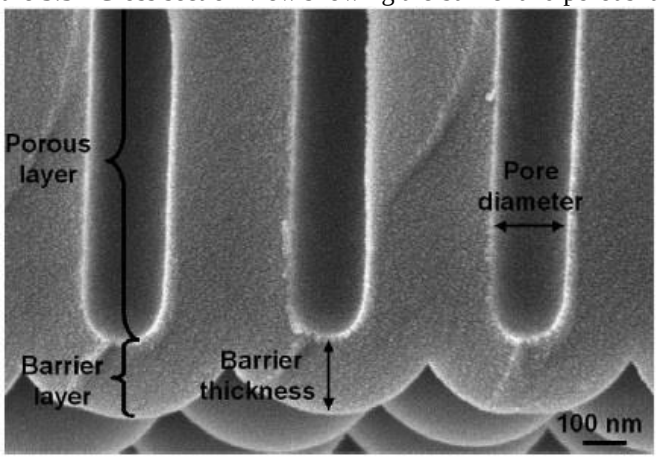

Source: Le Coz; Arurault; Datas, 2010.

The properties of the AAO, like the thicknesses of the two layers as well as the pore diameters can be controlled by appropriate selection of the anodizing bath and the anodizing conditions, such as applied voltage and bath temperature (THOMPSON et al., 1999; WHELAN; CASSIDY; DUFFY, 2013). The literature reports that the porosity and the pore diameter mainly depend on the anodizing voltage and temperature (THOMPSON et al., 1999; (AERTS et al., 2007). With increased anodizing voltage at a constant temperature, the current density increases forming pores with higher diameters and reducing the porosity (DEBUYCK; MOORS; VAN PETEGHEM, 1993; ONO; MASUKO, 2003; AERTS et al., 2007; THEOHARI; KONTOGEORGOU, 2013). In the same sense, with increased temperature and keeping constant the applied voltage the electrolyte aggressiveness increases enhancing chemical dissolution of the anodic film and widening the pores (AERTS et al., 2007). On the other hand, the barrier layer thickness is directly proportional to the anodizing voltage, with thickening rate usually in the range from 1.0 to 1.5 $nm.V^{-1}$ depending on the electrolyte composition (BOGDANOV et al., 1990; BREVNOV et al., 2004; PATERMARAKIS; PLYTAS, 2016). Conversely, the thickness of the porous layer is proportional to the total charge involved in the electrochemical oxidation (LEE; PARK, 2014), which depends on the applied current density and anodizing time (DIGGLE; DOWNIE; GOULDING, 1969).

3.4 Mechanism of anodic film formation and growth

The formation mechanism of barrier and porous layers in aluminium alloy has been studied for more than five decades (ZHU et al., 2009). Aluminium oxide is a poor electronic conductor and, therefore, the charge transport during AAO growth is ensured by means of mobile ions. Generally, during AAO growth, it is accepted that Al^{3+} cations as well as oxygen bearing ions, O^{2-} or OH^-, are mobile species, being involved in the growth of the anodized layer. According to Lee and Park (2014), when a valve metal is anodized, the ionic transport across the oxide layer takes place mainly due to the high electrical field that is established through the layer, even though the authors emphasize that some models predict that stress gradients within the layer may also contribute to the ionic transport. According to the proposed growth mechanism, Al^{3+} ions egress and O^{2-}/OH^- ions ingress sustain the barrier layer thickening. Conversely, the inward migration of O^{2-}/OH^- ions is the solely responsible for porous layer formation, i.e., Al^{3+} ions responsible for ionic current transport during the growth of porous AAO layer are ejected to the electrolyte at the oxide/electrolyte interface by one of several proposed mechanisms (THOMPSON et al., 1997; GARCIA-VERGARA et al., 2007a). Therefore, during the barrier layer growth, the oxide thickening reactions (oxide formation) occur simultaneously at the oxide/electrolyte and at the metal/oxide interface whereas during the porous layer thickening process new oxide is formed solely at the metal/oxide interface.

In the review article published by Lee and Park (2014) the authors report that the following reactions take place during the growth of the AAO layer:

(i) At the metal/oxide interface

$$Al \longrightarrow Al^{3+}_{(ox)} + 3e^- \tag{3.4}$$

$$2Al^{3+}_{(ox)} + 3O^{2-}_{(ox)} \longrightarrow Al_2O_3 \tag{3.5}$$

(ii) At the oxide/electrolyte interface

$$2Al^{3+}_{(ox)} + 3O^{2-}_{(ox)} \longrightarrow Al_2O_3 \tag{3.6}$$

$$Al_2O_3 + 6H^+_{(aq)} \longrightarrow 2Al^{3+}_{(aq)} + 3H_2O_{(liq)} \tag{3.7}$$

$$Al^{3+}_{(ox)} \longrightarrow Al^{3+}_{(aq)} \tag{3.8}$$

$$2O^{2-}_{(ox)} \longrightarrow O_{2(g)} + 4e^{-} \quad (3.9)$$

$$2H_2O_{(liq)} \longrightarrow O^{2-}_{(ox)} + OH^{-}_{(ox)} + 3H^{+}_{(aq)} \quad (3.10)$$

In the proposed mechanism, reactions (3.7) to (3.9) induce the dissolution of the oxide layer, contributing to reduce the current efficiency, whereas reaction (3.10) represents the heterolytic dissociation of water molecules, which supplies oxygen anions to form the anodic oxide. Reaction (3.5) results in the growth of the anodic oxide film at the metal/oxide interface by ingress of O^{2-}, whereas reaction (3.6) represents the same process at the oxide/electrolyte interface by Al^{+3} ions egress.

As the anodizing of porous AAO takes place in acid baths, O'Sullivan and Wood (1970) propose that O^{2-} or OH^{-} ions can also be generated from the interaction between water molecules with electrolyte anions adsorbed onto the positively charged alumina surface. Some of these acids can form ions with different valences by successively losing protons as exemplified in eq. (3.11) for sulphuric acid (O'SULLIVAN; WOOD, 1970):

$$H_2SO_4 \rightarrow H^+ + HSO_4^- \rightarrow H^+ + SO_4^{2} \quad 3.11$$

Figure 3.4 schematically shows the interaction between adsorbed water molecules and SO_4^{2-} anions. Figure 3.4 (A) illustrates the formation of hydrogen bonds between the hydrogen atoms of adsorbed water molecules and the oxygen atoms of the adsorbed oxyanions. This process weakens the covalent O-H bonds within the adsorbed water molecules and, with the help of the electric field, the hydrogen cation is removed from its original bond establishing a covalent bond with the adsorbed oxyanion (Figures 3.4 (B) and (C)). If only one hydrogen is removed, OH^- is formed, whereas removal of both hydrogen cations (H^+) results in O^{2-} ion (O'SULLIVAN; WOOD, 1970).

Figure 3.4 - Schematic representation of O^{2-} and OH^- ions generation from water interacting with adsorbed SO_4^{2-} anions.

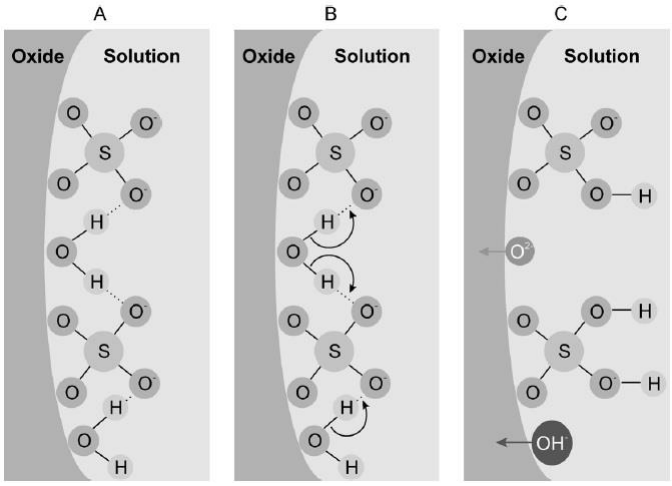

Source: O'Sullivan; Wood, 1970.

Figure 3.5 schematically shows the elementary reactions proposed by Lee et al. (2014) that are possible to occur at the interfaces during the growth of the (a) barrier and (b) porous AAO layer. The barrier layer is formed 60 % at the metal/film interface and 40 % at the film/electrolyte interface (THOMPSON et al., 1999); therefore, the ionic current within the oxide layer is mainly transported by oxygen bearing ions. This ionic transport proportion is approximatively maintained during porous AAO growth (TAKAHASHI; NAGAYAMA, 1978), however, as already mentioned, Al^{3+} ions does not contribute to the formation of new oxide at the oxide/electrolyte interface and are ejected to the acid electrolyte within the pores.

Figure 3.5 – Schematic diagrams showing elementary interfacial reactions for (a) barrier and (b) porous layer growth.

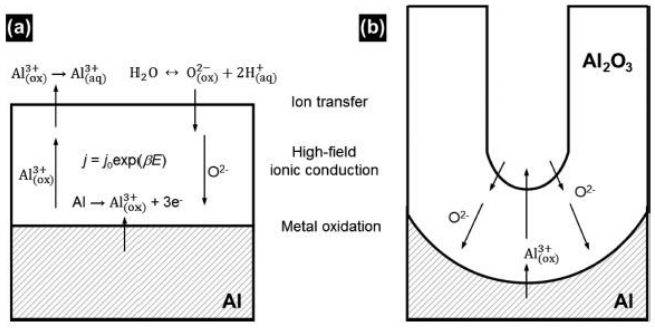

Source: Lee et al., 2014.

Figure 3.6 (a) schematically shows the current variation with time (current transient) during potentiostatic anodization of a barrier and a porous type AAO layer. For the barrier type oxide, when the anodic potential is applied, the thin barrier film starts to thicken over the entire surface of the metal resulting in a gradual increase of the series resistance (R) of the anodizing circuit. At this initial stage, current is maintained at the limit value (i_{limit}) of the power supply, and the potential (U) linearly increases with time according to the relation: U = R.i (LEE, PARK, 2014). After the barrier layer thickness (proportional to the resistance) has reached a certain value in such a way that Ri_{limit} equals the chosen anodizing potential, the applied potential stabilizes and the current starts to decay exponentially until it reaches a constant value. This constant current is typically very low and corresponds to an electronic current (DIGGLE; DOWNIE; GOULDING, 1969). At this point, the thickness of the barrier layer (t_b) achieves a constant value, which is dependent on the applied anodizing potential. The dependence of t_b with the applied potential (V) is denominated anodizing ratio (AR = t_b/V), the inverse of which corresponds to the electric field (LEE; PARK, 2014). For this type of anodizing, the barrier layer thickening occurs with the highest efficiency and at both interfaces: Al/oxide by O^{2-} ions ingress and oxide/electrolyte by Al^{3+} ions egress (ZHU et al., 2009).

For the growth of porous AAO layer the sequence of phenomena is exactly the same to that described for the barrier layer oxide up to point “A”(Figure 3.6 (a)), where both curves start to diverge. From this point on, the decreasing rate of the current transient for the porous AAO becomes lower than that for the barrier layer, and, after a short period, a minimum is reached in the current transient curve (Figure 3.6 - region II). This region of the curve has been associated with pore initiation (DIGGLE; DOWNIE; GOULDING, 1969) and it is suggested that current is concentrated in certain regions of the oxide layer either associated with local imperfections (O’SULLIVAN; WOOD, 1970) or to cracks developed in the barrier layer due to accumulated tensile stress (THOMPSON, 1997), both issues developing penetration paths for the electrolyte and leading to local thinning of the AAO with the consequent local increasing in the electric field. At this point, a high number of embryo pores are submitted to field-assisted oxide dissolution (FAD) (ascending part of segment II) and an interaction with the acid electrolyte results in shallow irregular pores (LEE; PARK, 2014; ZHU et al., 2009).

Region II is terminated by a local maximum, which has been associated with the ready diffusion of the electrolyte to the embryo pores base (LEE; PARK, 2014). Following, region III is characterized by a new current decrease that has been attributed to a decrease in the

pores density ascribed both to deepening of dominant pores formed by merging of several embryo pores and the dying of some of these latter that do not succeed to growth (LI; ZHANG; METZGER, 1998). As a consequence of pore development, the electric field becomes concentrated at the base of major pores, which are the precursors of regular pores formation (ZHU et al., 2009). At this stage, the outward migrating Al^{3+} ions do not contribute anymore to the thickening of the oxide layer and are ejected to the electrolyte at the pores base due to the enhanced electric field; therefore, the oxide layer is formed only at the metal/oxide interface by continuous ingress of O^{2-} ions (ZHU et al., 2009). Finally, the current transient reaches a steady state value (region IV) where the pores growth in a stable manner. The longer the anodizing time, the thicker the porous oxide layer.

Figure 3.6 (b) depicts the growth process of the porous layer associated with each one of the regions demarcated in Figure 3.6 (a). The proposed model takes into account that the formation mechanism of the pores occurs by field-assisted dissolution (FAD), which is widely accepted to explain the growth of the AAO porous layer (ZHU et al., 2009). The pores deepen downward by FAD due to the dissolution of the barrier layer (reaction 3.7), being a process assisted by the acidic electrolyte. When this process becomes dominant, the thickening of the porous layer occurs and Al_2O_3 is formed only at the metal/oxide interface, regenerating the barrier layer dissolved at the oxide/electrolyte interface (ZHU et al., 2009).

Figure 3.6 - (a) Schematic current-time curve for the potentiostatic anodization of a barrier and a porous AAO film. (b) Schematic representation of the four segments growth process of the porous AAO layer assisted by the FAD model.

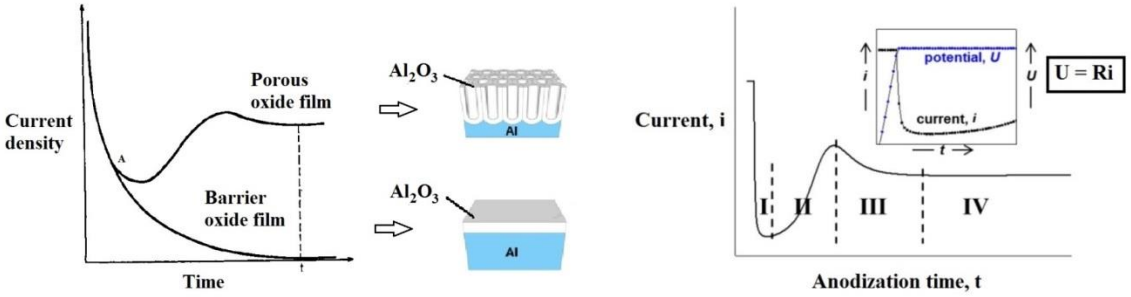

(a)

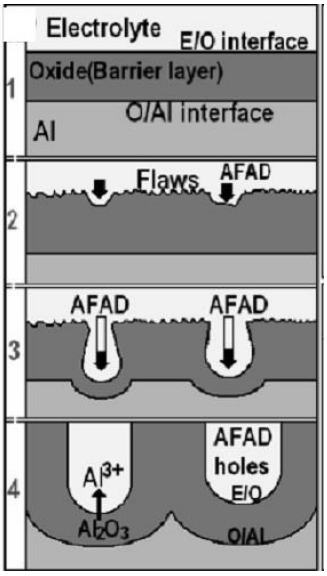

(b)

Source: Lee; Park, 2014; Diggle; Downie; Goulding, 1969; Zhu et al., 2009.

Two key points are associated with the current transient curve associated with the growth of the porous AAO layer depicted in Figure 3.6 (a): the first one is the formation of the pore embryo (begin of region II) and the second is the steady state current region, where pores grow and the porous layer thickens. Whereas it is almost consensual that field assisted dissolution (FAD) occurs in the initial stages of pore formation (Baron-Wiechéc et al., 2013; Garcia-Vergara et al., 2007a), different mechanisms have been proposed to explain the steady state pore growth regime, all of them considering that the barrier layer thickness must be kept constant due to a balance between the oxide layer growth at the metal/oxide interface and its dissolution at the oxide/electrolyte interface. In the FAD model it is considered that at the oxide/electrolyte interface aluminium oxide is decomposed to Al3+ and O2- due to the high electric field (HOAR; MOTT, 1959). O'Sullivan and Wood (1970) propose that the high electric field polarizes the Al–O bonds. According to these authors (O'SULLIVAN; WOOD, 1970) near and at the oxide/electrolyte interface the Al–O bonds increase in length because the field tends to pull the O2- ions into the oxide and to push the Al^{3+} ions into the solution, lowering the activation energy for bond dissociation, thus facilitating the solvation of Al^{3+} ions by water molecules. The process would be faster at the pore base due to concentration of the electric field in this region, providing pore growth. Garcia-Vergara et al. (2007a) investigated the development of a porous AAO layer formed in chromic acid electrolyte on a sputtered-deposited aluminium substrate at which a tungsten tracer was introduced. The

authors verified that both the aluminium and the tungsten tracer were lost to the electrolyte at the pores base. Moreover, it was verified that the tungsten band progressed into the porous layer with low distortion in relation to its initial geometry in the sputtered aluminium deposit. In the discussion section of the paper, the authors compared these features with those found for porous AAO layers formed in other acidic electrolytes on tracers-bearing sputtered-deposited aluminium where anions incorporation takes place (no chromium was detected in the investigated anodic film), and where the tracers are retained within the film (no loss to the electrolyte) but in a distorted band in relation to their initial position in the sputtered deposit. Taking into account these differences, they proposed that field assisted dissolution must play a key role in the growth of the porous AAO layer in chromic acid electrolyte (GARCIA-VERGARA et al., 2007a).

The direct cation ejection mechanism considers that Al^{3+} ions are lost into the electrolyte without contributing to the porous oxide formation (LEE; PARK, 2014). It is supported by the fact that the amount of Al^{3+} ions found in the electrolyte after anodizing is superior to that generated by pore formation (LEE; PARK, 2014). Pore filling experiments performed by Takahashi and Nagayama (1978) by anodizing a porous AAO layer in a 0.5 $mol.L^{-1}$ H_3BO_3-0.05 $mol.L^{-1}$ $Na_2B_40_7$ solution (pH = 7.4, 20 °C), therefore, a barrier AAO layer forming electrolyte, have confirmed that the transport number of Al^{3+} ions is 0.4. The authors (TAKAHASHI; NAGAYAMA 1978) also suggested that during the pore filling experiment the current preferentially flows through the progressively filled pores instead of through the walls of the porous layer. Consequently, considering that the Al^{3+} ions do not contribute to the porous layer formation it is possible to suppose that much of the Al^{3+} ions would be lost to the electrolyte through a mechanism that does not involve oxide layer formation (LEE; PARK, 2014). Zhou et al. (2012a and 2012b) also propose that the decreasing efficiency of film formation with decreasing current density and with increasing temperature (at a constant current density) during porous anodizing of aluminium in oxalic acid solution indicate enhanced field assisted ejection of Al^{3+} cations at the pore base during porous oxide growth.

Garcia-Vergara and co-workers produced porous AAO layers from sputtered deposited aluminium substrate containing a tungsten tracer in different anions containing electrolytes and analysed the formed films mainly by TEM and Rutherford Backscattered Spectroscopy (RBS) (GARCIA-VERGARA et al., 2006c, 2007d, 2007e). Similar results were reported for all the electrolytes and will be briefly commented. Initially, the results of the RBS analysis showed that the tungsten tracer was retained in the oxide film, i.e., it was not dissolved in the

different electrolytes. This is at variance with the previsions of the conventional models for pore growth based on field-assisted ejection and dissolution, as aluminium and tungsten should migrate towards the film electrolyte interface and dissolve in order to maintain a constant thickness of the barrier layer. The results of the TEM analysis showed that, when the porous layer was more developed (higher anodizing time) the tracer band within the porous wall lies ahead of the tracer band below the pore bottom. This was also an outcome that goes against the expectations of the field-assisted dissolutions models, which predict a faster migration rate at the pore bottoms due to the increased electric field in this region; therefore, the tungsten species distribution within the film was inverted with respect to expectations of the dissolution models. Moreover, there was no tungsten-rich layer at the base of the pores, which should occur from preferential dissolution of aluminium species if tungsten species were to reach the film/electrolyte interface. Based in these results and in other articles published by the Manchester Group (GARCIA-VERGARA et al, 2006a, 2007b), it was proposed that during the porous layer growth there is no significant alumina dissolution at the oxide/electrolyte interface, and that the "the constant thickness of the barrier film is maintained by flow of oxide from the barrier layer towards the cell wall, driven by compressive stresses from electrostriction and possibly through volume expansion due to oxidation" (GARCIA-VERGARA et al, 2006a). According to the authors, the flow is facilitated by the plasticity of the barrier layer due to participation of most of the film constituents in ionic transport, whereas the displacement of the anodic oxide towards the cell wall is accommodated by the expansion factor of the film in relation to the oxidized metal (GARCIA-VERGARA et al, 2006a). Figure 3.7 shows a schematic diagram of tungsten distribution within the porous AAO layer for increasing anodizing time (GARCIA-VERGARA et al, 2006a).

Figure 3.7 - Schematic diagrams showing the relative distributions of tungsten in anodic films at intervals of 60 s of anodizing at 5 $mA.cm^{-2}$ in 0.4 $mol.L^{-1}$ phosphoric acid solution at 293 K: (a) 180 s (b) 240 s and (c) 300 s. The distribution of (c) assumes a similar displacement of tungsten as in the previous 60 s.

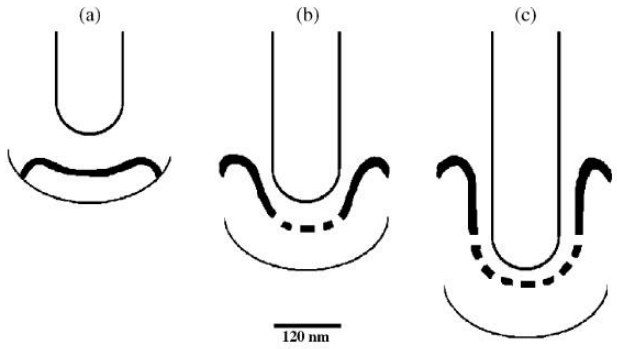

Source: Garcia-Vergara et al., 2006a.

In further development of the flow model, the authors verified that the tungsten tracer is not uniformly distributed within each cell, which, consistently with the slow outward migration of W^{6+} ions in the barrier layer, is constituted by an outer region (close to the anodizing bath) of alumina containing little tungsten relative to the remainder of the cell (GARCIA-VERGARA et al., 2009). Moreover, the presence of a thin band with increased tungsten content was observed at the cell boundary, which was suggested to result from the transport of tungsten enriched in the alloy to the cell boundary by the moving alloy/film interface (GARCIA-VERGARA et al., 2009). The behaviour of tracer specimens with different migration rates in the alumina oxide when compared to Al^{3+} was also investigated, and their distribution within the anodic film as well as their retention rate in the anodic film were verified to be coherent with the predictions of the flow model (GARCIA-VERGARA et al., 2010).

Other authors have suggested that pore growth takes place due to chemical dissolution at the oxide/electrolyte interface due to Joule's heat-induced effect (KELLER; HUNTER; ROBINSON, 1953; LI; ZHANG; METZGER, 1998). According to the model, at high voltages, the temperature may locally rise at the pore bottom due to Joule heating effect and local oxide dissolution, introducing a large thermal stress in the barrier layer and at the metal/oxide interface, thus, assisting oxide dissolution (LI; ZHANG; METZGER, 1998). To support their model, Li et al. (1998) report data from the literature where a temperature rise of 25 K was achieved at the pore bottom in the absence of convection. However, this growth model has been highly discredited by other researchers results reporting that only negligible

temperature rise (< 1 K) takes place at the pore base at the steady state (NAGAYAMA; TAMURA, 1968, O'SULLIVAN; WOOD, 1970).

3.4.1 Electrolyte anion incorporation into aluminium anodic oxide film

Incorporation of anions from the electrolyte into AAO during anodizing is a well-known phenomenon (DIGGLE; DOWNIE; GOULDING, 1969; LEE; PARK, 2014). It occurs by inward migration under the influence of the electric field (E) during aluminium anodization. They are initially incorporated into the barrier layer as O_2^- by decomposition of H_2O and also as ions supplied by the anodizing bath (for example, SO_4^{2-} ions for sulphuric acid solution and PO_4^{3-} for phosphoric acid solution) and then in the pore walls during the growth of the porous layer (PATERMARAKIS; CHANDRINOS; MOUSSOUTZANIS, 2001; FARNAN; DUPREE, 1989). In general, the incorporated anions are larger than O^{2-} and become immobile through the anodic layer once the strength of the electric field decreases with the distance from the surface. This leads to the formation of a layer of relative pure alumina near the metal/oxide interface, as schematically shown in Figure 3.8 (FUKUDA; FUKUSHIMA, 1989; SKELDON; SHIMIZU; THOMPSON; WOOD, 1995; GARCIA-VERGARA et al., 2006c; LE COZ; ARURAULT; DATAS, 2010). Garcia-Vergara et al. (2006c) report that there is no significant field-assisted dissolution of the alumina that would eliminate the presence of electrolyte species within the AAO.

Figure 3.88 – Schematic diagram of the porous anodic film showing the outer region of anion contaminated (shaded) and the relative pure inner pore wall oxide (cell boundary band).

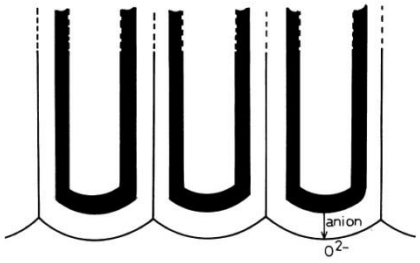

Source: Thompson, 1997.

Fukuda and Fukushima (1989) studied the SO_4^{2-} incorporation into the AAO films. They found that a relatively small ion content was present near the wall/solution interface, and that

it increased with the distance from the oxide surface, reaching a maximum at an intermediate distance between the wall/solution interface and the cell boundary, then decreasing slowly (FUKUDA; FUKUSHIMA, 1989, MATA-ZAMORA; SANIGER, 2005). This result was similar to those obtained with phosphoric acid and oxalic acid anodizing baths (FUKUDA; FUKUSHIMA, 1989).

The anions species are incorporated into the porous anodic films at the level of 12–14 wt.% sulphate, 6–8 wt.% phosphate and 2.4 wt.% oxalate (THOMPSON, 1997). Due to their larger sizes, they may influence the flow of material within the barrier layer, affecting cell and pore dimensions (GARCIA-VERGARA et al., 2006c).

The amount of anions incorporated into the anodic film increases with anodizing voltage (ZHOU et al., 2011; MÍNGUEZ-BACHO et al., 2015) due to the increase of the current density and the stronger electric field, based on the mechanism of anodic film formation and growth explained in the item 3.4. Han et al. (2013) observed a decrease in the anion incorporation rate with anodizing time related to the reduction of the electrolyte concentration in the steady state growth condition (voltage, temperature and current fixed).

The addition of tartaric acid (tartrate ions) into the anodizing bath does not significantly modify either the electrical properties or the morphology of the porous anodic film (CURIONI et al., 2009), as it is a weak acid not very aggressive to the oxide film formed during anodizing (CURIONI et al., 2009; BOISIER et al., 2008). Moreover, it requires high temperature and an applied voltage higher than 150 V to produce a dissolving action similar to that of sulphuric acid, thus, in the practical voltages applied during TSA anodizing there is no incorporation of tartrate ions into the anodic film (BOISIER et al., 2008). The major contributions of tartaric acid into the anodizing bath seem to be its influence in the field-assisted dissolution process during pore initiation (BOISIER et al., 2008; IGLESIAS-RUBIANES et al., 2007), decreasing the dissolution rate of the anodic oxide (CURIONI et al., 2009) and by limiting the dissolution of the outwardly mobile Al^{3+} species (BOISIER et al., 2008). Arenas, Conde and Damborenea (2010) and Curioni et al. (2009) reported that the addition of tartaric acid to the sulphuric acid anodizing bath improves the corrosion resistance of the anodic layers after hydrothermal sealing due to the presence of residual tartaric acid in the pore solution after anodizing. Arenas, Conde and Damborenea (2010) proposed a mechanism that assumes that the residual tartaric acid inside the pores might dissociate as a consequence of pH increase during the hydrothermal sealing, forming chelates with Cu(II) cations present in the oxide film. The removal of Cu^{2+} from the internal walls of the pores

would reduce the heterogeneity of the anodic film, leading to a more resistant layer (ARENAS; CONDE; DAMBORENEA, 2010).

3.4.2 Effect of alloying elements and intermetallic particles in the growth and morphology of the anodic layer

The literature shows that, in aluminium alloys, the composition and the microstructure of the matrix have strong influences in the morphology and composition of the AAO layer. It deviates from the ordered structure found in pure aluminium, negatively affecting its corrosion resistance. Investigations show that during anodizing the IMs particles can oxidize at faster, slower or at similar rates when compared to the alloy matrix (MA et al., 2001a; GUMINSKI et al., 1968; COTE et al., 1969; COTE; HOWLETT; LAMB, 1970) or remain relatively unchanged (COTE et al., 1969; COTE; HOWLETT; LAMB, 1970). The specific behaviour depending on the anodizing conditions and on the IM particles and electrolyte compositions (FRATILA-APACHITEI et al., 2002, 2004; SAENZ DE MIERA et al., 2010b). As a consequence of the differences in the composition between the IM particles and the aluminium matrix, it is reported that the composition of the oxide layers developed above both phases are different, and that the oxide layers formed above the particles are more defective and do not exhibit the usual honeycomb morphology associated with porous AAO (FRATILA-APACHITEI; DUSZCZYK; KATGERMAN, 2002; MA et al., 2001b). Moreover, oxygen generation can take place on semiconducting oxide particles embedded in the oxide formed above them (BROWN et al., 1988). All these features contributing to introduce defects and flaws in the anodized layer. In addition, in aluminium alloys where copper is present in solid solution, such as those from the 2000 and 7000 series, it is also reported the incorporation of copper in metallic or oxidized form in the anodic film (CURIONI et al., 2008a). This latter process is fundamental for triggering oxygen generation, which has an important role in the defective structure of the AAO layers formed above the matrix of high strength aluminium alloys, as will be discussed below.

The rate of anodic film formation at the film/electrolyte and metal/film interface can be significantly influenced by high concentrations of alloying elements in the alloy (CROSSLAND et al., 1999; HABAZAKI et al., 1997a). According to Thompson et al. (1999) the thermodynamic factor that governs cation oxidation is the Gibbs free energy per

equivalent ($\Delta G/n$). Alloying elements for which $\Delta G/n$ is less negative than $(\Delta G/n)_{Al}$ are not oxidized at the beginning of the anodizing process, and the anodic layer is initially formed due solely to aluminium oxidation. However, as a consequence of this process, the surface composition of the alloy matrix becomes enriched with these specific alloying elements until a critical enrichment level is reached. From this point, the alloying elements can also be oxidized and incorporated into the oxide layer (THOMPSON et al., 1999). On the other hand, alloying elements with more negative ($\Delta G/n$) must be immediately oxidized with aluminium entering in the composition of the oxide layer (PAEZ et al., 2000). The cations formed from the oxidation of the alloying elements and entering in the anodic film may migrate faster or slower than Al^{+3} ions under the influence of the high electric field; as a consequence, the oxide film composition may be, respectively, depleted (PAEZ et al., 2000) or enriched (GARCIA-VERGARA et al., 2007c) in each specific element when compared to the base matrix.

Due to the microstructural complexity of Al alloys with high mechanical strength and in order to separate the phenomena associated with the matrix and with the IM particles, many studies about the effects of the microstructure in the anodized layer were developed using model alloys and/or model second phase particles (IMs). Habazaki et al.(1995) and Paez et al. (1996) investigated the formation of barrier AAO layer (formed in ammonium pentaborate) on Al-Cu model alloys and showed that during anodizing a ~2-5 nm Cu-rich layer (~40 % at%) was formed just beneath the barrier layer due to preferential oxidation of aluminium, and which thickness was independent on the applied potential. The authors suggested that the incorporation of copper into the anodic film occurs at sites where Cu has achieved a critical concentration “by oxidation of discrete copper-rich regions, created by prior oxidation of aluminium, at the alloy/film interface” (HABAZAKI et al., 1995) and that this process introduces defects in the oxide layer structure. The results also revealed that the oxide film was Cu-depleted in comparison with the bulk alloy, which was ascribed to a faster migration of Cu^{2+} ions within the barrier film and their direct ejection to the solution at the film/electrolyte interface. Moreover, as a consequence of the proposed mechanism, “copper is incorporated non-uniformly both along the alloy/film interface, at a particular time, and at a particular site with time” (HABAZAKI et al., 1995) and “having achieved a steady (surface) level, incorporation of copper species into the alumina film proceeds at a constant rate, giving greater extents of incorporation than in the early stages of anodic oxidation” (PAEZ et al., 1996), i.e., even though copper atoms (oxidized or not) are incorporated in the AAO

microstructure, the copper content at the copper enriched layer is kept approximately constant. This model was lately extended to the generation of porous AAO in a study with a model Al-3.5 wt % Cu alloy (PAEZ et al., 2000). In this work it was reported that oxygen generation associated with Cu oxidized particles (Cu-O) plays an important role in the morphology of the anodized layer as a consequence of the formation of oxygen gas filled voids within the oxide layer microstructure. Significant pressure build up inside these voids causes their rupture, oxygen gas is liberated and the anodic film is deformed and cracked with consequent electrolyte access to the alloy surface. This causes the underlying matrix dissolution and subsequent re-anodizing. According to the authors this sequence of phenomena occurs concomitantly and cyclically, resulting in films with enhanced porosity (PAEZ et al., 2000).

From the discussion presented above, it is clear that during anodizing and prior to copper incorporation in the oxide layer, copper concentration builds-up at the alloy/film interface until a critical concentration is reached. From this point on copper oxidation can take place as well as oxygen generation at the semiconducting copper oxide particles (most likely CuO) distributed within the anodic film (IGLESIAS-RUBIANES et al., 2007; GARCIA-VERGARA et al., 2006b; MOLCHAN et al., 2010). This reaction is an electrochemical process that occurs within the barrier anodic layer close to or at the alloy/film interface (THOMPSON et al., 1999). The source of oxygen is the mobile O^{2-} ions that migrate towards the film/metal interface to form the barrier layer. The following reactions can be responsible for oxygen generation:

$$2O^{2-} \rightarrow O_2\uparrow + 4e \text{ or} \tag{3.12}$$

$$4OH^{-} \rightarrow O_2\uparrow + 2H_2O + 4e \tag{3.13}$$

The oxygen gas forms voids within the amorphous alumina film, which can grow, coalesce and eventually burst when pressure is sufficiently high. According to the literature, their sizes are in the range 10-100 nm with gas pressures of several hundred MPA (THOMPSON et al., 1999). In addition, the presence of such voids hinders ionic migration and the film is developed with roughness at both the metal/oxide(film) and oxide(film)/electrolyte interfaces, generating an oxide layer with non-uniform thickness. For alloys with low addition of alloying elements, oxygen gas may be trapped inside the film, because the pressure is insufficient to cause rupture and local detachment of the alumina. However, the greater the amount of alloying elements (specifically copper for 2XXX Al alloys) incorporated in the

oxide layer, the higher the number of oxygen-filled voids and the higher the probability of void burst. The rupture of the anodic film as a consequence of this process results in the access of the anodizing electrolyte to the base metal. This provides a preferential path for current flow and the alloy is reanodized until a new crack is produced. In high strength Al alloys, which bear a high Cu content, the irregular morphology is primarily a result of these rupture and growth processes (GARCIA-VERGARA et al., 2006b; CURIONI et al., 2008a). In Figure 3.9 is possible to observe the difference in the film morphology of a 99.999% Al and Al-0.05% Cu substrate, showing the occurrence of defects only in the Cu containing alloy (MOLCHAN et al., 2010).

Figure 3.9 – Comparison in the film formation of (a) 99.999 % Al and (b) Al-0.05 % Cu.

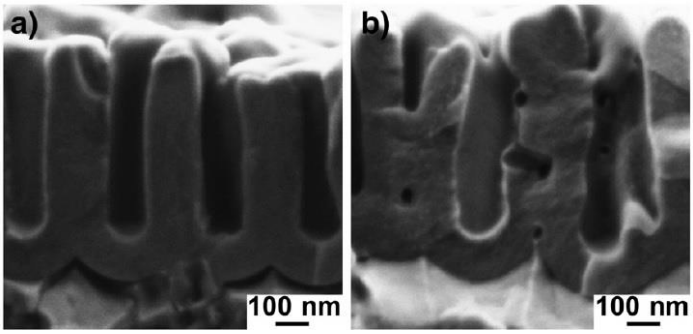

Source: Molchan et al., 2010.

The role of IM in the microstructure and morphology of porous AAO layers is also of great interest, as these microstructural features are abundant in high strength aluminium alloys (CHEN; GAO; WEI, 1996; BOAG et al., 2009; HUGHES et al., 2010). Curioni et al. (2008a) used a commercial 2024-T3 aluminium alloy, Al-Cu model alloy and high purity aluminium to investigate the effect of IM particles in the anodizing of aluminium alloys 2024-T3. Potentiodynamic polarization experiments of the 2024-T3 alloy in sulphuric acid solution at different sweep rates showed the presence of two characteristic current peaks indicating the contribution of additional electrochemical reactions to the total current. The first one, at 0 V (SCE), had little or no shape dependence on the sweep rate, whereas for the other, positioned in the potential range between 2.5 and 8 V (ECS), the commencement potential was not affected by the sweep rate but the peak terminated at increased potentials for increasing sweep rates. SEM analysis of samples after selected anodizing procedures allowed to ascribe the first peak to the oxidation of Mg-rich IMs (S phase), whereas the second was attributed to the

oxidation of IMs with low Mg content (basically Cu-rich ones). Therefore, at anodizing potentials higher than the second peak, most of the particles that are exposed to the electrolyte at the alloy surface must be oxidized. The influence of the processes associated with these peaks in the morphology of the anodized layer was investigated by the authors by means of TEM analysis of the cross-section of AAO layers of AA2024 samples submitted to low potential anodization. At potentials above 6 V the typical layered structure already reported by Iglesias-Rubianes et al. (2007) in a previous article (commented below) was observed. According to the authors, above this potential, oxygen generation takes place in oxidized copper particles embedded in the anodic film contributing to barrier layer rupture (oxygen-filled voids burst), access of the electrolyte to the alloy surface and reanodizing originating the layered morphology. On the other hand, AAO produced below 3 V presents a similar morphology to pure Al as the anodic film is free from copper ions (copper enriched particles can be occluded in the film but not oxidized) and no oxygen is generated within the barrier layer. Finally, between 3 and 6 V, copper-rich regions can develop and oxidize, however in this potential range oxygen cannot be produced and the layered morphology of the AAO layer was also not observed.

By employing model alloys produced by magnetron sputtering representing IM particles and the matrix regions of AA2024-T3 and AA7075-T6 alloys, Saenz de Miera et al. (2008) confirmed that the transient anodic currents during potentiodynamic polarization of the commercial alloys was really associated to specific IM particles composition. The experimental results showed that the current density in the potentiodynamic polarization curves for the model IMs presented a rapid increase at potentials close to the peak potentials of the potentiodynamic curves for the commercial alloys (2024-T3 and 7075-T6), showing their fast oxidation at these specific potentials. The authors also verified that during galvanostatic anodizing of the commercial alloys a potential plateau was observed when the potential reached the value required to oxidize the model IMs, indicating that second phase particles (IMs) with composition similar to the model IMs were preferentially oxidized. Consumption or isolation of these second phase particles from the alloy matrix during the anodizing procedure produced a potential rise, indicating that matrix oxidation with oxide layer formation becomes the predominant process. In the paper, the preferential oxidation of model IMs at low potentials was further confirmed with an experimental setup where galvanostatic anodizing was performed in galvanically coupled model alloy matrix (Al-1.3 at.%Cu)-model second phase particle (Al_2Cu). For the electrically coupled specimens the

supplied current was almost totally consumed in the oxidation of the model IM during the initial stage of the anodizing procedure, keeping the cell potential at relatively low values; however, as the coupled model IM was oxidized a rapid potential rise in the circuit was verified and the current flowing through the model IM felt to negligible values. Interestingly, TEM micrographs also revealed that the morphology of the porous AAO layer formed in the coupled model alloy was very similar to that found in a 2024-T3 alloy submitted to galvanostatic anodization, and was constituted of two different regions: an outer layer, generated at relatively low potential (when most of the anodizing current was flowing through the model IM), with a finer structure, and an inner layer with coarser morphology, developed after consumption of the model IM, when the potential increased and the supplied current was mostly passing through the model alloy circuit. Similar results both for the potential and current behaviour and for the porous AAO morphology formed on the model alloy were reported by Saenz de Miera et al. (2010a) for a model alloy (Al-1.3 at.%Cu) galvanically coupled to a model IM with more complex composition (Al_7Cu_2Fe).

Saenz de Miera et al. (2010b) used a commercial Al 7075-T6 alloy, a model 7075 alloy (Al-5 at.% Cu) and several model second phase particles obtained by magnetron sputtering to disclose the role of IMs in the formation of AAO layers in sulphuric (SAA) or chromic (CAA) acid anodizing. From the surface analysis of the Al 7075-T6 alloy, it was verified that CAA was more efficient for IM dissolution than SAA, which can lead to anodic layers with fewer defects. Potentiodynamic polarization experiments showed that the oxidation rates of all model IMs were higher than the model alloy (Al-5%Cu) and demonstrated that, in CAA, the Mg-rich model IMs passivate at low potentials. It was also observed that the oxidation behaviour of the model IMs containing Cu and Fe was similar in both anodizing electrolytes, with slightly higher oxidation rates in CAA. TEM cross-sections analysis of anodic oxide layers formed on selected model IMs in both anodizing baths showed the formation of thin spongy anodic films with relatively uniform thicknesses, which compactness increased with increasing iron content. Further, the typical porous nature of AAO was not disclosed, film disruption was verified for the model IM with high Cu content, probably as a consequence of oxygen evolution, and thicker films were produced in SAA when compared to CAA. Finally, charge calculations performed from the RBS measurements revealed that the charge used in forming the anodic films was relatively low and that the major part of the charge (approximately 80 %) was consumed for oxygen generation. RBS data also revealed that the amount of SO_4^{2-} ions trapped within the spongy oxides layers was superior to that typically

found on anodic films formed in high purity aluminium. From the obtained results, authors claim that oxide films formed above second phase particles composed of highly reactive and mobile cations, like Mg, may form defective oxides which are highly soluble in the acidic environment of the anodizing bath exposing the underlying metal to the acidic environment and resulting in high rates of consumption. On the other hand, AAO formed incorporating more stable oxides with, nevertheless, semiconducting properties, like Cu-O and Fe-O, have their stability compromised due to oxygen generation, which form gas filled voids that, upon rupture, breaks the oxide layer in the close proximity of the underlying metal. At these sites accelerated local growth of the oxide layer (reanodizing) takes place until the formation of new oxygen-filled void that will burst in a cyclically repeated process. This process being more deleterious for increasing content of Cu-O. In the practical alloy these processes result in almost complete dissolution of Mg-rich IMs during anodizing, whereas IMs with more stable oxide layers are partially dissolved due to the cyclic disruption of the oxide layer.

The morphologies of oxide layers formed above the IMs presented in the microstructure of commercial alloys were also investigated by several authors. TEM micrographs presented by Saenz de Miera et al. (2010a) showed that the porous film formed in the vicinity of copper and/or iron rich second-phase particles of the anodised AA7075-T6 presents a finer morphology with respect to the inner coarser textured region formed above the alloy matrix (Figure 3.10). SEM cross-section images presented by Curioni et al. (2008a) of samples submitted to the same anodizing charges but at different potentials also evidenced that the charge drawn by the oxidation of IM particles affect the thickness of the oxide layer formed above the aluminium matrix (Figure 3.11). In Figure 3.11 (a) anodizing was performed at 2 V, a potential at which copper is not anodized, therefore, must of the passed charge was drawn to oxidize the aluminium matrix forming a thicker oxide layer. On the other hand, for the sample anodized at 8 V (Figure 3.11 (b)), a potential at which Cu oxidation takes place, must of the passed charge was drawn to oxidize the IM particle resulting in a thinner aluminium oxide layer.

Figure 3.10- Transmission electron micrograph of anodised AA7075-T6 alloy in sulphuric acid, showing a second-phase particle at the film surface.

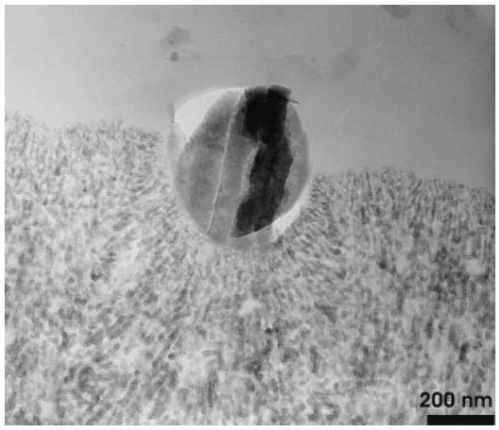

Source: Saenz de Miera et al., 2010a.

Figure 3.11 – (a) Scanning electron micrograph of a section of the alloy 2024-T3 after anodizing at 2 V (SCE); (b) Scanning electron micrograph of a section of the alloy 2024-T3 after anodizing at 8 V (SCE). Anodizing processes performed in 0.46 mol.L^{-1} sulphuric acid electrolyte for a charge of 0.6 C.cm^{-2}.

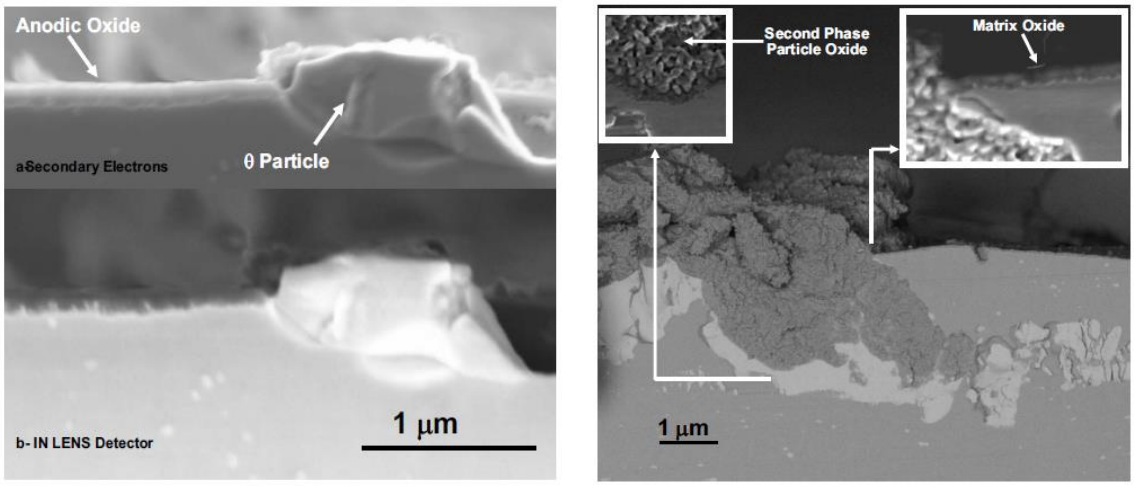

(a) (b)

Source: Curioni et al., 2008a

The interest in the TSA process as a potential substitute for CAA has led to the investigation of the morphology of porous AAO layers formed in this electrolyte. Iglesias-Rubianes et al. (2007) investigated the influence of copper on the morphologies of porous AAO layers formed in either sulphuric acid electrolyte or the same electrolyte but with addition of tartaric acid. The films were formed under current and voltage control using a sputtering deposited Al–2.7 at.% Cu model alloy or a commercial AA2024-T3 alloy. In accordance with some of the works described previously, a Cu-enriched surface layer was identified just beneath the anodic barrier layer when the model alloy was anodized in 0.53 mol.L^{-1} tartaric acid

electrolyte (pH = 1.6), which was followed by copper incorporation in the oxide film (at a lower amount compared to the matrix), and oxygen generation within the barrier film at sites of copper oxidized species. According to the authors, the identification of this copper enriched layer in porous AAO is not easy due to the irregularity of the underlying metal, therefore, this part of the investigation was performed with a barrier layer forming electrolyte. By anodizing the model alloy in sulphuric acid electrolyte without or with tartaric acid, it was verified that the film was also depleted in copper when compared to the matrix (RBS) and that, in addition to the normal alignment of the pores, the film presented lateral porosity in the porous layer and a layered appearance in the TEM cross-section micrographs, both facts associated to the presence of copper in solid solution and oxygen generation at copper rich sites within the anodic film. These features were also found in the investigations with the film formed above the matrix of the alloy 2024 in regions without IMs, indicating that the model alloy adequately reproduced the behaviour of the commercial one. The authors attributed the altered morphology of the films formed on both materials to the enrichment of copper, the presence of oxygen within the film (gas-filled voids), and the release of oxygen to the electrolyte (burst of the gas-filled voids), or a combination of these factors, and their interactions with pore formation mechanisms. The authors claim that the interception of oxygen bubbles within the film or its rupture due to gas release may change the pore propagation direction leading to films with less regular pores, contributing also to the lateral aspect of the pore morphology and the layered structure of the porous AAO, as pores tend to reassume their normal orientation. The authors emphasize that, within the detection limits of the measurements, the addition of tartaric acid to the electrolyte only provoked a reduction in the steady current for film growth (10 % for the model alloy and 20 % for the commercial 2024 alloy) and does not influence aspects related to the film morphology.

A detailed investigation of the porous AAO oxide growth in TSA was performed by Ma et al. (2011a). The influence of Cu in solid solution on the morphology of the porous AAO layer formed in TSA was investigated using AA2099-T8 as substrate, which, as the 2524 alloy, also has a high copper content (MA et al., 2011a). The TEM images obtained from the anodic layer produced by potentiodynamic anodizing revealed that the outer region of the film (produced at lower voltages) presented a finer microstructure with a relatively high number of embedded copper nanoparticles. On the other hand, the inner region of the film, produced at higher voltages, presented a coarse morphology with evidences of lateral porosity. Moreover, as a consequence of the increased voltage, pore diameter and cell dimensions were higher at

the inner part of the anodized layer. The authors claim that copper oxidation plays an important role in the changing morphology of the anodized film through its cross-section, thus, in the outer region, where copper cannot be oxidized, copper nanoparticles are occluded within the film and the porous AAO grows similarly to high purity aluminium, with continuous cells and perpendicular pores. Conversely, at the inner region (produced at higher potentials) copper can be oxidized to semiconductive copper oxide favouring O^{2-} oxidation within the film and leading to the formation of oxygen gas-filled voids, which consequences in the anodic film morphology were already discussed in this section: the cyclic process of surface copper enrichment, copper oxidation, oxygen gas-filled voids formation, their rupture, local deformation of the film with consequent electrolyte access to the metal matrix and reanodizing resulting in lateral porosity in addition to the well-defined hexagonal cells. The authors also report that copper-rich ridges tend to form at the hexagonal cell boundaries suggesting copper transportation from other regions of the copper-enriched surface layer due to stress arising from the growing anodic film (flow mechanism for growing oxide). It was also verified that the coalescence of copper-rich nanoparticles from adjacent cells leads to the formation of elongated shape copper-rich nanoparticles evident at cell boundaries.

Ma et al. (2011b) performed a detailed investigation of the effect of constituent particles (Al-Fe-Mn-Cu containing IMs) and dispersoids (Al–Cu–Mn–Li and Al_3Zr) in the composition and morphology of porous AAO films formed in an aluminium alloy 2099-T8 in TSA. They verified that the anodizing behaviour of the IMs was dependent on their copper content: low-copper-containing particles anodized more slowly than the alloy matrix, forming a highly porous anodic oxide film; and the medium- and high-copper containing particles were rapidly dissolved, resulting in defects (voids) in the anodic film. It was verified that particles with low anodizing rate (low copper content) may protrude within the porous anodic film also forming oxide films with different compositions from the alloy matrix at their anodized surface. The composition of the film presented in the article was depleted in Cu, Fe and Mn in relation to the particle original composition indicating that these cations migrate at faster rates than Al in the oxide. Moreover, due to the enrichment of the oxide in Cu and Fe oxide, oxygen can be generated forming gas-filled voids that eventually rupture provoking local deformations in the oxide film. Occlusion of these particles within the porous AAO film may eventually occur. On the other hand, IM particles with increased anodizing rates (high Cu content) when compared to the alloy matrix may form cavities that extended below the film alloy interface. Regarding the behaviour of the dispersoids, Al-Mn-Cu-Li particle anodizes at rates slightly

lower than the alloy matrix, forming less regular films and with different morphologies from the AAO layer, whereas Al_3Zr particle anodizes at a similar rate to the matrix. Al-Cu-Mn-Li dispersoids may protrude within the AAO layer or eventually be occluded within the anodized layer, which is compatible with their slower anodizing rate. In addition, copper oxide incorporation in the oxide film above the particles may enhance oxygen generation and the formation of gas filled voids, which rupture is the main responsible for the irregular film morphology. On the other hand, due to their similar anodizing rate in relation to the matrix, Al_3Zr dispersoids are completely oxidized and Zr rich regions with the same round shape of the original dispersoid could be detected within the porous AAO layer. According to the authors, this is consistent with the observation that the Gibbs free energy per equivalent for formation of zirconium oxide is close to that for alumina formation and that the mobility of Zr^{4+} and Al^{3+} species within anodic oxide film are similar.

It is important to emphasize, however, that in the discussion section of the article (MA et al., 2011b), the authors also related the high anodizing rates of the high copper content IMs to an increased amount of Li found in these particles, which would be incorporated in the oxide layer, facilitating its dissolution in the anodizing electrolyte due to the high migrating rates of Li ions. However, they also pondered that an increased rate of oxygen generation in the film formed above these Cu-rich IMs may contribute to their fast dissolution. For these particular compositions an increased amount of copper oxide is expected in the oxide layer formed above the IMs. As already discussed, oxygen generation is enhanced in copper oxide containing AAO layer due to the semiconducting properties of this oxide. Therefore, in the oxide formed above these particles it is expected that the rupture of gas-filled voids would be more frequent providing an easier access of the anodizing solution to the particle accelerating its dissolution.

Ma et al. (2011b) also pointed that the mechanical properties of the film, like fatigue and corrosion resistances, may be affected by the discontinuities in the anodic film. Specifically, cavities and residual IM particles occluded in the AAO film may serve as potential crack initiation sites, compromising the fatigue properties, and/or may compromise the AAO film compactness and effective thickness, negatively affecting its corrosion resistance. Not to be forgotten is that defective oxides may also acts as preferential pathways for aggressive electrolyte penetration also hindering the corrosion resistance of the anodized metal.

3.5 Anodizing of aluminium alloys in the aircraft industry

In this item, the main technological issues related with the two main anodizing processes applied to aluminium alloys aiming at producing porous AAO layers will be addressed, namely: chromic acid anodizing (CAA) and sulphuric acid anodizing (SAA). Technical details about the tartaric-sulphuric anodizing (TSA) procedure will also be presented.

CAA is largely employed in the aircraft industry for aluminium alloy anodizing (MANSFELD; KENDIG, 1988; CHIDAMBARAM; CLAYTON; HALADA, 2003). The anodic layer formed has excellent corrosion resistance due to the inhibiting characteristics of the chromate ions and due to its ability to regenerate defective regions in the oxide layer (KENDIG et al., 2001; ZHAO et al., 2001). Moreover, the produced porous layers serve as an excellent anchoring base for organic coatings application. As a consequence of the passivating properties of chromate ions, the electrolyte used in the CAA anodizing process is of low aggressiveness towards aluminium, this generates another great advantage of this procedure. Due to the porous nature of AAO produced in acidic media, it is practically impossible to remove all the anodizing solution from within the pores. If the retained electrolyte is aggressive towards aluminium (like sulphuric acid) corrosion may take place, this is not the case for chromic acid (ASSOCIAÇÃO BRASILEIRA DO ALUMÍNIO, 1996). Therefore, CAA is highly recommended when the piece to be anodized contains rolled or pleated edge parts (ASSOCIAÇÃO BRASILEIRA DO ALUMÍNIO, 1996) or, still, in components such as riveted and welded assemblies, where complete removal of the anodizing solution is difficult or almost impossible (ASSOCIAÇÃO BRASILEIRA DO ALUMÍNIO, 1996; COTELL; SPRAGUE; SMIDT, 1994). However, toxicological and environmental concerns associated with the use of Cr(VI) have led to the development of safer alternatives[2].

For industrial CAA processes, typically, the concentration of CrO_3 (chromium oxide as source of H_2CrO_4) lies within 3 to 10 wt%, whereas the pH of the bath is between 0.5 and 1.0 (COTELL; SPRAGUE; SMIDT, 1994). In order to equilibrate the oxidation-dissolution process during the growth of the anodizing layer, a rigorous control of the temperature is required. Therefore, for laminated parts the temperature is set at 40 ± 2 ºC, whereas for castings it must be set at 30 ± 2 ºC (ASSOCIAÇÃO BRASILEIRA DO ALUMÍNIO, 1996).

[2] Cromium (VI). Retrieved from: http://www.epa.gov/iris/subst/0144.htm. Date acessed: May, 9th, 2015.

In general, milder anodizing conditions must be applied for castings due to the porous nature of the substrate (COTELL; SPRAGUE; SMIDT, 1994). Regarding the anodizing conditions, one of the most widely used procedures is the Bengough-Stuart process (1923), consisting in progressively increasing the voltage to 40 V within 10 minutes, which is then kept for 20 min at 40 V, and finally another progressive increase of the voltage to 50 V during the last 10 min (ASSOCIAÇÃO BRASILEIRA DO ALUMÍNIO, 1996). The total treatment time is of about 40 min. Nevertheless, commercial processes are available where the voltage (ASSOCIAÇÃO BRASILEIRA DO ALUMÍNIO, 1996) or the current is kept constant (COTELL; SPRAGUE; SMIDT, 1994).

According to the technical and scientific literature, the typical thickness of an anodized layer obtained in the CAA process lies within 4-10 μm (ASSOCIAÇÃO BRASILEIRA DO ALUMÍNIO, 1996; COTELL; SPRAGUE; SMIDT, 1994). Depending on the film thickness, colour can vary from yellow to dark-olive, whereas a grey colour predominates in alloys with high copper content (COTELL; SPRAGUE; SMIDT, 1994). The process is highly indicated for alloys with high Si contents, whereas its maximum tolerance to copper is 5 at% (ASSOCIAÇÃO BRASILEIRA DO ALUMÍNIO, 1996). The operational conditions are very sensitive to chloride ion contamination in the anodizing bath as they can cause pitting corrosion (COTELL; SPRAGUE; SMIDT, 1994).

Currently SAA is the most industrially used anodizing process for aluminium alloys with a wide range of applications (ASSOCIAÇÃO BRASILEIRA DO ALUMÍNIO, 1996). In the process, the concentration of sulphuric acid in the anodizing solution varies between 12 to 20 wt% (COTELL; SPRAGUE; SMIDT, 1994). The process is extremely versatile regarding the properties of the anodized layer, which can be controlled relatively easily by changing either the voltage or the temperature of the anodizing bath.

Two kinds of SAA can be performed: conventional and hard anodizing. The main differences between them are the operating temperature, the use of additives and the voltage and current density at which the processes occur (COTELL; SPRAGUE; SMIDT, 1994). Typical hard anodizing operating temperature ranges from 0 to 10 ºC, whereas the applied current densities lie between 2 and 3.6 $A.dm^{-2}$. On the other hand, for conventional SAA, the process is operated near room temperature (20-25 ºC) with lower current densities (COTELL; SPRAGUE; SMIDT, 1994). Due to the operating conditions (lower temperatures, higher current densities/voltages), hard anodizing produces a considerably heavier (thicker) coating then conventional SAA in a given length of time. Hard sulphuric acid anodizing is highly

recommended when increased resistance to abrasion is required. Table 3.2 presents the operation conditions for SAA to produce different kinds of goods applications (ASSOCIAÇÃO BRASILEIRA DO ALUMÍNIO, 1996).

Table 3.2 - Operation conditions of SAA baths to produce goods of different technical grades.

Operation conditions	**Architectural**	**Consumers Goods**	**Technical purposes (Hard)**
H_2SO_4 concentration ($g.L^{-1}$)	160 – 210	110 – 130	100 – 180
Voltage (V)	14 – 20	12 – 18	> 20
Temperature (^oC)	17 – 21	18 – 24	-2 – 2
Current density ($A.dm^{-2}$)	1.2 – 2.0	1.0 – 1.5	2.5 – 4.0
Layer thickness (µm)	11 – 25	5 – 15	50 – 100

Source: Associação brasileira do alumínio, 1996.

The SAA has been established as an alternative to replace CAA (VIEJO et al., 2010; FELIU et al., 2008). However, one negative point associated with the process is the fatigue strength reduction (ASSOCIAÇÃO BRASILEIRA DO ALUMÍNIO, 1996; COTELL; SPRAGUE; SMIDT, 1994), reaching 46 % in thicker parts of the alloy (RATEICK et al. 2005). Another drawback associated with SAA is the corrosive action of the electrolyte retained within the structure of the porous aluminium anodized layer (AAO) towards the aluminium substrate (ASSOCIAÇÃO BRASILEIRA DO ALUMÍNIO, 1996; COTELL; SPRAGUE; SMIDT, 1994). Therefore, this type of anodizing is not recommended when pieces of complex shapes are to be anodized, as complete removal of retained electrolyte is a difficult task (COTELL; SPRAGUE; SMIDT, 1994).

Other anodizing processes used less frequently but of increasing industrial interest includes anodizing baths where sulphuric acid is mixed with other acids like oxalic, phosphoric, boric, sulfosalicylic, sulfophthalic, or tartaric (COTELL; SPRAGUE; SMIDT, 1994). According to the technical literature, the addition of organic acids to SAA inhibits the dissolution of the anodic layer by the electrolyte (ASSOCIAÇÃO BRASILEIRA DO ALUMÍNIO, 1996), whereas scientific works report the improvement of the fatigue life of anodized samples when the process is performed in sulphuric acid solutions in the presence of other acids (DOMINGUES et al. 2003; CREE et al. 2010; CAI et al. 2007).

Of special interest to this project is the addition of tartaric acid to the SAA bath, giving the so-called tartaric-sulphuric anodizing (TSA). As other organic acids (ONO; SAITO; ASOH, 2005; SULKA, STEPNIOWSKI, 2009), tartaric acid seems to be able to produce anodic aluminium films with self-ordered porosity (GOROKH et al., 2006). TSA has been chosen in Europe to replace the CAA (MUSEUX; THEILMANN, 2009; ARENAS et. al., 2010), and, motivated by this industrial interest, there are several scientific works at which the morphology and corrosion resistance of high strength Al alloys anodized in this medium was investigated (CURIONI et al., 2009; GARCIA-RUBIO et al. 2010, MUBAROK et al., 2015). In some of them, in order to increase the corrosion resistance, post-treatments were adopted (ARENAS et. al. 2010; GARCIA-RUBIO et al. 2009a), some of these works will be detailed later in this bibliography survey.

Concerning the fatigue strength reduction, Lee et al (2012) showed that the fatigue strength of the Al alloy 7050-T7451 anodized in TSA is superior to CAA and SAA; regarding the corrosion resistance, the authors indicated that it is similar for the three types of anodizing. On the other hand, Zhao et al. (2015) report the reduction of the fatigue strength of a TSA anodized AA2024-T3 when compared to the matrix, which was ascribed both to residual tensile stress arising from the elastic mismatch between the oxide film and the substrate and to the brittle nature of the oxide film. In addition, an important role was ascribed to pits generated during the anodizing procedure, eliminating the pitting initiation period and, thus, reducing the fatigue life. The authors also report that increasing anodizing voltage also decreases the fatigue life due to increased number of crack initiation sites (ZHAO et al., 2015).

Studies have shown that the addition of tartaric acid to the sulphuric acid bath provides corrosion resistance properties compatible with the requirements of the aerospace industry with appropriate paint adhesion being comparable to the oxide layer produced with chromic acid baths (GARCÍA-RUBIO et al., 2009b; GARCÍA-RUBIO et al., 2010).

Information available from a technical publication from Airbus (MUSEUX; THEILMANN, 2009) shows that TSA is already being used as a substitute for CAA in applications where corrosion resistance is required. It is also reported that the fatigue life of TSA anodized parts is similar to that exhibited by CAA treated ones, even though, for both treatments, a reduction in fatigue life is reported when compared to non-anodized aluminium parts. Table 3.3 shows a comparison between the process parameters for TSA and CAA reported in this specific publication. An important issue associated with the presented data is the reduction in the

anodizing time and applied voltage when TSA is employed, decreasing both the processing time and energy consumption. It is also cited that due to the less toxic nature of TSA when compared to CAA fungus growth in the treatment line can take place, requiring preventive actions. At this point, it is important to emphasize that the operating parameters adopted in the present work is within the range employed by this important aircraft producer, highlighting the importance of the theme for industrial use.

Table 3.3 - Comparative process parameters for CAA and TSA in Airbus plant.

Parameter	CAA	TSA
Film thickness	3-5 µm	3-5 µm
Temperature	40 ºC	37-43 ºC
Process time	45 min	20-25 min
Voltage	40 V or 21 V	13-15 V

Source: Museux; Theilmann, 2009.

3.6 Hydrothermal sealing of anodic film

The porous structure of the AAO produced in acid baths provides a surface with remarkable potential for decorative purposes like colouring and painting; on the other hand, it offers a preferential pathway for aggressive species penetration, reducing the durability and the aesthetic properties of the anodic film and the substrate, especially in aggressive atmospheres (LÓPEZ et al., 2006). Therefore, for several industrial and architectural applications, the porous layer must be sealed and/or painted in order to improve the corrosion resistance of the AAO or even to maintain the desired aesthetical properties.

Numerous procedures are available for pore sealing, like immersion in a hot aqueous solution containing nickel acetate (HAO; CHENG, 2000; COTELL; SPRAGUE; SMIDT, 1994), or either cold sealing in a nickel fluoride solution at 25-30 ºC followed by water/saturated vapour exposure at 50-60 ºC (ASSOCIAÇÃO BRASILEIRA DO ALUMÍNIO, 1996; LOPEZ et al., 2006). Other of these procedures is the hydrothermal sealing (HTS), which consists simply in the immersion of the anodized part in a deionized boiling water bath for a given time. Due to its simplicity and probably the absence of chemicals, HTS is industrially used as a post-treatment for porous AAO to improve corrosion resistance and to prevent aesthetic

deterioration. In addition, in the research field, this post-treatment is frequently employed as a control in investigations concerning the effectiveness of different post-treatment protocols for the anticorrosion protection of porous AAO (LÓPEZ et al., 2006; WHELAN et al., 2013; CAPELOSSI et al., 2014; CARANGELO et al., 2016, WOJCIECHOWSKI et al., 2016), as it was done in the present work.

From a literature survey published in 1962 devoted to the investigation of sealing of porous anodic oxides films on aluminium, Hoar and Wood (1962) wrote: "*In water and steam sealing, the main process is blockage of the pores due to the formation of the less dense crystalline boehmite ($Al_2O_3.H_2O$ or AlO(OH)) from quasi-amorphous Al_2O_3, or micro-crystalline γ or γ'- Al_2O_3. This occurs most readily at around pH 7 and above 80 °C.*" The overall chemical reaction is presented below (HOAR; WOOD, 1962; ZUO; ZHAO; ZHAO, 2003; HAO; CHENG, 2000):

$$Al_2O_3 + H_2O \rightarrow 2AlO(OH)\ \text{(boehmite)} \qquad (3.14)$$

However, the pores sealing process is complex and consists of several successive stages that can evolve for years when unsealed or sealed porous AAO is exposed to aggressive or mildly aggressive atmospheres (GONZÁLEZ et al., 1999; HAO; CHENG, 2000; LOPEZ et al., 2006), resulting in an improvement of the anticorrosion properties of the anodized part with exposure time. For instance, López et al. (2000) report an increase of the porous layer resistance with exposure time to the atmosphere of the Campus of the University of Madrid of commercial pure aluminium anodized in oxalic acid and then hydrothermally sealed (HTSed), whereas the results presented by González et al. (1999), besides corroborating with those of López et al. (2000) for HTSed samples, also showed an equivalent impedance response for unsealed porous AAO layers after several years of exposure to mildly aggressive atmosphere.

Lopez et al. (LOPEZ et al., 2006) proposed the following sequence of events for complete pore sealing of HTSed porous AAO, which is physically depicted in Figure 3.12. The scheme presents the sequence of events taking place during HTS and afterwards, when the anodized part is exposed to the environment, and does not take into account the influences of the underlying substrate in AAO morphology (the model was derived for pure or commercial pure aluminium):

1 – Initially the pores are filled with water (sealing solution), and pores mouths plugged by a top surface layer of acicular pseudoboehmite crystals and a compact intermediate layer

(Figure 3.12 (a) and (b)). Below this latter layer the pore is occupied by an aluminium hydroxide gel;

2 – Partial dissolution of the pore walls with an increase of 50-60 % of the pore diameter - represented in the Figure 3.12 (c) and (d). This phenomenon starts during the sealing process and may continue for a long period upon exposure to mildly aggressive environments. Boehmite gel is present within the pores;

3 – The gel inside the pores is saturated by the progressive dissolution of the pore walls and precipitate as bayerite, Al_2O_3-$3H_2O$, which is stable at ambient temperature, plugging the entire length of the pores (Figure 3.12 (e) and (f)). During this stage, volume contraction occurs generating some gaps that are filled during exposure at humid environments by the diffusion of water through the acicular and intermediate layers that blocks the pore mouth (Figure 3.12 (e)). According to the authors, this part of the sealing process occurs mostly upon exposure of the sealed sample to mildly aggressive environments as HTS is too short for bayerite precipitation;

4 - Agglomeration and growth of hydrated alumina crystals during ageing as a result of an agglomeration process from smaller crystals and a consumption of intercrystalline water (Figure 3.12 (g) and (h)). This process can continue during years and its speed depends on the exposure conditions (aggressiveness and the presence of humidity).

Figure 3.12 – Schematic diagram for the hydrothermal sealing process (a) and (b) filling of the pores with sealing solution, plugging of the pore mouths, and formation of acicular and intermediate layers, (c) and (d) dissolution of the walls and widening of the pores, (e) and (f) saturation of the hydroxide gel, precipitation with contraction of volume and plugging of the pore along its entire length by diffusion of water through the plug, (g) and (h) agglomeration and growth of hydrated alumina crystals during aging.

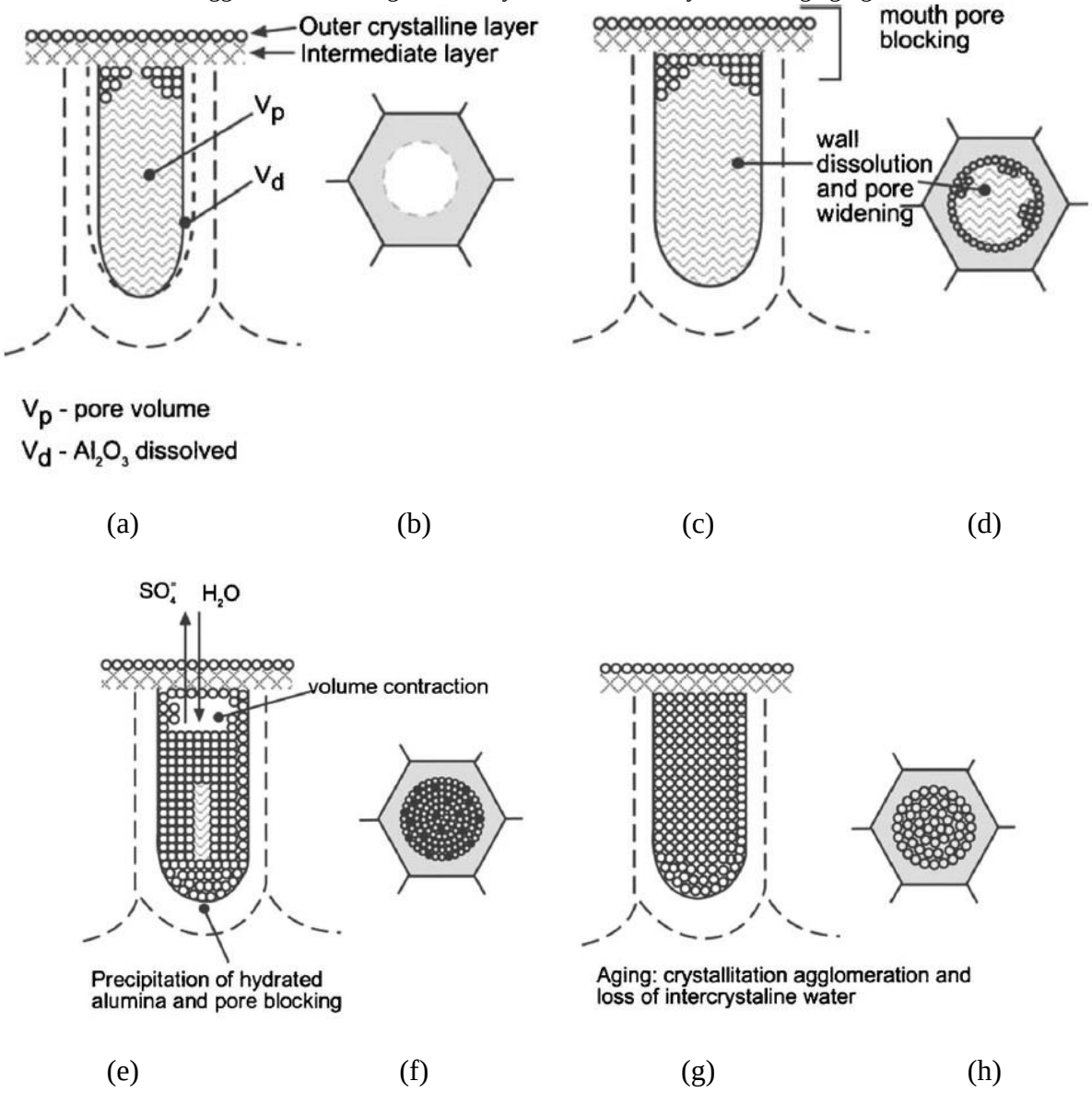

Source: Lopez et al., 2006.

It is important to emphasize that the complete model presented above is valid for a total sealing process, which usually takes place when the anodized part is exposed in service through several years to mildly aggressive atmospheres. Therefore, the exposure of a recently anodized and HTSed sample to an aggressive aqueous solution like NaCl, as done in the present study, may hinder some of the precipitation steps and, as a consequence, an increase in the corrosion resistance with exposure time may not be verified. Indeed, for the conditions

employed in the present work, only pore sealing and boehmite precipitation must be considered as relevant processes and possibly only stage (a) to (d) of Figure 3.11 are involved in the behaviour that will be reported. Nevertheless, pore blocking and boehmite precipitation lead to an effective increase in the resistance and an improvement in the dielectric properties of the anodized layer (ASSOCIAÇÃO BRASILEIRA DO ALUMÍNIO, 1996, p.93; ZUO; ZHAO; ZHAO, 2003). Therefore, EIS is an effective tool to evaluate the influence of the sealing parameters (specifically sealing time) on the corrosion resistance of aluminium parts protected by porous AAO layers, as shown in the work González et al. (1999).

3.7 Hybrid sol-gel coatings

The development of environmentally acceptable surface treatments and coatings is a critical need of the aerospace industry. The US Air Force has been studying coatings with these features to ensure more than 30 years of service without damage and with good performance (DONLEY et al., 2003).

Inorganic sol-gel coatings are obtained from short chain alkoxides, such as those derived from the metals Si, Zr, Ti, and Al, and have been investigated as a barrier for corrosion control of aluminium alloys, steel and galvanized steel, among others. One of the most studied of them is the tetraethylorthosilicate (TEOS) ($Si(OC_2H_5)_4$), which the widespread use is applied to obtain inorganic materials that require the presence of silicon (AIROLDI; FARIAS, 2004). Inorganic oxide coatings can provide good protection on metal substrates, but they present some drawbacks: oxide films formed are brittle and thicker coatings (> 1µm) are difficult to achieve without cracking; they have poor flexibility and low compatibility with organic coatings. Furthermore, generally high temperatures (400–800 ºC) are required to achieve good properties of the film (KAKDE; MANNARI, 2009; WANG; BIERWAGEN, 2009). The use of functional silanes may partially overcome these drawbacks as softer and thicker coatings can be obtained that are cured at much lower temperatures: normally below 150 ºC.

Two important issues associated with the inorganic part of the sol-gel coatings are the bonding properties with the metallic substrate and the formation of the Si-O-Si network within the coating structure. Zhu and Ooij (2003) and Ooij et al. (2005) reported that the stronger interfacial adhesion of functional bis-silanes displays superior protection on metal surfaces when compared to the use of functional mono-silanes solely. The main difference

between them is the number of hydrolysable OR groups: each bis-silane molecule contains 6 hydrolysable OR groups, while each mono-silane molecule has only 3 SiOH groups, as can be seen in the Figure 3.13 (a) and (c) (ZHU, OOIJ, 2003). A greater number of Si-OH groups of the bis-silane molecules are capable of forming a high density of Al-O-Si bonds with the substrate and building up a Si-O-Si network of an appreciable thickness on the top. The use of mono-silanes are not capable to achieve this higher density network, as shown in Figure 3.13 (b) and (d) (ZHU; OOIJ, 2003; OOIJ et al. 2005). The authors stressed that the protective properties of the bis-silanes can be enhanced when used in conjunction with organofunctional mono-silane treatments for adhesion to other organic layers.

Figure 3.13 - Structures of (a) mono-silane molecule, (c) bis-silane molecule, (b) bonding mechanism in mono-silane/Al and (d) bonding of bis-silane/Al.

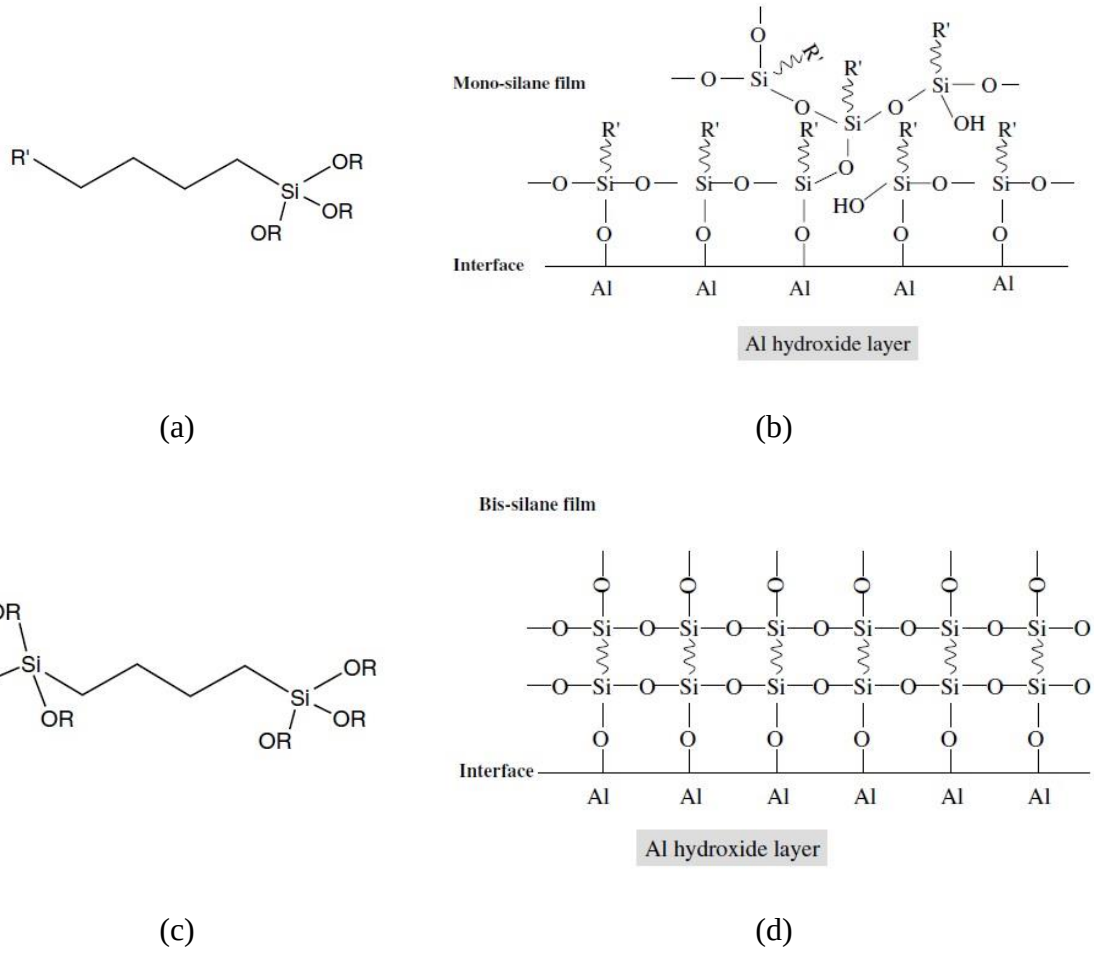

(a) (b)

(c) (d)

Source: Zhu; Ooij, 2003.

Hybrid sol-gel coatings are obtained by the combination of inorganic and organic precursors, where increasing the organic content yields coatings of a more polymeric nature (VOEVODIN et al., 2003). Organic-inorganic hybrid films are a very promising alternative to replace the typical treatments using hexavalent chromium ions due to their potential to incorporate chemical elements that improve corrosion resistance (OOIJ et al., 2006). It has been proved that such coatings can provide good corrosion resistance because of the combination of mechanical and chemical characteristics of the formed networks, producing films that are flexible, dense, and functionally compatible with organic coatings systems (KAKDE; MANNARI, 2009). The modification of an inorganic coating by the organic substituent induces a quasi-plastic response with improvement of adhesion properties compared with classical inorganic coatings (DRUART et al., 2011). There are many advantages of using it, the main ones are listed below (WANG; BIERWAGEN, 2009):

- sol-gel process usually occurs at low temperatures, typically close to room temperature. Thus, thermal volatilization and degradation of organic inhibitors is minimized;
- once the precursors are liquid, it is possible to coat complex shapes without the need for machining or melting;
- sol–gel films are non-toxic and environmentally compliant. The precursors employed do not introduce impurities into the end product being a waste-free method and excludes the stage of washing.

Generally, the sol–gel formation occurs in four stages (DONLEY et al., 2003; WANG; BIERWAGEN, 2009; KAKDE; MANNARI, 2009; DRUART et al., 2011.

a) hydrolysis;
b) condensation and polymerization of monomers to form chains and particles,
c) growth of the particles;
d) agglomeration of the polymer structures followed by the formation of networks that extend throughout the liquid medium resulting in thickening, which forms a gel.

Once the hydrolysis reaction has initiated, condensation reaction occurs simultaneously. As can be seen in Figure 3.14, the hydrolysis and condensation steps generate low-molecular weight by-products such as alcohol and water (WANG; BIERWAGEN, 2009; BALBYSHEV et al., 2003; DONLEY et al., 2003).

Figure 3.14 - Hydrolysis and condensation reactions involved in sol–gel process.

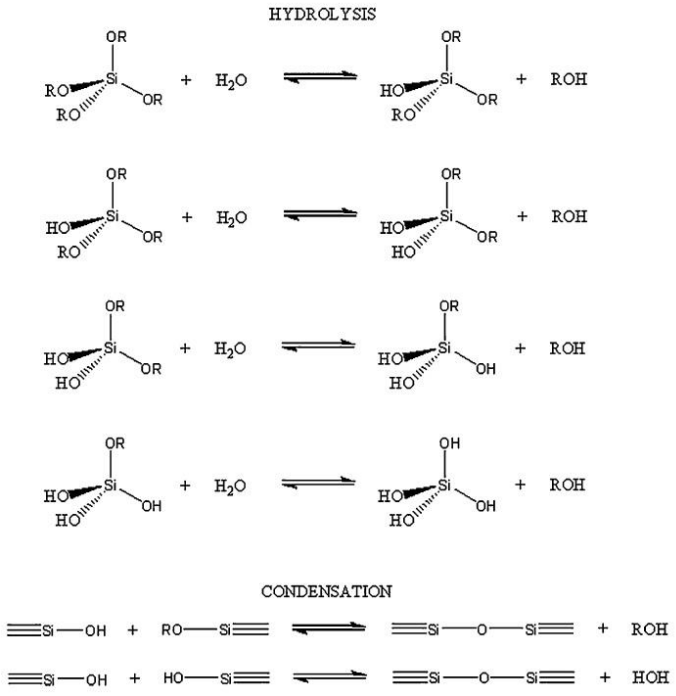

Source: Wang; Bierwagen, 2009.

The kinetics and equilibrium of hydrolysis and condensation reactions of silanes depend on the organofunctional groups, the concentration of silanes and water, the temperature and the ageing of the solution, but pH is the most important factor that affects the stability of silanes in aqueous solutions (OOIJ et al., 2005). The pH dependency of the hydrolysis and condensation reactions of a typical silane is shown in the Figure 3.15. In acid or basic media, the rates of hydrolysis and condensation reactions are fast, while at or near neutral pH they are slow. When the reactions are OH^- catalysed, a high rate of condensation is favoured with rapid gelation and when the reactions are H^+ catalysed, a high rate of hydrolysis is favoured with slow gelation (OOIJ et al., 2005).

Figure 3.15 - Hydrolysis and condensation rate of a typical silane

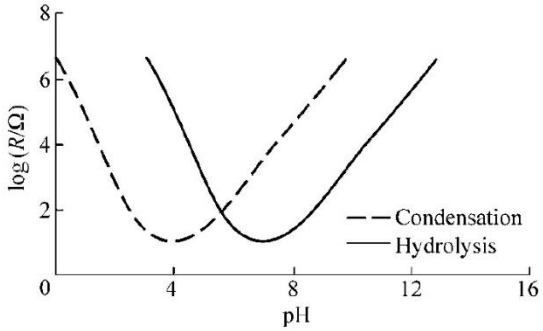

Source: Ooij et al., 2005.

Generally, the curing of a polymeric film induces a better crosslinking of the layer. In the case of silane films the cross-linking due to the condensation reaction results in a better corrosion protection of the metallic substrates, once the cross-linked silane film is a more effective physical barrier between the metallic substrate and the aggressive environment (FRANQUET; TERRYN; VEREECKEN, 2003). When metals are immersed in a dilute silane solution 2-5 % (vol.) for a few seconds (ZHU; OOIJ, 2003), silanol groups (SiOH) are spontaneously adsorbed onto the metal surface through hydrogen bonds (WANG; BIERWAGEN, 2009), as shown schematically in Figure 3.16 (ZHU; OOIJ, 2003). After drying or curing, the condensation reaction between these groups and the metal hydroxyls (MeOH) from the metal surface forms covalent metallo-siloxane bonds (MeOSi) and water evaporates during this process, according to reaction 3.15 (ZHU; OOIJ, 2003):

$$MeOH_{(metal\ surface)} + SiOH_{(solution)} \leftrightarrow SiOMe_{(interface)} + H_2O \qquad (3.15)$$

The excess silanol groups (SiOH) adsorbed on the metal can react among themselves and contribute to the formation of a network of siloxane (SiOSi) through the condensation reaction (3.16):

$$SiOH_{(solution)} + SiOH_{(solution)} \leftrightarrow SiOSi_{(silane\ film)} + H_2O \qquad (3.16)$$

Figure 3.16 – Simplified schematic of bonding mechanism between silane molecules and metal surface hydroxide layer (a) before condensation (b) after condensation.

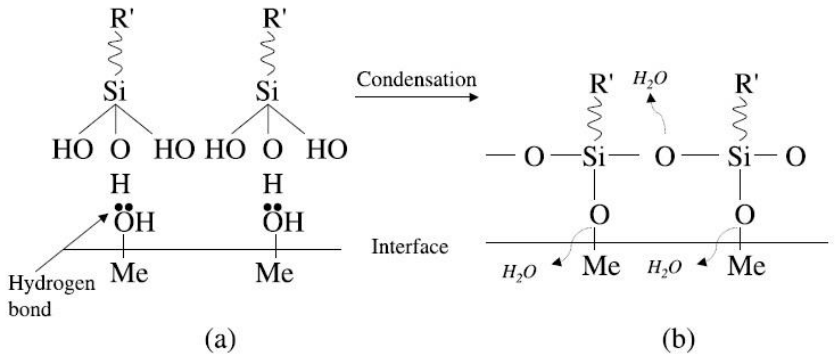

Source: Zhu; Ooij, 2003.

Organofunctional mono and bis-silanes of general formulas R`-Si(OR)$_3$ and Si(OR)$_2$-R`-Si(OR)$_2$ have been studied as adhesion promoters, which offer a linkage between a metal surface and a polymer through covalent bonding of a hydrolysable silicate group with the metal surface and a subsequent interaction of the organofunctional group R` with the polymer material of the coating (KHRAMOV et al., 2003). Some of the most used silanes are (3-glycidoxypropyltrimethoxysilane (GPTMS), dodecyl-trimethoxysilane (DTMS), tetraethoxysilane (TEOS), vinyltriethoxysilane (VTES) among others (JI et al., 2007).

Figure 3.17 to 3.20 show the proposed reactions between the aluminium oxide and the hybrid organic-inorganic sol-gel coating using as precursors TEOS and GPTMS (CLAYDEN; GEEVES; WARREN, 2012; FIGUEIRA; SILVA; PEREIRA, 2015). The formation of acid catalysed sol gel occurs through distinct electronic mechanisms that occur simultaneously. The hydrolysis of TEOS by protonation of its oxygen atoms through acetic acid releases acetate ions and silicon cationic intermediate (Figure 3.17 – step I). After that, water molecules react with the silicon, releasing ethanol as by-product (Figure 3.17 –stages II and III) and regenerating the acetic acid (Figure 3.17 –stage IV) returning, thus, the catalytic cycle and favouring the complete hydrolysis of TEOS (Figure 3.17).

Figure 3.17- Scheme 1 Electronic mechanism of TEOS hydrolysis. The "Me" means methyl group and "Et" the ethyl group.

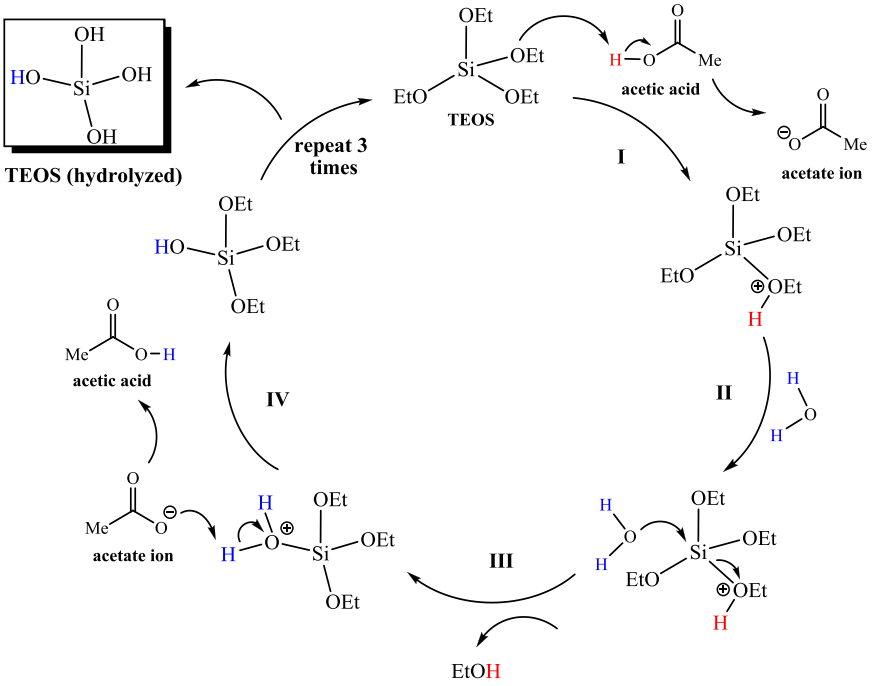

In the same way that TEOS was hydrolysed (Figure 3.17), the trimethoxysilyl group of the GPTMS (acid medium) is hydrolysed by acetic acid to trihydroxysilyl, releasing methanol as by-product (Figure 3.18-step Ia). Simultaneously, the glycidyl group of the GPTMS is protonated by acetic acid, yielding a highly electrophilic site (Figure 3.18 – step Ib), which is subsequently attacked by hydroxyl groups of the hydrolysed TEOS, resulting in a new hydroxyl group (Figure 3.18 – step II). The acetate ions released in steps Ia and Ib (Figure 3.18) are then protonated favouring the regeneration of the acetic acid and the formation of the bis-orthosilicate (Figure 3.18 – step III).

Figure 3.18 - Electronic mechanism of bis-orthosilicate formation from GPTMS-silyl hydrolysed.

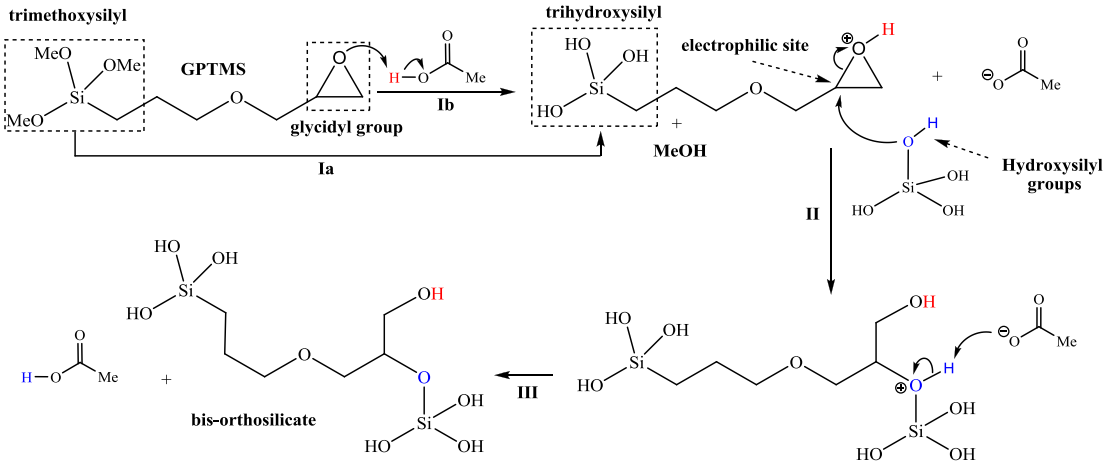

The acetic acid can protonate the hydroxyl groups of the bis-orthosilicate produced (Figure 3.18-step III) leaving the silicon more electropositive (Figure 3.19-step I) and susceptible to the attack by oxygen atoms present in the metal surface (aluminium oxide – Al_2O_3), yielding a cationic intermediate with a new Si-O-Al bond (Figure 3.19-step II). The acetate ions formed during step I (Figure 3.19) are protonated again regenerating the acetic acid and favouring the formation of Si-O-Al bonds.

Figure 3.19 - Reaction of sol-gel (bis-orthosilicate) with aluminium surface.

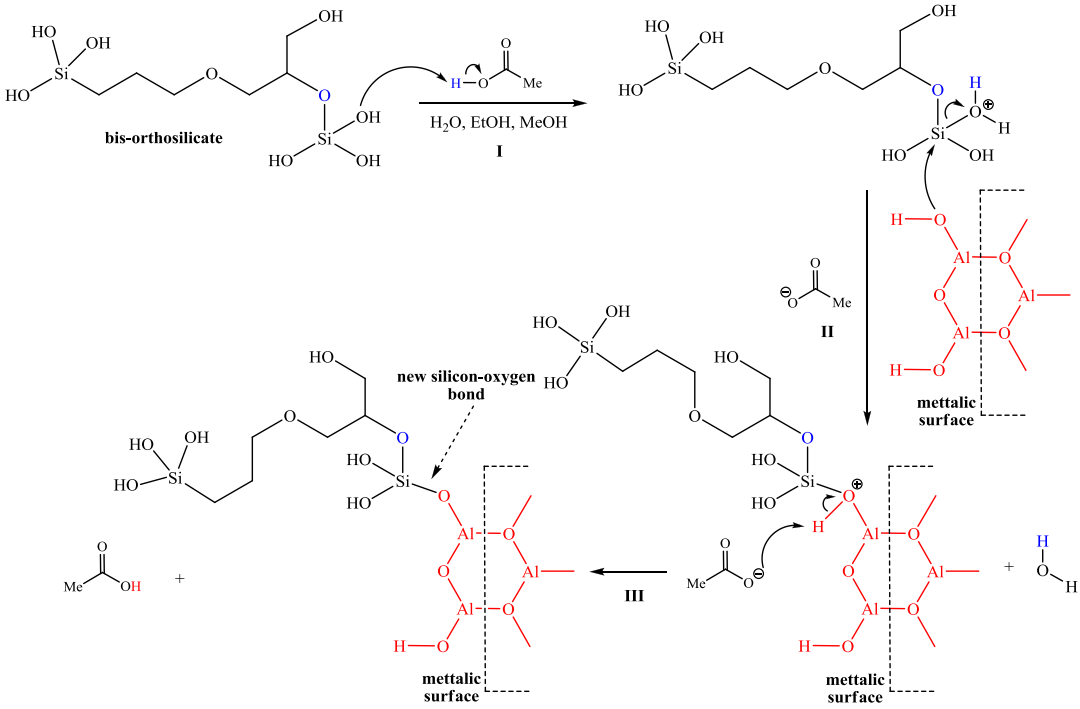

Likewise the hydroxyl groups (OH) attached to the aluminium (Al-OH) can react with silicon (Figure 3.19 - stage II), the OH groups of the Si-OH or H_2C-OH can also react with the silicon atoms, forming Si-O-Si or H_2C-O-Si, until all the Si atoms are connected with 4 groups OR (R = carbon chain or Al) or has no more acetic acid in contact with the reagents, as shown in Figure 3.20.

Figure 3.20 – Schematic representation of the bonding between siloxane molecules

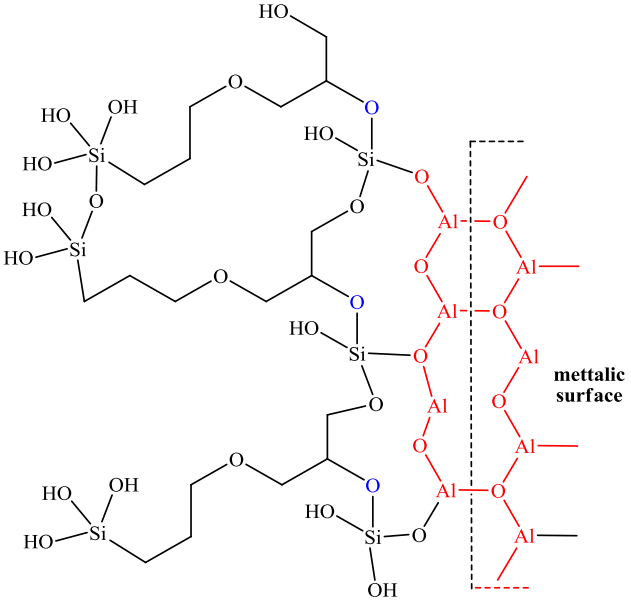

3.7.1 Sol-gel ageing

Before application on the aluminium alloy or any other substrate, the silanes need to be hydrolysed to have the highest number of silanol (Si-OH) groups to interact with the metal substrate (OOIJ et al., 2005). As described before, the hydrolysis and condensation reactions occur concurrently, and, immediately after hydrolysis, the formed silanol groups can undergo condensation reactions (Si-OH group with other Si-OH group) to form siloxane (Si-O-Si) (Equation 3.16), leading to cluster formation, which results in slow polymerization and eventual precipitation of these compounds (OOIJ et al., 2005; CHEN et al., 2011).

The total amount of silanol groups (Si-OH) available in the hydrolysis solution changes with time (ageing). The number of OH-groups reaches a maximum enhancing the formation of condensed species (Si-O-Si groups), consequently the amount of Si-OH groups available in the hydrolysis solution decreases. This can hinder the formation of compact and adherent film on the metal surface, negatively affecting the anticorrosion performance. Therefore, for long

sol-gel ageing (hydrolysis time), the concentration of Si-O-Si groups in the hydrolysis solution increases and, due to insufficient number of Si-OH groups, the silane-metal interaction decreases, resulting in less anchoring Al-O-Si bonds and poor corrosion protection (GANDHI et al., 2006).

The knowledge of hydrolysis time of a specific sol-gel solution is of high importance. OOij et al. (2005) reported that a water based silane like bis-UPS (ureidopropyltriethoxysilane) hydrolyses very fast from 15 min to 1 h while solvent-based silanes like bis-sulphur take 18 h to 48 h to hydrolyse (OOIJ et al., 2005). As the corrosion protection has a strong dependence on the bath composition, information about the stability of the hydrolysis solution after different ageing times is necessary especially for industrial scale-up of the process (GANDHI et al., 2006).

3.8 Electrochemical Impedance Spectroscopy (EIS) for characterization of porous AAO layers

EIS has been used as an effective tool for obtaining detailed information of the properties of the porous and barrier layers formed on aluminium alloys anodized under different conditions, as well as to get some insight on the corrosion process developed in these systems (WHELAN; CASSIDY; DUFFY, 2013; DOMINGUES et al., 2003; GONZÁLEZ et al., 1999; ZHAO et al., 2006). Other techniques, such as X-ray photoelectron spectroscopy (XPS), ellipsometry, and transmission electron microscopy (TEM), are also useful to study the properties and structure of these two layers (GARCÍA-RUBIO et al., 2009a). However, they require long specimen preparation and operation times. Therefore, EIS is being preferentially used due to its capability as an in-situ detection technique, sensibility, good feasibility for specimen handling and data interpretation (VAN DER LINDEN; TERRYN; VEREECKEN, 1990).

An important advantage of EIS over other electrochemical techniques is the use of very small amplitude signals without significantly disturbing the properties of the system, i.e., during the measurement the sample remains in quasi-steady state. This makes EIS extremely suitable to follow the evolution of the corrosion response of specimens immersed in aggressive electrolytes. To make an EIS measurement, a small amplitude sinusoidal a.c. signal, usually between 5 and 50 mV, is applied to a specimen at stationary state over a wide range of

frequencies, from few millihertz up to tens or hundreds of kilohertz. The frequency response analyser (FRA) registers the current and potential signals at each frequency and calculates the impedance as the Fourier or Laplace transform of the potential in relation to current. Impedance is a complex number, and the results are commonly presented as Nyquist (complex plane) or Bode plots.

As will be demonstrated in this part of the work, two main methodologies are frequently used to analyse EIS results. One is by evaluating the changes occurring in the diagrams as a function of a certain variable: immersion time, solution pH, temperature, post-treatment etc. The other consists in fitting the experimental EIS diagrams with electrical equivalent circuit (EEC) analogues conceived based on a physical model representing the interface under investigation. Due to its particular morphology: composed of a porous and a barrier layer with quite different properties, EEC fitting of EIS diagrams allows to separate the contributions of each layer to the overall impedance response as well as to detect any effect associated with the onset of corrosion (WHELAN; CASSIDY; DUFFY, 2013). According to González et al. (1999), EIS is able to detect any transformation occurring throughout the thickness of the anodized film, like modifications in its electrical properties, changes in the integrity of the barrier and porous layer, and the effect of any factor that can influence the sealing and ageing of the film (GONZÁLEZ et al., 1999).

The use of impedance and EEC analogues to investigate the properties of porous AAO layers started long before the use of computers and FRA to control the impedance response of an interface. In an article dating back to 1962, Hoar and Wood (HOAR, WOOD, 1962) employed a.c. bridge measurements (WOOD; COLE; HOAR, 1960) of the electrical impedance to investigate in-situ the sealing progress of porous AAO produced by SAA and sealed in different solutions. The influences of sealing time, porous layer thickness, type of sealing solution and temperature were discussed based on the variation of the resistance and capacitance of the a.c. bridge at different frequencies. The authors also proposed a model for pore sealing based on the inward movement of the pore walls, reducing the sectional area of each pore, together with the formation of a plug in the pore mouth of much higher average specific resistance than that of the electrolyte inside the pore. Even though less refined, this sealing model is very much alike to that discussed in section 3.6. In this same article, the authors (HOAR and WOOD, 1962) also proposed models of EEC analogues representative of unsealed and sealed porous AAO layer, which, at a time:

were consistent with the physical model conceived for the unsealed and sealed porous layer;

gave good agreement with the resistance and capacitance values determined for the layers by the a.c. bridge methodology for different frequencies;

the values ascribed to the passive elements of the EEC analogues were consistent with the physical properties they were supposed to represent.

Figure 3.21 presents the physical model of the unsealed porous AAO layer (a) and the EEC analogue conceived to represent it (b) (HOAR, WOOD, 1962).

Figure 3.21 - (a) Structure of unsealed porous film; (b) Simple electrical analogue for unsealed porous film after Jason and Wood.

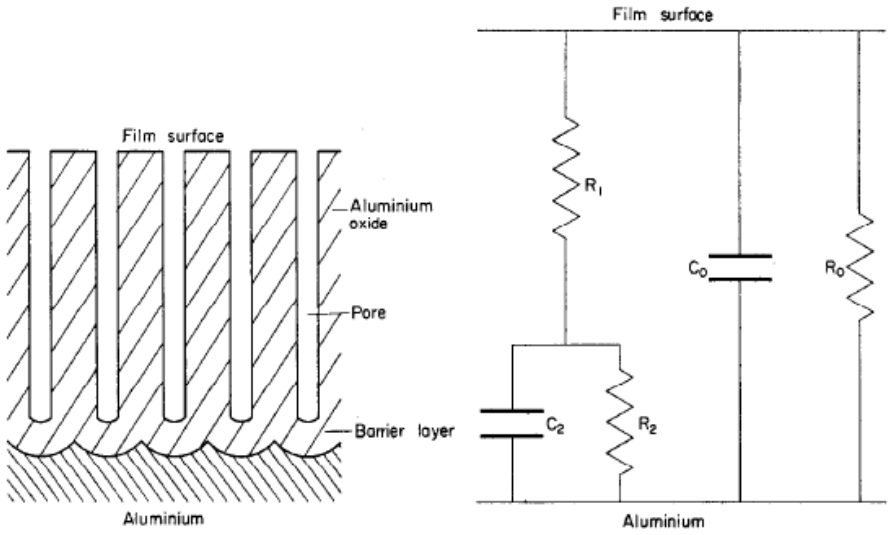

(a) (b)

Source: Hoar; Wood, 1962.

According to the authors, the physical meanings of the components (passive elements) of the EEC analogue of Figure 3.21 (b) are as follows (HOAR; WOOD, 1962):

R_0 – resistance of the hexagonal columns of alumina in the films (pore walls);

C_0 – capacitance of the hexagonal columns in the film (capacitance of the pore walls);

R_1 – resistance of the sealing solution in the pores;

R_2 – resistance of the barrier layer between the bottom of the pores and the metal;

C_2 – capacitance of the barrier layer.

According to the authors (HOAR; WOOD, 1962) the value of R_0 is so high that its inclusion in the complex impedance has no significant effect at any frequency, i.e., the current will pass through the other circuit elements which will offer lower impedance. Moreover, C_0 has an extremely low value (in the order of $nF.cm^{-2}$) and R_2 can be extremely high, according to the purity of the alumina layer. From these remarks, it can be inferred that, from the practical point of view of EIS data fitting with EEC, the pore walls resistance (R_0) will never be estimated by the procedure and C_0 only offers a pathway for the a.c. impedance sign at extremely high frequencies.

Hoar and Wood (HOAR; WOOD, 1962) also proposed an EEC analogue representative of the sealed porous layer, which is presented in Figure 3.22 (a) together with the suggested model for the progress of the pore sealing process (Figure 3.22 (b)). In Figure 3.22 (a), a transmission line represents the impedance response inside the pores: $C_{1\text{-}1}$ in parallel with $R_{1\text{-}1}$ and $C_{1\text{-}2}$ in parallel with $R_{1\text{-}2}$. This representation takes into account both the closure of the pores by the precipitation of boehmite as well as the physical changing of the sealed pore properties along its extension (distribution of properties). For instance, the pore mouths close quite quickly during sealing (see section 3.6); therefore, the resistance and capacitance of this region must be higher and lower, respectively, than in the remainder of the pore extension. Even though a good agreement between the impedance response of the EEC analogue Figure 3.22 (a) and the a.c. bridge impedance response was obtained at each investigated frequency, Hoar and Wood state that a higher number of parallel resistances and capacitances would better represent the impedance of the partially sealed pore (HOAR; WOOD, 1962).

Figure 3.22– (a) Modified electrical analogue for partially sealed porous films. (b) Schematic diagram of progress of sealing: O – wall of unsealed pore; I, II, III – successive stages of sealing.

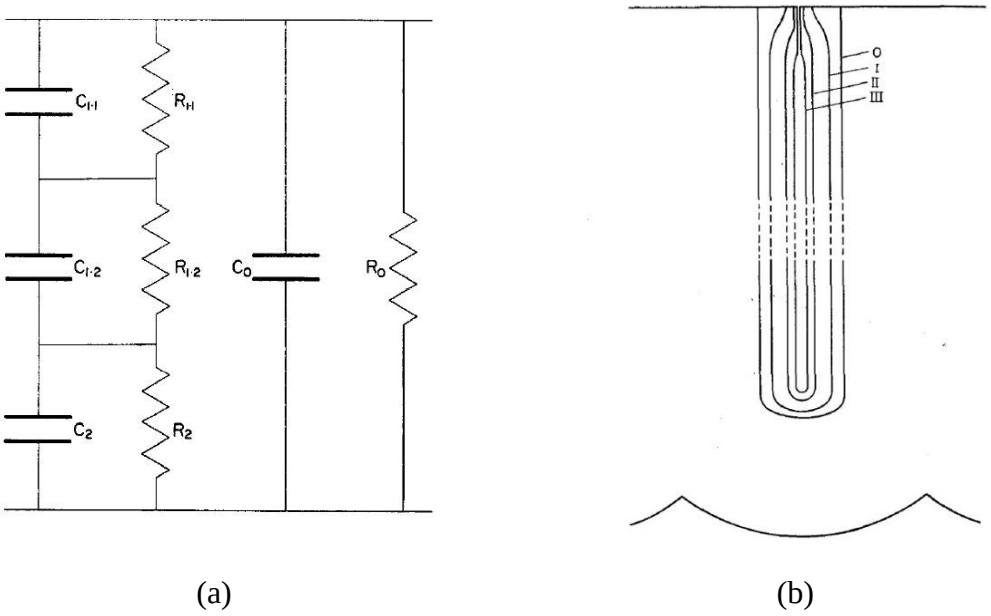

(a) (b)

Source: Hoar; Wood, 1962.

With the development of the FRA system, the use of EIS to investigate the properties and the corrosion behaviour of aluminium and its alloys protected with anodized layers became more widespread. Of interest to the present research, some works published during the eighties are extremely didactics in the interpretation of EIS data of sealed porous AAO and, therefore, will be commented in the following paragraphs.

Hitzig et al. (1984) employed EIS to investigate the influence of anodizing parameters (current density and anodizing time) as well as of the sealing time in the properties of the porous layer by using high purity Al as a substrate and testing the samples in non-aggressive electrolytes. In the model description section, the authors employ theoretical considerations and EEC simulation to demonstrate the ideal response of a sealed porous AAO layer. Figure 3.23 (a) and 3.23 (b) present, respectively, the EEC used to simulate the diagrams and the simulated Bode diagrams. The data used to perform the simulation are given in the Figure caption.

Figure 3.23– (a) Electrical equivalent circuit (EEC) used to fit/simulate the EIS diagrams of a sealed porous layer. (b) Simulated Bode diagrams for the EEC of (a): $R_p = 10^5\ \Omega$, $C_p = 10^{-9}$ F, $C_b = 5 \times 10^{-7}$ F. Note the high value of R_p, indicating that authors are investigating a sealed porous layer.

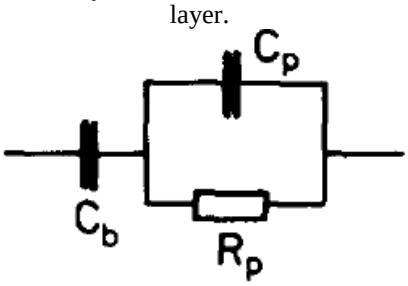

(a)

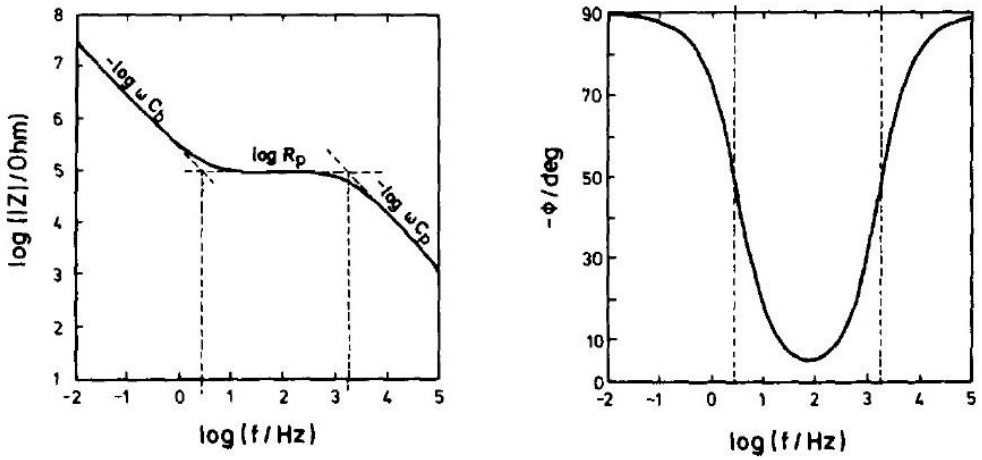

(b)

Source: Adapted from Hitzig et al., 1984.

For the diagram simulation, the resistance of the barrier layer (R_b) was not considered due to its extremely high value (HITZIG et al., 1984), as already proposed by Hoar and Wood (1962). However, in our opinion, a problem is associated with the assignment of C_p in Figure 3.23 (a), which Hitzig et al. (1962) ascribed to the capacity of the pore walls. Considering that all the analysed samples were sealed, it should be attributed to the capacity of the sealing (precipitated) products inside the pores. Therefore, another capacity short-circuiting the whole EEC of Figure 3.23 (a) should be added, as in the EEC model proposed by Hoar and Wood (1962) (Figure 3.22 (a)). However, as, generally, the capacity of the pore walls (C_0 in the Hoar and Wood EEC model - Figure 3.22 (a)) is of the same order of magnitude of the capacity of a sealed pore (see the discussion of the fitting results presented in section 5.7.3) this assignment does not affect the interpretation of the results. Taking into account this

remark, in the subsequent analysis, C_p will be ascribed to the capacity of the products inside the pores.

In the diagrams of Figure 3.23 (b) the high frequency (HF) time constant is ascribed to the response of the sealed porous layer, whereas the low frequency (LF) one is due to the barrier layer. As an ideal system, a capacitive response (phase angle = -90^o) is associated with each one of them, and the HF and LF slopes in the |Z| is equal to -1. Moreover, due to the great difference between the capacities of the barrier (very thin) and porous (thick) layers, these two time constants are well separated, which is a response frequently verified in sealed porous AAO layers (ARENAS; CONDE; DAMBORENEA, 2010; GONZÁLEZ et al., 1999). A plateau in the medium frequency zone is ascribed to the pore resistance (R_p). Variations in the values of C_p, R_p and C_b result in parallel displacements of the linear parts of the impedance modulus (log |Z|) diagram (HITZIG et al., 1984).

Figure 3.24 depicts the Bode diagrams for samples with porous oxide layers with different thicknesses. They were produced at the same current density (same barrier layer thickness) and their sealing times were proportional to their porous layer thicknesses at 3 $min.\mu m^{-1}$ (HITZIG et al., 1984). As reported by the authors, at frequencies higher than 1 Hz, log |Z| is shifted to higher values with increasing oxide layer thickness (HITZIG et al., 1984). Calculations presented in the article show that R_p increases and C_p decreases linearly with increasing porous layer thicknesses. The Bode phase angle diagrams also show that the thicker the layer the lower the frequency of the phase angle minimum.

Figure 3.24 - Bode diagrams for porous aluminium oxide layers of different thicknesses d = 10 µm (○), 20 µm (□) and 40 µm (△), prepared at constant formation current density i = 16 $mA.cm^{-2}$, and sealing time t_s = 3 $min.\mu m^{-1}$.

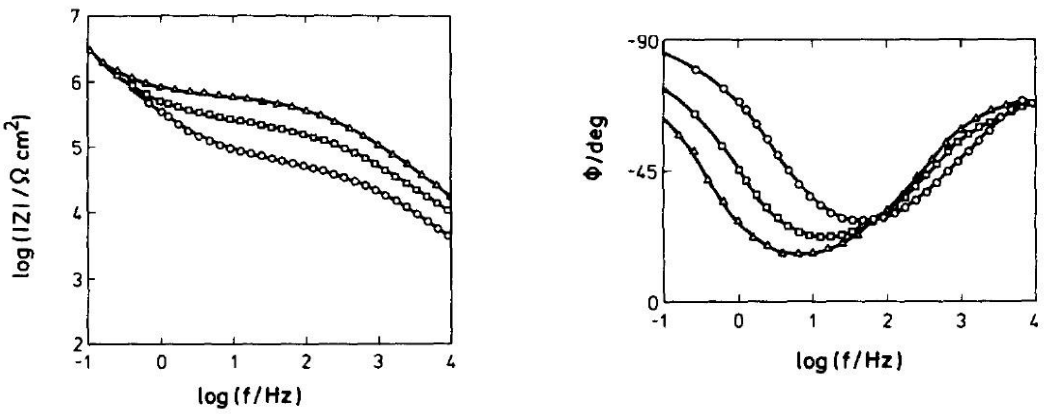

Source: Hitzig et al., 1984.

Figure 3.25 shows the effect of sealing time in the impedance response of the anodized aluminium sample. Only the impedance associated with the porous layer is affected by this variable and the longer the sealing time the higher the impedance in the HF region, which is a consequence of both R_p increase and C_p decrease (HITZIG et al., 1984). Similar response was found for the ageing effect (Figure 3.26): aged samples present higher impedance of the porous layer, which is a consequence of both the continuation of the sealing process during atmospheric exposure (see section 3.6) and the dehydration of the porous layer (HITZIG et al., 1984).

Figure 3.25 - Influence of the sealing time, t_s, on the Bode diagrams of porous aluminium oxide layers of constant thickness, d = 10 µm, prepared at a formation current density i = 16 mA cm^{-2}. Sealing time in min per µm thickness: t_s = 0.5 (◇), 1 (○), 2(□), 3(Δ).

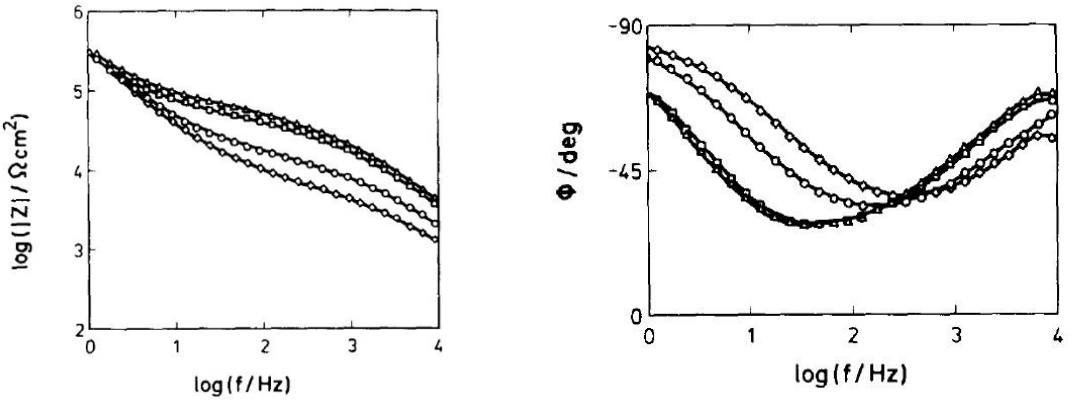

Source: Hitzig et al., 1984.

Figure 3.26 – Ageing effect of AC-impedance data obtained for an aluminium oxide layer of 10 µm thickness prepared at constant formation current density, i = 16 mA.cm^{-2}, and sealing time t_s = 3 min.μm^{-1}. Time of exposure to laboratory air: 1 day (Δ) and 60 days (○).

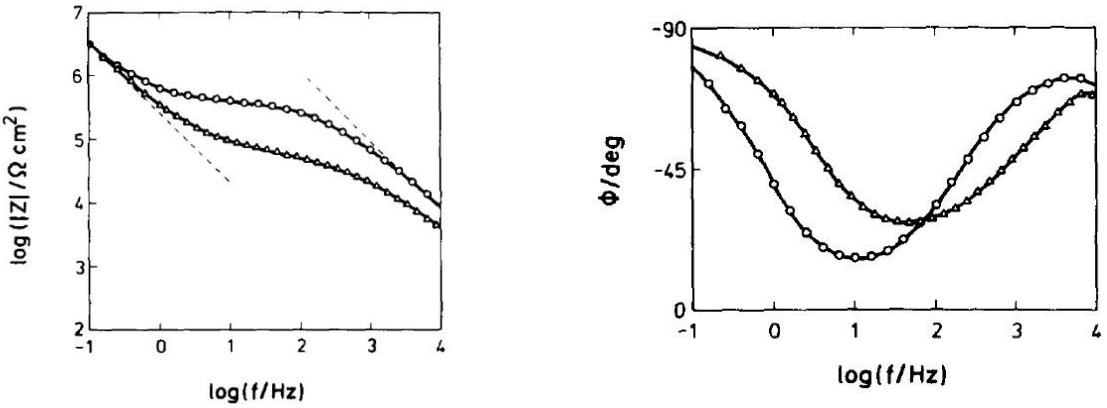

Source: Hitzig et al., 1984.

In a later article, published in 1986, Hitzig et al. (1986) evaluated the impedance response of sealed porous AAO under corrosion by drilling a varying number of artificial “passive” and “active” pits in aluminium samples protected by porous AAO (the paper does not specify the methodology to produce such pits). Figure 3.27 presents the physical model conceived for an anodized surface with “passive pits” (a) as well as the experimental Bode plots (b) for samples with different number of such pits (HITZIG et al., 1986). A critical observation of the physical model presented in Figure 3.27 (a) may lead the reader to suppose that it is an unsealed porous layer. However, the authors are only representing the locus where the porous layer was damaged, without, nevertheless, damaging the barrier layer; therefore some of the protective properties of the anodizing treatment remains at this particular point, as well as the corrosion resistance at the remainder of the undamaged sealed porous layer.

Figure 3.27 - (a) Schematic representation of an inhomogeneous oxide layer on aluminium with a passive pit; (b) corresponding experimental Bode diagrams for samples with increasing number of “passive” pits: 0 (Δ), 3 (□), 6 (○). System: Al (7075)/0.2 mol.L^{-1} K_2SO_4.

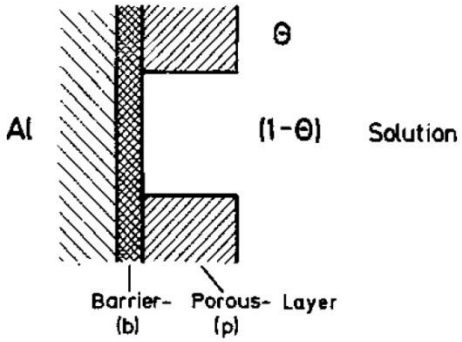

(a)

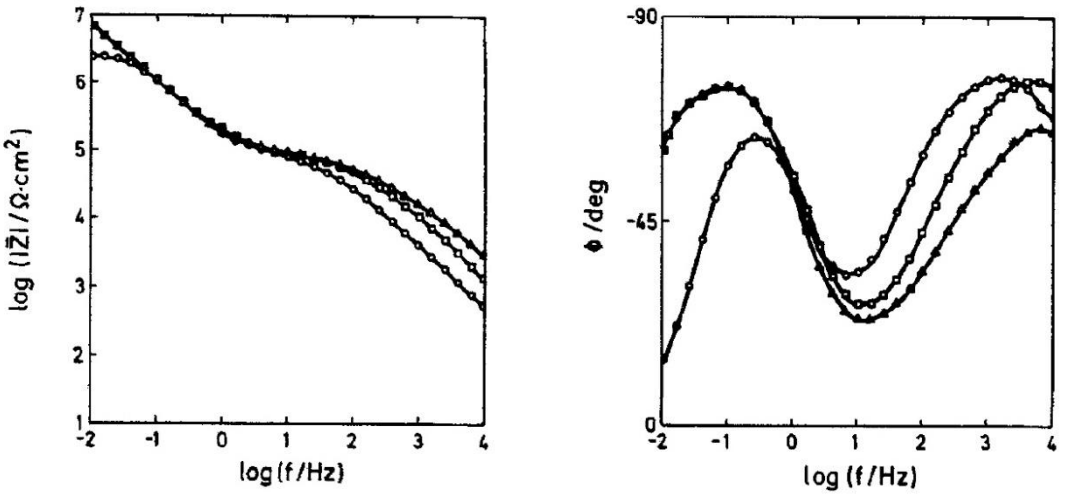

(b)

Source: Hitzig et al., 1986.

The Bode diagrams of Figure 3.27 (b) exemplify the EIS response of the anodized alloy with increasing number of conductive pathways to the barrier layer (increasing number of "passive" pits). In the HF region ($f \geq 10$ Hz) the impedance modulus decreases, as a consequence of the lower resistance of the defective sealed porous layer (HITZIG et al., 1986). Still in the HF region, a shift of the capacitive phase angles to lower frequencies was verified (not commented by the authors), which may be a consequence of the partial drift of the a.c. signal through the defective regions of the porous layer (the EEC proposed by the authors also seems to indicate that). In the LF region, after a certain number of pits were introduced, a plateau arises, ascribed by the authors to the inadequate recovery of the protective properties of the barrier layer (thinning) after the defect introduction (HITZIG et al., 1986), which also provokes the big change observed in the phase angle diagram.

Figure 3.28 (a) presents the physical model of the sealed porous anodized layer with "active" pits reaching the metal substrate, whereas Figure 3.28 (b) exhibits the corresponding Bode plots for anodized aluminium samples with increasing number of such defects (HITZIG et al., 1986). In the HF region, the Bode diagrams exhibit the same features already presented for Figure 3.27 (b), with the difference that changes were more dramatic, as no barrier layer is interposed at the bottom of active pits making the conductive pathways less resistant. However, the more important feature of the present situation is the huge impedance modulus decrease in the LF part of the diagrams with increasing number of pits (HITZIG et al., 1986), a consequence of the corrosion process taking place at the interface. Moreover, the impedance plateau in the medium frequency region disappears for the diagram with higher number of pits, due to the poorer separation of the two time constants (HITZIG et al., 1986). A displacement of the LF phase angle maximum to higher frequencies was also observed, resulting from the diminution of the interfacial resistance, being also an indication of the acceleration of the interfacial processes.

Figure 3.28 - (a) Schematic representation on an inhomogeneous oxide layer on aluminium with an "active" pit; (b) corresponding experimental Bode diagrams for samples with increasing number of "active pits: 0 (Δ), 3 (▼), 12 (○). System: Al 99.5 in 0.5 mol.L^{-1} NaCl.

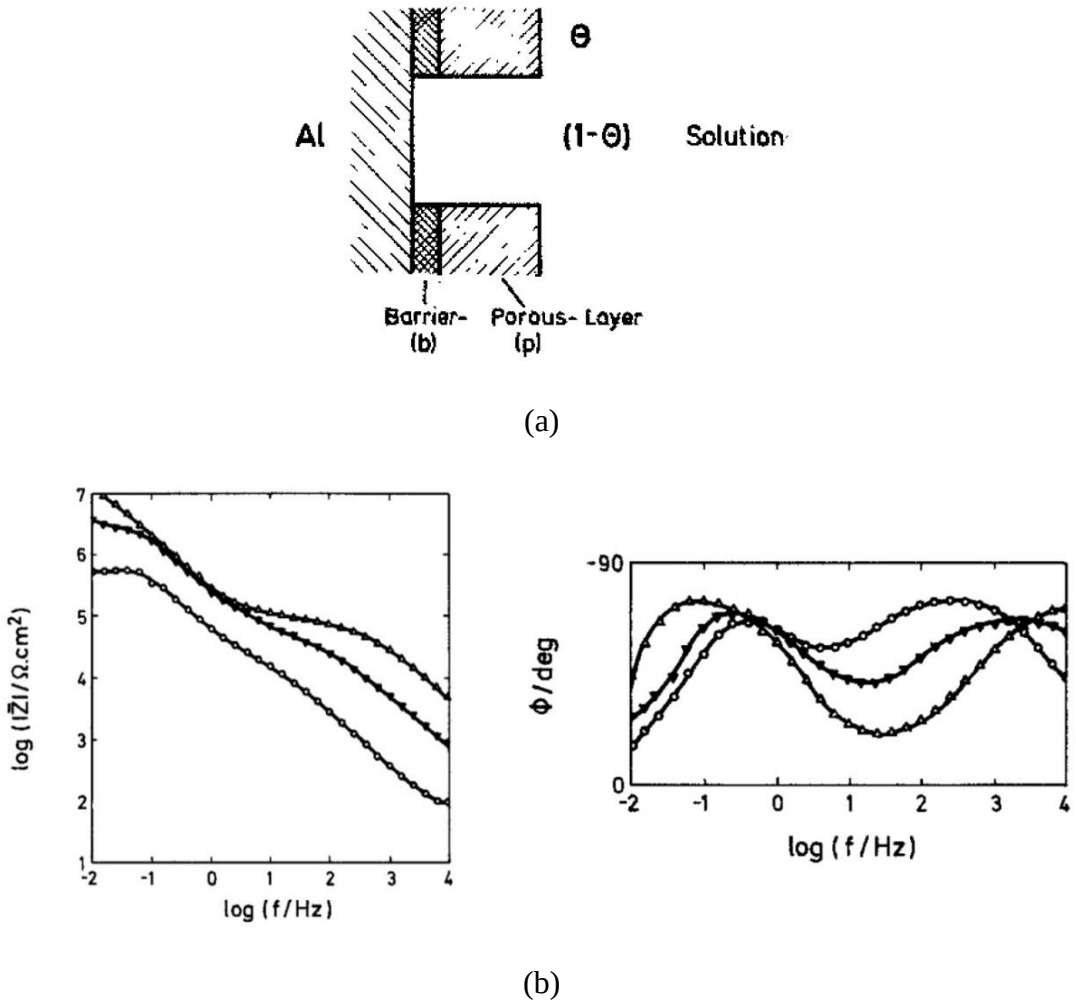

Source: Hitzig et al., 1986.

In the article, the authors show simulations of EIS diagrams for the different studied situations based on proposed EEC analogues, presented in Figure 3.29 for: undamaged (a), with "passive" (b) and "active" (c) pits (HITZIG et al., 1986). Some remarks: in all the circuits, the capacitive response of the pore walls is not considered (R_p and C_p correspond to phenomena taking place within the pores), and the differences between the analogues in (b) and (c) are the values ascribed to the R and C elements of the parallel subcircuit. Those were coherent with the expected properties: barrier layer for the passive pits and interfacial properties (double layer capacitance and charge transfer resistance) for active pits.

Figure 3.29 - Electrical equivalent circuits analogues for sealed porous layers: (a) undamaged, (b) with “passive” and (c) “active” pits.

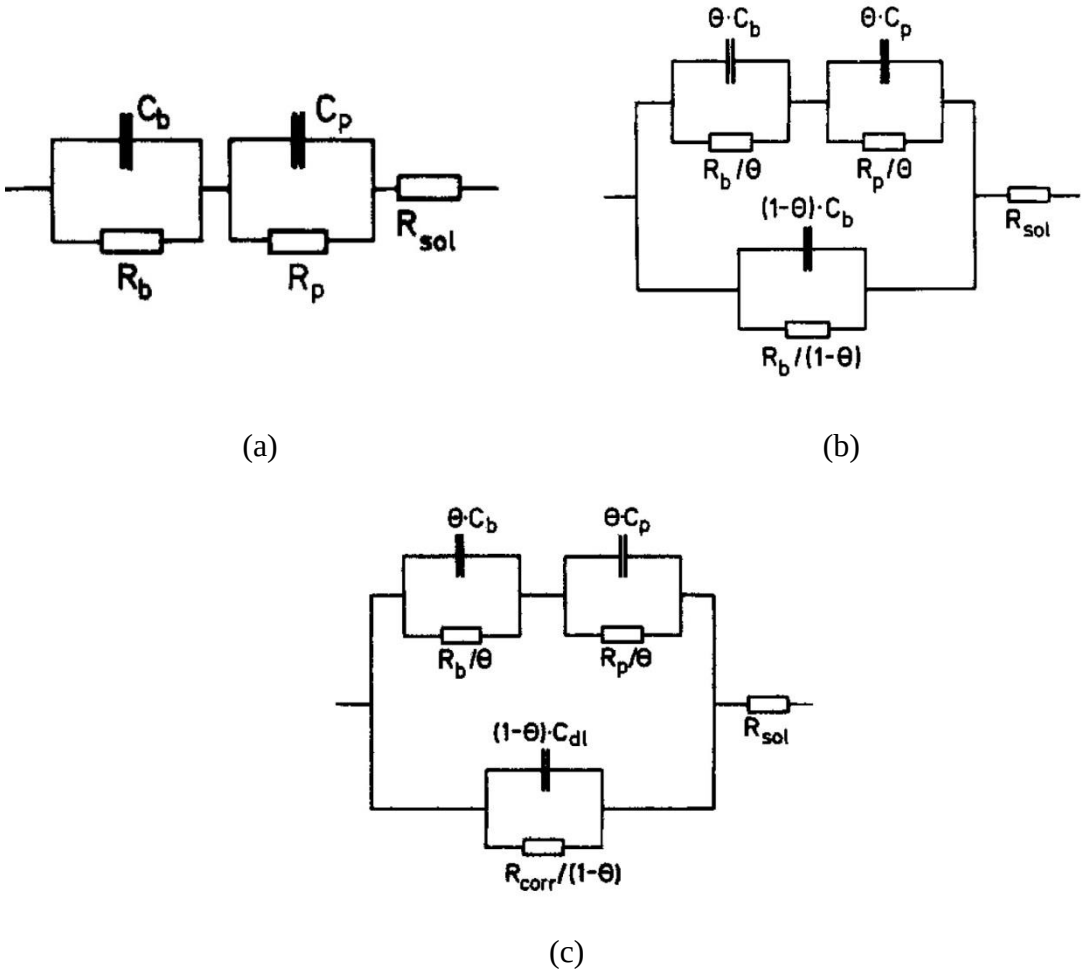

Source: Hitzig et al., 1986.

Mansfeld and Kendig (1988) employed EIS to characterize the surfaces of anodized Al alloys during exposure to 0.5 $mol.L^{-1}$ NaCl solution, evaluating the effects of anodizing bath (sulphuric acid, chromic acid), sealing procedure (unsealed, hot water, dichromate), and alloy chemistry (A12024, A16061, A17075). The results of this work emphasize the sensitivity of EIS to access both differences in the corrosion resistance as well as differences in the sealing mechanisms. Figure 3.30 indicates that the mechanism of sealing is different in hot water and dichromate solutions (HF phase angle and impedance modulus responses of this latter are very similar to that of the unsealed sample); whereas Figures 3.31 and 3.32 highlight that dichromate sealing process is more effective for the 7075 than for 2024. The impedance of the former alloy remains practically unchanged during the whole test, whereas huge changes were verified for this latter, both in the HF and in LF regions, indicating that the corrosion process damages the barrier and porous layer properties. In the article, the authors also present and

discuss the EEC analogues most commonly used to fit impedance data (similar to those previously presented) and propose a damage function based on the impedance at 0.1 Hz to describe the corrosion behaviour (MANSFELD; KENDIG, 1988).

Figure 3.30 - Bode plots for CAA Al2024 (BWS or DS).

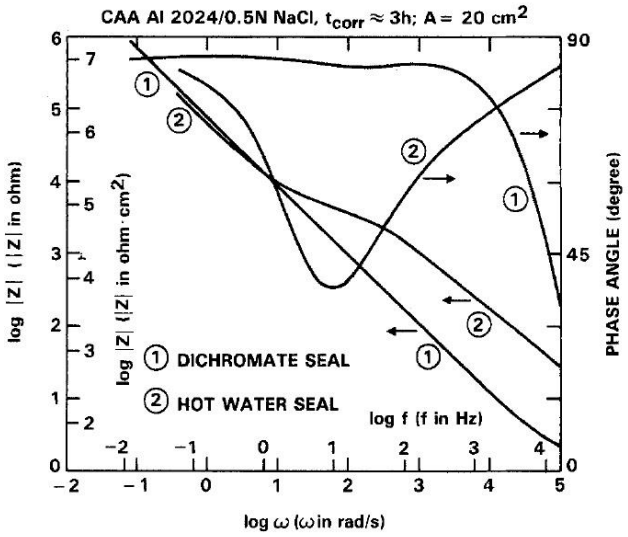

Source: Mansfeld; Kendig, 1988.

Figure 3.31 - Bode plots for dichromate sealed-chromic acid anodized Al7075 as a function of t_{corr}.

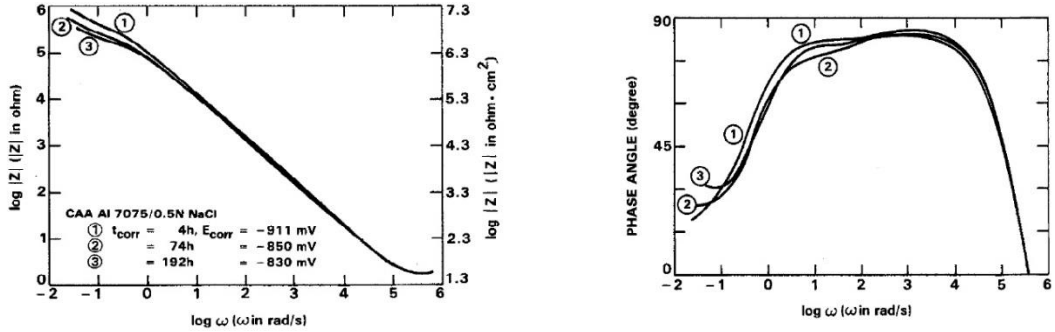

Source: Mansfeld; Kendig, 1988.

Figure 3.32 - Bode plots for dichromate sealed-chromic acid anodized Al2024 as a function of t_{corr}.

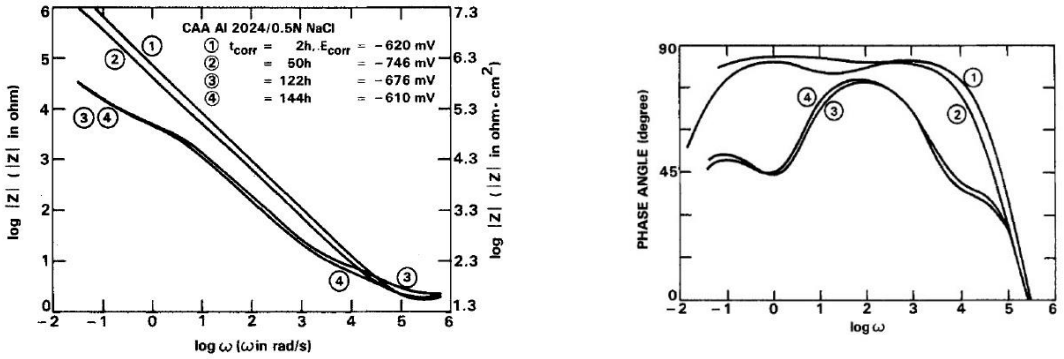

Source: Mansfeld; Kendig, 1988.

Finally, to clearly exemplify the differences normally found between unsealed and sealed porous AAO, Figure 3.33 extracted from the paper of González et al. (1999) shows that a single time constant characterizes an unsealed porous oxide layer. This Figure stresses again that as sealing time increases the HF impedance modulus increases (no modification of the LF response occurs) and the phase angle minimum is displaced to lower frequencies as a consequence of the increased resistance of the pores to current passage, therefore, the two time constants become more separated.

Figure 3.33 - Variation of impedance with the time of sealing in boiling deionized water. (○) Unsealed specimen. Specimens sealed for (+) 2 min, (■) 6 min, (□) 15 min and (●) 45 min. Diagrams acquired in unstirred aerated 3.5% K_2SO_4 solution.

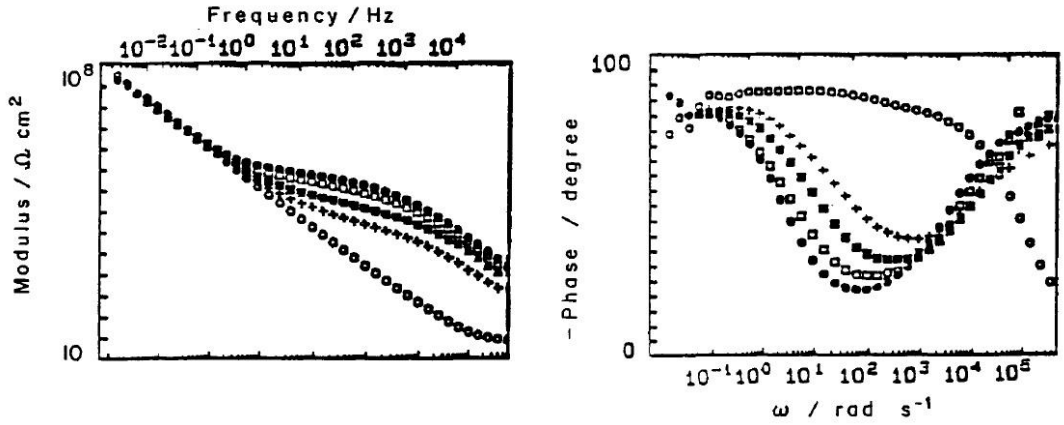

Source: González et al. 1999.

As shown in the previous paragraphs the EEC analogues proposed to fit the EIS diagrams of porous AAO use a combination of resistances and capacitances. In these first works (HOAR, WOOD, 1962; HITZIG et al. 1984, 1986; MANSFELD; KENDIG, 1988) the authors did not mentioned systems non-ideality, and pure capacitors were used to build the proposed EEC analogues. However, macroscopic electrodes are not homogeneous at the microscopic level. For instance, roughness, segregations, second phase particles, grain boundaries, etc. create heterogeneities within the same macroscopic surface. Therefore, each microscopic region may present a different electrochemical activity. Figure 3.34 schematically depicts the current flow through the electrode surface. At the microscopic scale, the current flow is composed of discrete events, and each one of the capacitances ($C_{0(i)}$) or Faradaic impedances ($Z_{F(i)}$) represented in Figure 3.34 may be slightly different from one another. Thus, a distribution of reactivity may exist at the electrode surface and it may not present the same electrochemical reactivity throughout the whole surface.

Figure 3.34– Schematic representation of the current flow through the electrode surface. Each element of the equivalent circuit may be different from each other moving the system away from an ideal behaviour.

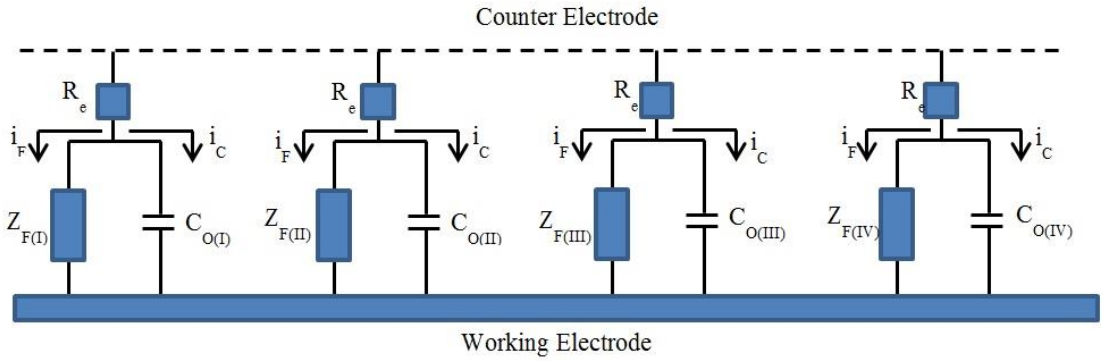

When performing an impedance experiment the setup records the sum of all discrete events occurring at the interface. Therefore, due to the distribution of electrochemical reactivity, a non-ideal response can be obtained and the EIS diagram cannot be adequately fitted using ideal capacitors in the EEC analogue. In order to take into account this non-ideal behaviour, capacitances can be substituted for constant phase elements (CPE). The following equation is proposed for the impedance of a CPE (ZOLTOWSKI, 1998; GARCIA-RUBIO et al., 2009a):

$$Z_{CPE} = 1/Y_0(i\omega)^n \qquad (3.17)$$

The parameter ω is the frequency, Y_0 is the pseudo-capacitance and n is the frequency dispersion factor, which varies from 0 to 1. When n = 1 the CPE can be considered as a

capacitor, when n = 0 it represents a resistor and when n = 0.5 diffusion-controlled processes are taking place (Warburg impedance). The closer the “n” is to one, the more the system approaches the ideal behaviour.

3.8.1 Electrochemical Impedance Spectroscopy (EIS) for characterization of AAO layers produced in TSA baths

In this section, scientific works on the EIS investigation performed in aluminium alloys anodized in TSA baths will be presented and discussed. Similarly to the proposal of the present work, most of them also evaluated the corrosion resistance of the anodized substrate after the application of a post-treatment step. As will be seen, EEC analogues similar to those proposed by Hoar and Wood (HOAR and WOOD, 1962) (Figures 3.21 (b) and 3.22 (a)) were frequently used to fit experimental EIS diagrams acquired for the porous AAO layers. In these circuits, the capacitances were most of the time substituted for constant phase elements (CPEs), which can be ascribed to the non-homogeneity of the system, as previously discussed. However, in most of the cases, the exponents of the CPEs associated to the pore walls (when determined) and the barrier layer were very close to one (BOISIER et al., 2008; GARCIA-RUBIO et al., 2010; CAPELOSSI et al., 2014) allowing determining the thicknesses of these layers (ZHAO et al., 2006; GARCIA-RUBIO et al., 2009a; GONZÀLEZ et al., 1999). Moreover, the assumption of a transmission line-like behaviour, represented in Figure 3.22 (a), which takes into account the distribution of properties inside the sealed pores is very useful for understanding the capacitive response of the time constant associated to the sealed pores (BOISIER et al., 2008; CAPELOSSI et al., 2014). This occurs because the properties of the boehmite precipitated in the pore mouth is different from the aluminium hydroxide precipitated inside the pore, which, in its turn, is not homogeneous throughout the pore. Scientific works relevant to the comprehension of the impedance diagram interpretation as well as the EEC fitting procedures were chosen. Several works present a comparison between the corrosion behaviour of SAA and TSA anodized samples (CURIONI et al. 2008a, 2008b, 2009, 2012; BOISIER et al. 2008; IGLESIAS-RUBIANES et al., 2007; ARENAS; CONDE; DAMBORENEA, 2010) whereas hydrothermal sealing was used as post-treatment step (BOISIER et al. 2008; ARENAS; CONDE; DAMBORENEA, 2010).

The specific role of tartaric acid on the corrosion resistance of the porous AAO was investigated by Curioni et al. (2009) and by García-Rubio et al. (2010). In the work of Curioni et al. (2009) the authors anodized AA2024-T3 in SAA or TSA baths at the same conditions (galvanostatically up to 6 V) in such a way that only the barrier layer was formed. Following, each anodized samples was immersed in their respective anodizing bath (without current or potential application). EIS diagrams acquired with immersion time showed the presence of only one time constant, confirming that only the barrier layer was formed, and faster impedance modulus and phase angle decrease for the sample immersed in the SAA bath, indicating faster deterioration rate of the barrier layer in this solution. The authors confirmed this tendency by determining the barrier layer thickness as a function of immersion time after fitting the EIS diagrams to a proposed EEC (with only one time constant, as only the barrier layer was present). The same trend was verified for a barrier layer produced in ammonium pentaborate bath exposed to the same solutions, the dissolution rate decreased in the following order: 0.46 mol.L^{-1} H_2SO_4 > 0.46 mol.L^{-1} H_2SO_4 + 0.53 mol.L^{-1} $C_4H_6O_6$ > 0.46 mol.L^{-1} H_2SO_4 + 1 mol.L^{-1} $C_4H_6O_6$. Authors suggest that the presence of tartaric acid derived species in the pore solution may have a beneficial effect on the pH stability (buffering action), preventing local alkalinisation or acidification associated with the corrosion process.

García-Rubio et al. (2010) studied by EIS the corrosion resistance of AA2024, AA6061 and AA7475 anodized in TSA bath and left immersed in the bath after termination of the anodizing procedure for 0, 5, 10 and 20 min before rinsing with deionized water. According to the authors, the immersion time in the electrolyte after current interruption and before rinsing is critical, since the newly formed oxide can be attacked by the acidic bath solution. After the different procedures the samples were tested in several electrolytes either unsealed or after sealing by immersion in boiling distilled water for 20 min. Figures 3.35 (a) and (b) present the EIS diagrams obtained for unsealed AA2024 samples in 0.5 mol.L^{-1} Na_2SO_4 and 0.5 mol.L^{-1} NaCl, respectively. The diagrams present only one time constant (which complexity is discussed by the authors as a function of the test electrolyte), and, for both electrolytes, the impedance modulus diminishes and the phase angle plot narrows with increasing immersion time in the anodizing bath, indicating decreasing anticorrosion properties. The analysis of the LF part of these diagrams reveals the stronger aggressiveness of the chloride containing solution towards the anodized alloy. In this solution impedance modulus strongly decreases for longer immersion times (almost three orders of magnitude for the 20 min sample), a LF impedance modulus plateau is established, indicating a pure

resistive response and great changes in the phase angle take place, approaching zero at the lowest frequency. The EIS spectra of the hydrothermally sealed AA2024 specimens in 0.5 mol.L^{-1} NaCl (Figure 3.35 (c)) revealed an additional time constant at high frequencies, associated with the presence of hydrated aluminium oxides within the pores. A decrease of |Z| at low (barrier layer) and high frequencies (porous layer) was observed with increase of immersion time in the anodizing bath, indicating the deterioration of the protective properties of both layers. After immersion in the anodizing electrolyte for 20 min, only one time constant was observed, and the impedance modulus was reduced by 2–3 orders of magnitude at all frequencies, suggesting that the porous anodic oxide was largely removed and that the barrier layer is highly damaged. Overall, the impedance behaviour of the other two alloys were similar, however, the non-copper bearing alloy (AA6061) presented the best behaviour for all situations. The authors also presented a strategy for fitting the EEC for the unsealed samples which is worth consulting, but that will not be commented as it is out of the scope of the present work. The authors conclude that the contact of the anodized layer with the TSA bath after anodizing termination degrades the barrier layer properties and gives rise to the appearance of local defects, hindering the anticorrosion performance.

Figure 3.35 - EIS diagrams of the TSA anodized AA2024 samples withdrew from the TSA bath after different times: (a) unsealed samples tested in 0.5 mol.L^{-1} Na_2SO_4; (b) unsealed samples tested in 0.5 mol.L^{-1} NaCl; (c) sealed samples tested in 0.5 mol.L^{-1} NaCl.

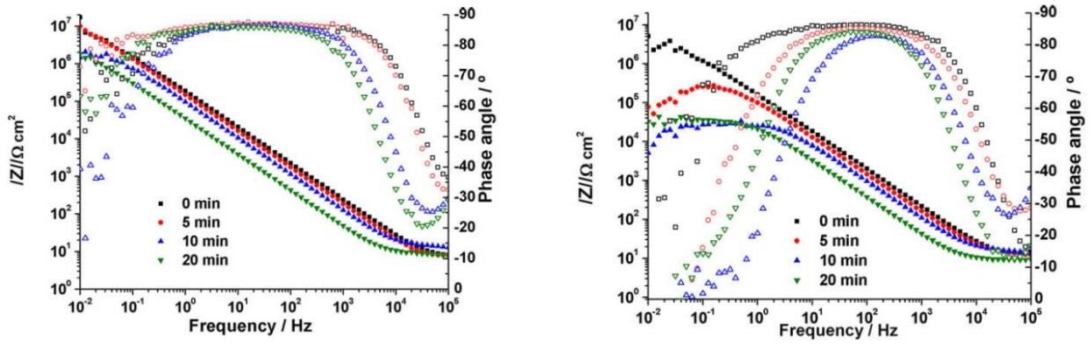

(a) (b)

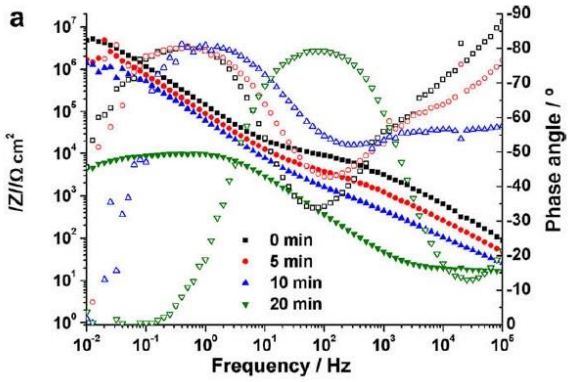

(c)

Source: Garcia-Rubio et al., 2010.

Boisier et al. (2008) used EIS to compare the anticorrosion properties of AAO produced in SAA and TSA. The anodic layers were produced using the same parameters and were tested either under unsealed or hydrothermally sealed (HTSed) conditions. FESEM characterization revealed a better pore distribution for the film formed in TSA as well as lower pore volume. This latter feature was ascribed to a possible limiting effect of tartaric acid on the dissolution of the outwardly moving Al^{3+} ions. The EIS diagrams for both unsealed samples (Figure 3.36 (a) - 0.5 mol.L^{-1} Na_2SO_4) were very similar, except in the LF region, and presented two not well separated time constants, which were fitted with a two time constants EEC (Figure 3.36 (b)). This EEC is similar to the one proposed by Hoar and Wood (HOAR and WOOD, 1962) (Figure 3.21 (b)) without the resistance ascribed to the pore walls (R_o), which, as said by these authors, is too high to be determined by EIS. From the fitting procedure, a higher barrier layer resistance was determined for the layer produced in SAA, which, nevertheless, showed a lower thickness. The authors recognized this contradiction and proposed deeper investigation. For the samples anodized in TSA and HTSed, Bode plots acquired after 2 h immersion in 0.5 mol.L^{-1} NaCl (Figure 3.37 (a)) clearly illustrate the physical changes occurring in the porous layer with increasing sealing time, also demonstrated by FESEM analysis. Thus, for 30 and 90 s of sealing, the impedance diagrams are typical of unsealed (or partially sealed) pores, i.e., present two time constants that are not well-separated, whereas, only after 5 minutes two well-defined time constants were obtained, indicating effective pore plugging. To fit the experimental EIS diagrams the authors used the EEC presented in Figure 3.37 (b), which is very similar to the one presented in Figure 3.22 (a), except that only one sub-circuit was employed to represent the impedance response within the sealed pores. Interestingly, the

results of the fitting procedure revealed low exponent for the CPE. The authors (BOISIER et al.; 2008) suggest that a transmission line model would better take into account the sealed pore structure, as suggested in the EEC of Figure 3.22 (a). Besides this feature, the fitting procedure revealed that R_p increased with sealing time, whereas the remainder of the elements of the EEC remained relatively constant. Even though the diagrams were not presented, the authors state that sample produced in SAA and HTSed presented similar results, however with lower R_p values, indicating a poorer sealing. This superior performance was confirmed in the long-term immersion tests, where higher R_p and R_b values were always determined for the TSA produced sample. To explain these results, the authors suggested that the pores formed in TSA are better sealed due to their low diameter and that tartrate ions presented in the solution within the pores may influence the rate of pore sealing.

Figure 3.36 - (a) Bode plots of unsealed anodic films formed in TSA (●) and SAA (○) baths obtained after 2 h of immersion in 0.5 mol.L^{-1} Na_2SO_4 (b) Physical model of the unsealed porous layer and EEC analogue employed to fit the EIS diagrams.

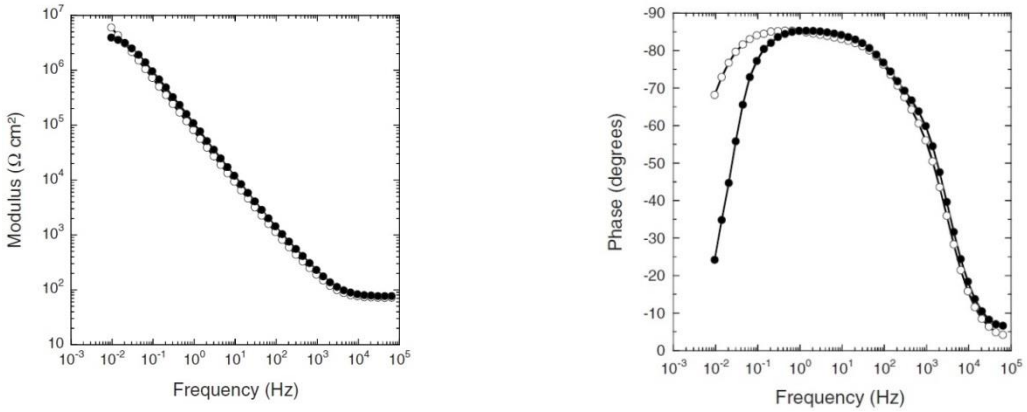

(a)

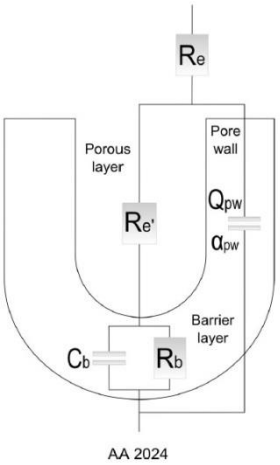

(b)

Source: Boisier et al., 2008.

Figure 3.37 - (a) Bode plots of anodic films formed in TSA solution and then sealed for different times in boiling water obtained after 2 h of immersion in 0.5 mol.L^{-1} NaCl (b) Physical model for the sealed porous layer and EEC analogue employed to fit the EIS diagrams.

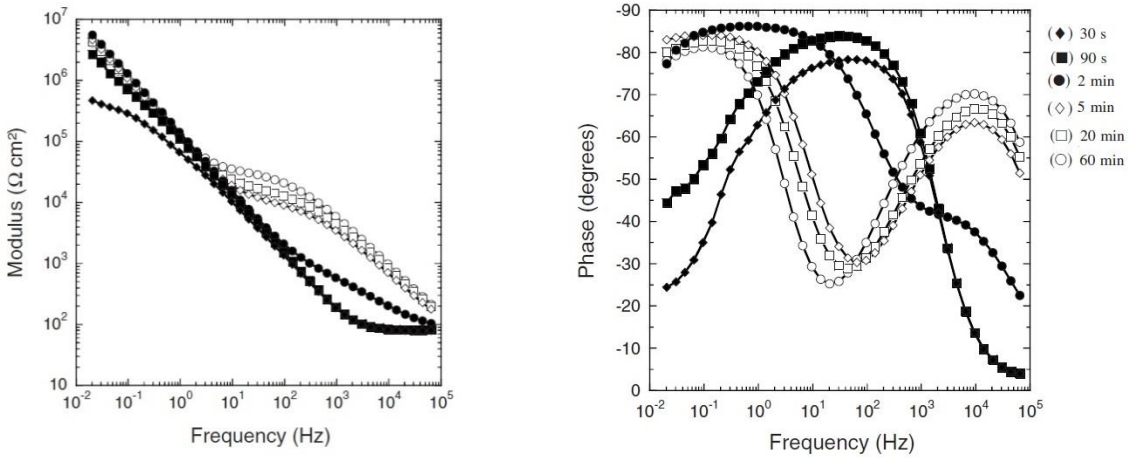

(a)

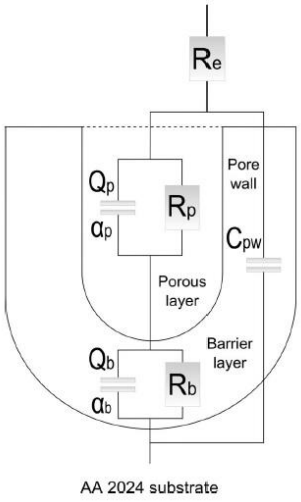

(b)

Source: Boisier et al., 2008.

Arenas et. al. (2010) obtained EIS spectra in 3 wt% NaCl for AA2024-T3 anodized in SAA and TSA baths and sealed in boiling water. In agreement with the results presented by Boisier et al. (2008), the Bode plots presented two well-defined time constants after 30 min of sealing, indicating that an effective sealing process of the porous layer has occurred. The maximum of the phase angle was identified for the TSA anodizing, while this value was outside the frequency range measured in the test for the SAA, suggesting a less resistive layer obtained with this latter treatment, as shown in Figure 3.38. The porous layer resistance could

be estimated from the impedance value at the intermediate frequencies in the |Z| Bode diagram, where higher impedance values were found for the sample anodized in TSA, indicating better protective properties. In the conclusion, the authors propose that residual tartaric acid inside the pores might dissociate during the hydrothermal sealing as result of an increase in pH. Tartrate ions would form chelate complexes with Cu(II) cations available in the oxide film. The removal of Cu^{2+} from the internal walls of the pores reduces the heterogeneity of the anodic film, leading to a more resistive layer.

Figure 3.38 - Evolution of impedance diagrams with immersion time in 3 wt% NaCl solution of sealed (a) SAA and (b) TSA anodized specimen.

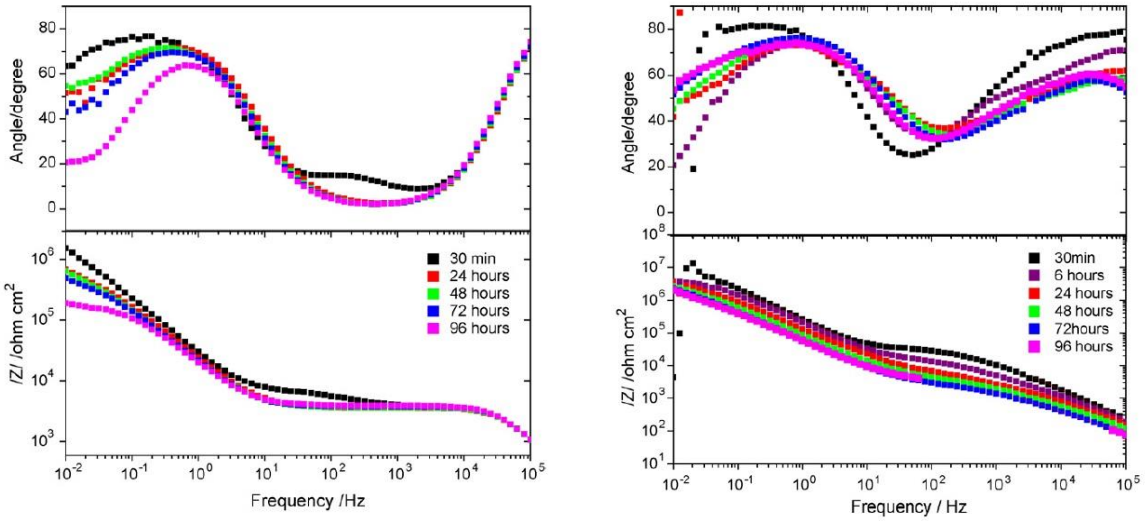

(a) SAA (b) TSA

Source: Arenas et. al. 2010.

Porous AAO is frequently sealed or painted to improve the corrosion resistance. In the latter case, it is normal to apply a post-treatment with corrosion protection capabilities prior to the final top coating application. Therefore, EIS has also been employed to evaluate the corrosion resistance of aluminium alloys anodized in TSA and submitted to a post-treatment step; in general hydrothermal sealing was used as reference to compare the results. With the purpose to evaluate the effectiveness of the classical post-treatments used in the aircraft industry on the TSA anodic films and their corrosion resistance behaviour, Garcia-Rubio et al. (2009a) anodized clad and unclad AA2024, which were then post-treated by hot water sealing (HWS), dichromate sealing (DS) and immersion in Henkel Alodine (cold concentrated chromate solution) (HA). Immersion tests, polarization curves and EIS were employed to evaluate the

corrosion behaviour. As a good diagnostic test for the sealing procedure, the phase angle plots for the unsealed samples (TSA and TSA + HA), both for the unclad and clad alloys, presented only one time constant, whereas two time constants were detected for the sealed samples (TSA + HWS and TSA + DS). In addition, for the two substrates, due to pore plugging, diagrams acquired after 1 h immersion in 0.5 $mol.L^{-1}$ NaCl showed higher |Z| in the HF region for the sealed samples, even though similar LF |Z| were determined for sealed and unsealed samples. Figure 3.39 presents the evolution of the EIS response with immersion time in the 0.5 $mol.L^{-1}$ NaCl electrolyte for unsealed (a) and sealed (b) unclad AA2024 samples. For the unsealed samples (Figure 3.39 (a)) |Z| greatly decreased with immersion time and a shift from capacitive to resistive behaviour was observed in the LF limit, which can be verified both by phase angle decreasing and by the incipient |Z| plateau established in this frequency range. This indicates that these samples were heavily affected by corrosion. On the other hand, for the sealed samples (Figure 3.39 (b)), the overall decrease of |Z| with immersion time was lower than for the unsealed ones. These diagrams (Figure 3.39 (b)) also indicate that the damage both to the sealed porous layer and to the barrier layer was lower for the TSA + DS sample than for the TSA + HWS one, a feature that can be directly identified in the plots by the lowering of |Z| in the HF and LF domains, respectively. Note that, according to the discussion and results presented by the authors (GARCIA-RUBIO et al., 2009a), the correct symbols that identify HWS (▼) and DS (▲) after 720 h of immersion time in 0.5 $mol.L^{-1}$ NaCl solution is showed in the phase angle graph presented in the Figure 3.39 (b).

The fitting of the impedance diagrams with the EEC of Figure 3.39 (c) for the unsealed samples and Figure 3.39 (d) for the sealed ones, gave insight into the deterioration mechanisms. Thus, for the unsealed samples it was verified that, for short immersion time, R_b was higher and C_b lower for TSA + HA, indicating better corrosion behaviour. However, for longer immersion periods (720 h), R_b and C_b were of the same order of magnitude for both unsealed samples, indicating that the Alodine post-treatment is not able to prevent degradation of the barrier layer. For the sealed samples, even though no flaws were visually identified after 720 h of test, the variation of the components of the EEC indicated that the TSA + DS sample was more stable than the TSA + HWS. EIS diagrams for the clad AA2024 showed more stable behaviour than the bare alloy, and, in accordance with the previously discussed results, the unsealed samples were less stable than the sealed ones. The diagrams also revealed a self-sealing process for the unsealed samples, characterized by the onset of a HF

time constant for longer immersion times. Also for these samples, EEC fitting was performed and their evolution discussed.

Figure 3.39 - (a) Bode plots for unsealed (TSA and TSA + HA) unclad AA2024 specimens as a function of immersion time in 0.5 mol.L^{-1} NaCl solution; (b) Bode plots for sealed (TSA + HWS and TSA + DS) AA2024 specimens as a function of immersion time in 0.5 mol.L^{-1} NaCl solution. EEC employed to fit the EIS diagrams of the (c) unsealed unclad samples; (d) sealed unclad samples.

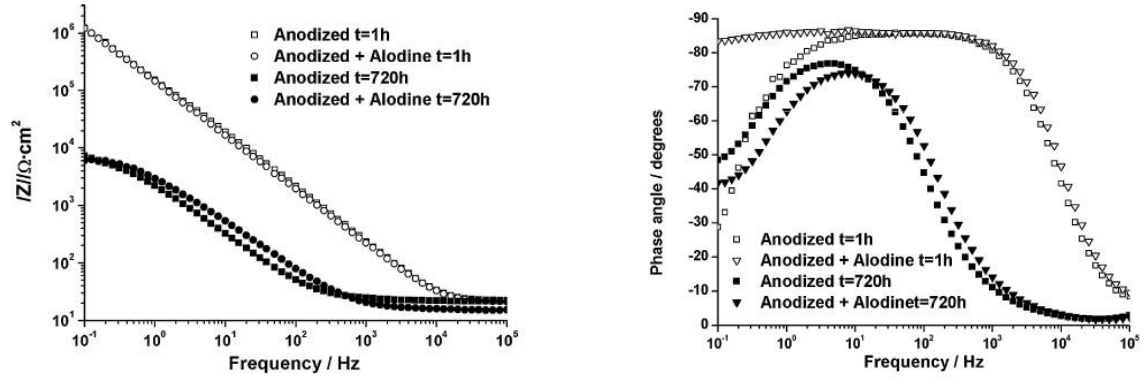

(a)

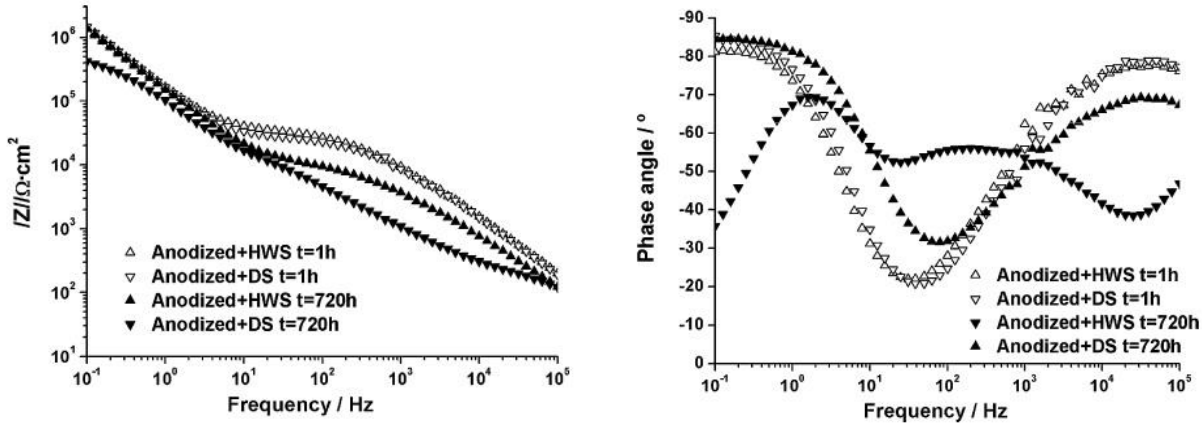

(b)

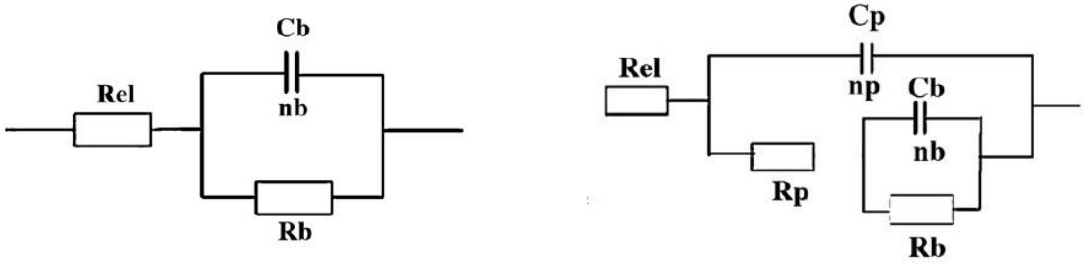

(c) (d)

Source: Garcia-Rubio et al., 2009a

Boisier et al. (2009) investigated the use of carboxylic acids (hydrophobic molecules) as a post-treatment for sealed AA2024 anodised in tartaric–sulphuric acid electrolyte. In this work EIS played an important role both in the determination of the carbon chain length of the molecule with the best protective properties as well as to determine the treatment time. Regarding the former strategy, unsealed anodised samples were exposed for 30 min at 75 °C to pure molten acids with different chain lengths and then EIS experiments were performed after 2 h of immersion in non-aggressive electrolyte (0.5 mol.L^{-1} Na_2SO_4). The results showed that for the post-treated specimens a HF time constant (similar to that of a sealed porous layer) was present that became more evident and well separated from the LF one with increasing chain length. This time constant was associated with the carboxylic acid response, which could penetrate in the pores of the unsealed anodized layer. By fitting the HF part of the EIS diagrams with a simple R//CPE circuit it was determined that the acid with the longest chain length provided the best film properties (higher resistance). For determining the influence of post-treatment time, sealed anodized samples were immersed in the molten solution of the acid with the best protective performance for different periods of time, and their impedances followed with immersion time in 0.5 mol.L^{-1} NaCl solution. At this point it is interesting to present the strategy adopted by the authors to fit their impedance diagrams to EEC. As shown in Figure 3.40 (a), at a first sight, EIS diagrams are composed by only two time constants. However, the authors verified that with three time constants a better fitting could be achieved. This third time constant could be explained by the presence of the carboxylic acid film on top of the sealed anodic layer, as depicted in Figure 3.40 (b). From fitting the EIS data with this EEC it was determined that the films obtained after the highest post-treatment time (60 min) offered the best anticorrosion protection, characterized by a more stable film resistance (R_f) and higher values for the resistance of the sealed pores (R_p) (the barrier layer resistance remained practically constant irrespectively to the post-treatment time). The authors discussed their results in terms of a possible reaction between the carboxylic acid and the alumina layer, forming alumoxanes, which seems to be an aluminium soap with hydrophobic properties.

Figure 3.40 - (a) Bode plots of sealed anodic layers obtained after post-treatment for 60 min at 75 °C in pure molten stearic acid (diagrams plotted after 2 h and 336 h of immersion in 0.5 mol.L^{-1} NaCl). Results fitted with 3 or 2 time constants. (b) Equivalent circuit used to model the impedance diagrams of the post-treated sealed anodic layers (R_f: electrolyte resistance in the pores of the organic film/Q_f and α_f: CPE parameters associated to the organic film/R_p: porous layer resistance/Q_p and α_p: CPE parameters associated to the sealed porous layer/R_b: barrier layer resistance/Q_b and α_b: CPE parameters associated to the barrier layer).

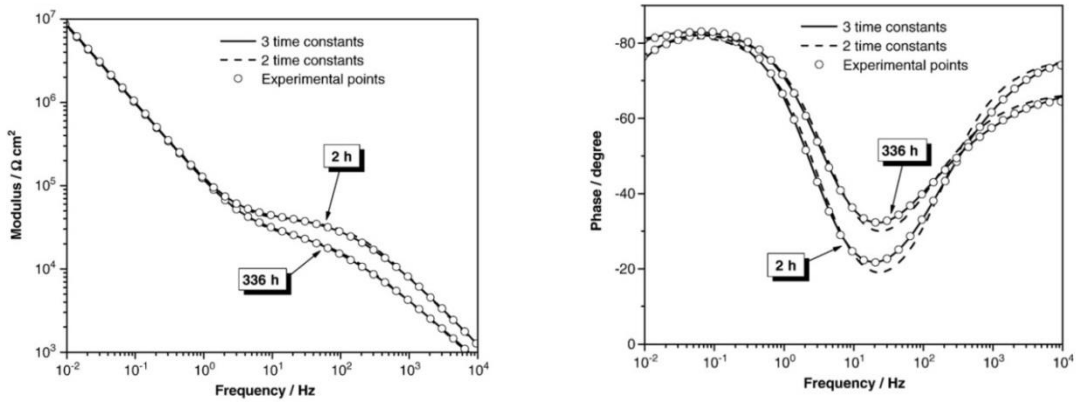

(a)

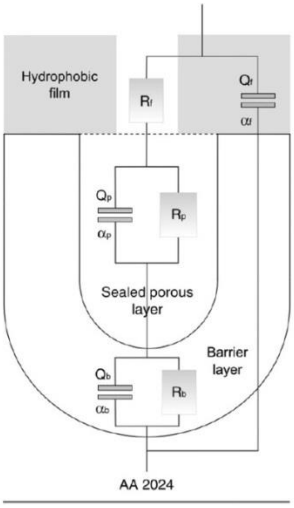

(b)

Source: Boisier et al., 2009.

3.8.2 Use of sol gel coatings to protect porous AAO from corrosion

Even though the sol-gel methodology has been widely used for corrosion protection of aluminium and other metals (DONLEY ET AL., 2003 WANG; AKID, 2007; FENG et al., 2010; NICOLAY ET AL., 2015), only few works are available where porous AAO were protected with such coatings aiming to improve the corrosion resistance.

Hirai et al. (1998) used the sol-gel methodology to apply a zirconium oxide coating on commercially pure Al anodized in phosphoric acid. The authors report an increase by a factor of 24–50 of the alkaline corrosion resistance of the composite film when compared to the same coating applied on naturally growth oxide. Further improvement of the performance upon immersion in boiling water after the termination of all dip coating procedure was verified, which, nevertheless, was not ascribed to pore sealing, but, instead, to some reactions taking place between the sol gel and the testing electrolyte (HIRAI et al., 1998).

Liu et al. (2010) applied a TiO_2 sol-gel coating by the sol-gel methodology on porous AAO anodized in oxalic acid. A vacuum dip-coating technology was employed to guarantee penetration of the sol-gel solution within the pores. The investigation of the corrosion resistance in sterilized seawater (1 h immersion) showed that the coating diminished the corrosion current density and increased |Z| for approximately two orders of magnitude. Interestingly, in the phase angle diagrams two well-defined time constants were detected for the anodized sample (apparently unsealed), whereas for the TiO_2 coated substrate a strong overlapping of the HF and LF time constants was verified, which is a different response from those previously reported. In a posterior work, the same group (HIRAI et al., 1999) employed ultraviolet radiation for curing the same TiO_2 sol-gel coating. The authors report the formation of thinner films with, however, higher alkaline corrosion resistance than the thermally treated coating (2.4-2.6 times). This was ascribed to a better densification of the sol-gel coating using this new curing procedure (HIRAI et al., 1999).

In a kind of technical work published in 2003, Zemanova and Chovancova (2003) used a sol-gel methodology to apply an alumina coating to porous AAO produced in SAA. The corrosion resistance of the sol-gel treated sample was compared with HTS (30 min) by ASTM D 2247 (100 % air humidity and 35 ºC) and the authors reported the weight gain of each specimen after different exposure periods. They related the higher weight gain of the sol-gel protected sample with a superior corrosion resistance, ascribing this to the formation of secondary products on the coating.

The works reported in the previous paragraphs applied inorganic sol-gel coatings to the porous AAO. However, due to the poor affinity of these inorganic chemicals with organic moieties, adherence with organic top-coatings used in the aerospace industry must be hindered or not enough to meet security requirements. Therefore, the use of functional silanes (organically modified silicates) or hybrid organic-inorganic sol-gel coatings seems to be a more adequate approach. Whelam, Cassidy and Duffy (2013) applied an acid or base

catalysed TEOS or hybrid coating (Tetraethylorthosilicate (TEOS) + Phenyltriethoxysilane (PhTEOS)) to an AA3003-H14 (Al-Mn) substrate anodized in sulphuric, oxalic (OAA) or phosphoric acid (PAA). Investigations of the particles sizes distributions showed that, irrespectively to the hydrolysis conditions, this parameter was compatible with the pore sizes of the different anodized layers. Moreover, according to a classification presented in the article, low pore penetration was verified in some instances, even when the particle sizes were largely below the pore diameters, ruling out particle sizes as a restrictive factor for the sol gel penetration within the pores. The authors discussed this behaviour in terms of the influence of surface tension and surface charge both of the colloidal sol-gel and of the aluminium oxide in the penetration of the sol gel within the pores, even though no specific determination was made of these two properties. Regarding the corrosion resistance, the authors state that the combination of anodising process and sol–gel must be chosen carefully to prevent deterioration. In this sense, for SAA, TEOS + PhTEOS based-catalysed sol-gel gave superior resistance, whereas for OAA and PAA TEOS + PhTEOS acid-catalysed were the best ones. It was also shown that some of the TEOS formulations gave inferior results compared with the unsealed samples (left to naturally age during one week). Interestingly, in most of the presented phase angle plots (Figure 3.41) there was no distinction between the porous and anodized layers. The authors attributed this feature either to the fact that the porous layer sealing was inhibited by the sol gel treatment or that the electrochemical response from the sol gel and barrier layer could not be distinguished.

Figure 3.41 - Bode phase angle plots for sol gel sealed anodic films after 0 h exposure to 3.5% w/v NaCl: (a) SAA; (b) OAA; (c) PAA.

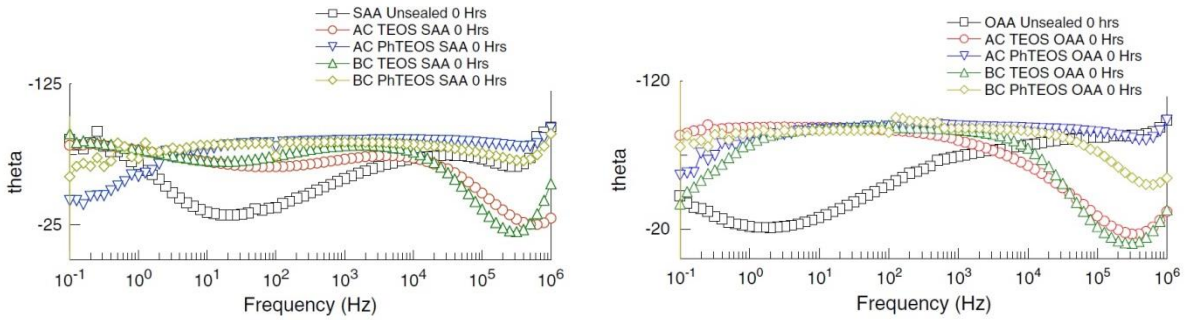

(a) (b)

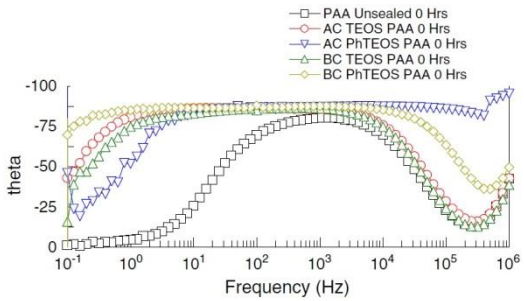

(c)

Source: Adapted from Whelan; Cassidy; Duffy, 2013.

Capelossi et al. (2014) compared by EIS the corrosion resistance in 0.5 mol.L^{-1} NaCl of a clad AA2024 anodized in TSA and protected with a hybrid sol–gel coating (TEOS + GPTMS) or hydrothermally sealed (HTS) in deionized water. The EIS spectra for both post-treated samples exhibited two well-separated time constants, attributed to the porous and barrier layer, throughout the whole test time (Figure 3.42). From the diagrams they observed that the properties of the porous layer were very stable with time for the HTS samples, as no significant modification on the HF region of the diagrams was observed (Figure 3.42 (a)). However, in the LF region a slight decrease of |Z| and a phase angle decrease and shift to higher frequencies indicated the deterioration of the barrier layer properties. For the samples protected with the hybrid sol–gel coating (Figure 3.42 (b)) changes both in the HF and LF time constants were verified indicating deterioration of the properties of both the porous and barrier layer.

Figure 3.42 - Bode diagrams in 0.5 mol.L^{-1} NaCl for clad AA2024-T3 anodized in TSA: (a) hydrothermally sealed; (b) protected with the hybrid sol–gel coating.

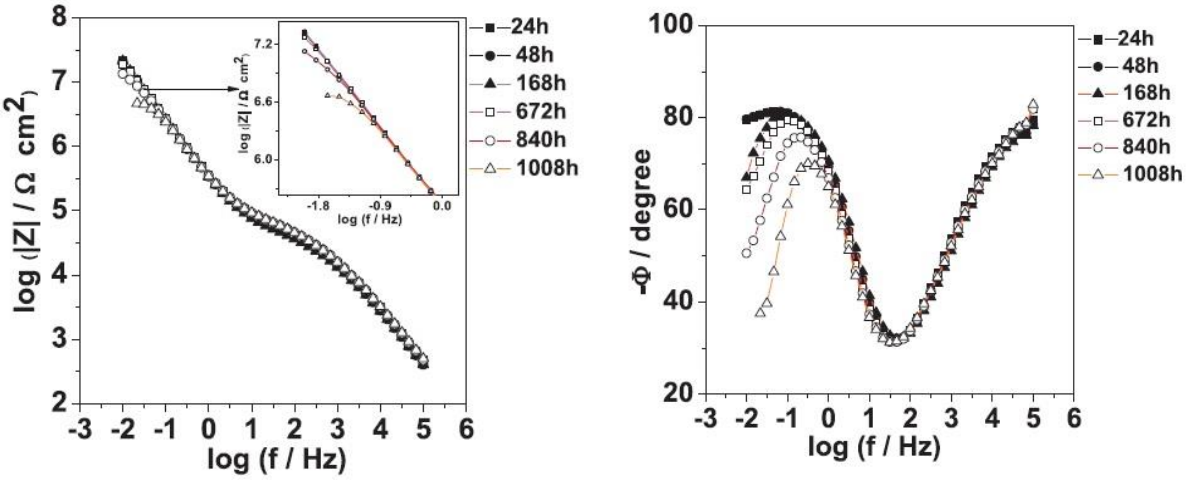

(a) hydrothermally sealed

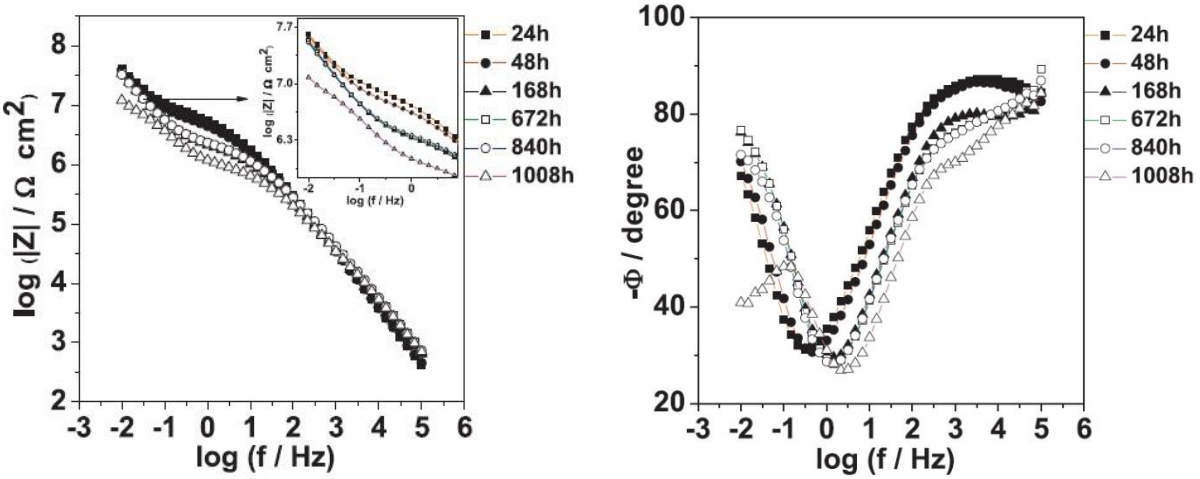

(b) sol-gel coating

Source: Capelossi et al., 2014.

Figure 3.43 shows the physical model of both post-treated AAO layers as well as the EEC analogues employed to fit the EIS diagrams (CAPELOSSI et al., 2014), which are similar to those previously proposed by Hoar and Wood (1962). The HTS model was conceived by taking into account that pore sealing was not complete (Hoar and Wood, 1962, already demonstrated that upon sealing during 24 h the properties of the porous layer still changes) and for the sol gel protected sample considering complete penetration of the pores by the sol gel solution, as indicated by GDOES measurements results. The fitting procedure showed that R_{HL} (the hybrid layer resistance within the pores) was almost two orders of magnitude superior to R_P (resistance of the sealed porous layer). Accordingly, R_b (barrier layer

resistance) could be estimated for HTS sample, whereas it was not possible to determine a reliable value for R_b for the hybrid-protected sample as a consequence of the high R_{HL} value. The salt-spray test results confirmed that the hybrid-coated sample was less sensitive to pitting corrosion, however a blistering phenomenon was observed after 332 h of test indicating delamination of the surface sol gel layer.

Figure 3.43 - Physical models of the post-treated anodized layers and equivalent electric circuits used to fit the EIS diagrams: (a) hydrothermally sealed; (b) protected with the hybrid sol–gel coating

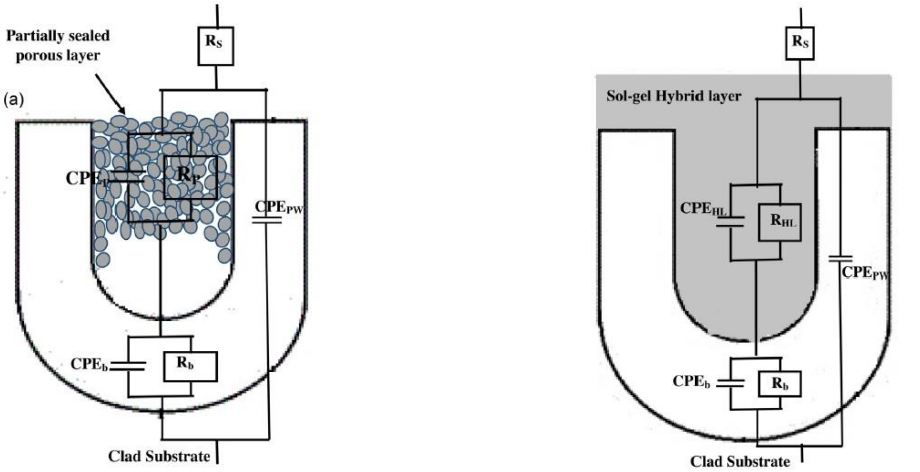

(a) hydrothermally sealed (b) sol-gel coating

Source: Capelossi et al., 2014.

In a very recent paper Wojciechowski et al. (2016) applied a functional silane (triethoxyoctylsilane) or a hybrid coating (triethoxyoctylsilane + tetraethoxysilane) to unsealed or sealed (5 min in boiling water) Al-Mg alloy anodized either in SAA or OAA. In all the cases, the hydrolysis reactions were performed in almost anhydrous conditions. Particle size analysis showed that for the silane hydrolysis solution the distribution was 120-270 nm whereas for the hybrid it was between 190-470 nm. On the other hand, the mean pore diameters of the anodized layer were 9-15 nm (SAA) and ~ 27 nm (OAA). It was concluded that the sol gel solution could not penetrate within the pores. From the EIS measurements it was concluded that the higher corrosion resistance was obtained when the hybrid or silane coating was applied to the unsealed oxide layers. According to the authors, the air trapped inside the pores would greatly improve the corrosion resistance of the system. In addition, for each situation, unsealed or sealed AAO layers, higher impedance was obtained with the

hybrid coating then with the silane coating. Fitting of the EIS diagrams were also performed with EEC analogues presented in Figure 3.44. For the diagrams with higher impedance R_b could not be determined.

Figure 3.44- EEC analogues employed to fit the EIS data of Wojciechowski et al. (2016)

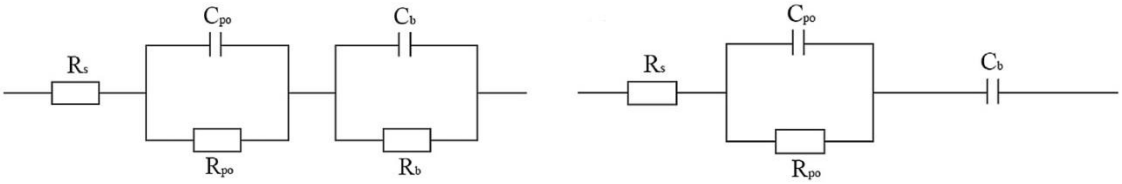

Source: Wojciechowski et al. 2016.

In our opinion the work of Wojciechowski et al. (2016) has some results that deserve criticism. First of all the size distribution of the colloidal particles in the hydrolysis solution seems too big 120-470 nm (all conditions comprised) when compared to that presented by Whelam, Cassidy and Duffy (2013): 4-34 nm (all investigated conditions comprised), indicating agglomeration of the colloidal particles. The authors (WOJCIECHOWSKI et al., 2016) also measured the OCP of the different samples and drawn some conclusions about corrosion resistance based simply on the positive shift of the OCP. Even though coincident with the results from other techniques, this seems precipitate, since, as widely known, a shift of the corrosion potential to nobler direction can be a result of the depolarization of the cathodic process, which would result in an increase of the corrosion rate. Therefore, OCP as a standalone technique cannot be used to conclude about corrosion resistance.

Wojciechowski et al. (2016) also employed polarization curves to evaluate the corrosion resistance of the different system. First of all, due to the extremely resistive characteristic of the studied systems, which presented impedance modulus in the order of 10^8 $\Omega.cm^2$ or higher, the dc signal of the polarization measurement must be mainly lost as Ohmic drop through the very resistive anodic aluminium oxide coated with the silanes. Moreover, the authors also used the polarization curves to perform Tafel extrapolation, which, as widely known, can be employed only when activation controlled processes are taking place at the interface. This is not the case for the coated anodic layer.

In addition, in the EIS results of Wojciechowski et al. (2016) it was assumed that the porous layer was completely sealed after 5 minutes of immersion in deionized water (see the physical

model presented in Figure 9 of this article), which is completely unrealistic with sealing times used in several scientific works. Finally, the authors ascribe higher impedance to the unsealed samples coated either with the organically modified silane or with the hybrid coating. Figure 3.45 reproduces the impedance modulus results for both the SAA and OAA anodized samples presented in the article as well as the Nyquist plots for some OAA samples. For guidance, Tables 3.4 and 3.5 reproduce, respectively, the nomenclature for the different samples and polarization resistance values (sum of all the resistances) derived from EEC fitting. The former table discriminates the type of anodizing solution, if the sample is unsealed (O) or sealed (S) and if it is coated only with the organically modified silane (OTES) or with the hybrid coating (OTES + TEOS). As can be seen in Figure 3.45 (a) and (b), the impedance modulus of the "s-2" samples is higher than for the "o-1" sample, which is not in accordance with the data presented in Table 3.5. Of course EEC fitting can change this classification according to some special features of the diagrams. However, this seems not to be possible from the visual analysis of Figure 3.45 (b) (the only Nyquist plot presented in the article), which clearly demonstrates that for the sample anodized in the OAA bath the impedance modulus of the sample OA-o-1 is lower than for the sample OA-s-2.

Figure 3.45 - Impedance modulus for samples with or without deposited silane coatings after 240 minutes immersion in 3.5% NaCl: (a) anodized in oxalic acid bath; (c) anodized in sulphuric acid bath. (b) Nyquist plots for some of the samples anodized in oxalic acid bath. For samples nomenclature see Table 3.4.

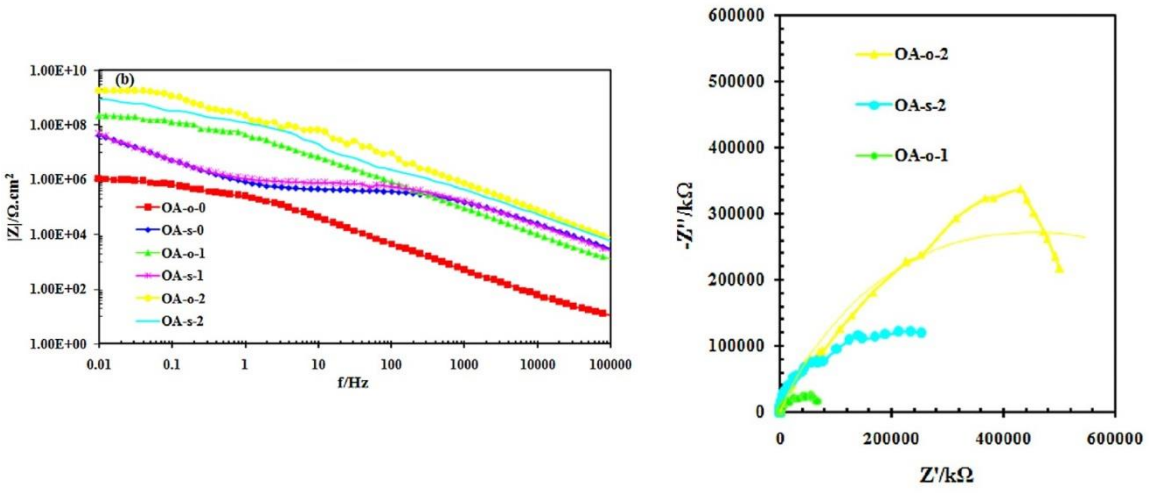

(a) (b)

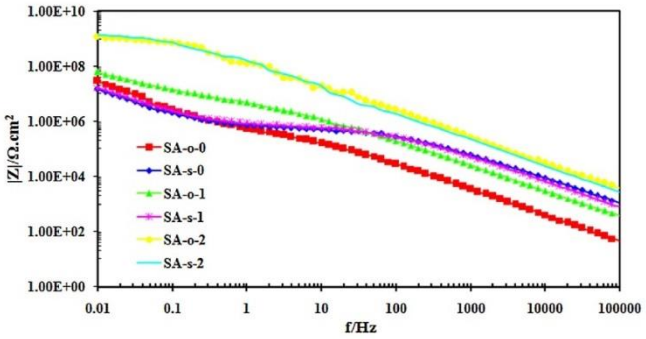

(c)

Source: Wojciechowski et al. 2016.

Table 3.4 - Nomenclature of bare aluminium and all combinations of AAO samples with or without deposited silane coatings.

Sample	Acid	Pores	Silane coating
Aluminium	-	-	-
OA-o-0	oxalic	open	-
OA-s-0	oxalic	sealed	-
OA-o-1	oxalic	open	OTES
OA-s-1	oxalic	sealed	OTES
OA-o-2	oxalic	open	OTES+TEOS
OA-s-2	oxalic	sealed	OTES+TEOS
SA-o-0	sulfuric	open	-
SA-s-0	sulfuric	sealed	-
SA-o-1	sulfuric	open	OTES
SA-s-1	sulfuric	sealed	OTES
SA-o-2	sulfuric	open	OTES+TEOS
SA-s-2	sulfuric	sealed	OTES+TEOS

Source: Wojciechowski et al. 2016.

Table 3.5 - Polarisation resistance (Rp) values of samples anodised in oxalic acid with or without deposited silane coatings. Rp values were determined using the EC-Lab Software®. For samples nomenclature see Table 3.4

Sample	R_p/kΩ
OA-o-0	76
OA-s-0	127
OA-o-1	79800
OA-s-1	231
OA-o-2	794000
OA-s-2	259

3.9 GDOES

Glow discharge optical emission spectroscopy (GDOES) is a relatively new technique. The first modern direct current (dc) GDOES source was invented by Grimm in 1967, with the first commercial dc instrument released in 1979 (SHIMIZU et al., 2003). GDOES is a powerful and promising technique for depth profiling analysis of different types of materials (FERNÁNDEZ; PEREIRO; SANZ-MEDEL, 2010), by reason of the combinations of fast sputtering rate, high depth resolution, excellent sensitivity and multi-element capability and low cost (LIU; YU; WANG, 2015). GD ensures a high sputtering rate due to the high flux of energetic species. The species contributing to sputtering are of relative low energy (<50 eV), resulting in a low penetration depth and limiting the surface damage to a very shallow layer of about 2 nm thick, thus allowing for high depth resolution (FERNÁNDEZ; PEREIRO; SANZ-MEDEL, 2010).

Compared with atomic emission spectrometry (AES), x-ray photoelectron spectroscopy (XPS) and secondary ion mass spectrometry (SIMS) depth profiling techniques, the rapid measurement of GDOES is unique and its sputter rate could be as fast as the order of 1 mm/min (LIU; YU; WANG, 2015). This method allows depth profile analysis of surface regions, from the first nanometre to depths of several tens of microns (SHIMIZU et al., 2003).

Glow discharges (GD) are used in various application fields as organic molecular, alloy films, galvanized or painted steels, hard coating, plasma display panels, environmental and biomedical applications and analytical chemistry (LIU; YU; WANG, 2015; SHIMIZU et al., 2003; BAUNACK; HOFFMANN; ZAHN, 2007). GDs are current implemented as routine technique for quality control in many industries (steel, aluminium, car-manufacturing, etc.)

and as a valuable tool in materials science (FERNÁNDEZ; PEREIRO; SANZ-MEDEL, 2010).

GD traditional instruments incorporated a direct current (dc) power supply to get the breakdown of the discharge gas and to provide the ion and electric currents necessary for successful operation. This requires the sample, normally the cathode, to be a conducting material or at least capable of incorporation into some conducting matrix (in this latter case "spatial information" is lost). The radiofrequency (rf) discharges have attracted great interest because they can be directly applied not only to electrically conductive samples, but also to those that are non-conductive, whether bulk or layered materials (FERNÁNDEZ; PEREIRO; SANZ-MEDEL, 2010). Because of this ability of rf sources, research is continuing aimed at using rf-GD sources for the routine quantitative analysis of any coating type (PAYLING; MICHLER; AEBERHARD, 2002; PISONERO et al., 2006).

The source is central to the operation of the instrument and accounts for many of its specific characteristics. The operation of the source is easy as the sample just needs to be placed on an 'o' ring facing the anodic tube in which the plasma will be confined.

GD is a low pressure plasma, therefore, no ultra high vacuum is needed, moreover the analysis relies on a very low flow (< 0.3 L/mn) of high purity plasma gas (usually air). Cooling of the sample (when high power non-pulsed mode is used) is assured by a recirculated cooler. The sample compartment is spacious allowing large samples to be readily analysed. By the same token, strategies and accessories exist for small, non-flat or porous samples that would not fit to the 'o' ring. The plasma ensures both the erosion "layer by layer" of the sample, and the excitation of the sputtered species (Figure 3.46). This is a dynamic process offering real time measurement as a function of depth. The sensitivity is directly linked with the speed of sputtering. The more materials that enter the plasma per unit of time, the more signals that can be collected. The two mechanisms of sputtering and excitation are spatially separated. The sputtering is material dependent, but the emission taking place in the gas phase is nearly independent from the material. This absence of matrix effects is a clear advantage over Secondary Ion Mass Spectrometry (SIMS) and allows for easy quantification[3].

[3] Horiba Scientific. Pulsed rf Glow discharge optical emission spectroscopy. Retrieved from: <http://www.horiba.com/fileadmin/uploads/Scientific/Documents/GDS/BRO_GD_March_2014.pdf>. Accessed date: December, 11th 2016.

Figure 3.46 - Principle of GD sputtering.

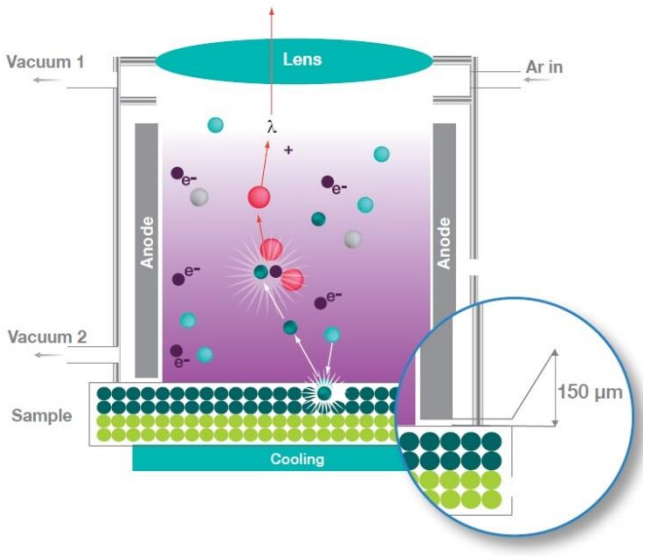

Source: Horiba Scientific. Pulsed rf Glow discharge optical emission spectroscopy[3]

Like other sputter depth-profiling techniques, GD devices have certain limitations. The sputtering in the GD occurs in a sampling area of approximately 4 mm in diameter, so surface imaging and micro-spot analysis are limited (PISONERO et al., 2006). The main distortional effects upon GDOES depth profiling come from the atomic mixing, the surface/interface roughness, the preferential sputtering, the non-linearity response between measured intensity and surface concentration, and the crater effect due to non-homogenous sputtering flux, redeposition, and surface diffusion (LIU; YU; WANG, 2015). However, GDOES offer several advantages when compared with established techniques as AES, XPS and SIMS, for depth-profiling analysis, in particular, its unique combination of fast sputtering, high depth resolution and experimental simplicity, with no requirement for ultrahigh vacuum for depth-profiling analysis (PISONERO et al., 2006).

4 MATERIALS AND METHODS

The experimental work can be divided in two parts. The first one consists of the preliminary tests carried out at the University of São Paulo (USP), aiming to investigate the microstructure of the 2524 aluminium alloy as well as to explore its corrosion behaviour after different pre-treatments procedures and potentiodynamic polarization tests in the anodizing baths. In the second part, the anodizing and post-treatment procedures performed at the University of Mons are described. For the preliminary tests, the results and the experimental procedures reported by Curioni et al. (2008a) and by Saenz de Miera et al. (2008) were taken as reference in order to compare the behaviour of AA2024 and AA2524, once no investigation on the anodizing behaviour of this latter alloy was found in the literature.

4.1 Materials

4.1.1 Aluminium alloy

The AA2524 with composition: 4.07 wt.% Cu, 1.66 wt.% Mg, 0.60 wt.% Mn, 0.10 wt.% Zn, 0.11 wt.% Fe, 0.03 wt.% Ti, 0.01 wt.% Si, 0.02 wt.% others and Al balance, were kindly supplied by EMBRAER S.A as sheets with 2.0 mm thickness. The elemental analysis was determined by a Bruker handheld x-ray fluorescence (XRF) analyzer (model S1-Turbo) with a silicon drift detector (SDD).

4.1.2 Solutions

The solutions were prepared with analytical grade reagents and deionized water.

The compositions of the anodizing baths were:

- Sulphuric acid anodizing (SAA) - H_2SO_4 40 $g.L^{-1}$ at 37 ºC;

- Tartaric-sulphuric anodizing (TSA): 40 $g.L^{-1}$ H_2SO_4 and 80 $g.L^{-1}$ $C_4H_6O_6$ at 37 ºC.

A naturally aerated 0.1 mol.L^{-1} NaCl maintained at room temperature (RT) was used for all the corrosion tests.

4.1.3 Coatings

4.1.3.1 Hybrid sol-gel hydrolysis solution preparation

The sol–gel hydrolysis solution was prepared by the addition of tetraethoxysilane (TEOS) (20 % v/v) and 3-glycidyloxypropyl-trimethoxysilane (GPTMS) (10 % v/v) in a mixture of ethanol (10 % v/v) and deionized water (58 %v/v). The pH was adjusted to 2.3-2.5 by adding acetic acid to the continuously stirred sol-gel solution. All the reagents were purchased from Aldrich and used as received without further purification. For the hydrolysis solution preparation, firstly, deionized water was added, then ethanol and finally TEOS, GPTMS and acetic acid added drop by drop to reach the desired pH.

In most cases, the hydrolysis was carried out for 2 h at RT before its use. However, in order to investigate the effect of the solution ageing on the corrosion protection afforded by the hybrid sol-gel coating, some solutions were hydrolysed for 24 h, 72 h, 168 h and 336 h prior to application on the chosen substrate.

4.1.3.2 Epoxy coating preparation

Epoxy coatings are one of the most important methods for corrosion protection of metals (DALMORO et al., 2015) due to their high chemical resistance and strong adhesion to the metal surface (JIANG et al., 2015). Environmental problems related to the use of volatile organic solvents have led researchers to apply solvent free organic coatings (DUONG et al., 2016). They have minimal OH&S (occupational, health and safety) issues because the

workers are not in contact with the solvent and they do not release solvent during drying, being environmentally friendly[4].

Epoxy coatings are widely used on steel substrates to protect against corrosive species through a physical barrier between the metal surface and the corrosive environment (VAKILI; RAMEZANZADEH; AMINI, 2015). They are produced through the reaction of phenols with acetone or formaldehyde and then further reacted with epichlorohydrin. The resulted reactions form diglycidyl ethers called Bisphenol A epoxies, Bisphenol F epoxies, or phenolic novolac epoxies. The crosslinking occurs by polymerization reactions with various curing agents[5].

The adhesion of the organic coating with the metal is a very important property for a good corrosion protection (DALMORO et al., 2015; JIANG et al., 2015). Diffusion of corrosive species as oxygen, water and chloride ions into the epoxy coating may deteriorate the adhesion and decrease the corrosion resistance of the painting system (JIANG et al., 2015). The hydroxyl ions (OH^-) produced at the metallic surface increase the pH and can decrease the coating adhesion, accelerating corrosion of the metal beneath the coating (VAKILI; RAMEZANZADEH; AMINI, 2015). In this way, surface treatments are applied in order to improve the physical-chemistry interactions of the interface between metal and paint (DALMORO et al., 2015). As discussed before, treatments using chromate compounds are widely used, especially in the aerospace industry, due to their good corrosion properties and paint adhesion, but due to the environmental restrictions, sol-gel process has been used as a promising substitute for chromate surface treatments. The hybrid sol-gel provides excellent interaction with the substrate and can be compatible with organic coating. When epoxy coatings are applied on the silane coating a physical barrier is formed improving, thus, the corrosion resistance of the substrate.

The organic coating used in this work was an epoxy (EPON 828) produced from bisphenol A resin and epichlorohydrin with an amine based curing agent (EPIKURE 8537-WY-6), both produced by Hexion, and mixed in the proportion of 2.5 to 1, respectively, obtaining a colourless top coating. The epoxy resin was ultrasonically degassed for 1 h before adding the curing agent. The coating solution was then stirred magnetically for 10 min prior to application at room temperature on the substrate surface.

---

[4] Moisture Issues with Solvent Free Epoxies. Retrieved from: <http://www.epoxyproducts.com/solventfree.pdf>. Data: Date accessed: October 20th 2016.

[5] Coating Manual. Basics on coatings chemistry: what the generic types mean practically. Retrieved from: <http://www.hrsd.com/pdf/Coatings%20Manual/2011/APPENDIX%20C.pdf>. Date of access: October 19th 2016.

4.2 Methods

4.2.1 Preliminary tests

4.2.1.1 Potentiodynamic behaviour in the TSA anodizing bath of AA2524 after different surface treatments

The performance of any surface protection procedure largely depends on the quality of the surface pre-treatment employed (REIS, 2015). The alkaline and acid etching pre-treatment steps normally used for Al alloys affect the microstructure and the composition of the surface layer, improving the corrosion resistance and providing a more homogeneous surface for the application of the chosen surface treatment (SHI; SONG; ATRENS, 2006).

The role of the alkaline cleaning stage prior to anodizing is to remove the existing aluminium oxide layer (CRITCHLOW; BREWIS, 1996) and to promote a slight chemical attack of the substrate (REIS, 2015). The reaction of the aluminium with sodium hydroxide forms sodium aluminate (hydrated) with hydrogen release (COSTA et al., 2006; DOCHE et al., 1999; REIS, 2015).

$$2Al_{(s)} + 2NaOH_{(l)} + 4H_2O_{(l)} \rightarrow 2NaAlO_2.2H_2O_{(l)} + 3H_{2(g)} \quad (4.1)$$

The alkaline etching usually removes several microns from the alloy surface, leaving exposed regions of residual second phases and alloy matrix with a scalloped texture (CRITCHLOW; BREWIS, 1996). Enrichment of certain alloying elements in the oxide during etching, such as copper in AA2000 and AA7000 series, may darken or stain the surface.

The enrichment mentioned in the previous paragraph is located in a ~2 nm-thick alloy layer just beneath the surface oxide film (HABAZAKI et al., 1995; PAEZ et al., 1996) and arises from preferential oxidation of aluminium, leaving a smut layer which is normally removed by a brief dip in concentrated acid bath for a few seconds (LUNDER; NISANCIOGLU, 1988) (LIU et al., 2008). The most used bath contains nitric–hydrofluoric acids (CAMPESTRINI; WESTING; WIT, 2001). When the aluminium alloy is in contact with an acidic environment, a strong attack takes place smoothing the metal surface and greatly changing its morphology and microstructure. Etching by the aggressive medium results in a reduction of the number of superficial second phase particles, provoking a decrease in the electrochemical reactivity of

the surface (CAMPESTRINI; WESTING; WIT, 2001). The process induces severe corrosion of the aluminium surface in the presence of halogen acids (HCl, HBr, HF) resulting in the formation of soluble compounds. For example, in the presence of fluoride ions (F^-), soluble AlF_3 compounds formed during immersion in hydrofluoric acid solution largely enhances the attack rate (CAMPESTRINI; WESTING; WIT, 2001):

$$2Al + 6H^+ \leftrightarrow 2Al^{3+} + 3H_2 \quad (4.2)$$

$$Al^{3+} + 3F^- \rightarrow AlF_{3(aq)} \text{ and/or } Al^{3+} + 6F^- \leftrightarrow AlF^{3-}_{6(aq)} \quad (4.3)$$

The cleaning and IM removal of the substrate surface contributes for obtaining an anodic layer with fewer defects and, consequently, more protective.

Several works have shown that two anodic potential peaks ascribed to the dissolution of IM particles characterize the potentiodynamic behaviour of high strength aluminium alloys, either of the 2XXX or of the 7XXX series, when immersed in sulphuric acid anodizing bath (CURIONI et al. 2008; SAENZ DE MIERA et al. 2008, 2010a). As no scientific work on anodizing of the AA2524 alloy was found in the literature, it was decided in a first step to evaluate the electrochemical response of the alloy using this methodology in order to assess the response of the studied alloy and to compare its behaviour with others Cu-rich aluminium alloys.

In order to perform the tests, round-shaped samples with 1.6 cm diameter were cut from the original sheets and sequentially ground with 500, 1200 and 4000 grit silicon carbide emery papers and then polished with diamond paste up to 1 μm using ethanol as lubricant. Between each step of the grinding and polishing procedure, the samples were thoroughly rinsed with deionized water and at the end of the treatment washed with deionized water and degreased by sonication in acetone for 10 min. Afterwards, they were submitted to one of the following etching procedures:

1 – Immersion in 10 % (wt.) sodium hydroxide (NaOH) solution at 60 ºC for 30 s (alkaline etching) with subsequent dismutting by immersion in 30 % (wt.) nitric acid (HNO_3) for 30 s at RT. This pre-treatment was applied because it was used by Curioni et al. (2008a) and Saenz de Miera et al. (2008) in a similar procedure applied to aluminium alloy 2024-T3 potentiodynamically polarized in sulphuric acid (SAENZ DE MIERA et al. 2008) and in sulphuric acid or ammonium pentaborate (CURIONI et al. 2008a) anodizing baths. Therefore, they will be used as reference for the analysis of the results.

2 – Immersion in 0.5 mol.L^{-1} acetic acid (AA) for 1 or 5 min at RT. This treatment was used by Palomino (PALOMINO, 2007) and, according to the author, it reduces the surface copper content of 2XXX aluminium alloys.

3 – Immersion in 30 % (wt.) HNO_3 for 30 s followed by immersion in 0.5 mol.L^{-1} AA for 1 or 5 min and a new immersion in 30 % (wt.) HNO_3 for 30 s. All the steps were performed at RT.

4 – Degreasing in a commercial alkaline cleaner bath (Turco 4215 NCLT) at 50 ºC for 10 min. After that, the specimens were immersed in 40 g.L^{-1} NaOH at 40 ºC for 30 s and then in a chromate-free commercial acid dismutting bath (Turco® Smutgo-Henkel) at RT for 15 s. Turco smutgo is a dark brown concentrate liquid containing nitric and hydrofluoric acids[6].

5 - Immersion in 10 % (wt.) NaOH at 60 ºC for 30 s followed by immersion in 0.5 mol.L^{-1} AA for 5 min and then immersion in 30 % (wt.) HNO_3 for 30 s, both at RT.

Aiming to remove any traces of the solutions, between each step of the etching procedures, the specimens were sonicated for 2 min using an ultrasonic cleaner with deionized water and dried in a hot air stream. At the end of the treatment, the samples were again sonicated for 2 min in deionized water, washed with ethanol and acetone and dried with a hot air stream.

The treated samples were then introduced in a flat specimen holder, model K0105 manufactured by Princeton Applied Research, leaving an exposed area of 1 cm^2.

Potentiodynamic polarization experiments with samples submitted to each of the previously described pre-treatments were carried out in the SAA and TSA baths, from the open-circuit potential (OCP) to 9 V (Ag/AgCl) at different sweep rates: 0.250, 1, 2, 3, 5 and 7 V.min^{-1}. For these measurements, the temperature of the anodizing baths was kept constant using a silicone bath.

The potentiodynamic curves were acquired using a classical three-electrodes cell arrangement with the sample in the flat holder as working electrode, an Ag/AgCl(KClsatd) reference electrode (+0.207 V vs. SHE) and a platinum sheet as counter electrode. The tests were performed in triplicate for each condition in order to verify their reproducibility.

The experiments were carried out using a potentiostatic/galvanostatic AUTOLAB, model AUT70896 or AUT-85559, connected to a microcomputer and controlled with the software NOVA 1:11.

---

[6] Technical Process Bulletin. Available in: <http://www.aerospares.hu/files/loctite/hst_liquidsmutgonc.pdf>. Access: January 24th 2017.

4.2.1.2 Potentiostatic anodizing of AA2524 in the SAA and TSA baths after different surface treatments

AA2524 samples submitted to the same surface treatment and etching procedures described in the previous item (4.2.1.1) were potentiostatically anodized at 2, 4, 6 or 8 V in the SAA and TSA baths for 600 s.

These preliminary anodizing experiments were performed using the same experimental setup previously described (4.2.1.1), including the sample in the flat holder as working electrode. Therefore, the anodized area was 1 cm^2.

4.2.2 Corrosion behaviour of AA2524 anodized in TSA

4.2.2.1 Anodizing procedure

AA2524 specimens with dimensions of 4.5 cm x 5.0 cm x 0.105 cm were initially degreased by sonication in acetone for 10 min and dried in a hot air stream.

The anodizing pre-treatment consisted in dipping the samples in an alkaline etching solution: NaOH (40 $g.L^{-1}$) at 40 ºC for 30 s and in a chromate-free commercial acid dismutting bath (Turco® Smutgo-Henkel) at room temperature for 15 s. Between each step of surface preparation the specimens were thoroughly washed with deionized water and dried in a cold air stream. The pre-treatment using Turco was chosen due to the better reproducibility achieved in the preliminary tests.

Samples were potentiostatically anodized in a TSA bath (TSA) (4.1.2) using a lead sheet with an exposed area of 36 cm^2 as cathode. Anodizing time was set at 20 min and the electrolyte was magnetically stirred during all the procedure. Four different anodizing voltages were applied: 8 V, 10 V, 14 V and 16 V. This voltage range is chosen to be close to the industrial applied voltage (14 V) and to avoid the breakdown of the anodic layer (RENAUD, Alexis)[7].

[7] Personal communication. Studied developed by Alexis Renaud as part of the FLYCOAT project financed by the Region Wallonne (Belgium). Report not available.

The voltage was supplied by an Elektro-Automatic EA-PS 2016-100 laboratory power supply and the temperature was controlled using a heater with a contact thermometer. Figure 4.1 shows a picture of the device.

Figure 4.1 - Equipment used in the anodizing procedure.

4.2.2.2 Anodizing post-treatments

After anodizing, some specimens were either immediately rinsed with deionized water and hydrothermally sealed in boiling deionized water for 40 min or coated with the hybrid organic–inorganic sol–gel layer (previously prepared according to the description presented in 4.1.3.1). This latter procedure was performed using a KSV Nima dip-coater, with immersion time of 2 min and withdrawal rate fixed at 100 $mm.min^{-1}$. Curing of the sol gel coating was carried out at 150 ºC for 1 h in a furnace.

4.2.2.3 Evaluation of the corrosion resistance of TSA anodized samples by means of electrochemical impedance spectroscopy (EIS)

The corrosion resistance of the as prepared (non post-treated) and post-treated (hydrothermally sealed and sol-gel coated) TSA anodized samples was evaluated by means of triplicate EIS experiments.

The measurements were carried at the open circuit potential (OCP) after different immersion times (Table 4.1) in a 0.1 mol L^{-1} NaCl solution at RT. The EIS diagrams were acquired in the frequency range from 10^5 kHz to 10 mHz, with 10 points per decade and an ac perturbation amplitude of 20 mV (rms), using a Princeton Applied Research Parstat 2273 (Ametek) potentiostat-frequency response analyser system controlled by the Power Suite® software. A three-electrode cell was employed, with a platinum sheet and an Ag/AgCl(KClsatd) (+0.207 V vs. SHE) as counter and reference electrode, respectively. The cell was completed with a working electrode with 7.07 cm^2 exposed area.

The cells were mounted by gluing (silicon neutral (Wurth)) hollow Plexiglas® cylinders with the appropriate diameter on to the anodized sample surface. The experiments were started after 24 h by pouring 50 mL of the test solution.

EIS experiments of non-anodized samples were also performed. The samples were pre-treated as described in 4.2.2.1 and then coated with the hybrid sol-gel applied as described in 4.2.2.2.

Table 4.1 - Immersion periods for evaluation of the EIS response of the anodized samples and of the pre-treated and hybrid sol-gel coated sample (non-anodized).

Sample	EIS experiment (h)
As-prepared (anodized and not post-treated) (*)	1, 6, 24, 48, 72, 168
Anodized and hydrothermally sealed (**)	1, 6, 24, 48, 72, 168, 336, 504, 672, 840, 1008
Anodized and coated with the hybrid sol-gel	1, 6, 24, 48, 72, 168, 336, 504, 672, 840, 1008
Pre-treated and sol-gel coated (not anodized) (*)	1, 6, 24, 48, 72

(*) EIS experiments were interrupted when the samples failed

(**) The sample anodized at 8 V was interrupted after 168 h due to the sample failure

4.2.2.4 Salt spray tests

The anodized and post-treated samples (hydrothermally sealed and hybrid sol-gel coated) were submitted to salt spray test according to ASTM B117-11 standard. Samples anodized at the four voltages were tested in a chamber Q-FOG Cyclic Corrosion Tester.

AA 2524 specimens with dimensions of 4.5 cm x 5.0 cm x 0.105 cm were anodized and post-treated as described, respectively, in 4.2.2.1 and 4.2.2.2. The edges were protected by a vinyl tape (3M). During the test, the chamber was kept at 35 ± 1 ºC and was fed with a fogging solution of 5% NaCl in the pH range from 6.5 to 7.2.

After 6 h, 24 h, 48 h, 72 h, 96 h, 168 h, 240 h, 336 h and 504 h of exposure, the samples were withdrawn from the chamber and observed with a Leica MZ12 stereomicroscope to detect corrosion initiation and follow its development. Images of the samples surfaces were recorded using a photographic camera Canon EOS 350D.

4.2.3 Ageing effect of the sol-gel solution after different hydrolysis times on the corrosion protection afforded by the hybrid sol-gel coating to AA2524 anodized in TSA bath

The ageing effect of the hydrolysis solution on the corrosion protection afforded by the hybrid sol-gel coating to AA2524 samples anodized in the TSA bath was investigated by means of EIS. For this, hydrolysis solutions were prepared according to the procedure described in 4.1.3.1 and left to hydrolyse for 24 h, 72 h, 168 h and 336 h. The coating was then applied on AA2524 samples potentiostatically anodized at 14 V in TSA bath (4.2.2.1) according to the protocol described in 4.2.2.2.

EIS measurements were performed in triplicate following the procedure described in 4.2.2.3.

4.2.4 Corrosion protection afforded by an Epoxy organic coating (EOC) – preliminary investigation

The corrosion protection afforded by an Epoxy organic coating (4.1.3.2) (EOC) applied on selected samples was investigated by means of EIS and salt-spray tests (ASTM B117-11 standard).

The EOC films were deposited using a spin-coating (POLOS model) at a rotation speed adapted for the required film thicknesses (normally between 2200-3000 rpm/sin). The application procedure consisted in pouring one teaspoon of the EOC prepared according to the procedure described in 4.1.3.2 above the sample and then starting the rotation in the spin

coating equipment for 20 s at the selected rotation speed, as can be seen in the Figure 4.2. The coated samples were left to polymerize and dry at RT for 24 h and then cured at 60 °C for 12 h.

Figure 4.2 - Spin coating equipment

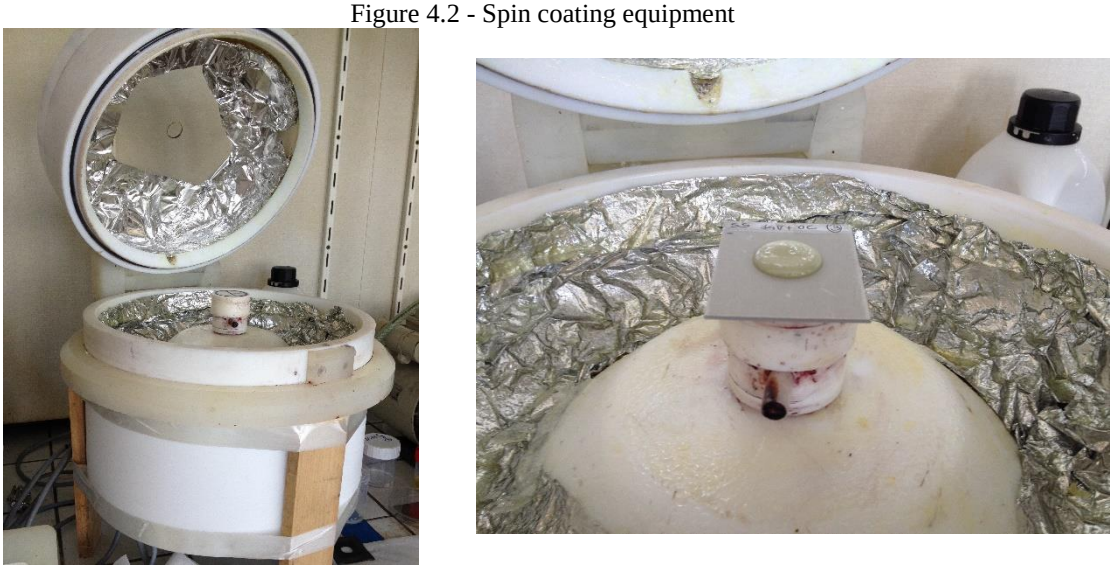

The following samples were used for applying the EOC:

- pre-treated according to the procedure described in 4.2.2.1 (samples preparation for the anodizing procedure) – sample AA2524 + EOC;
- pre-treated according to the procedure described in 4.2.2.1 and protected with the sol-gel coating applied following the procedure described in 4.2.2.2 – sample AA2524 + SG + EOC;
- anodized in TSA at 14 V (4.2.2.1) – sample AA2524 anodized + EOC;
- anodized in TSA at 14 V (4.2.2.1) and then post-treated with the sol-gel coating applied according to the procedure described in 4.2.2.2 – sample AA2524 anodized + SG + EOC.

The measured film thicknesses (Elcometer 456 coating thickness gauge) are shown in Table 4.2. Coatings about 20 to 30 µm thicker were obtained for the sol-gel treated samples. These differences will be commented and explained in the discussion section:

Table 4.2 - Average thickness of the epoxy film applied on the different samples

Condition	Average Thickness (µm)
AA2524 + EOC	59.6 ± 2.23
AA2524 + SG + EOC	83.33 ± 7.32
AA2524 anodized+ EOC	50.93 ± 4.25
AA2524 anodized+ SG + EOC	80.33 ± 5.07

The corrosion resistance of the EOC coated samples was evaluated by means of EIS experiments and salt-spray tests (ASTM B117-11 standard). The experimental procedure and setup used in the former test are described in 4.2.2.3, whereas for the latter the protocol presented in 4.2.2.4 was employed with the difference that the total exposure period was 1008 h and that microscopy observations were also made after 672 h and 1008 h of test.

4.2.5 Fitting of the EIS diagrams with electrical equivalent circuits (EEC)

Quantitative evaluation of the EIS data acquired in the experiments described in 4.2.2, 4.2.3 and 4.2.4 was performed by fitting the diagrams with EEC. The EEC models were determined according to physical models based on the film characterization (FE-SEM and GDOES) of the different systems and in accordance with the literature.

The fitting of the diagrams was carried out with the commercial program Zview®.

4.3 Physicochemical characterization and surface analyses

4.3.1 Rheological characterization of the hybrid sol-gel solutions

The rheological behaviour of the sol-gel solutions after different hydrolysis times (2 h, 24 h, 72 h, 168 h, 336 and 504 h) was determined by monitoring the flow curves and the viscosity obtained from the shear stress *versus* shear rate at 25 °C using a controlled rheometer (RS-150, Haake) with cylinder geometry (DG-41) and equipped with a thermostat (TC501). The

shear rate was controlled between 0 and 1000 s^{-1} for 10 min. The solution volume under test was 6.3 mL.

4.3.2 SEM microstructural characterization

Field emission scanning electron microscopy (FE-SEM) coupled to energy dispersive X-ray spectrometry analysis was employed to perform the microstructural characterization of different samples. Analyses were performed with different devices:

- FE-SEM JEOL-JBM-7401F - at the Chemistry Institute of the University of São Paulo;
- FEI Inspect F50 and Philips XL 30 - at the Metallurgical and Materials Engineering Department of the University of São Paulo;
- Hitachi SU8020 microscope - at Materia Nova Research Centre in Mons.

The following samples were characterized:

- polished AA2524;
- AA2524 samples pre-treated with the procedures described in 4.2.1.1;
- AA2524 samples anodized in TSA (surface and cross-section analysis) at the different voltages: 8 V, 10 V, 14 V and 16 V;
- AA2524 samples anodized in TSA at the different voltages and hydrothermally sealed;
- AA2524 samples anodized in TSA at the different voltages and protected with the hybrid sol-gel coating;

4.3.3 Glow Discharge Optical Emission Spectroscopy (GDOES)

Composition depth profiles and layer thicknesses of the sol gel coated samples were determined by means of GDOES using a Horiba Jobin Yvon profiler instrument operated at an air pressure of 650 Pa and power of 40 W. The GDOES instrument was equipped with a standard 4 mm diameter anode, a polychromathor with 28 acquiring channels, an Rf-generator (13.6 MHz) and a Quantum XP software. The instrument was equipped with a 0.5 m Paschen Runge polychromator with nitrogen purged optical path. The working method was calibrated

using 30 CRM (Certified Reference Materials) and SUS (Setting Up Samples) samples in order to obtain quantitative results. These measurements were performed at the University of Udine (Italy) by Dr Alex Lanzutti under the supervision of Prof. L. Fedrizzi.

5 RESULTS AND DISCUSSION

5.1 Microstructural characterization of AA2524

The polished surface of AA2524 alloy was examined by SEM. A large number of IMs with dimension in the micrometric range was observed distributed throughout the whole matrix surface with no apparent tendency of clustering, as shown in Figure 5.1. This can be another main advantage of 2524 alloy over the 2024-T3. Recent literature has shown that the development of stable pits in this latter alloy is frequently associated with clustering of IMs. Boag et al. (2010) report the development of stable pits when anodic (Mg-rich) and cathodic (Cu and Fe-rich) IMs are close to each other. This was later confirmed by Hughes et al. (2011) who, from surface examination, demonstrated the development of rings of corrosion products surrounding clusters of IMs particles where corrosion activity has developed. In a different outcome from previous articles, the authors state (HUGHES et al., 2011) that the initiation of co-operative corrosion leading to stable pitting is dominated by clustering of cathodic particles, which in later stages will drive the electrochemical activity into superficial and subsuperficial intergranular corrosion. As demonstrated in other articles (GLENN et al., 2011; ZHOU et al., 2012b), Boag et al. (2010) and Hughes et al. (2011) also state that stable pits do not develop from isolated IM particles. These are mainly Al-Cu-Mg particles that corrode soon after the immersion of the 2024-T3 alloy in the aggressive electrolyte (BOAG et al., 2011). Therefore, the IM surface distribution of 2524 alloy indicates less susceptibility to develop stable pits in aggressive environments than AA2024-T3.

Figure 5.1 - SEM micrograph of the AA 2524 surface after polishing.

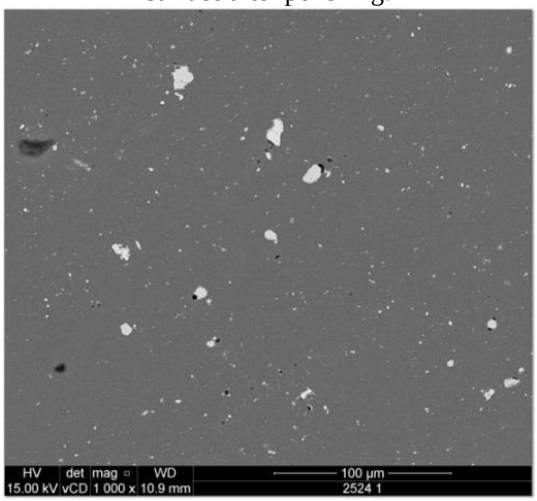

The following IMs were identified in through surface analysis of AA2524:

- **Al-Cu-Fe-Mn** - sometimes round-shaped (Figure 5.2 (a)), but generally presents a brittle appearance with irregular shape ((Figure 5.2 (b)). Few rod-shaped particles were also found (Figure 5.2 (c)). They are the dominant IM in the microstructure of the alloy, agreeing with Cervantes et al. (2001). The Cu/Fe ratio in these IMs varies between 3.7 – 5.0.

Figure 5.2 - SEM micrographs and composition determined by EDS of the Al-Cu-Fe-Mn IMs in AA2524 (a) compact and round- shaped; (b) brittle and irregular; (c) rod-shaped.

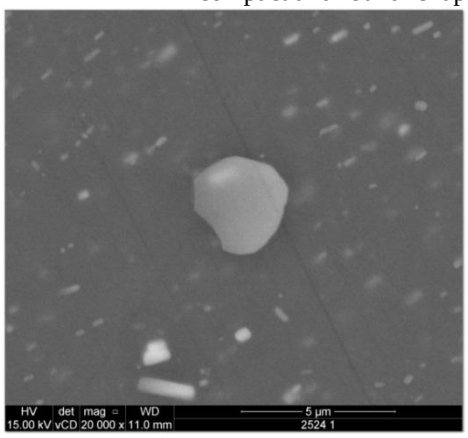

Element	Wt. (%)	At. (%)
Al	82.8	90.5
Mn	1.5	0.8
Fe	2.4	1.3
Cu	11.7	5.4

(a)

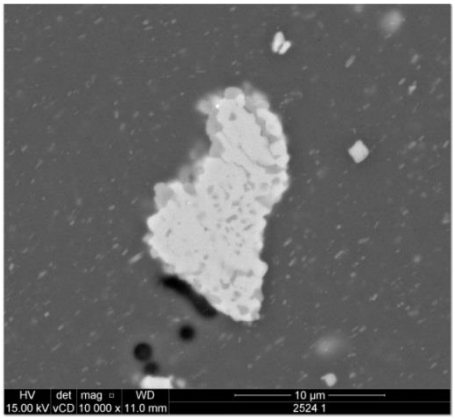

Element	Wt. (%)	At. (%)
Al	51.8	68.7
Mn	5.4	3.5
Fe	8.8	5.6
Cu	32.3	18.2
O	1.8	4.0

(b)

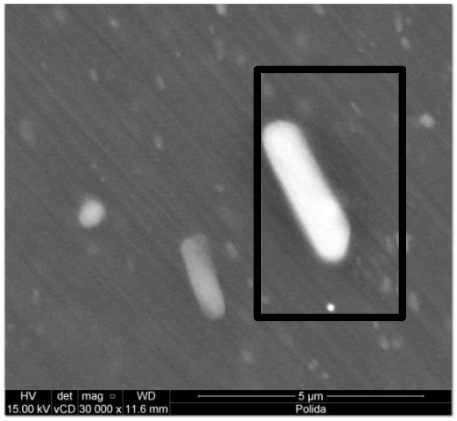

Element	Wt. (%)	At. (%)
Al	62.2	78.0
Mn	2.7	1.7
Fe	6.8	4.1
Cu	27.0	14.4

(c)

- **Al-Cu-Mn -** rod-shaped with light-grey colour, compact and well distributed in the alloy surface. Few of them present dimensions ranging between 1 and 3 µm, as shown in Figure 5.3. They are likely dispersoids particles that might have coarsened (STARKE; STALEY, 1996). Their role is to control the grain structure, delaying recrystallization and refining the grain size. Note in Figure 5.3 (b) the presence of a great number of smaller rod-shaped precipitates, which must be also Al-Cu-Mn dispersoids, which typical sizes ranges from 0.2 to 0.8 µm (PAREL et al., 2010).

Figure 5.3 - SEM micrographs and composition determined by EDS of the Al-Cu-Mn dispersoids in the AA2524 (a) and (b) compacts and rod-shaped.

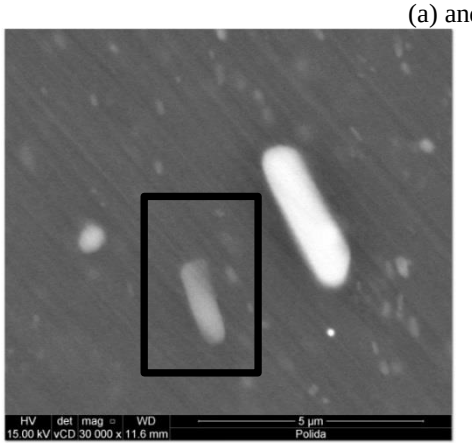

Element	Wt. (%)	At. (%)
Al	84.7	91.2
Mn	7.3	3.7
Cu	6.3	2.9

(a)

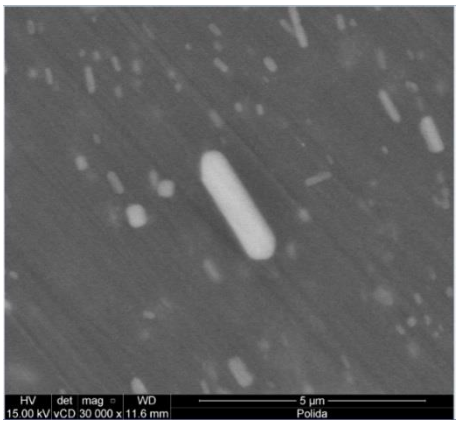

Element	Wt. (%)	At. (%)
Al	86.7	92.2
Mn	5.6	2.9
Cu	5.8	2.6

(b)

- **Al-Cu** (θ-phase) **-** round-shaped IMs, compact with dimensions close to 1 µm. The composition is close to Al_2Cu (Figure 5.4).

Figure 5.4 - SEM micrographs and composition determined by EDS of the Al-Cu IM in the AA2524.

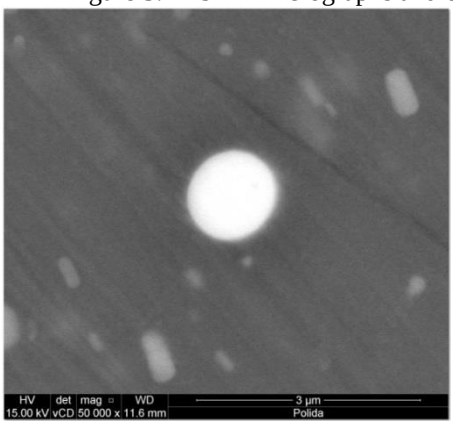

Element	Wt. (%)	At. (%)
Al	63.0	78.9
Cu	35.3	18.8

- **Al-Cu-Mg** (S-phase) - the Mg composition is close to 20 % (at.), as observed for the AA2024-T3 (QUEIROZ et al., 2008). The morphology of these IMs is compact, round-shaped with dimensions close to 10 µm, as shown the micrographs in the Figure 5.5. The dimensions of these S-phase particles are bigger than those found in AA2024-T3, which is reported to be mostly around 5 µm (BOAG et al., 2010).

Figure 5.5 - SEM micrographs and composition determined by EDS of the Al-Cu-Mg IM in the AA2524.

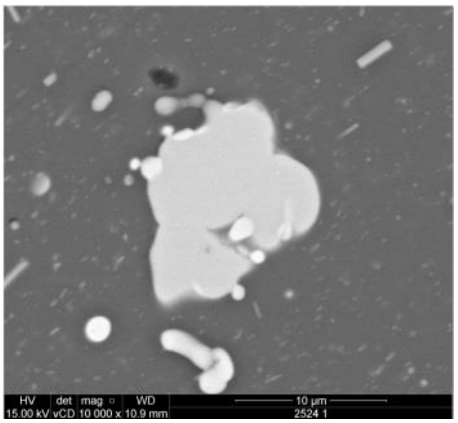

Element	Wt. (%)	At. (%)
Mg	15.74	22.21
Al	38.41	48.84
Cu	43.23	23.34
O	2.62	5.62

(a)

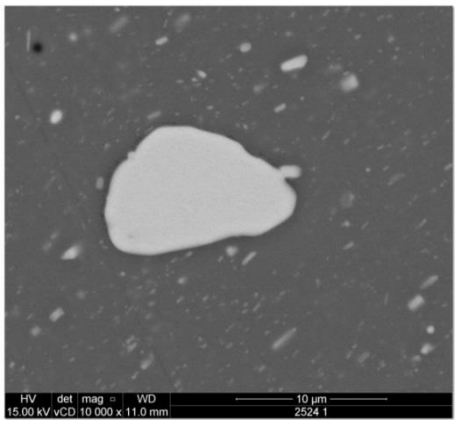

Element	Wt. (%)	At. (%)
Mg	15.87	22.31
Al	38.70	49.02
Cu	42.78	23.01
O	2.66	5.67

(b)

5.2 Surface characterization of AA2524 alloy after the anodizing pre-treatments

As already stressed in the Materials and Methods section, pre-treatment plays an important role in the final quality of the anodizing process. Therefore, after the microstructural characterization, the AA2524 was submitted to different surface treatments in order to remove surface IMs, and also to activate the surface prior to the anodizing procedure.

Figure 5.6 shows the SEM micrographs (5000 X) of the alloy surface after the anodizing pre-treatments described in the item 4.2.1.1.

Figure 5.6 - SEM micrographs of AA2524 (a) only polished, and polished and pre-treated with: (b) NaOH (30 s, 60 ºC) and HNO_3 (30 s, RT); (c) AA (1 min, RT); (d) AA (5 min, RT); (e) HNO_3 (30 s, RT), AA (1 min, RT) and HNO_3 (30 s, RT); (f) HNO_3 (30 s, RT), AA (5 min, RT) and HNO_3 (30 s, RT); (g) turco (turco degrease (10 min, 50 ºC)) NaOH (30 s, 40 ºC), turco smutgo (15 s, RT); (h) NaOH (30 s, 60 ºC), AA (5 min, RT) and HNO_3 (30 s, RT). RT - room temperature.

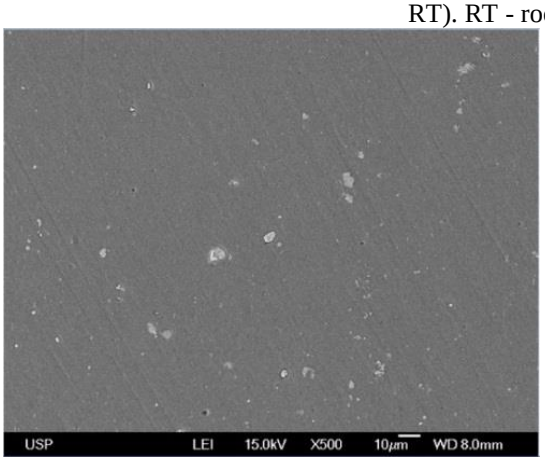

(a)

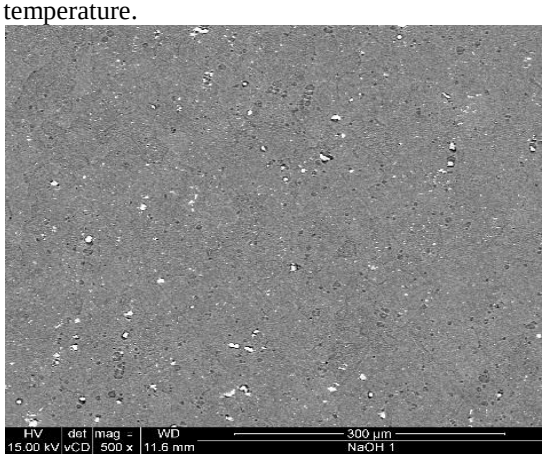

(b)

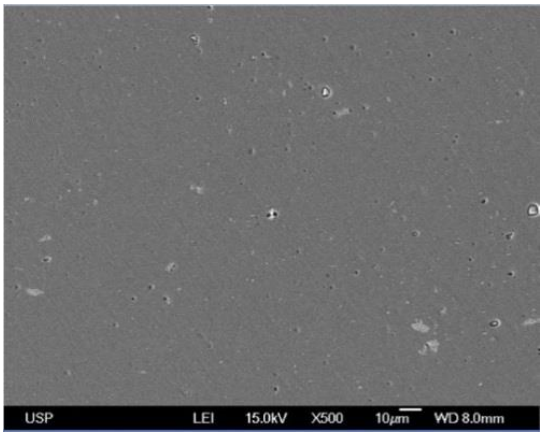

(c)

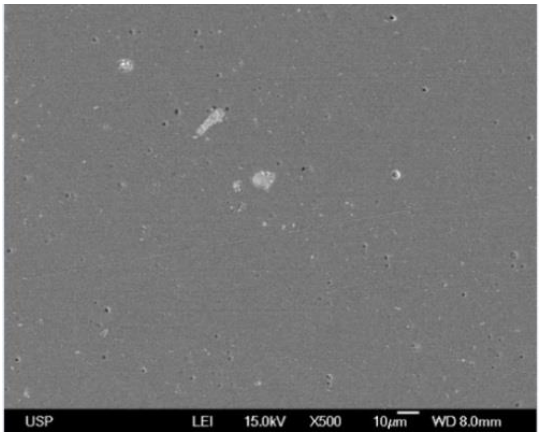

(d)

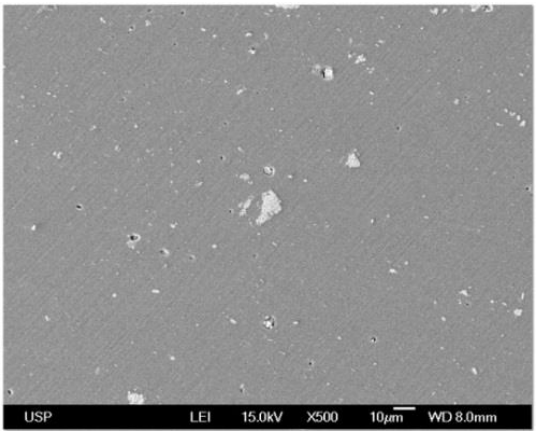

(e)

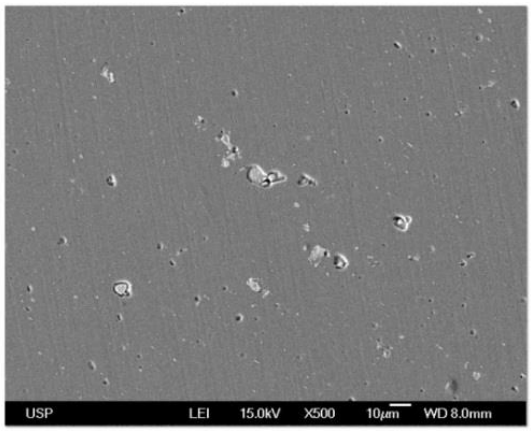

(f)

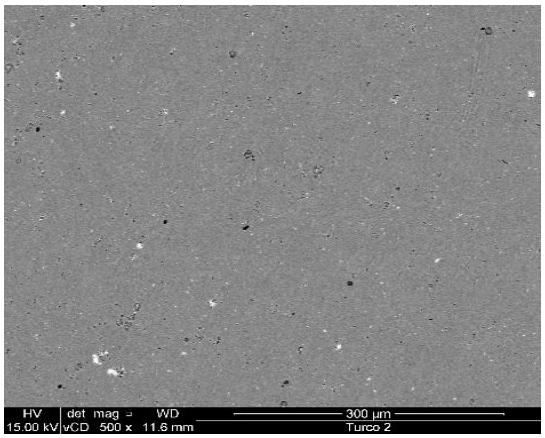

(g)

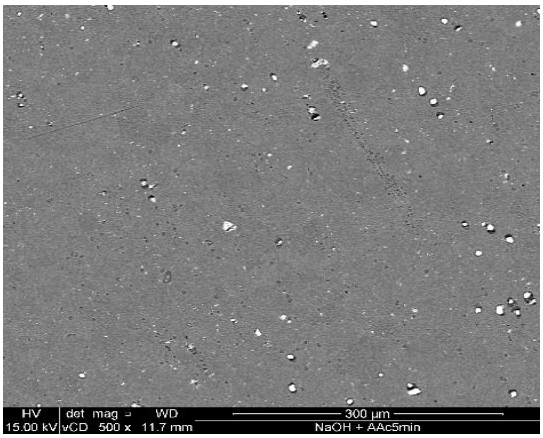

(h)

In general, it was possible to distinguish two different behaviours for the investigated surface pre-treatments: those that employed NaOH and those where NaOH was not used. In the micrographs of Figures 5.6 (b), (g) and (h), where the AA2524 alloy was immersed in

$NaOH/HNO_3$, turco degrease/NaOH/turco smutgo and NaOH/AA (5 min)/HNO_3, respectively, the alloy surface was profoundly etched with a large amount of surface IM removal. For the remainder of the treatments preferential dissolution of the IM occurred, whereas the matrix surface remains relatively unattacked, in Figures 5.6 (c), (e) and (f) polishing marks are still visible, indicating poor surface oxide removal.

As exposed in the item 4.2.1.1, NaOH removes the aluminium oxide layer, making it thinner and more homogeneous, favouring the subsequent action of HNO_3 (PALOMINO, 2007). The acid attack with HNO_3 or with the commercial product turco smutgo (nitric and hydrofluoric acid base) removes the smut resulting from the alkaline etching and makes the substrate surface more homogeneous and active (REIS, 2015). Among the samples etched with NaOH, the one treated with the commercial products turco degrease and turco smutgo showed the largest surface particles removal, with the lowest attack of the alloy matrix. The other two treatments using NaOH promoted a severe attack of the alloy matrix, particularly the one at which the desmutting procedure used only HNO_3. The metal surface also exhibits a larger number of IMs when compared to the pre-treatment using the commercial products.

5.3 Linear anodic polarization (potentiodynamic curves) for the AA2524 alloy in sulphuric acid (SAA) or in tartaric-sulphuric acid (TSA) bath after different pre-treatments

As shown in the literature review, no scientific work was found studying the anodizing behaviour of AA2524. Therefore, due to the similarities of this alloy with AA2024-T3, in the preliminary step, the anodizing behaviour of the AA2524 was compared to that found for AA2024-T3. The works taken as references were those from Curioni et al. (2008a, 2009) and Saenz de Miera et al. (2008), extensively used in the literature review of the present work. These authors made investigations on the potentiodynamic anodization of AA2024-T3 in both SAA (CURIONI et al., 2008a; SAENZ DE MIERA et al., 2008) and TSA (CURIONI et al., 2009) baths, relating the responses with microstructural features of the AA2024-T3.

Figure 5.7 shows the linear anodic polarization (potentiodynamic) curves obtained at different scan rates in SAA (a) and TSA (b) for a polished sample pre-treated in NaOH and HNO_3. This pre-treatment was chosen to start the discussion, as it was the same employed by Curioni et al. (2008a, 2009) in their works as well as by Saenz de Miera et al. (2008).

Figure 5.7- Linear anodic polarization curves at different scan rates for AA2524 polished and pre-treated with NaOH and HNO_3 (a) in sulphuric acid (SAA); (b) and tartaric-sulphuric acid (TSA).

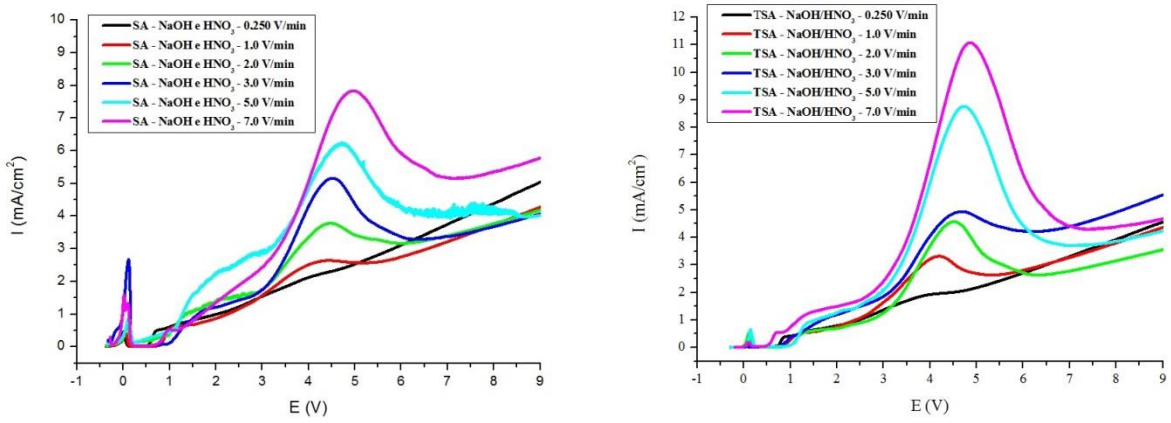

(a) (b)

The linear polarization curves of Figure 5.7 (a) were quite similar to those obtained by Curioni et al. (2008a) and by Saenz de Miera et al. (2008), indicating that the behaviour of the AA2524 is similar to that of AA2024-T3. The current density at each potential increases with scan rate and two current peaks are clearly visible: the first one at approximately 0 V (Ag/AgCl), located close to the OCP, and the second was positioned in the potential region between 2.5 and 7 V (Ag/AgCl). Regarding the first peak, little or no dependence of the shape was assigned to the scan rate. However, for the second peak, its starting potential was not affected by the scan rate, but there was a trend of the peak to terminate at higher potentials with increasing scan rate.

Concerning the two peaks discussed in the previous paragraph, Curioni et al. (2008a) and Saenz de Miera et al. (2008) assigned the peak at lower potential to the dissolution of Mg-rich second phase particles (S phase-Al_2CuMg). The origin of the second peak was investigated in detail by Saenz de Miera et al. (2008). By acquiring linear polarization diagrams for Al_2Cu and Al_7Cu_2Fe model alloys in SAA, these authors verified an increase in the current density at potential values similar to the onset of the second peak. Further, by using an Al-28%Fe model alloy, they verified that the initiation of the second peak was delayed and the current density reduced (SAENZ DE MIERA et al., 2008). The authors suggested that increasing amount of iron reduces the current density at a given potential (SAENZ DE MIERA et al., 2008). Curioni et al. (2008a) also presented SEM cross section images showing that upon applying a constant anodizing potential of 8 V much of the charge passed was used to oxidize a θ-phase particle (Al_2Cu) and only a thin oxide was formed on the Al matrix, confirming a high

oxidation rate of Cu-rich second-phase particles. The two authors mention oxygen evolution for potentials higher than 2 V.

Comparing the diagrams acquired in SAA and TSA it can be verified that the first peak almost vanished in this latter bath. Curioni et al. (2009) report the absence of the first peak when performing linear polarization anodizing in TSA bath. The authors suggest that the addition of tartaric acid to the anodizing bath prevents the preferred oxidation of S-phase at such potential (CURIONI et al., 2009). Regarding the second peak, almost no change was verified when comparing the behaviour in the two anodizing baths. It seems that higher peak intensity was observed in the TSA bath, however, this can be ascribed to heterogeneity in the samples microstructure.

Figure 5.8 shows the comparison between I/E diagrams for all the surface pre-treatments obtained both in SAA and TSA baths for the following scan rates: 1.0 $V.min^{-1}$, 3.0 $V.min^{-1}$ and 5.0 $V.min^{-1}$. The efficiency of the surface pre-treatments was evaluated in relation to the current density of the second peak: a lower value indicates that the surface pre-treatment was more efficient for removing the surface IMs. Therefore, the intensity of the current associated to their oxidation decreases.

Figure 5.8- Linear anodic polarization curves at different scan rates for AA2524 polished and pre-treated with the different pre-treatments: (a) 1.0 $V.min^{-1}$ in SAA (b) 1.0 $V.min^{-1}$ in TSA (c) 3.0 $V.min^{-1}$ in SAA (d) 3.0 $V.min^{-1}$ in TSA (e) 5.0 $V.min^{-1}$ in SAA (f) 5.0 $V.min^{-1}$ in TSA.

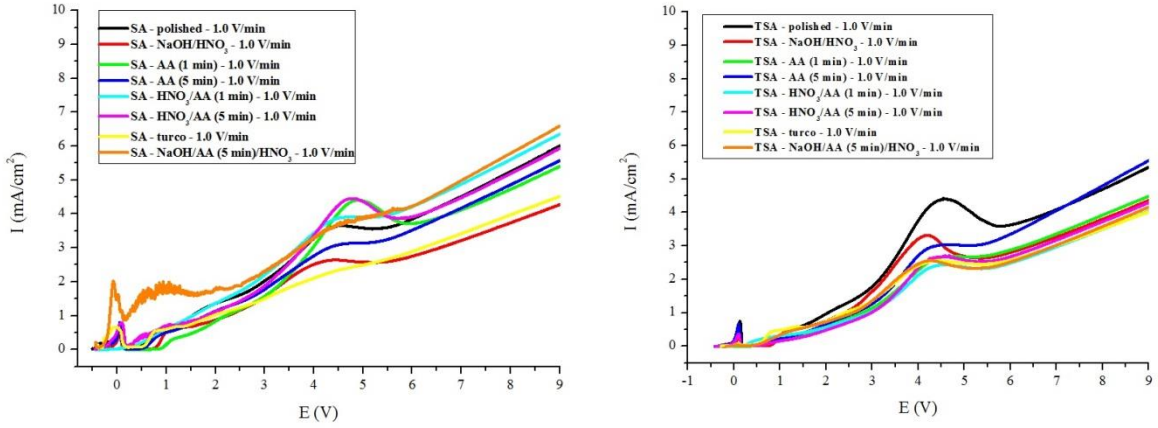

(a) (b)

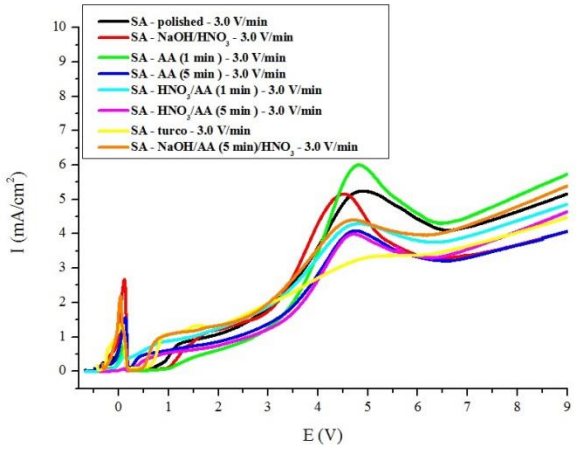

(c)

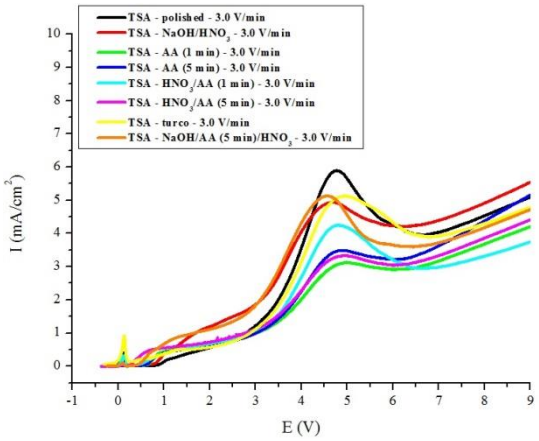

(d)

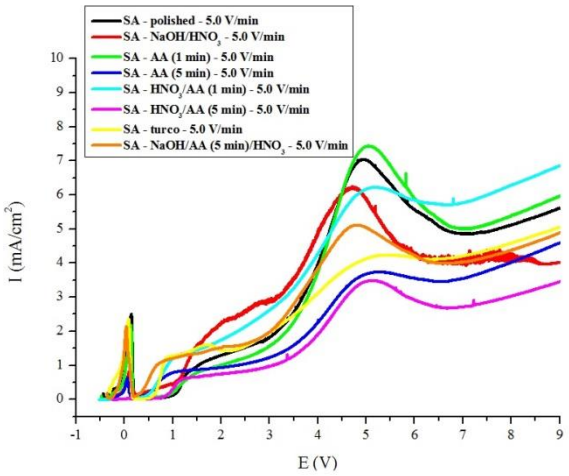

(e)

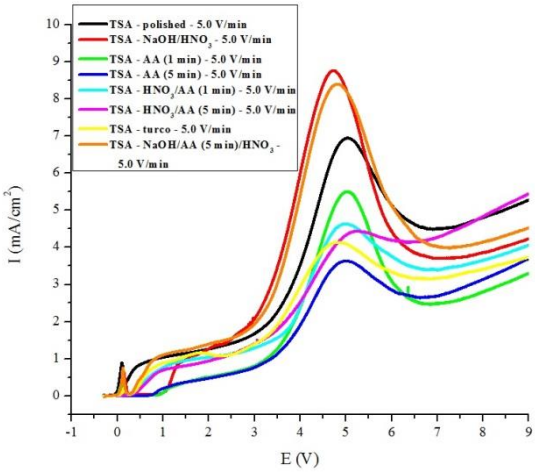

(f)

In general, for the experiments carried out in SAA (Figure 5.8 (a), (c), (e)), the lowest peak current densities values (best response for the adopted criteria) were obtained for the pre-treatments using turco, HNO_3/AA 5 min and AA 5 min. From these, the former pre-treatment gave the best response for the scan rates of 1 and 3 $V.min^{-1}$, whereas for 5 $V.min^{-1}$ the lowest current was obtained for the HNO_3/AA 5 min pre-treatment. However, for the scan rate of 1.0 $V.min^{-1}$, the highest current peak was obtained with this latter pre-treatment.

For the experiments performed in the TSA bath at 1 $V.min^{-1}$ (Figure 5.8 (b)), except for the pre-treatment in $NaOH/HNO_3$, all other samples showed similar values for the second peak current density. For the scan rate of 3.0 $V.min^{-1}$ (Figure 5.8 (d)) the pre-treatments that presented the best results were those using acetic acid: AA 5 min, HNO_3/AA 5 min and AA 1 min with peaks current densities very close to each other. Finally, the best results for the scan rate of 5 $V.min^{-1}$ (Figure 5.8 (f)) were obtained for the pre-treatments involving AA, with and without HNO_3 attack, and turco.

From the results of this step of the work, it can be concluded that, for both anodizing baths, the best results were obtained with the following surface pre-treatments: turco, AA 5 min, HNO_3/AA 5 min, HNO_3/AA 1 min and AA 1 min. However, the analysis of the micrographs presented in Figure 5.6 shows that these pre-treatments using acetic acid (AA) almost do not remove the native aluminium oxide layer; therefore, surface activation may be deficient.

5.4 Potentiostatic anodizing at low voltages

The literature survey showed that, generally, the anodizing procedure is performed by applying a stationary potential to the aluminium alloy. This is particularly true for TSA anodizing. Potentiostatic anodizing at 2 V, 4 V, 6 V and 8 V were carried out in the AA2524 alloy aiming to investigate the effect of voltage in the oxide formation and to compare to previous published results. In order to reach this goal, samples polished and treated with turco were potentiostatically anodized at 2 V, 4 V, 6 V and 8 V and the samples only polished and polished and treated with NaOH/HNO_3 were anodized at 6 V and 8 V. It is important to emphasize that, at this point of the work, no equipment was available allowing performing the anodizing treatment at 14 V.

The reasons for choosing the conditions presented in the last paragraph were:

1 - The procedure using turco, besides being one of the pre-treatments studied that had the best potentiodynamic anodizing curves, is widely used in the aircraft industry;

2 - The pre-treatment with NaOH/HNO_3 was used for Curioni et al. (2008a, 2009) and by Saenz de Miera et al. (2008) for their study using the AA2024-T3 alloy;

3 – The samples only polished allow ensuring a better reproducibility.

Figure 5.9 shows the current density versus time (I/t) curves for the alloy AA2524 potentiostatically anodized in SAA and TSA at different potentials for the three chosen conditions.

Figure 5.9 - Potentiostatic curves obtained during anodizing of AA2524 in SAA (a), (c), (e) and TSA (b), (d), (f). Polished samples and treated with turco (a) and (b), samples just polished (c) and (d) and samples polished and treated with $NaOH/HNO_3$ (e) and (f).

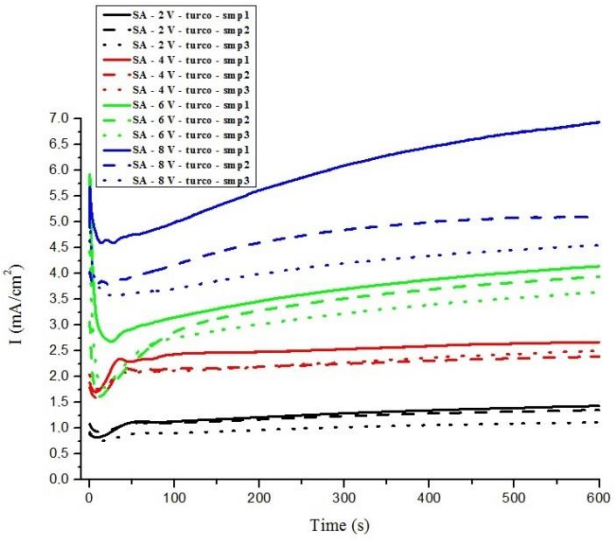

(a)

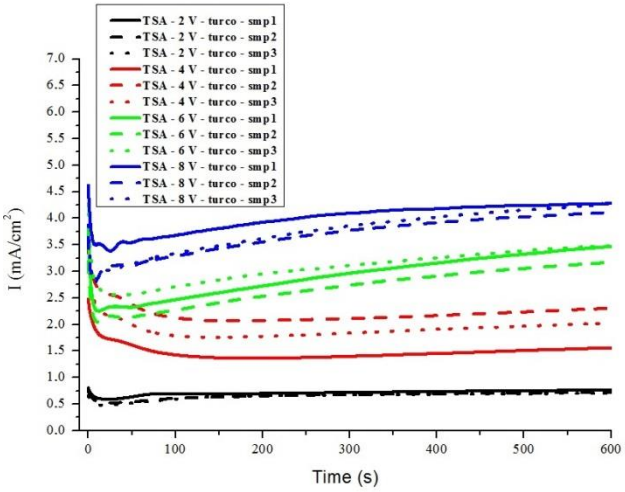

(b)

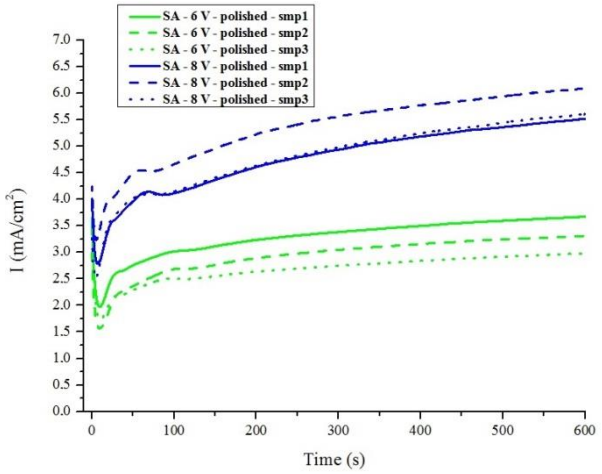

(c)

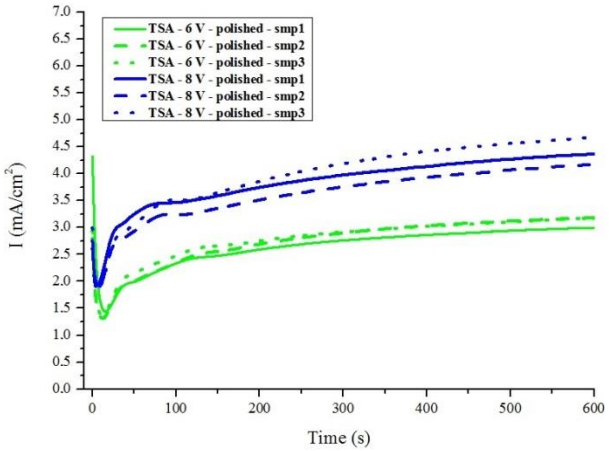

(d)

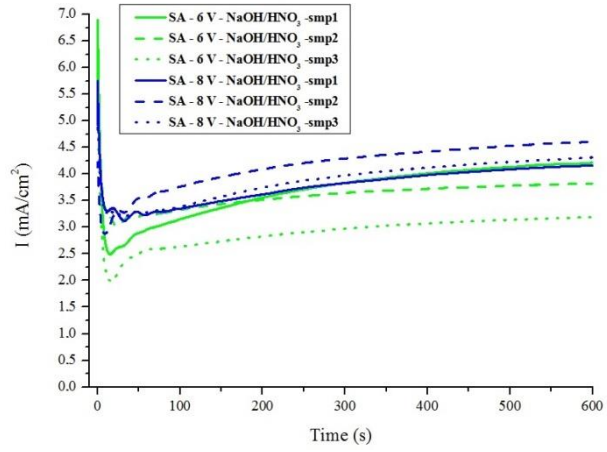

(e)

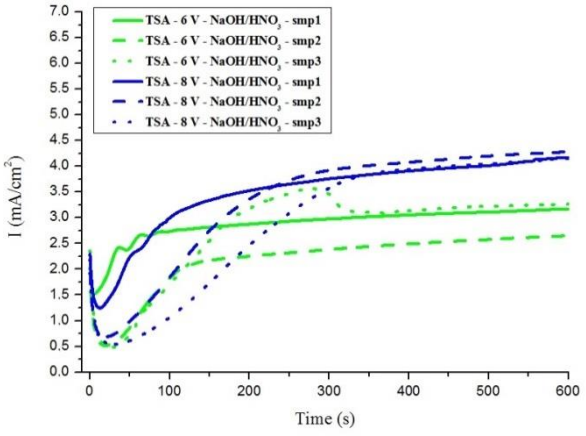

(f)

In general, the diagrams presented in Figure 5.9 were similar to those published in the literature for high strength Al alloys potentiostatically anodized in SAA (CURIONI et al 2008a; CURIONI et al, 2012) or TSA (CURIONI et al., 2012, MA et al., 2011b) baths. The curves show an initial current surge at the beginning of the procedure due to the high potential applied through the thin oxide film present on the sample surface (CURIONI et al., 2012). Subsequently, the current reaches a minimum and starts to increase gradually to a relatively steady state. The initial current density decrease verified after the current surge is due to the thickening of the barrier oxide layer on the surface of the alloy (LEE, PARK, 2014). After that, the gradual increase of current density is due to the non-uniform barrier layer thickening and pore initiation on the surface of the alloy (LEE; PARK, 2014). In this stage, the current and consequently the electric field, concentrates on local imperfections existing on the initial barrier layer (LEE; PARK, 2014). The steady current density region is associated with relatively uniform thickening of the porous anodic film (CURIONI et al., 2008a).

The diagrams obtained after treatment with turco (Figures 5.9 (a) and (b)) can be divided into two groups: the samples anodized at 2 V and 4 V and those obtained at 6 V and 8 V. In the first group, the current in the plateau, associated with porous layer thickening, remained almost constant, whereas for the second group a slow current increase with time is observed. Curioni et al. (2008) studied the effect of alloying elements in the anodizing of 2024-T3 aluminium alloy and found that for potentials below 2 V, the second phase particles remained largely unchanged. At 3 V the number and size of the cavities increased, indicating zones of increasing anodic activity, but most of the second phase particles remained on the alloy surface. For 6 V and above, the authors (CURIONI et al., 2008a) described the preferential oxidation of particles of high copper content and negligible amounts of magnesium, with consequent oxygen evolution. The oxidation of these particles, which causes a defective oxide layer, can explain the slight current increase with anodizing time in the quasi-steady zone attributed to the porous layer thickening. However, it is important to note that, in this region, the diagrams presented by Curioni et al. (2008a) showed a constant current, regardless of the applied potential.

Another difference between the results of Figures 5.9 (a) and (b) and those presented by Curioni et al. (2008a) is that these authors did not identified a minimum current in their galvanostatic curves acquired at anodizing potentials superior to 5 V. Indeed, they verified a current decay towards the current plateau, which duration increased for increasing anodizing voltage (CURIONI et al., 2008a). The authors explained their results by suggesting that the

transient current may originate from the superposition of the oxidation of the second-phase particles and the aluminium matrix (CURIONI et al., 2008a). Therefore, a lower quantity of IMs in the microstructure of 2524 as compared to 2024, may explain the difference between the present results and those from Curioni et al. (2008a).

The diagrams presented in Figure 5.9 show that the addition of tartaric acid to the SAA bath does not modify the anodizing response. However, it is clear that the current density in TSA anodizing is lower than in SAA for all the tests, in agreement with the previous work published by Boisier et al. (2008) and Curioni et al. (2009). According to Curioni et al. (2012), tartaric acid (probably tartrate ions) is adsorbed on the oxide surface reducing significantly its dissolution. Furthermore, these authors report that, according to the literature, by increasing the tartaric acid concentration the conductivity of the anodizing solution decreases. These two factors may explain the lower current values observed in all experiments.

Finally, within the reproducibility limit of the experiments, it was not possible to identify an effect of surface pre-treatment on the current values obtained for a specific anodizing bath.

5.5 Morphological characterization of AA2524 samples anodized in TSA

5.5.1 Morphological characterization of unsealed AA2524 anodized in TSA

Figure 5.10 shows SEM micrographs of the top surfaces of unsealed AA2524 specimens anodized in TSA at 8 V (a), 10 V (b), 14 V (c) and 16 V (d), where the porous nature of the top layer is highlighted. The pore morphology is irregular when compared to anodic layers produced in pure Al (LE COZ; ARURAULT; DATAS, 2010; ONO; SAITO; ASOH, 2005), which is a characteristic of AA2XXX alloys (MA et al., 2011b; FRATILA-APACHITEI; DUSZCZYK; KATGERMAN, 2002; MOLCHAN et al., 2010; SAENZ de MIERA et al., 2010a,2010b). This layer morphology is ascribed to copper enrichment at the substrate surface during the anodizing procedure leading to the incorporation of copper species into the anodic film and to oxygen generation (FRATILA-APACHITEI; DUSZCZYK; KATGERMAN, 2002; CURIONI et al., 2008a, PAEZ et al., 1996, 2000) and to the differences in the anodizing rates of IMs in relation to the base matrix (GARCIA-VERGARA

et al., 2006, SAENZ DE MIERA et al., 2010b; COTE et al., 1969; COTE; HOWLETT; LAMB, 1970). It is documented that oxygen bubbles generated during anodic process can affect the distribution of stress in the film that is critical to pore formation (GARCIA-VERGARA et al., 2006; IGLESIAS-RUBIANES et al., 2007; GARCÍA-RUBIO et al., 2010). The damage in the anodic film is partly due to the release of oxygen gas within the alumina that can generate pressures of several hundred MPa (GARCIA-VERGARA et al., 2006). Indeed, oxygen evolution could be observed at the sample surface during the anodizing procedure but this amount was not quantified. According to Thompson et al. (1999) "the combination of roughness and stresses created by the growth of bubbles may eventually lead to mechanical rupture of the film with release of the oxygen gas". Therefore, anodic film damages can be partially ascribed to the inhomogeneous microstructure of the alloy but it seems to be mostly affected by the release of oxygen gas during the growth of the porous layer.

Figure 5.10 - Top surface FE-SEM micrographs of anodic aluminium oxide produced by anodizing AA2524 in TSA bath. Anodizing voltages: (a) 8 V (b) 10 V (c) 14 V and (d) 16 V.

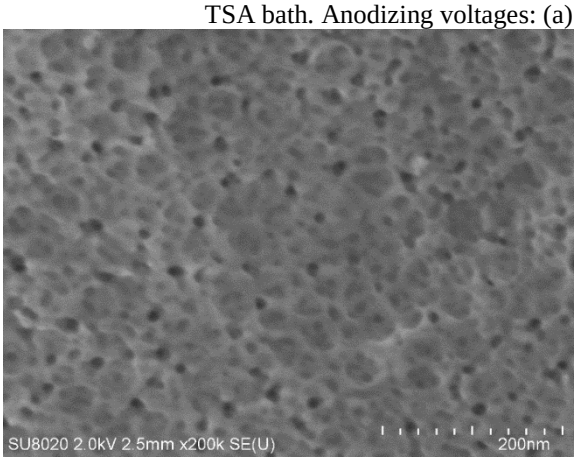

(a) 8 V – unsealed

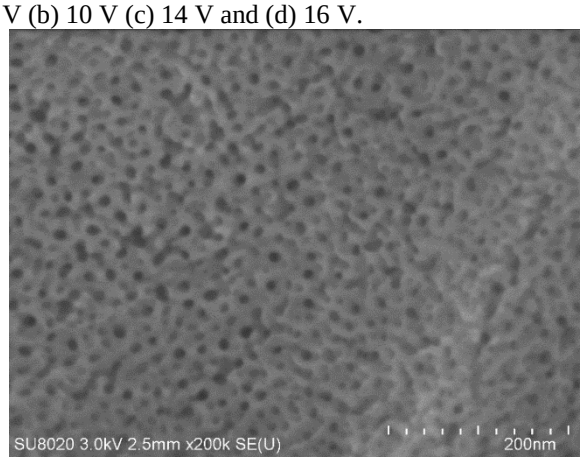

(b) 10 V – unsealed

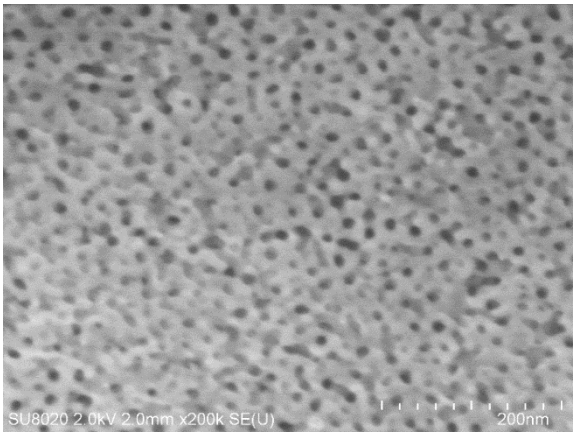

(c) 14 V – unsealed

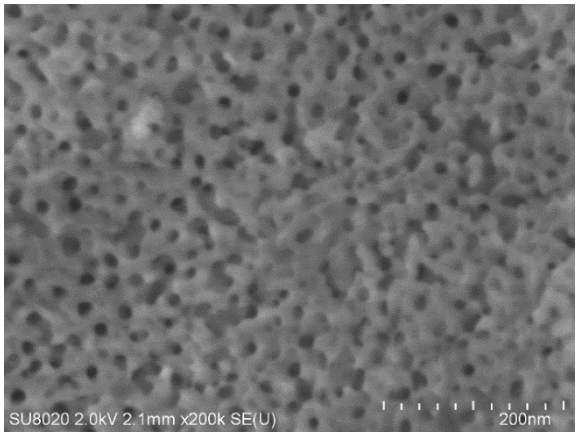

(d) 16 V – unsealed

For the sample anodized at 8 V (Fig. 5.10 (a)) the pore mouths are not very well defined and the distribution is quite irregular compared to the other anodizing voltages. The anodizing of aluminium and its alloys in acidic electrolyte is initiated by the thickening of the barrier oxide layer up to a certain thickness, proportional to the applied voltage, when it becomes insulating to ionic conduction (LEE; PARK, 2014; JESSENSKY; MÜLLER; GÖSELE, 1998). In potentiostatic procedure, this process is characterized by a sharp current rise followed by a steep current decrease, as shown in Figure 5.9. At this stage, pores nucleate from certain locations of the barrier layer and should grow as hexagonal self-organized perpendicular arrays separated from the metal surface by the insulating barrier layer. According to Jessensky et al. (1998), in order to explain pore self-organization and growth, the existence of repulsive interactions between growing neighbouring pores have to be assumed. This behaviour depends on the stress generated by the volume expansion of the aluminium oxide during its formation. On the one hand, when insufficient voltage is applied during the anodizing process, the repulsive stress originated from the volume expansion is unable to press the cells against one another and self-organization does not occur, resulting in poor-defined porous structure (VOON et al., 2014). On the other hand, when the applied voltage is too high, a large increase in volume expansion may occur, also resulting in structural defects in the alumina and irregular pore growth (VOON et al., 2014). This latter feature can explain the less organized structure of the porous layer formed at 16 V (Fig. 5.10 (d)) when compared to 10 V (Fig. 5.1 (b)) and 14 V (Fig. 5.10 (c)). Therefore, optimized anodizing conditions must be employed in order to improve the distribution of the pores in the anodic aluminium oxide layer.

The average pore diameters measured from FE-SEM micrographs and the surface porosity as a function of the anodizing voltage are displayed in Table 5.1. The porosity was determined using ImageJ software on higher resolution images of the oxide surface. In the procedure, the SEM images were transformed to a binary format and then a program command called “analyze particles” was applied for the estimation of the percentage (%) of the total surface occupied by the pores. Taking into account the large standard deviation of the pore diameters for the sample anodized at 14 V, it is possible to verify that, in accordance with the findings of other authors for different anodizing electrolytes (VOON et al., 2014; WOOD; O’SULLIVAN, 1970; CHAHROUR et al., 2015), pore diameter slightly increases with anodizing voltage. In the opposite, the porosity of the layer decreases with the applied voltage as observed for 8 V, 10 V and 14 V. This behaviour can be explained by the decrease of the

pore number with voltage, higher voltage favouring the growth of the layer compared to its dissolution at the same temperature (SAFRANY, 2008). The higher porosity measured at 16 V could be related to the increase of oxygen bubbles generation, Joule effect in the pores and layer defects (BROWN et al., 1988; LI; ZHANG; METZGER, 1998; GARCÍA-RUBIO et al., 2010).

Table 5.1- Pore diameter and porosity determined from Image J (PIJ) and from Eq. 5.1 for ideally ordered porous AAO: P_1 - using Eq. 5.2 to determine the interpore distance; P_2 – using Eq. 5.3 to determine the interpore distance.

Voltage (V)	**Pore diameter (nm) – Average**	**PIJ (%)**	**P_1 (%)**	**P_2 (%)**	**Anodic Layer (µm)**
8	12.30 ± 0.56	40.07	48.0	43.9	1.41
10	12.35 ± 0.62	39.84	42.0	38.8	2.13
14	11.95 ± 1.31	30.62	32.5	30.6	3.24
16	14.00 ± 1.11	34.21	34.7	32.8	3.91

From simple geometric considerations Lee and Park (2014) proposed Equation (5.1) to calculate the porosity (P(%)) for an ideally ordered porous AAO:

$$P(\%) = \left(\frac{\pi}{2\sqrt{3}}\right)\left(\frac{D_P}{D_{int}}\right)x100 \qquad 5.1$$

Where D_P and D_{int} are, respectively, the pore diameter and the interpore distance. Eq. (5.1) was applied to calculate and compare the sample porosity to that determined with the software Image J (column PIJ in Table 5.1). However, due to the inhomogeneity of pore distribution (Fig. 5.10), the experimental determination of the interpore distance would involve great incertitude. Therefore, the two formulas provided in the review article of Lee and Park (2014) were used for the estimation of the interpore distance as a function of applied potential for aluminium oxide produced in sulphuric (Eq. 5.2) and oxalic (Eq. 5.3) acids. The results are presented, respectively, in Table 5.1 (P_1 and P_2). Except for a larger deviation for the sample anodized at 8 V when using Eq. 5.2, the calculated values are in fairly good agreement with those determined using ImageJ, indicating that the software provides reliable porosity values.

$$D_{int} = 12.1 + 1.99\,U \quad (\text{U = 3-18 V}) \qquad 5.2$$

$$D_{int} = 14.5 + 2.00\,U \quad (\mathrm{U} \leq 20\ \mathrm{V}) \qquad 5.3$$

Figure 5.11 shows cross section SEM micrographs of samples anodized at 8 V (a), 10 V (b), 14 V (c) and 16 V (d). The layer seems to be compact, uniform and adherent to the substrate surface. From these images, it was possible to determine the thickness of the anodic layer as a function of the anodizing voltage displayed in the micrographs, in Table 5.1 and in Figure 5.12. This latter Figure shows that the anodic layer thickness exhibits an almost linear dependence with the applied anodizing voltage. It is well documented that the barrier layer thickness is directly proportional to the anodizing voltage, usually in the range of 1.0 to 1.5 $nm.V^{-1}$ (BOGDANOV et al., 1990; BREVNOV et al., 2004; BONORA; DEFLORIAN; FEDRIZZI, 1996), whereas the thickness of the overall layer (basically the porous one) is proportional to the total charge involved in the electrochemical oxidation (LEE; PARK, 2014), which depends on the applied current density. This anodic current density was not measured during the anodic process. Nevertheless, knowing that the anodizing time was the same for each applied voltage, the results of thicknesses determination seem to indicate that the ratio between the voltage and the film resistance U/R_{film} remains constant whatever the applied voltage in the investigated range.

Figure 5.11 - SEM cross section micrographs of the porous anodic aluminium oxide produced by anodizing AA2524 in TSA bath. Anodizing voltages: (a) 8 V (b) 10 V (c) 14 V and (d) 16 V.

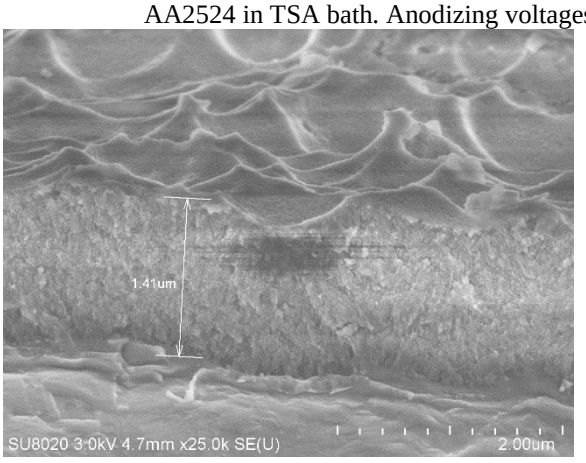

(a) 8 V – unsealed

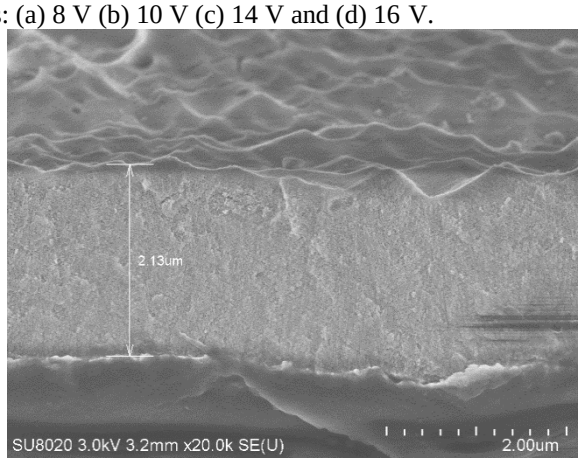

(b) 10 V – unsealed

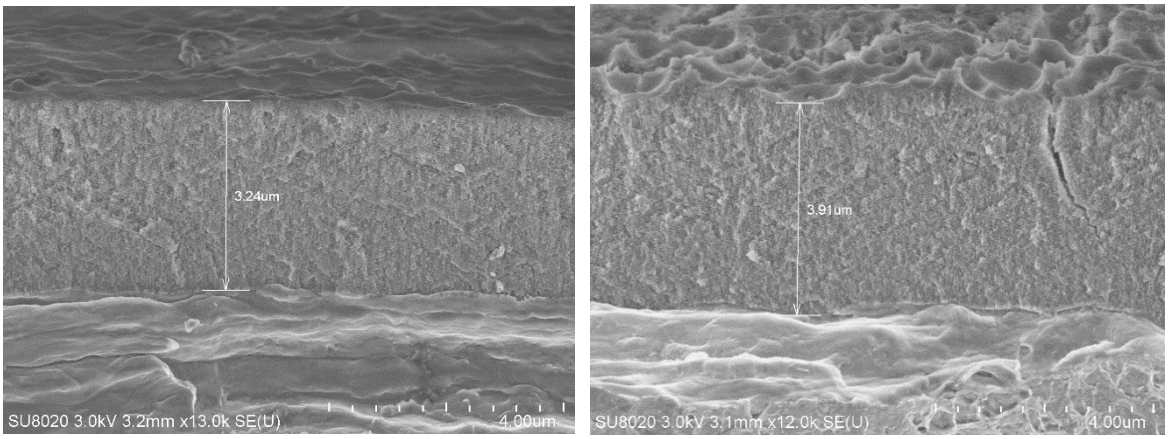

.(c) 14 V – unsealed (d) 16 V – unsealed

Figure 5.12 - Variation of the thickness of the anodic layer as a function of the anodizing voltage.

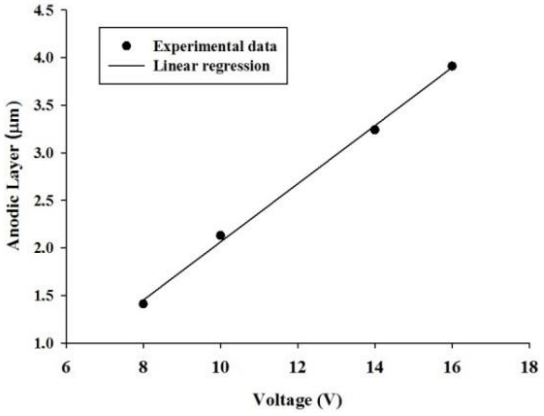

5.5.2 Morphological characterization of AA2524 anodized in TSA and then hydrothermally sealed in boiling water

Figure 5.13 presents SEM micrographs of the top surfaces of AA2524 samples anodized in TSA at 8 V (a), 10 V (b), 14 V (c) and 16 V (d) and then hydrothermally sealed (HTSed) in boiling water.

Figure 5.13 - Top surface SEM micrographs of AA2524 samples anodized in TSA at 8 V (a), 10 V (b), 14 V (c) and 16 V (d) and then hydrothermally sealed (HTSed) in boiling water

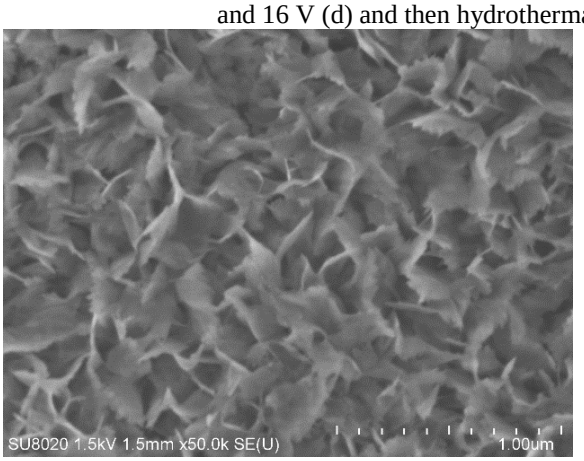

(a) 8 V – hydrothermally sealed

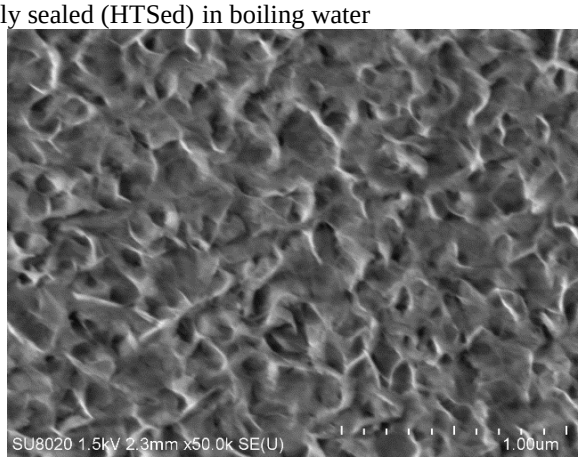

(b) 10 V – hydrothermally sealed

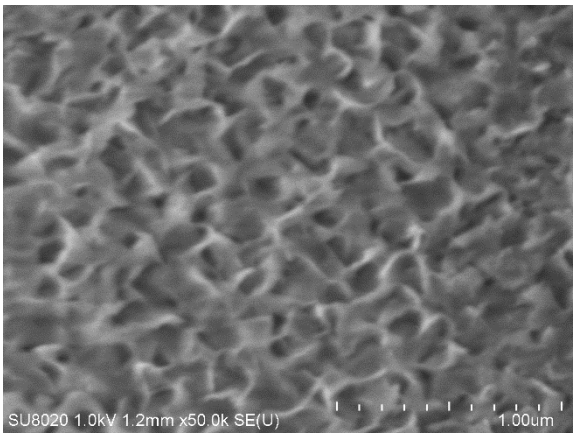

(c) 14 V – hydrothermally sealed

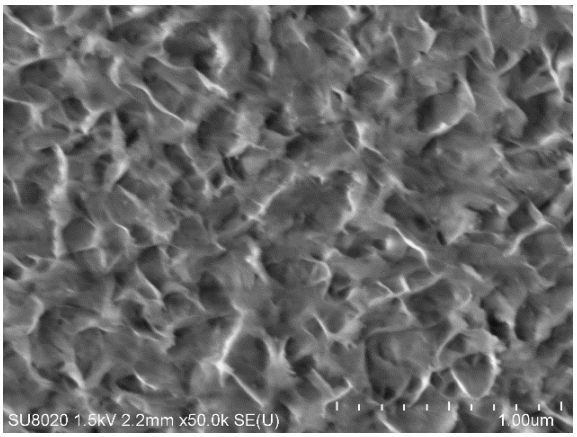

(d) 16 V – hydrothermally sealed

The HTSed samples (Fig. 5.13) clearly show the growth of "petal-shaped" crystals on the top surface, denominated smudge, being in good agreement with the literature (BOISIER et al., 2008, CAPELOSSI et al., 2014). The initial porous structure disappears during the sealing process because of the initial precipitation of boehmite on the pore mouths followed by the dissolution of the pore walls (LOPEZ et al., 2006). This former process plugs the upper part of the pores, preventing environmental access to their interior (GARCÍA-RUBIO et al., 2009; BOISIER et al., 2008). As shown in the literature review, pore plugging seems to take place after only a few minutes of the initiation of the boiling water treatment (LOPEZ et al., 2006). During the remainder of the HTS treatment, aluminium hydroxide precipitates within the pores, effectively blocking them and increasing the corrosion resistance (HOAR; WOOD, 1962; ZUO; ZHAO; ZHAO, 2003; HAO; CHENG, 2000).

5.5.3 Morphological characterization of AA2524 hybrid anodized in TSA and coated with sol–gel

Figures 5.14 and 5.15 show, respectively, SEM micrographs of the top surfaces and of the cross section of AA2524 samples anodized in TSA at 8 V (a), 10 V (b), 14 V (c) and 16 V (d) and subsequently protected with the hybrid sol-gel coating. The micrographs of Figures 5.14 (a) and 5.15 (a), for 8 V, and of Figures 5.14 (b) and 5.15 (b), for 10 V, reveal that the sol-gel coating has a good coverage on the AA2524 top surface. On the other hand, for 14 V (Fig. 5.14 (c) and 5.15 (c)) and 16 V (Fig. 5.14 (d) Fig. 5.15 (d)) the surface is not homogeneously covered, and some pores can still be detected on the sample surface.

Figure 5.14 - Top surface SEM micrographs of AA2524 anodized in TSA and coated with the hybrid sol-gel layer. Anodizing voltage: (a) 8 V, (b) 10 V, (c) 14 V and (d) 16 V.

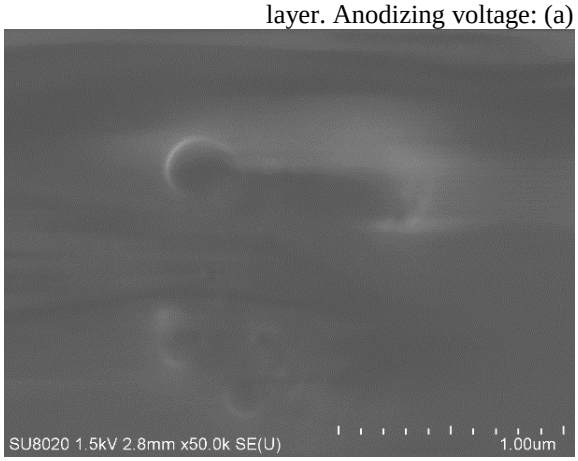

(a) 8 V - coated with the hybrid sol-gel layer

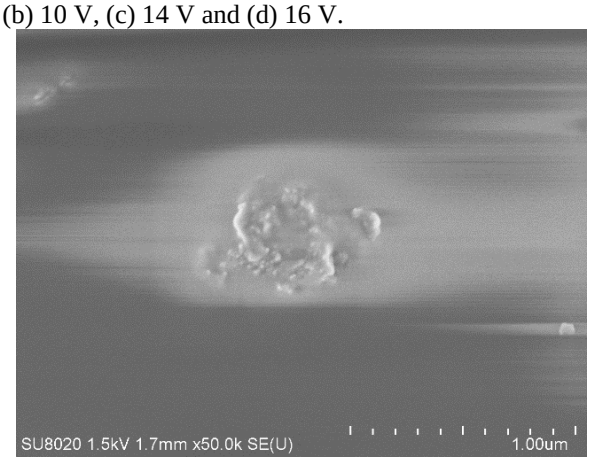

(b) 10 V - coated with the hybrid sol-gel layer

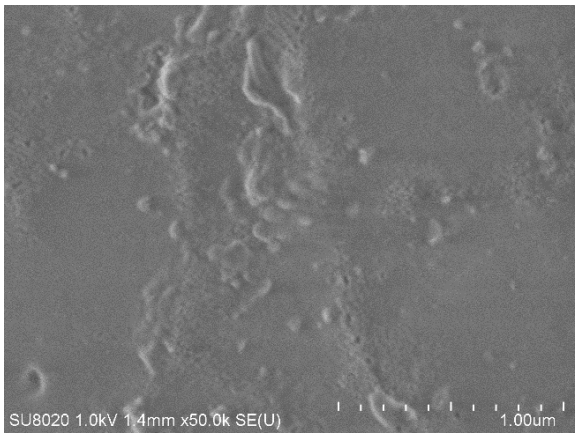

(c) 14 V - coated with the hybrid sol-gel layer

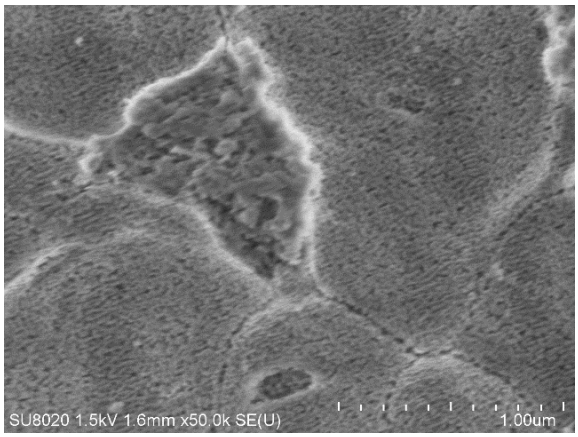

(d) 16 V - coated with the hybrid sol-gel layer

Figure 5.15 - SEM cross section micrographs of the anodic layer on AA2524 anodized in TSA and coated with the hybrid sol-gel layer. Anodizing voltage: (a) 8 V, (b) 10 V, (c) 14 V and (d) 16 V.

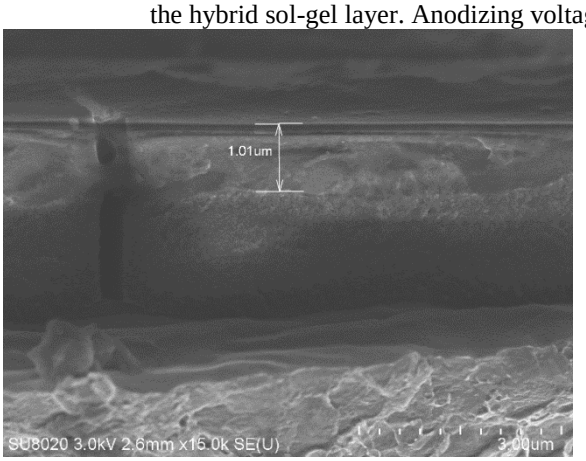

(a) 8 V - coated with the hybrid sol-gel layer

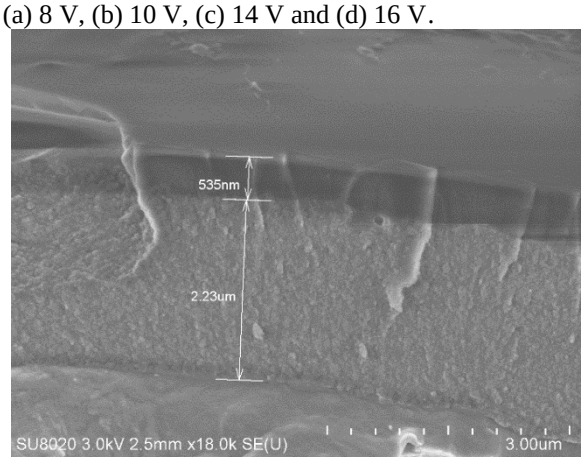

(b) 10 V - coated with the hybrid sol-gel layer

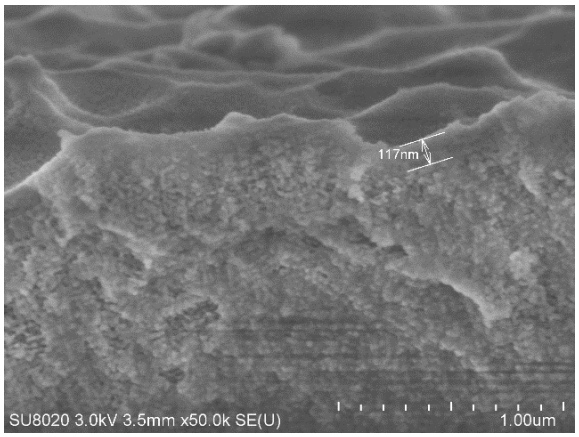

(c) 14 V - coated with the hybrid sol-gel layer

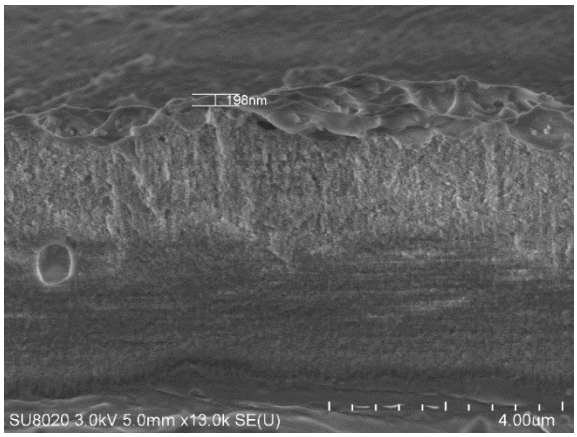

(d) 16 V - coated with the hybrid sol-gel layer

The literature survey showed that, even though a large amount of scientific work has been carried out to investigate the corrosion protection afforded by sol-gel layers to aluminium substrates, only few works are available where this methodology was employed to protect anodized aluminium. Initially, sol-gel oxide (inorganic) films were applied to porous AAO layers (HIRAI et al., 1998; LIU et al., 2010) and only recently sol-gel coatings from organo-functional silanes were used for anticorrosion protection (WHELAN; CASSIDY; DUFFY, 2013; CAPELOSSI et al., 2014; WOJCIECHOWSKI et al., 2016). The literature survey also revealed that sol-gel penetration within the porous layer has always been a major concern for the scientists. Thus, Liu et al. (2010) employed a vacuum system and several dip coating cycles to achieve good anticorrosion protection, whereas Miao et al. (2010) and Xu et al. (2003) employed potentiostatic polarization in order to produce highly ordered nanowires using porous AAO with pore diameters lower than 20 nm as template. However, the recent

work of Whelan et al. (2013) showed that, if there is no interference of the liquid surface tension and if there is compatibility between the charge of the hydrolysed hybrid molecules and the surface charge of the porous aluminium oxide, sol-gel penetration within the pores will occur when the sizes of the sol-gel particles are sufficiently small, .i.e. when their dimensions are lower than the pore diameter. In their work, they showed that an acid catalysed hybrid sol-gel with size distribution in the range from 3 nm to 15 nm was able to penetrate pores with diameters of 10-15 nm (WHELAN; CASSIDY; DUFFY, 2013). Considering that an acid hydrolysis was performed in the present work and that the pore diameters presented in Table 5.1 are of the same order of magnitude of those reported by Whelan et al. (2013), it is likely that the pore diameters of the porous layer produced by TSA on the AA2524 alloy will not be an obstacle for the sol-gel solution penetration.

For a better comprehension of the structure of the AAO and also to gather information of how the hybrid coating covers and penetrates the porous layer thicknesses produced with the different anodizing voltages, GDOES analyses (Fig. 5.16) were performed for samples produced according to the conditions exhibited in Figure 5.14. In good agreement with the SEM thickness determinations (Fig. 5.11), the oxygen signal depth increases with anodizing voltage, confirming the formation of thicker anodic layers. In addition, the depth profiles for this element and for Al reveal that the interface between the anodic layer and the metallic substrate is not well-defined, as their percentages in the atomic composition of the sputtered layers slowly decrease and increase, respectively, when the metal interface is reached. In accordance with the literature (DIGGLE; DOWNIE; GOULDING, 1969; LEE; PARK, 2014), the sulphur sign in the GDOES depth profiles also show the incorporation of sulphate ions from the anodizing bath in the AAO.

Figure 5.16 - Glow discharge optical emission spectrometry profiles of AA2524 anodized in TSA and coated with the hybrid sol-gel layer. Anodizing voltage: (a) 8 V, (b) 10 V, (c) 14 V and (d) 16 V.

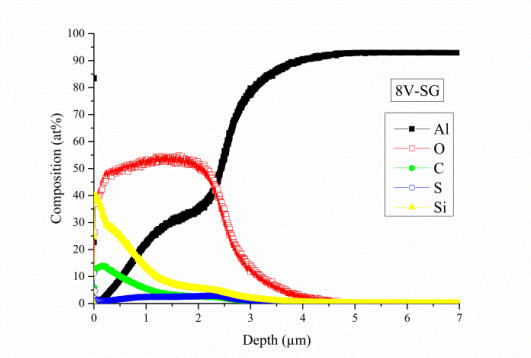

(a) 8 V

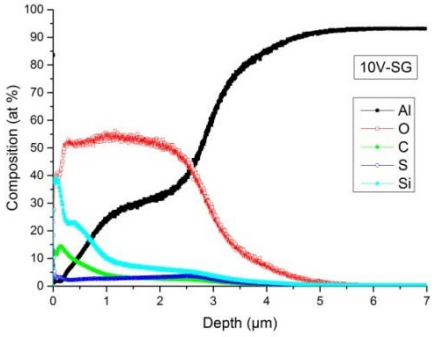

(b) 10 V

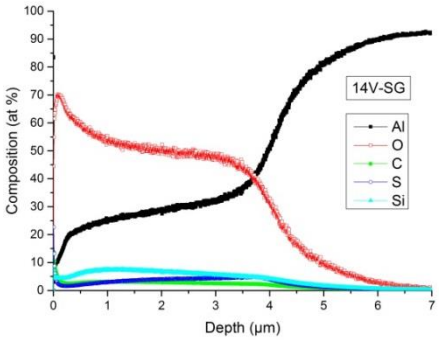

(c) 14 V

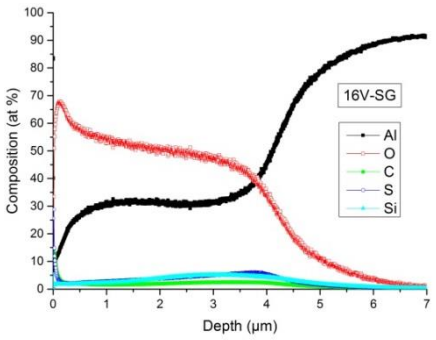

(d) 16 V

The GDOES depth profiles of Si and C are representative of the deposition of the sol-gel coating on the AAO. Figure 5.17 presents a magnified representation of the GDOES depth profile of this former element on samples produced with the four different voltages investigated in the present study. The plot shows that, irrespectively to the anodizing voltage, the hybrid sol-gel solution penetrates the porous layer, and, in good agreement with the SEM images (Fig. 5.11), confirms that the percentage of Si near the sample surface decreases as the anodizing voltage increases. Thus, for the two samples with good hybrid coating surface coverage (8 V and 10 V) the percentage of Si near the surface is around 40 %, whereas for the samples anodized at 14 V and 16 V, the Si surface percentages were around 5 % and 2 %, respectively. The Si GDOES depth profiles for the samples anodized at 8 V and 10 V also allow estimating the thickness of the hybrid coating, which is around 1 μm, and indicate that, for these two anodizing conditions, the pores are completely filled by the coating, as the dimensions of the Si percentage plateau are compatible with the AAO thicknesses determined from the SEM cross section micrographs (Fig. 5.11 (a) and (b)). On the other hand, the GDOES depth profiles for the samples anodized at higher voltages (14 V and 16 V) indicate that the hybrid sol-gel solution fills the pores from the bottom to the top, as higher Si percentages were found closer to the anodic layer-aluminium interface.

Figure 5.17 - Comparison of the glow discharge optical emission spectrometry profiles of Si for the AA2524 samples anodized in TSA at 8 V, 10 V, 14 V and 16 V and coated with the hybrid sol-gel.

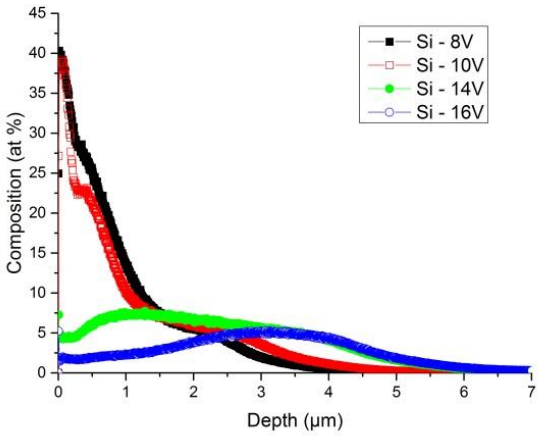

Based on these measurements and on the morphological characterization of the porous layers, the filling of the pores seems to be mainly conditioned by the thicknesses of the porous layers and not by the porosities and pore diameters, which were verified to be quite similar in the investigated range of voltages. Whatever the applied voltage, the compatibility between alumina and the Si precursors in the solution is particularly high that can be explained by the surface charges of these species. At the acidic pH of the hydrolysis solution (2.5), the charge of the alumina surface is positive, because its isoelectric pH is around 8 in aqueous solution (KOSMULSKI, 2016), and the silica colloids formed during hydrolysis (but not detected by Dynamic light scattering) and during condensation and solvent evaporation is slightly negative (isoelectric pH is reported to be lower than 2) (KOSMULSKI, 2016). The electrostatic interaction is, therefore, favourable. As the same dip coating procedure was used for the different applied voltages, the same quantity of sol-gel solution must be withdrawn during the application process. At lower voltages (8 V and 10 V), the porous layer thickness is around 1 and 2 µm, respectively. For these thicknesses, due to the low Newtonian viscosity of the sol-gel solution (0.003 Pa.s), the withdrawn solution is incorporated by capillarity in the pores structure plugging them during the condensation and curing processes. The excess of solution remains at the top surface and covers the porous AAO layer (Figures 5.14 (a) and (b)). For the higher voltages (14 V and 16 V), the thicknesses of the porous AAO layers are around 3 and 4 µm, respectively, and the sol-gel solution quantity is insufficient to completely

fill the pores and to keep an excess of solution at the top surface of the AAO (Figures 5.14 (c) and (d)). The capillary forces help to fill the pores from the bottom up to the top.

5.6 Electrochemical characterization

5.6.1 EIS of AA2524 coated with the hybrid sol-gel (non-anodized samples)

Non-anodized pre-treated AA2524 aluminium samples were coated with the hybrid sol-gel and their EIS responses were followed with immersion time in 0.1 mol.L^{-1} NaCl solution. The coating showed quite poor anticorrosion properties as can be seen in Figure 5.18 and 5.19, which show, respectively, the EIS response with immersion time and the picture of the sample after 3 days of immersion in the test solution.

In the initial immersion period (1 h), the impedance behaviour depicted in Figure 5.18 indicates that the sol-gel coating acts as an effective physical barrier against the penetration of water and corrosive ions. The EIS diagram presents a strongly capacitive high frequency (HF) time constant, and the impedance modulus is superior to 1 MΩ.cm^2. However, the progress of the experiment shows that the coating rapidly loses its protective properties. After 6 h of immersion, the impedance modulus drops more than one order of magnitude and the capacitive response of the HF time constant is strongly diminished, being also displaced to lower frequencies, in addition, a low frequency (LF) time constant is developed. These two latter features indicate, respectively, water uptake by the coating (BONORA; DEFLORIAN; FEDRIZZI, 1996) and the onset of corrosive activity at the substrate surface underneath the coating. This means that conductive pathways quickly develop through the coating, allowing aggressive species penetration and corrosion activity onset at the metal surface, explaining the strong impedance modulus drop and the development of a new time constant.

For longer immersion periods (more than 24 h) the impedance modulus remains approximately constant, however the coating deterioration continues to take place as the HF capacitive response turns to a shoulder. Moreover, new LF time constants appear, indicating that the corrosion process at the substrate surface becomes more complex. Precipitation of corrosion products on the substrate surface may explain why impedance modulus remains almost constant for the tests performed after longer immersion times. The development of

corrosion activity through the precipitated corrosion product may be responsible for the LF response with several time constants.

Figure 5.18 - Bode plots as (a) impedance modulus and (b) phase angle for non-anodized AA2524 coated with the hybrid sol-gel and exposed to 0.1 mol.L^{-1} NaCl solution for different immersion times.

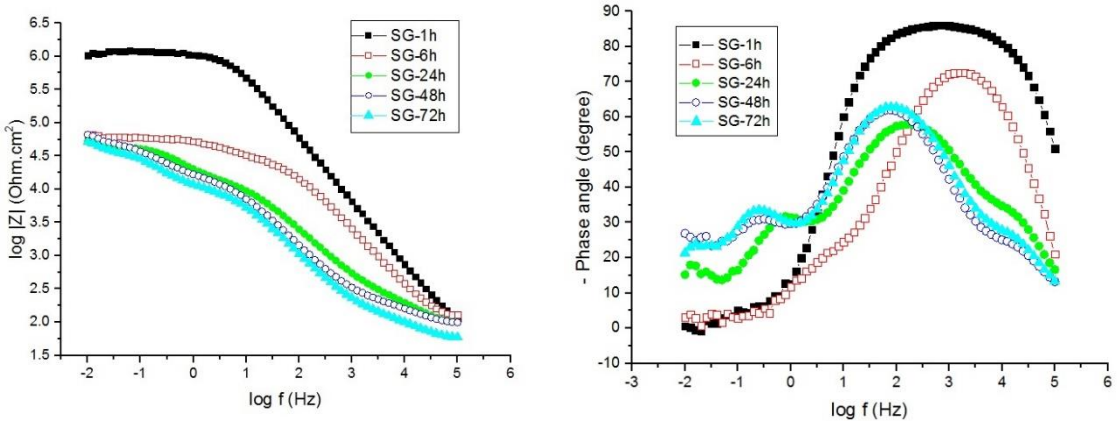

(a) (b)

Figure 5.19 - Photograph of non-anodized AA2524 coated with the hybrid sol-gel after 72 h of immersion in 01 mol.L^{-1} NaCl.

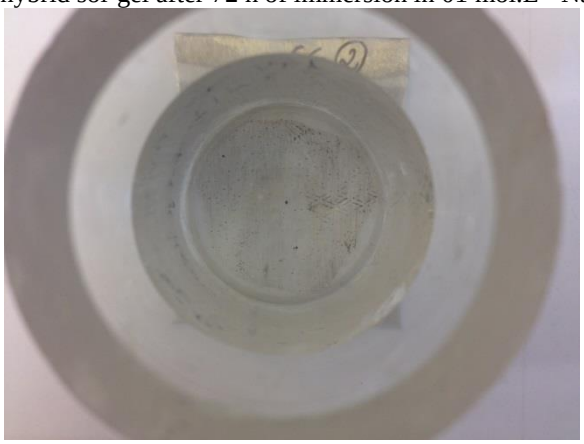

In order to have a better insight about the evolution with immersion time of the anticorrosion properties of the non-anodized samples coated with the hybrid sol-gel, the EIS diagrams were fitted with the EEC analogues presented in Figure 5.21, whereas Figure 5.20 shows the schematic physical representation of the AA2524 sample coated with the intact sol-gel layer. The first circuit proposed (Figure 5.21 (a)) is formed by a capacitance and resistance of the sol-gel coating (C_{SG} and R_{SG}) at HF and by the double layer capacity (C_{dl}) and charge transfer resistance (R_{ct}) at LF. These two latter parameters are related to the corrosion reaction at the

metal/coating interface: C_{dl} is associated to the substrate surface exposed to the electrolyte through the pores of the coating and due to topcoat delamination and R_{ct} is directly associated to the corrosion rate at the coating/metal interface at these exposed areas (JI et al., 2007). After 6 h of immersion in 0.1 mol.L^{-1} NaCl the sol-gel layer is already strongly degraded, and in order to take into account the non-ideality of the system, the capacitive response of the double layer was replaced by a constant phase element (CPE_{dl}) (Figure 5.21 (b)). From 24 h to 72 h, CPE_{corr}/R_{corr} elements were introduced in the EEC model due to the corrosion reactions taking place at the surface of the aluminium (Figure 5.291 (c)).

Figure 5.20 - Physical model of the non-anodized AA2524 coated with an intact hybrid sol-gel layer.

Figure 5.21 - EEC used to fit the EIS data of the non-anodized AA 2524 coated with the hybrid sol-gel after (a) 1 h (b) 6 h and (c) 24 up to 72 h of immersion in 0.1 mol.L-1 NaCl.

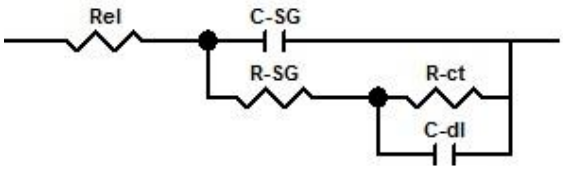

(a) non-anodized and coated with sol-gel - 1 h

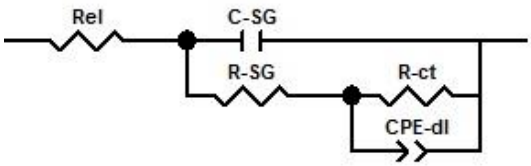

(b) non-anodized and coated with sol-gel - 6 h

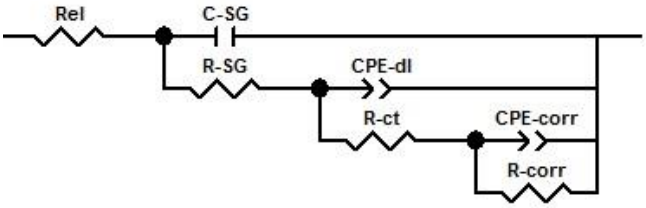

(c) non-anodized and coated with sol-gel - 24 h, 48 h, 72 h

Table 5.2 shows the results of the fitting procedure of the EIS diagrams of the non-anodized AA2524 coated with the hybrid sol-gel with the EEC analogues of Figure 5.21. The C_{SG} values gradually increases with immersion time pointing either to water uptake or to a thinning of the hybrid coating, the strongest increase was verified between 1 h and 6 h of exposure. R_{SG} values decrease by about one-half from 1 h to 6 h and then more than two orders of magnitude for 24 h of test, indicating strong degradation of the coating during the

first day. Then, from 24 h to 72 h, R_{SG} decreases only slightly. Regarding the variation of R_{ct}, it strongly decreases from 1 h to 6 h, indicating that an intense electrochemical activity quickly develops at the metal surface, and then it decreases slowly up to the end of the experiment, showing that somehow the charge transfer process achieves almost a steady state. On the other hand, C_{dl}-CPE_{dl} constantly increases, pointing to an increase in the wet area. Interestingly, the C_{dl} value for the test performed after 1 h was particularly small (in the order of nF cm^{-2}), indicating that only a small portion of the substrate surface is really wetted. This is coherent with the very high value of R_{ct} determined for this experiment: in the order of MΩ cm^2. Finally, R_{corr} increases from 24 h to 48 h and then decreases at the end of the measurement. The oscillating behaviour of this variable can be attributed to the precipitation and dissolution of corrosion products in the confined environment underneath the hybrid coating, indicating a complex chemistry. On the other hand, CPE_{corr} constantly rises pointing to increased accumulation of polarizable ionic/molecular species at the metal interface[8]

Table 5.2 - Parameters obtained from the fitting procedure of the EIS diagrams for non-anodized AA2524 coated with the hybrid sol-gel with the EEC analogues of Figure 5.21.

Immersion time (h)	**C_{SG} ($\mu F.cm^{-2}$)**	**C_{dl} ($\mu F.cm^{-2}$)**	**CPE_{dl} ($\mu F.cm^{-2}.s^{(n-1)}$)**	**n_{dl}**	**CPE_{corr} ($\mu F.cm^{-2}.s^{(n-1)}$)**	**n_{corr}**	**R_{SG} ($k\Omega.cm^2$)**	**R_{ct} ($k\Omega.cm^2$)**	**R_{corr} ($k\Omega.cm^2$)**
1	$2.11x10^{-2}$	$6.17\ x10^{-3}$	-	-	-	-	22.30	1002.05	-
6	$6.50\ x10^{-2}$	-	3.28	0.51	-	-	12.28	52.43	-
24	$8.20\ x10^{-2}$	-	2.98	0.74	17.04	0.84	0.18	16.62	31.38
48	$1.02\ x10^{-1}$	-	4.02	0.79	37.82	0.71	0.11	16.31	52.72
72	$1.60\ x10^{-1}$	-	5.14	0.79	48.12	0.76	0.08	11.45	38.26

5.6.2 EIS of unsealed AA2524 anodized in TSA

Figure 5.22 shows EIS diagrams as a function of immersion time in 0.1 $mol.L^{-1}$ NaCl solution for unsealed AA2524 samples anodized in TSA at 8 V (a), 10 V (b), 14 V (c) and 16 V (d). Diagrams were acquired up to 168 h, when the samples surface were corroded (Figure 5.23). Overall, the impedance modulus dropped more than two orders of magnitude during the test period, indicating unsatisfactory corrosion resistance for this system.

[8] Capítulo 5 – Capacitância e Capacitores.Available in: <https://www.if.ufrgs.br/tex/fis142/mod05/m_s07.html - accessed in 02/21/17>. Access: February 22nd 2017.

The tendencies of the impedance modulus with immersion time for the unsealed samples indicate that the EIS behaviour is inversely related to the pore diameter. In this way, in general, the samples produced with higher anodizing voltage, even though exhibiting higher impedance modulus at the beginning of the exposure period, presented lower impedance at the completion of the tests. These samples must present thicker barrier layer due to increased voltage, explaining the higher initial impedance. However, as shown in Table 5.1, the wider pore mouths seem to allow the electrolyte to reach the substrate surface more easily, accelerating the corrosion process. Moreover, narrower pores may create a more confined environment near the metallic surface, favouring corrosion product precipitation and improving the long-term corrosion resistance of the samples produced with lower anodizing voltages. The inverse corrosion resistance with increasing anodizing voltage can also be verified by the photographs of the samples surface after 168 h of exposure to the test electrolyte shown in Figure 5.23.

For all the samples represented in Figure 5.22, the phase angle plots display two time constants since the beginning of the exposure period (not well-separated and sometimes represented by a wide phase angle), which is terminated by a well-defined LF impedance modulus plateau (except for the diagrams acquired after 1 h for the samples anodized at 14 V and 16 V). This behaviour is an indication of the onset of the corrosion process since the early immersion periods, once a resistive LF behaviour can be easily identified. As shown in the literature survey, the EIS response of non-sealed porous anodized layer is frequently composed of a wide and deformed phase angle (GONZÁLEZ et al., 1999; GARCIA-RÚBIO et al., 2009a, 2010, BOSIER et al., 2008), frequently fitted with two time constants EEC (GONZÁLEZ et al., 1999, BOISIER et al., 2008). The EIS responses of the diagrams of Figure 5.22 later progress to three time constants spectra, whose transition time is inversely dependent of the anodizing voltage: the higher the anodizing voltage the sooner the transition takes place.

Figure 5.22 - Bode plots as impedance modulus and phase angle plots for unsealed AA2524 anodized in TSA after different immersion times in 0.1 mol.L^{-1} NaCl solution. Anodizing voltages: (a) 8 V, (b) 10 V, (c) 14 V and (d) 16 V.

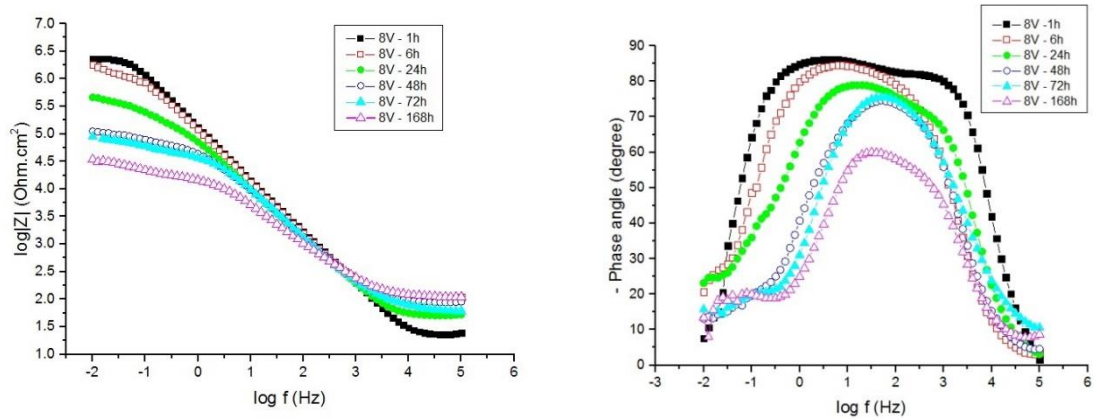

(a) 8 V – unsealed

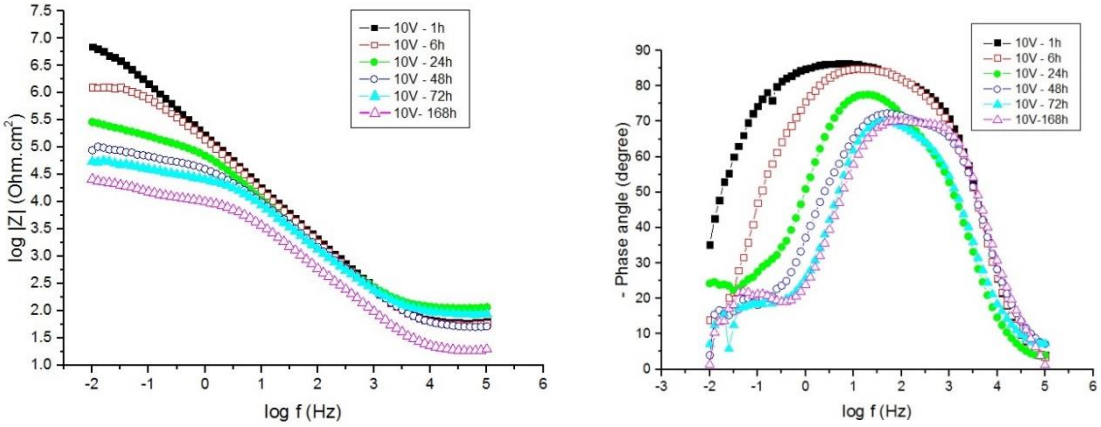

(b) 10 V- unsealed

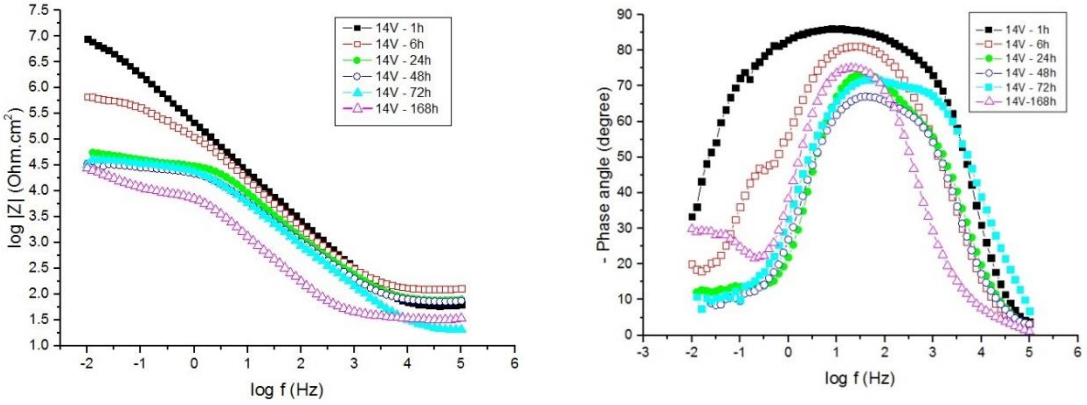

(c) 14 V- unsealed

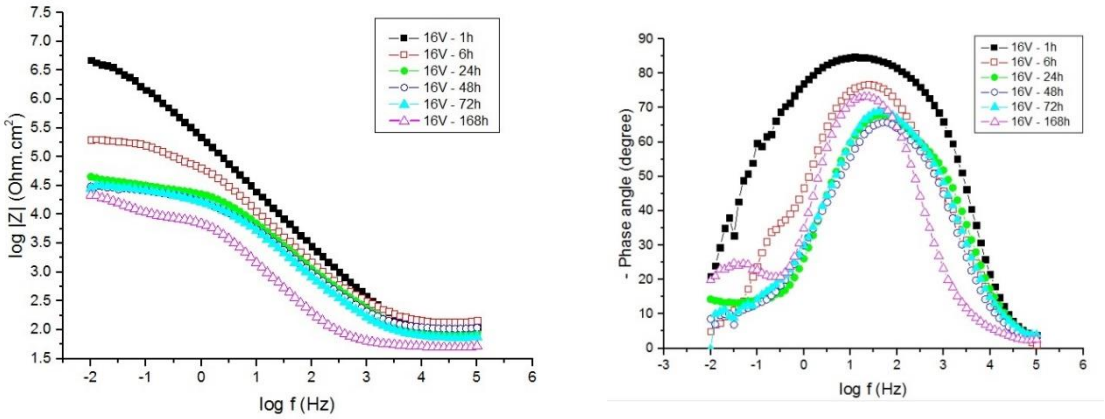

(d) 16 V- unsealed

Figure 5.23 - Photographs of unsealed AA2524 anodized in TSA after 168 h exposure to the 0.1 mol.L^{-1} NaCl: (a) 8 V; (b) 10 V; (c) 14 V; (d) 16 V.

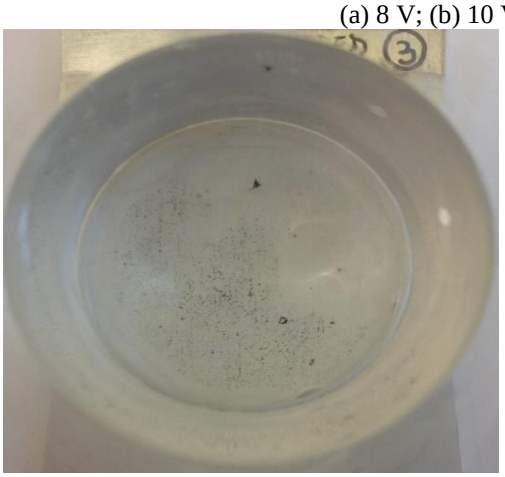

(a) 8 V – unsealed

(b) 10 V – unsealed

(c) 14 V – unsealed

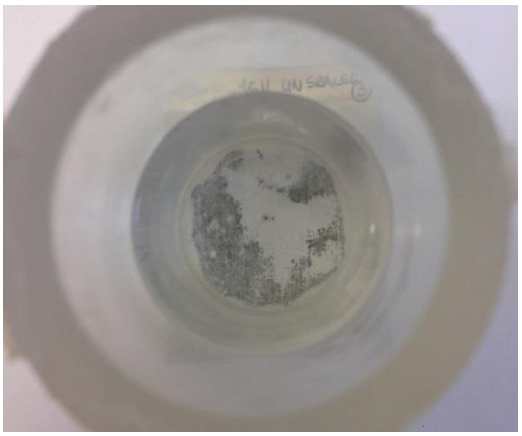

(d) 16 V – unsealed

Figure 5.24 presents the evolution with immersion time in the test electrolyte of the impedance modulus at 0.01 Hz of unsealed samples of AA2524 anodized in TSA at 8 V (a),

10 V (b), 14 V (c) and 16 V (d). It is possible to observe that at the beginning of the test the sample anodized at 14 V has higher LF impedance modulus, followed by 10 V, 16 V and 8 V, respectively, however, after 168 h of immersion the samples anodized at lower voltages present higher impedance modulus, which is in accordance with the degradation rates showed in Figure 5.23.

Figure 5.24 - Evolution with immersion time in 0.1 mol.L^{-1} NaCl of the impedance modulus at 0.01 Hz of unsealed AA2524 samples anodized in TSA at different voltages: 8 V, 10 V, 14 V and 16 V.

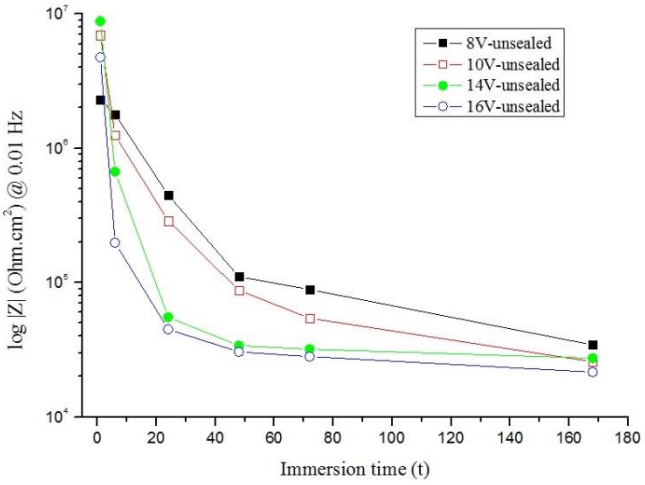

Based on these qualitative observations, the EEC showed in Figures 5.26 to 5.29 were used to fit the EIS responses of the anodized and unsealed samples, which physical model for an undamaged layer associated with the EEC valid for the first immersion hours are depicted in Figure 5.25. In the physical model and in the analysis of the results, it was considered that aggressive species could easily reach the barrier layer through the open structure of the unsealed pores, which is in parallel with the capacity of the pore walls (GONZÁLEZ et al.; 1999; BOISIER et al. 2008; GARCIA-RUBIO et al., 2010). In the EEC, R_{el} accounts for the electrolyte resistance in the bulk of the solution; $R_{el'}$ corresponds to the electrolyte within the open pore structure and C_{pw} the capacitance of the pore walls; CPE_b represents the capacitive properties of the barrier layer in parallel with the barrier layer resistance (R_b); finally, CPE_{dl} and R_{ct} are ascribed, respectively, to the double layer capacity and the charge transfer resistance, this latter time constant appearing only after longer immersion times. Following the evolution of the system, the EEC display two time constants at the beginning of the exposure period, later they exhibit three time constants, and, for longer exposure time, they exhibit two time constants again. In this latter situation, the system is heavily deteriorated,

and the ac sign does not sense the pore walls anymore, as the conductive pathways through the damaged barrier become much easier.

Figure 5.25 - Physical model associated with the EEC
for the undamaged unsealed AA2524 anodized in TSA.

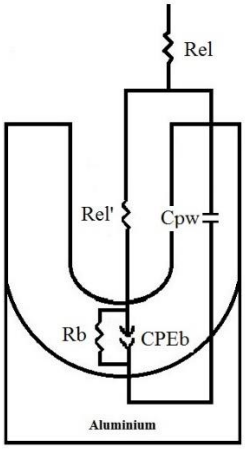

Figure 5.26 - Electrical equivalent circuits used to fit the EIS data of unsealed AA2524 anodized in TSA at 8 V after: (a) 1 h, 6 h, (b) 24 h up to 72 h and (c) 168 h of immersion in 0.1 mol.L^{-1} NaCl solution.

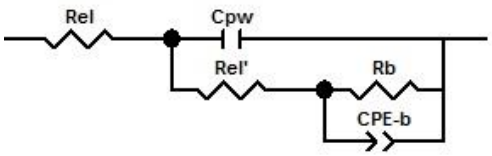

(a) 8 V – unsealed – 1 h, 6 h

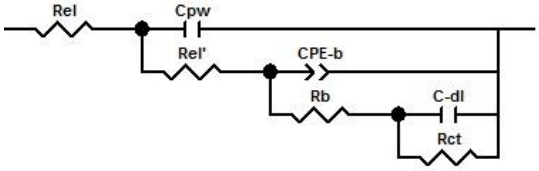

(b) 8 V – unsealed – 24 h, 48 h, 72 h

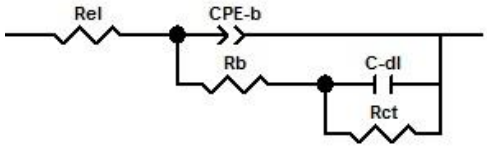

(c) 8 V – unsealed – 168 h

Figure 5.27- Electrical equivalent circuits used to fit the EIS data of unsealed AA2524 anodized in TSA at 10 V after (a) 1 h up to 6 h, (b) 24 h up to 72 h and (c) 168 h of immersion in 0.1 mol.L^{-1} NaCl solution

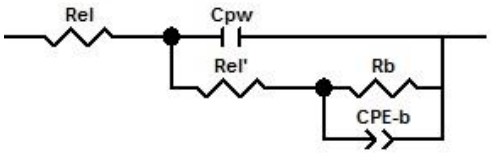

(a) 10 V – unsealed - 1 h, 6 h

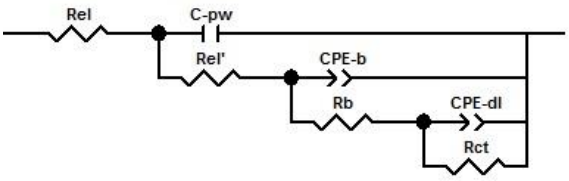

(b) 10 V – unsealed - 24 h, 72 h

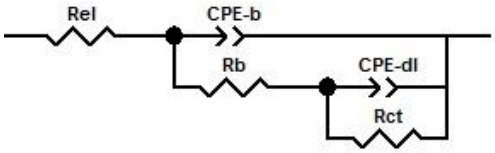

(c) 10 V - unsealed - 168 h

Figure 5.28 - Electrical equivalent circuits used to fit the EIS data of unsealed AA2524 anodized in TSA at 14 V after (a) 1 h (b) 6 h up to 48 h (c) 72 h and (d) 168 h of immersion in 0.1 mol.L^{-1} NaCl solution.

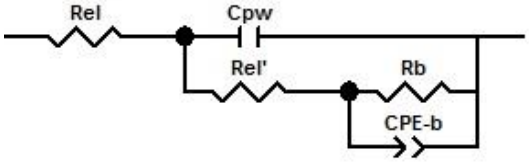

(a) 14 V – unsealed - 1 h

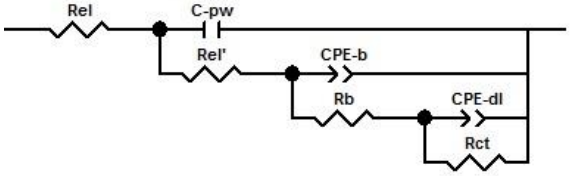

(b) 14 V – unsealed – 6 h, 24 h, 48 h

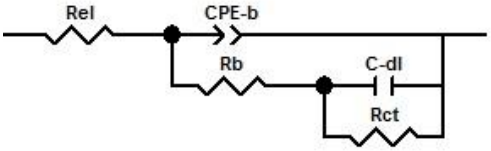

(c) 14 V – unsealed – 72 h

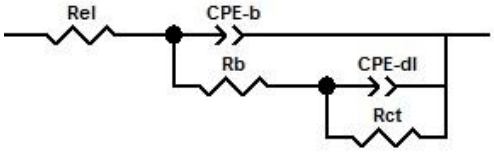

(d) 14 V – unsealed – 168 h

Figure 5.29- Electrical equivalent circuits used to fit the EIS data of unsealed AA2524 anodized in TSA at 16 V after (a) 1 h (b) 6 h (c) 24 h up to 72 h and (d) 168 h of immersion in 0.1 mol.L^{-1} NaCl solution.

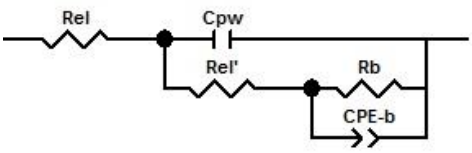

16 V – unsealed – 1 h

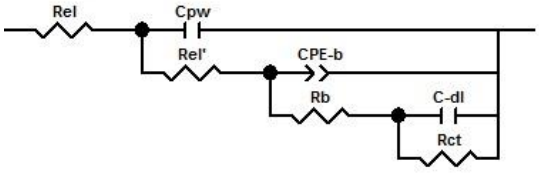

16 V – unsealed – 6 h

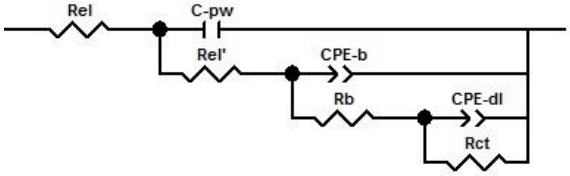

16 V – unsealed – 24 h, 48 h, 72 h

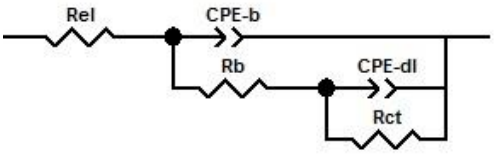

16 V – unsealed – 168 h

Tables 5.3 to 5.6 show the results of the fittings parameters for the EIS diagrams of the unsealed AA2524 samples anodized in TSA at 8 V, 10 V, 14 V and 16 V. Regarding the C_{pw} values, they remain relatively constant and were quite similar for all the samples up to 48 h of test indicating that the porous layer is not strongly deteriorated by the electrolyte. However, for the experiment performed after 72 h, C_{pw} decrease for the samples anodized at 8 V and 10 V and increases for the sample anodized at 16 V, whereas it was no longer detected for the sample anodized at 14 V. In this latter situation, it can be considered that the surfaces must be considerably corroded and that the fitting results must be affected by the presence of surface corrosion products. On the other hand, the comparison between $R_{el'}$ values seems to give a better insight of the deterioration of the corrosion protection afforded by the porous layer produced at different voltages. Initially, irrespectively to the anodizing voltage, they steadily decrease with immersion time indicating easier penetration of the electrolyte in the pores, which can be associated with pores widening due to the corrosion process. In addition, it can be verified that for the first 24 h of test, the lower the anodizing voltage, the higher $R_{el'}$, indicating that electrolyte penetration is more difficult the narrower the pores. This is in accordance with the slower impedance decrease for the samples anodized at lower voltages. For longer immersion periods, even though, in general, $R_{el'}$ remains higher for the samples anodized at lower voltages, an oscillating response was observed, which can be a consequence of the precipitation and dissolution of corrosion products within the confined pore environment. The decrease of R_b and R_{ct} associated to the increase in the values of CPE_b and CPE_{dl} with immersion time confirm the acceleration of the corrosion process at the surface of the electrode.

Table 5.3 - Fitted parameters with the EECs of Figure 5.26 for the EIS diagrams of the unsealed AA2524 anodized in TSA at 8 V.

Immersion time (h)	**C_{pw} ($\mu F.cm^{-2}$)**	**CPE_b ($\mu F.cm^{-2}.s^{(n-1)}$)**	**n_b**	**C_{dl} ($\mu F.cm^{-2}$)**	**$R_{el'}$ ($k\Omega.cm^2$)**	**R_b ($k\Omega.cm^2$)**	**R_{ct} ($k\Omega.cm^2$)**
1	0.79	0.45	0.91		3.56	2.9 x10^3	
6	0.76	0.71	0.87		1.09	1.2 x10^3	
24	0.79	1.65	0.83	9.88	0.80	229.1	187.49
48	0.53	2.82	0.78	61.2	0.06	73.0	32.2
72	0.33	2.36	0.85	67.4	0.07	49.3	34.21
168		7.68	0.75	205		19.7	14.66

Table 5.4 - Fitted parameters with the EECs of Figure 5.27 for the EIS diagrams of the unsealed AA2524 anodized in TSA at 10 V.

Immersion time (h)	C_{pw} ($\mu F.cm^{-2}$)	CPE_b ($\mu F.cm^{-2}.s^{(n-1)}$)	n_b	CPE_{dl} ($\mu F.cm^{-2}.s^{(n-1)}$)	n_{dl}	R_{el}, ($k\Omega.cm^2$)	R_b ($k\Omega.cm^2$)	R_{ct} ($k\Omega.cm^2$)
1	0.57	0.48	0.88			1.21	$8.70x10^3$	
6	0.58	0.76	0.85			0.47	$1.22\ x10^3$	
24	0.61	1.44	0.86	17.9	0.79	0.70	127	173
72	0.06	3.26	0.83	87	0.83	0.035	31.5	31.1
168		7.35	0.84	203	0.77		11.4	19.6

Table 5.5 - Fitted parameters with the EECs of Figure 5.28 for the EIS diagrams of the unsealed AA2524 anodized in TSA at 14 V.

Immersion time (h)	C_{pw} ($\mu F.cm^{-2}$)	CPE_b ($\mu F.cm^{-2}.s^{(n-1)}$)	n_b	CPE_{dl} ($\mu F.cm^{-2}.s^{(n-1)}$)	n_{dl}	C_{dl} ($\mu F.cm^{-2}$)	R_{el}, ($k\Omega.cm^2$)	R_b ($k\Omega.cm^2$)	R_{ct} ($k\Omega.cm^2$)
1	0.45	0.40	0.87				1.10	$9.8x10^3$	
6	0.46	0.78	0.89	3.34	0.92		0.47	232	386
24	0.62	1.68	0.88	131	0.75		0.54	33.6	30.5
48	0.76	4.57	0.76	555	0.98		0.37	28.2	7.68
72		5.29	0.83			553		34.6	11.3
168		16.5	0.91	335	0.83			34.6	29.5

Table 5.6 - Fitted parameters with the EECs of Figure 5.29 for the EIS diagrams of the unsealed AA2524 anodized in TSA at 16 V.

Immersion time (h)	C_{pw} ($\mu F.cm^{-2}$)	CPE_b ($\mu F.cm^{-2}.s^{(n-1)}$)	n_b	CPE_{dl} ($\mu F.cm^{-2}.s^{(n-1)}$)	n_{dl}	C_{dl} ($\mu F.cm^{-2}$)	R_{el}, ($k\Omega.cm^2$)	R_b ($k\Omega.cm^2$)	R_{ct} ($k\Omega.cm^2$)
1	0.37	0.50	0.84				0.74	3600	
6	0.43	1.55	0.87			10.62	0.37	103	89.5
24	0.59	3.81	0.78	165	0.58		0.32	26.9	40.1
48	0.65	7.02	0.71	248	0.81		0.10	24.2	9.29
72	5.54	5.08	0.78	82.0	0.62		0.14	19.0	16.4
168		15.2	0.91	378	0.86			9.29	17.2

5.6.3 EIS of AA2524 anodized in TSA and hydrothermally sealed

Figure 5.30 shows the EIS responses with immersion time in the 0.1 mol.L^{-1} NaCl solution of the AA2524 samples anodized in TSA at 8 V (a), 10 V (b), 14 V (c) and 16 V (d) and hydrothermally sealed (HTSed).

Figure 5.30 - Bode plots as impedance modulus and phase angle after different immersion times in 0.1 mol.L^{-1} NaCl solution of AA2524 samples anodized in TSA and hydrothermally sealed. Anodizing voltages: (a) 8 V, (b) 10 V, (c) 14 V and (d) 16 V.

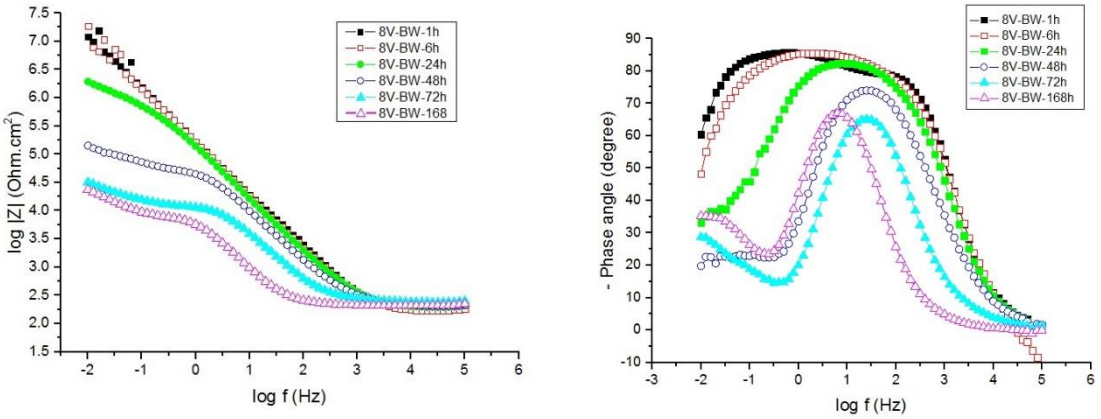

(a) 8 V- hydrothermally sealed

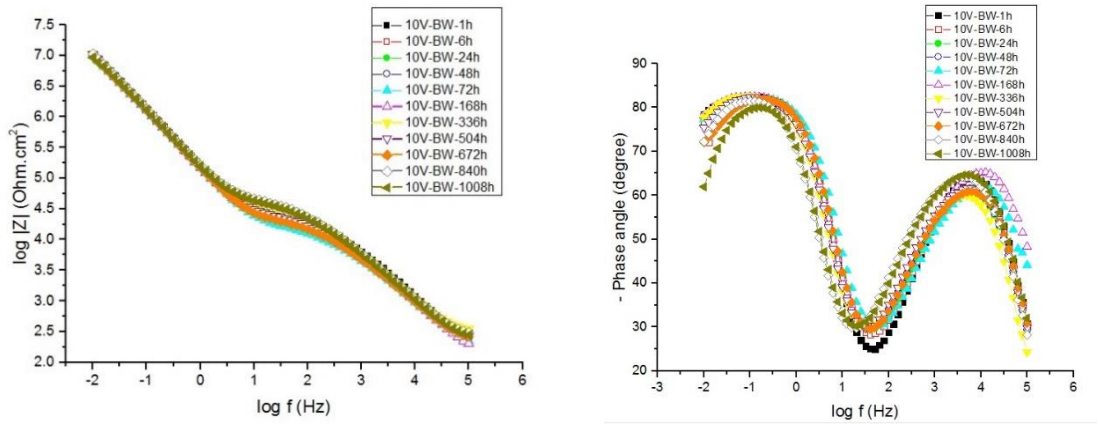

(b) 10 V- hydrothermally sealed

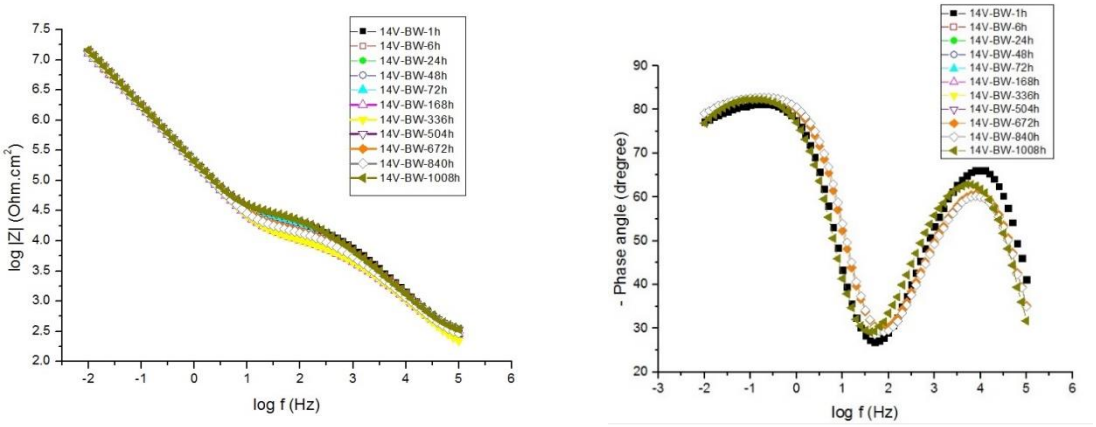

(c) 14 V- hydrothermally sealed

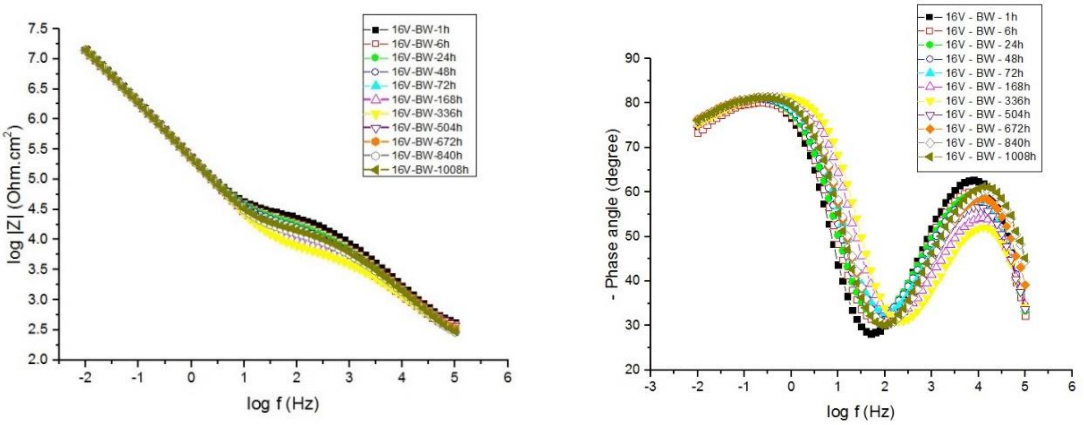

(d) 16 V- hydrothermally sealed

The impedance results obtained for the anodizing voltage of 8 V, Figure 5.30 (a), are very similar to those found for the unsealed samples (Fig. 5.22). Indeed, the impedance modulus drops relatively fast, and it is of the same order of magnitude of those presented in Figure 5.22 after 168 h (7 days) of test. At this time, the experiment was interrupted because the sample surface was completely corroded. Differently from the other anodizing conditions (10 V, 14 V and 16 V), Figure 5.30 (a) shows that the phase angle plot after 1 h of immersion for the HTSed sample anodized at 8 V is composed by a single and wide time constant. Domingues et al. (2003) reported that two time constants, one associated with the barrier layer and the other with the sealed porous layer, could only be clearly distinguished when a perfect sealing process is performed. Gonzalez et al. (1999) have also showed that the better the sealing process the more separated are the time constants associated with the oxide layer properties. Therefore, a poor sealing process seems to take place for this sample.

The SEM micrograph of the sample surface after anodizing at 8 V (Figure 5.10 (a)) shows that the structure of the anodized layer is very defective. Pores are sparsely developed and the anodized layer surface seems to be composed of peaks and valleys. In addition, the structure of the smudge formed after the hydrothermal sealing (Figure 5.13 (a)) seems to be less compact than for the other samples. These two features could allow easy electrolyte penetration explaining the poor anticorrosion behaviour displayed in Figure 5.30 (a). As the experiment proceeds, the diagrams of Figure 5.30 (a) show that the sample rapidly loses the HF capacitive response and a new time constant is developed in the LF domain, concomitantly, the impedance modulus drops.

In the phase angle diagrams presented in Figure 5.30 (b) (c) and (d) is possible to observe two well defined time constants during the whole test period, which lasted 1008 h (42 days). The impedance modulus diagrams also display a MF inclined plateau, which is often associated with the resistance of the sealed porous layer (GONZÁLEZ et al., 1997; LOPEZ et al., 2000). According to classical EIS data interpretation for anodized and sealed aluminium alloys (CAPELOSSI et al., 2014; GONZALEZ et al., 1999; BOISIER et al., 2008), the time constant at HF to medium frequency (MF) is related to the hydrothermally sealed layer (pores plugged by hydrated aluminium oxides), whereas the LF part is attributed to the barrier layer. This latter is the effective responsible for the corrosion resistance of the system (MANSFELD; KENDIG, 1998).

The EIS behaviours of the samples anodized at 10 V, 14 V and 16 V and then HTSed were very similar (Figures 5.30 (b) (c) and (d)). The LF impedance modulus remains quite stable with time and there are some changes in the HF phase angle, ascribed to the plugged pores. In addition, in the MF range of the impedance modulus diagrams there are also slight changes with immersion time. González et al. (1999) published EIS results of pure Al anodized and then HTSed for different times. Their diagrams show that, the longer the sealing time, the higher the impedance modulus in the MF range. Therefore, the changes in this frequency region of the impedance modulus diagrams (Fig. 5.30 (b) (c) and (d)) indicate modifications in the impedance response of the sealed pores. An increase should be associated with the continuation (ageing) of the pore sealing process (GONZALEZ et al., 1999), whereas a decrease represents a deterioration of this particular layer due to aggressive species penetration. However, the overall qualitative analysis indicates that there were not many modifications in the protective properties of these HTSed anodized layers due to the contact with the aggressive electrolyte, pointing to very good stability and anticorrosion performance.

Figure 5.31 shows a comparison between the EIS responses of the HTSed samples anodized at 8 V, 10 V, 14 V and 16 V for selected immersion times: 48 h, 504 h and 1008 h. The EIS diagrams presented in Figure 5.31 (a) clearly show that the sealing failed to close the pores with hydrated alumina for the sample anodized at 8 V, which was completely corroded after 168 h of immersion in the test electrolyte. On the other hand, the remainder of the EIS diagrams grouped in Figure 5.31 show that: the LF impedance moduli are quite similar for the samples anodized at 16 V and 14 V, which are superior to that produced at 10 V; the impedance modulus in the MF is higher for the sample anodized at 10 V, followed by 14 V and 16 V; and that the HF phase angle is more capacitive for the 10 V sample followed by the 14 V and 16 V ones. In the next paragraph, a trial qualitative correlation between these features and the physical structure expected for the hydrothermally sealed anodized layer will be presented.

As already stated, the LF time constant is associated with the barrier layer response, which is the main responsible for the corrosion resistance of the anodizing treatment (CAPELOSSI et al., 2014; GONZALEZ et al., 1999; BOISIER et al., 2008; MANSFELD; KENDIG, 1988). The thickness of this layer increases with the applied anodizing voltage (BREVNOV et al., 2004), hence the thicker layer produced at higher anodizing voltages must exhibit higher corrosion protection, as indicated in the EIS diagrams. On the other hand, the variation of both the MF impedance modulus and the HF phase angle seem to indicate that pores with smaller diameters (Table 5.1) are better sealed and retards the degradation process of the porous layer. Moreover, as the sealing time was equal for all the samples, it is likely that a more thoroughly sealing was achieved for the thinner porous layer, which is the one produced at 10 V.

Figure 5.31 - Comparison between the EIS responses in 0.1 mol.L^{-1} NaCl for AA2524 samples anodized in TSA and hydrothermally sealed: (a) 48 h immersion for anodizing voltages of 8 V, 10 V, 14 V and 16 V; (b) 504 h and (c) 1008 h immersion for anodizing voltages of 10 V, 14 V and 16 V.

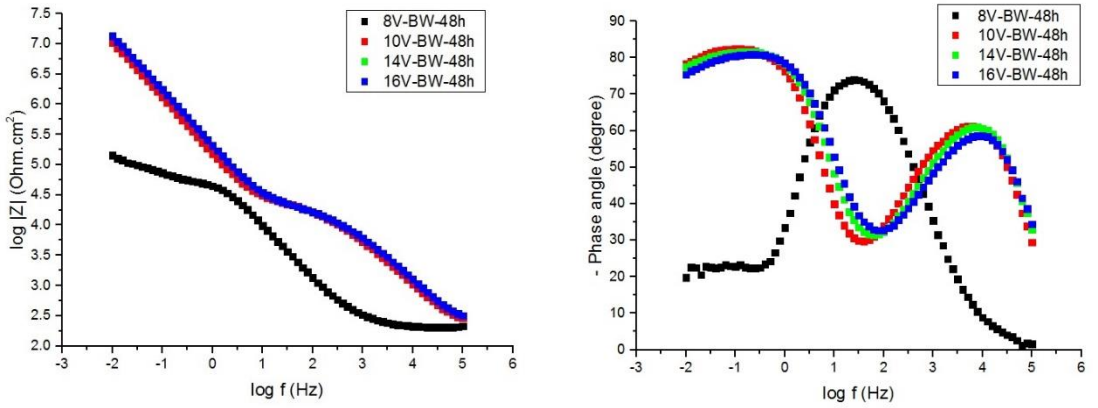

(a) 48 h of immersion time

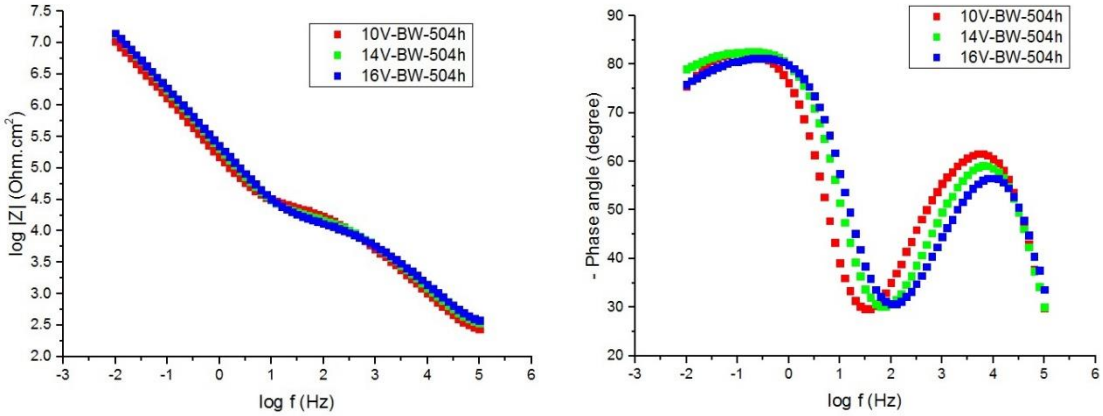

(b) 504 h of immersion time

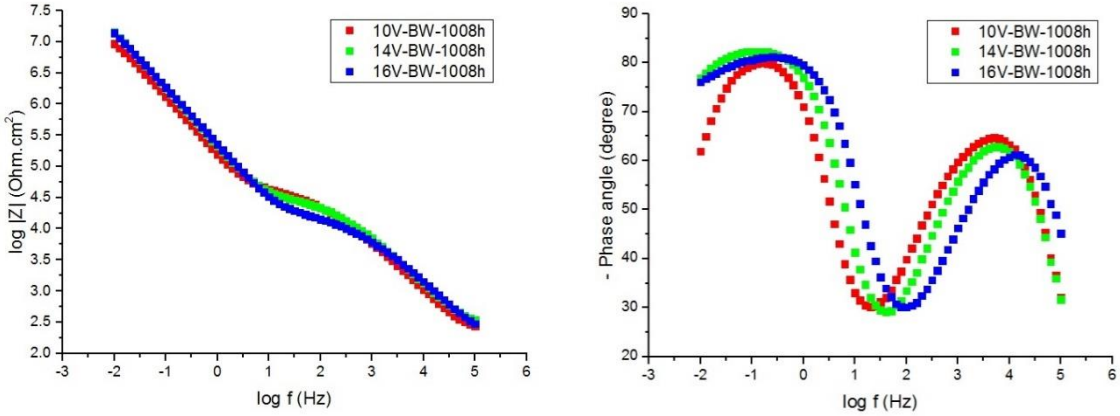

(c) 1008 h of immersion time

Figure 5.32 shows the evolution with immersion time in the test electrolyte of the impedance modulus at 0.01 Hz of HTSed samples of AA2524 anodized in TSA at the different voltages. Ultimately, the anticorrosion properties of a sealed porous layer can be evaluated by the

impedance modulus at LF, once the most important role of the sealing process is to impede the electrolyte to reach the substrate (KITTEL et al., 2003; BIERWAGEN et al., 2003; DUONG et al., 2016), even though it also contributes for increasing the corrosion resistance. From this criterion, the samples anodized at 16 V and 14 V exhibited superior corrosion resistance. The impedance moduli of these two samples are quite similar, but at the end of the test (1008 h), the one anodized at the lower voltage presented a slightly better response.

Figure 5.32 - Evolution with immersion time in 0.1 mol.L-1 NaCl of the impedance modulus at 0.01 Hz of AA2524 anodized in TSA at different voltages and then hydrothermally sealed.

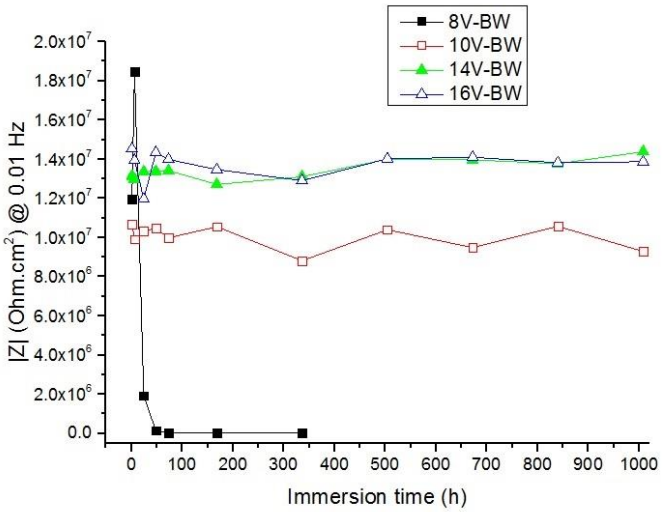

The impedance diagrams of Figure 5.30 were fitted using the EEC presented in Figure 5.33 and 5.34. Due to the different EIS response of the sample anodized at 8 V, for which impedance fast decreased, a different set of EEC, represented in Figure 5.33, was used for this particular sample.

In the EEC of the Figure 5.33(a), R_p represents the resistance of the HTSed pores in parallel with their capacity properties (CPE_p); R_b and CPE_b correspond, respectively, to the barrier layer resistance and its capacitive properties. When the anodic layer starts to deteriorate (6 h), a new time constant at LF, attributed to corrosion development at the interface, was included (Figure 5.33 (b)): C_{dl} (double layer capacitance) in parallel with R_{ct} (charge transfer resistance). It is important to mention that, due to the similarities between this diagram and the one previously acquired (1 h), attempts were made to fit it with a two time constants EEC. However, two main problems arose: the errors involved in the estimation of several passive

elements were too high and their variation in relation to the previous (1 h) and next (24 h) diagrams were not logical and continuous (BONORA; DEFLORIAN; FEDRIZZI, 1996). The use of a three time constants EEC solved these problems. In addition, an improvement in the quality of the phase angle fitting was verified. Similar approach was adopted by Boisier et al. (2009) in their investigation of the corrosion protection of AA2024 sealed anodic layers using the hydrophobic properties of carboxylic acids (BOISIER et al., 2009). Finally, for exposure times higher than 24 h up to the failure of the sample, the sealed porous layer response could not be detected by the impedance measurements, and, therefore, was no longer considered in the physical model presented in Figure 5.33 (c) (GONZÁLEZ et al., 1999; GARCIA-RUBIO et al., 2010; CAPELOSSI et al., 2014; BOISIER et al., 2008). Even considering that the sealed pores must present a much higher protection than the unsealed ones, as for the unsealed samples, the proposed EEC (Fig. 5.33 (c)) consider that the resistive pathways through the damaged sealed porous layer provide an easy pathway for the current to reach the metallic surface.

The EEC used to fit the EIS diagrams for the samples anodized at 10 V, 14 V and 16 V is presented in Figure 5.34 together with the physical model of the sealed pores. The electrolyte resistance is represented by R_{el} and C_{pw} is related to the capacitive response of the pore walls; CPE_p is the constant phase element and R_p the resistance of the HTSed porous layer; CPE_b and R_b are associated with the constant phase element and resistive response of the barrier layer.

Some considerations about this physical model:

- A pore wall resistance (R_{pw}) exists in parallel with the pore wall capacitance (C_{pw}), however, its value is very high and no conductive pathway is developed through this path (HOAR, WOOD, 1962);
- The aggressive electrolyte can only reach the barrier layer through the pores;

For the fitting procedure, the exponent of the CPE_p element, n_p, was fixed to 0.5 in order to minimize the errors and improve the fitting quality. In the literature, this low value has been associated with the complex nature of the boehmite precipitated at the pores mouth and of the aluminium hydroxide precipitated within the pores that present variable in-depth properties that could be better represented by a transmission line model (HOAR and WOOD, 1962, BOISIER et al., 2008). The use of such model to fit the impedance response of the sealed pores would take into account the changes in the properties of the sealing precipitates along its depth (HOAR and WOOD, 1962). However, its use is difficult with commercial software,

unless the values of some of these variable properties are known in advance, so, they can be fixed during the fitting procedure.

Figure 5.33 - Electrical equivalent circuits (EEC) used to fit the EIS data of the AA2524 anodized in TSA at 8 V and then hydrothermally sealed, after: (a) 1 h (b) 6 h and (c) 24 h up to 168 h of immersion in 0.1 mol.L^{-1} NaCl.

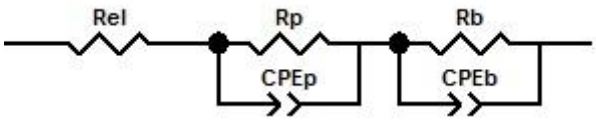

(a) 8 V – hydrothermally sealed - 1 h

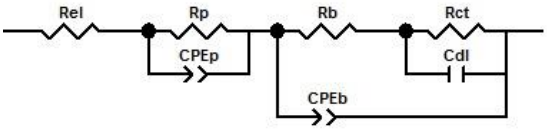

(b) 8 V – hydrothermally sealed – 6 h

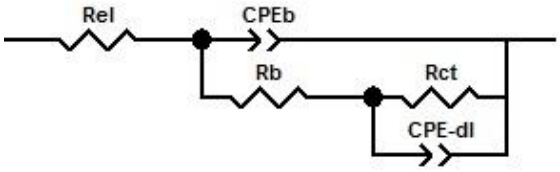

(c) 8 V – hydrothermally sealed – 24h, 48 h, 72 h, 168 h

Figure 5.34 - Electrical equivalent circuit (EEC) used to fit the EIS data of the AA2524 anodized in TSA at 10 V, 14 V and 16 V and hydrothermally sealed associated with the physical model of the interface

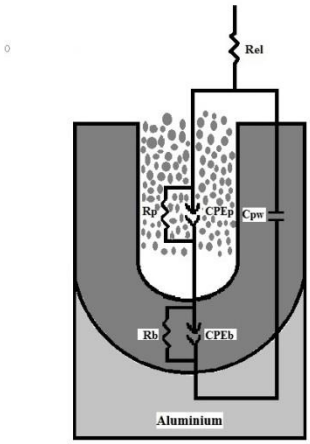

Tables 5.7 to 5.10 present, respectively, the results of the fitting procedure for the AA2524 anodized in TSA at 8 V, 10 V, 14 V and 16 V and then hydrothermally sealed. Due to the different characteristics of its impedance response, the results obtained for the samples anodized at 8 V will be presented and discussed separately.

The R_p values for the samples anodized at 8 V (Table 5.7) fast decrease and the CPE_p values strongly increase up to 6 h of immersion, pointing to fast deterioration of the sealing procedure. Interestingly, the values of CPE_p are very high, explaining why the capacity of the pore walls (C_{pw}) could not be detected for this sample, as the inadequately sealed pores would

constitute a much easier way for the passage of the ac sign. In addition, R_p values were very low compared to those commonly found in the literature (GONZÁLEZ et al., 1999; LÓPEZ et al., 2000; BOISIER et al., 2008) as well as with those reported in tables 5.8 to 5.10. During the whole test period, CPE_b continuously increased, indicating constant barrier layer degradation. However, this process was accelerated from 48 h of immersion, when a great decrease of the impedance modulus was observed (Figure 5.30 (a)). Accordingly, R_b uninterruptedly decreased, with a major drop occurring for the diagram acquired at 48 h. At the interruption of the test, after 168 h, this variable had decreased approximately four orders of magnitude, confirming the deterioration of the protective properties. The increase of C_{dl}//CPE_{dl} and decrease of R_{ct} is a consequence of the acceleration of the corrosion processes occurring at the matrix surface, increasing the unprotected area of the matrix and facilitating the charge transfer reactions.

For the samples anodized at higher voltages (Tables 5.8 to 5.10), due to the good sealing of the pores, C_{pw} could be detected. However, whichever anodizing voltage and immersion time, its value remained almost constant indicating that it is practically not affected by the aggressive medium. Noteworthy is the fact that, for short immersion times, when not much corrosion have occurred, the higher the anodizing voltage the lower C_{pw}, which is in accordance with the relation between the thickness of the porous layer and the applied voltage revealed in Figure 5.12.

Concerning CPE_b variation in Tables 5.8 to 5.10, their values remain almost constant throughout the test time and with an exponent close to 1 (n_b between 0.91 and 0.96). This indicates that the barrier layers behave practically as pure capacitors, and that their properties almost do not change as time elapses. In accordance with the lower anodizing voltage, CPE_b is slightly higher for the sample anodized at 10 V, indicating that it is thinner.

For the samples anodized at 10 V to 16 V, CPE_p initially increases, reaches a peak value and then decreases again. This is accompanied by an inverse tendency of R_p, which initially decreases and then increases again. Such behaviour can be explained by an initial electrolyte penetration within the plugged pores, followed by an ageing process ascribed to morphological changes of the precipitated alumina within the pores (GONZALEZ et al., 1999, 2002) as well as to the precipitation of corrosion products within the confined pores that can contribute to improve pores sealing.

The R_b presents a different response according to the anodizing voltage. For the 10 V sample (Table 5.8), it remains almost constant up to 336 h and then steadily decreases until the end of the experiment. Being thinner than the other barrier layers, it is likely that chloride ions penetrating the sealed porous layer reach the substrate surface starting the corrosion process by undermining the barrier layer properties. The aggressive species will remain trapped underneath the plugged pores and will continue their deleterious action even with the posterior increase of R_p. For the sample anodized at 14 V (Table 5.9), R_b increases up to 840 h and then decreases for the experiment performed after 1008 h. The initial increase in R_b can be ascribed to the precipitation of corrosion products within the confined environment of the pores that does not allow easy diffusion of aggressive species to the barrier layer surface. As this barrier layer is thicker (higher anodizing voltage and lower capacitance), it would be intrinsically more resistant to corrosion than the previous one. Therefore, initiation of the layer attack would be retarded, leading to the reduction of its resistance only after 1008 h (42 days) of exposure. Finally, for the sample anodized at the highest voltage (Table 5.10), R_b presents an oscillating behaviour: it initially increases, than decreases and increases again. The initial increase of R_b values coincides with relatively high values of R_p, indicating low penetration of aggressive species and possibly the precipitation of corrosion products within the pore environment as well as continuation of the sealing process. The decrease of R_b that follows is accompanied by a great reduction of R_p, pointing to faster electrolyte penetration. Consequently, a more aggressive environment would be created at the pores bottom, provoking damages on the anticorrosion properties of the layer, which, nevertheless, seems to be restored, as a new increase in R_p are observed for longer immersion times.

Finalizing this discussion, it must be emphasized that, for the three anodizing conditions (10 V, 14 V and 16 V), R_b remains very high throughout the whole test period, showing that hydrothermal sealing effectively hinder the corrosion process (MANSFELD; KENDIG, 1998). Readers must also have in mind that Al is a passive metal and repassivation of metastable micropits formed at the pores bottom can take place. This can partially explain the recovery of the anticorrosion properties of the barrier layer and the oscillating behaviour of R_b, which, nevertheless always presented values of the same order of magnitude.

Table 5.77 - Fitted parameters with the EEC of Figure 5.33 for the EIS diagrams of AA2524 anodized in TSA at 8 V and then hydrothermally sealed.

Immersion time (h)	CPE_p ($\mu F.cm^{-2}.s^{(n-1)}$)	n_p	CPE_b ($\mu F.cm^{-2}.s^{(n-1)}$)	n_b	C_{dl} ($\mu F.cm^{-2}$)	CPE_{dl} ($\mu F.cm^{-2}.s^{(n-1)}$)	n_{dl}	R_p ($k\Omega.cm^2$)	R_b ($k\Omega.cm^2$)	R_{ct} ($k\Omega.cm^2$)
1	11.0	0.81	1.0	0.96				2.8	$2.8x10^4$	
6	225.1	0.71	1.1	0.96	1.3			0.07	$1.1x10^4$	$5.7x10^3$
24			1.3	0.91		5.3	0.82		$1.1x10^3$	$2.2x10^3$
48			2.6	0.88		56.5	0.80		61	118
72			6.0	0.88		282	0.77		12.7	41
168			22	0.93		412	0.84		8.2	35

Table 5.8 - Fitted parameters with the EEC of Figure 5.34 for the EIS diagrams of AA2524 anodized in TSA at 10 V and then hydrothermally sealed.

Immersion time (h)	C_{pw} ($\mu F.cm^{-2}$)	CPE_p ($\mu F.cm^{-2}.s^{(n-1)}$)	CPE_b ($\mu F.cm^{-2}.s^{(n-1)}$)	n_b	R_p ($k\Omega.cm^2$)	R_b ($M\Omega.cm^2$)
1	$1.12x10^{-2}$	1.01	1.20	0.95	25.93	77.97
6	$1.16x10^{-2}$	1.32	1.21	0.94	25.98	53.68
24	$1.18x10^{-2}$	1.44	1.21	0.94	26.25	71.53
48	$1.17x10^{-2}$	1.39	1.20	0.94	29.50	76.20
72	$1.14x10^{-2}$	1.73	1.24	0.94	20.27	64.72
168	$1.13x10^{-2}$	1.50	1.21	0.95	28.32	75.53
336	$1.20x10^{-2}$	1.35	1.19	0.95	33.10	71.50
504	$1.22x10^{-2}$	1.40	1.20	0.95	31.23	53.05
672	$1.26x10^{-2}$	1.54	1.23	0.94	24.95	35.93
840	$1.24x10^{-2}$	1.11	1.18	0.96	56.30	40.88
1008	$1.23x10^{-2}$	1.18	1.21	0.95	51.03	21.84

Table 5.9 - Fitted parameters with the EEC of Figure 5.34 for the EIS diagrams of AA2524 anodized in TSA at 14 V and then hydrothermally sealed.

Immersion time (h)	C_{pw} ($\mu F.cm^{-2}$)	CPE_p ($\mu F.cm^{-2}.s^{(n-1)}$)	CPE_b ($\mu F.cm^{-2}.s^{(n-1)}$)	n_b	R_p ($k\Omega.cm^2$)	R_b ($M\Omega.cm^2$)
1	$1.09x10^{-2}$	0.72	0.90	0.93	27.80	85.52
6	$1.11x10^{-2}$	0.96	0.91	0.92	25.52	84.75
24	$1.15x10^{-2}$	1.06	0.89	0.93	26.16	99.01
48	$1.17x10^{-2}$	1.12	0.89	0.93	24.44	98.94
72	$1.18x10^{-2}$	1.15	0.89	0.93	23.60	99.88
168	$1.32x10^{-2}$	1.52	0.93	0.93	12.45	83.66
336	$1.33x10^{-2}$	1.45	0.91	0.93	12.31	92.52
504	$1.26x10^{-2}$	1.12	0.88	0.94	20.06	114.30
672	$1.31x10^{-2}$	1.10	0.89	0.94	19.01	118.30
840	$1.39x10^{-2}$	1.09	0.90	0.94	17.20	113.20
1008	$1.2\ x10^{-2}$	0.84	0.87	0.94	33.97	87.40

Table 5.10 - Fitted parameters with the EEC of Figure 5.34 for the EIS diagrams of AA2524 anodized in TSA at 16 V and then hydrothermally sealed.

Immersion time (h)	C_{pw} ($\mu F.cm^{-2}$)	CPE_p ($\mu F.cm^{-2}.s^{(n-1)}$)	CPE_b ($\mu F.cm^{-2}.s^{(n-1)}$)	n_b	R_p ($k\Omega.cm^2$)	R_b ($M\Omega.cm^2$)
1	$8.87x10^{-3}$	0.71	0.79	0.92	32.63	79.05
6	$9.55x10^{-3}$	0.95	0.80	0.91	27.26	70.81
24	$9.93x10^{-3}$	1.08	0.79	0.92	25.18	89.88
48	$1.02x10^{-2}$	1.19	0.80	0.92	21.99	89.99
72	$1.05x10^{-2}$	1.33	0.82	0.91	17.45	85.07
168	$1.15x10^{-2}$	1.60	0.84	0.91	10.55	76.70
336	$1.25x10^{-2}$	1.68	0.86	0.92	7.61	71.47
504	$1.03x10^{-2}$	1.19	0.82	0.92	15.97	86.93
672	$1.03x10^{-2}$	1.17	0.82	0.92	15.88	90.75
840	$1.05x10^{-2}$	1.18	0.83	0.92	15.16	86.05
1008	$1.02x10^{-2}$	1.08	0.83	0.92	17.83	86.08

Figure 5.35 shows a comparison between the fitted parameters for the AA2524 anodized in TSA at 10 V, 14 V and 16 V and then hydrothermally sealed. Figure 5.35 (a) shows that the pore resistance (R_p) of the sample anodized at 10 V is higher, followed by 14 V and 16 V. This indicates that aluminium hydroxide precipitation is more effective and/or more compact in narrower pores. The differences between the porous layer thicknesses of the samples can

also play a role, as the sealing process can be more effective for the thinner layer (produced at 10 V), considering that the sealing time was the same for all the samples. This is in accordance with the qualitative evaluation of the diagrams of Figure 5.31 previously presented.

Concerning the constant phase element associated with the porous layer (CPE_p) (Fig. 5.35 (b)) the values are very similar for the three samples, indicating similar variation of properties along the depth of the plugged pores.

The barrier layer resistance (R_b) (Fig 5.35 (c)) is clearly lower for the sample anodized at 10 V. This feature must be a consequence of the lower thickness of this layer for this particular sample. On the other hand, the layer produced at 14 V clearly show a better overall behaviour, even though the capacity determination (Figure 5.35 (d)) indicates that it is slightly thinner than the layer produced at 16 V. This can be a deleterious consequence of the higher quantity of SO_4^{2-} ions in the porous layer structure of this latter sample that would counterbalance the beneficial effect of its higher thickness.

The CPE_b values (Figure 5.35 (d)) are very stable with time. In accordance with the well-documented dependence of the barrier layer thickness with the applied potential (BOGDANOV et al., 1990; BREVNOV et al., 2004; PATERMARAKIS; PLYTAS, 2016), the higher the applied anodizing voltage the lower the capacity value, i.e., the thicker the layer. As the CPE_b exponents were close to 1, the estimates of this parameter were used to determine the thickness of the barrier layer (Table 5.11) using Equation 5.4, where the dielectric permittivity of vacuum is $\mathcal{E}_0 = 8.854 \times 10^{-14}$ F. cm^{-1} and the relative dielectric constant of alumina was considered to be $\mathcal{E}_r = 10$ (BOISIER et al., 2008; CAPELOSSI et al., 2014). The exposed surface area S = 7.07 cm^2 was not considered in the calculation as the presented impedance data is area averaged.

$$C = \mathcal{E}_0 \mathcal{E}_r / e \qquad (5.4)$$

Considering that the literature states that the thickness of the barrier layer increases 1.0 to 1.5 nm per applied volt (BOGDANOV et al., 1990; BREVNOV et al., 2004) and taking into account that the samples were exposed to 40 min immersion in boiling water, the calculated values seem underestimated when compared to theoretical ones. The hydrothermal sealing treatment may produce a more hydrated barrier layer. Consequently, a value higher than 10 for the dielectric constant of alumina ($\mathcal{E}_r$) should have be used in the calculations. For this reason, the barrier layer thicknesses presented in Table 5.11 may be underestimated.

The global analysis of the results of this section indicates that the HTSed AAO produced at anodizing voltages higher than 10 V can be an effective barrier against corrosion of AA2524. From the investigated voltages, 14 V exhibited the best anticorrosion properties, demonstrating, thus, that a compromise must be found between the pore structure and the barrier layer thickness. The former will guarantee a better sealing of the pores during the hydrothermal treatment, whereas the latter will sustain the effective corrosion resistance, which for a better performance depends on the hindrance of aggressive species access.

Figure 5.35 - Variation of (a) R_p, (b) CPE_p, (c) R_b and (d) CPE_b with immersion time in 0.1 mol.L^{-1} NaCl for AA2524 anodized in TSA at 10 V, 14 V and 16 V and then hydrothermally sealed.

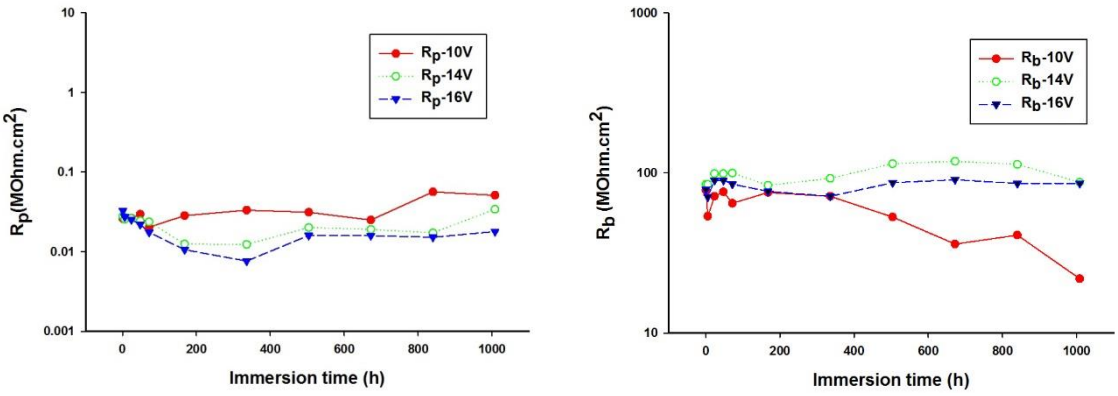

(a) (c)

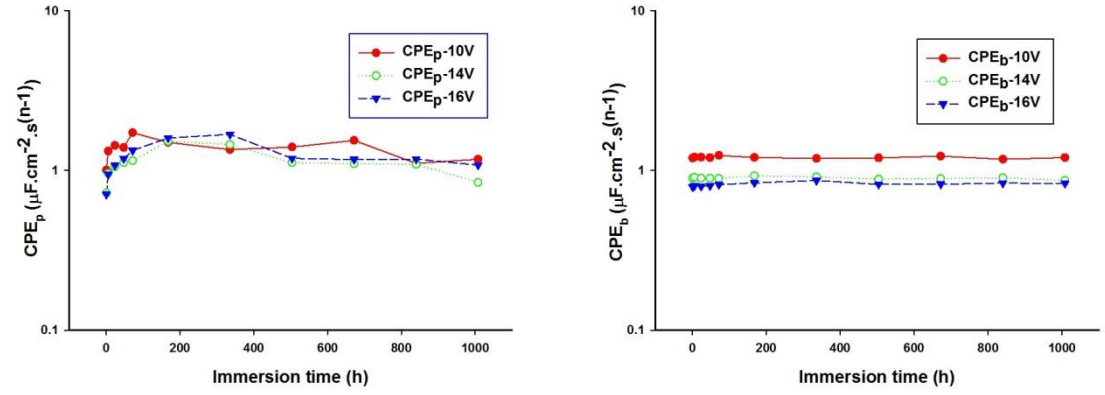

(b) (d)

Table 5.11- Barrier layer thicknesses determined with Eq. 5.4 using the CPE_b values from the fitting procedure presented in Tables 5-8 to 5-10.

	Thickness of the barrier layer (nm) hydrothermally sealed samples		
Immersion time (h)	**10 V**	**14 V**	**16 V**
1	7.40	9.87	11.24
6	7.30	9.77	11.06
24	7.32	9.90	11.15
48	7.36	9.90	11.04
72	7.13	9.93	10.86
168	7.33	9.57	10.58
336	7.45	9.69	10.25
504	7.38	10.03	10.81
672	7.20	9.95	10.79
840	7.52	9.83	10.64
1008	7.35	10.20	10.68

5.6.4 EIS of AA2524 anodized in TSA and coated with the hybrid sol-gel

Figure 5.36 shows the EIS responses with immersion time in the 0.1 $mol.L^{-1}$ NaCl test solution of the AA2524 anodized in TSA and coated with the hybrid sol-gel. Anodizing treatments were performed at 8 V (a), 10 V (b), 14 V (c) and 16 V (d). All phase angle plots present two well-defined time constants during the whole test period: 1008 h (42 days). The HF and LF time constants can be attributed, respectively, to the sol-gel coating within the pores and to the barrier layer response (CAPELOSSI et al., 2014). The diagrams also show that the LF impedance modulus remained relatively constant. However, modifications occurred with immersion time both in the MF range of the impedance modulus diagram, that diminishes, and in the phase angle plots, that show frequency and phase shifts. The former feature points to a deterioration of the protective properties afforded by the "sol-gel plugged" porous layer (GONZÁLEZ et al., 1999), likely associated with the increase in the number of conductive pathways through the hybrid coating, and can be straightforward associated with the diminution of the resistance within the pores (GONZÁLEZ et al., 1997; LOPEZ et al., 2000). On the other hand, the latter indicates an acceleration of the kinetics of the interfacial process (LF phase angle displaced to HF) and water and ions uptake by the coating (diminution of the HF capacitive response) (BONORA; DEFLORIAN; FEDRIZZI, 1996).

Figure 5.36 - Bode plots as impedance modulus and phase angle after different immersion times in 0.1 mol.L^{-1} NaCl for AA2524 anodized in TSA and coated with sol-gel. Anodizing voltages: (a) 8 V (b) 10 V (c) 14 V and (d) 16 V.

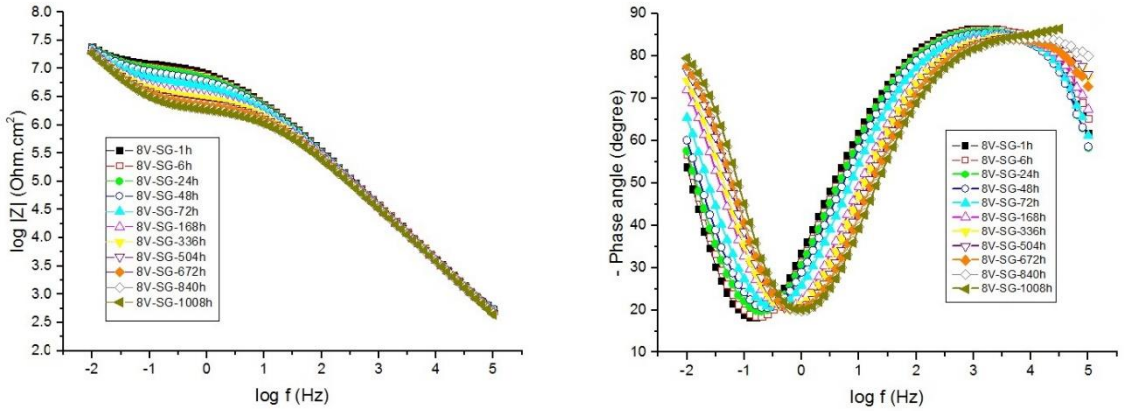

(a) 8 V – coated with sol-gel

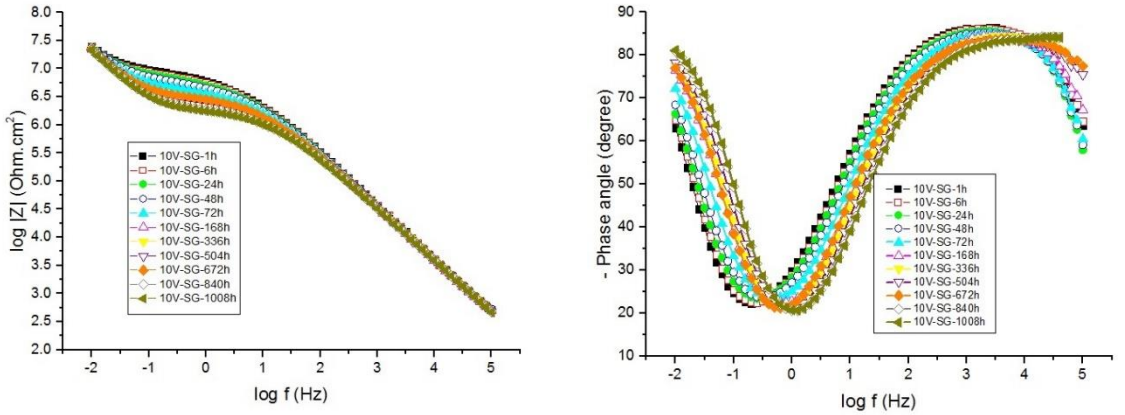

(b) 10 V – coated with sol-gel

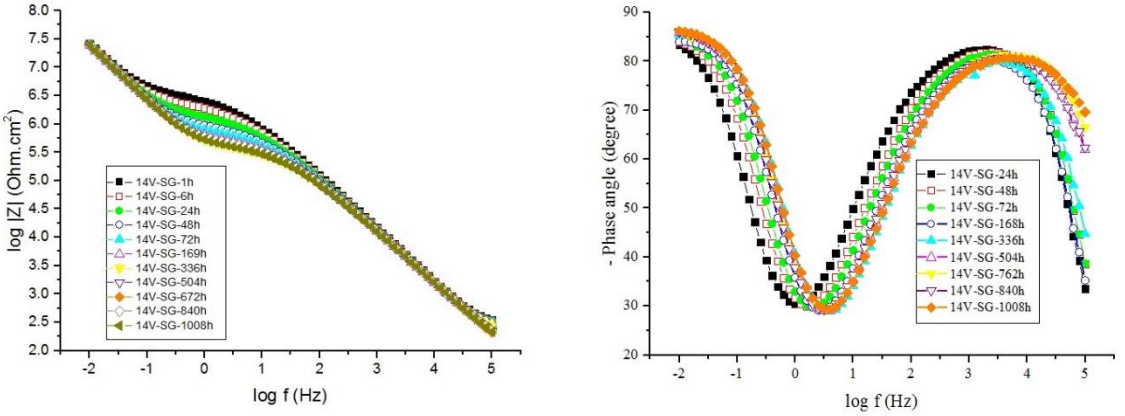

(c) 14 V – coated with sol-gel

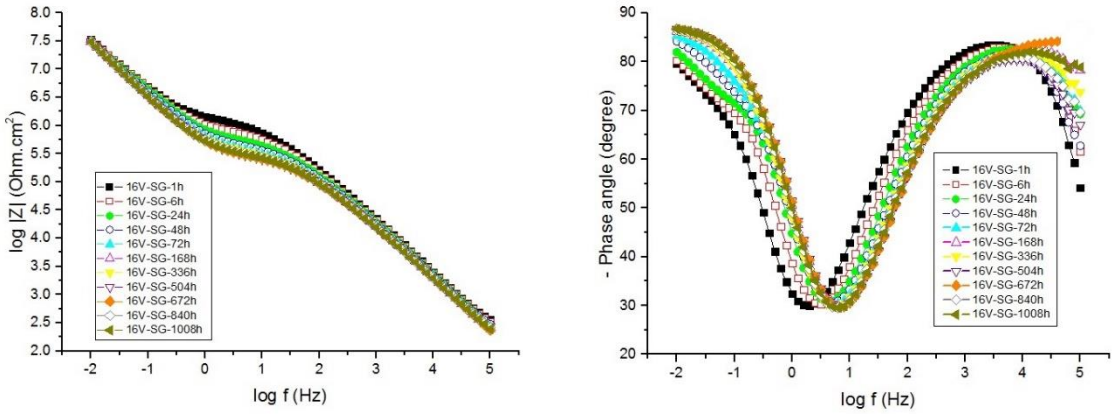

(d) 16 V – coated with sol-gel

Figure 5.37 shows a comparison between the EIS responses of hybrid coated samples anodized at 8 V, 10 V, 14 V and 16 V for selected immersion times: 48 h, 504 h and 1008 h. Considering the poor definition of the LF time constant for all the samples, the comparison based in the LF impedance modulus is just a tendency and cannot be unequivocally associated with the real corrosion behaviour for the barrier layer. Nevertheless, for all immersion times, the impedance modulus in the MF range is higher and the HF phase angle is more capacitive for the samples anodized at the lowest voltages (8 V and 10 V), indicating better anticorrosion behaviour, i.e., this ensemble blocks more effectively the penetration of the electrolyte and aggressive species that could reach the barrier layer (LF time constant) (GONZÁLEZ et al., 1999). This might be a consequence of the full penetration of the sol-gel solution within the pores for the samples anodized at these lowest voltages, as demonstrated by the GDOES measurements (Figure 5.17).

Figure 5.37 - Comparison between the EIS responses at the same immersion time for AA2524 anodized at different voltages in TSA and coated with the hybrid sol-gel. Test time: (a) 48 h, (b) 504 h and (c) 1008 h of immersion in NaCl 0.1 mol.L^{-1}.

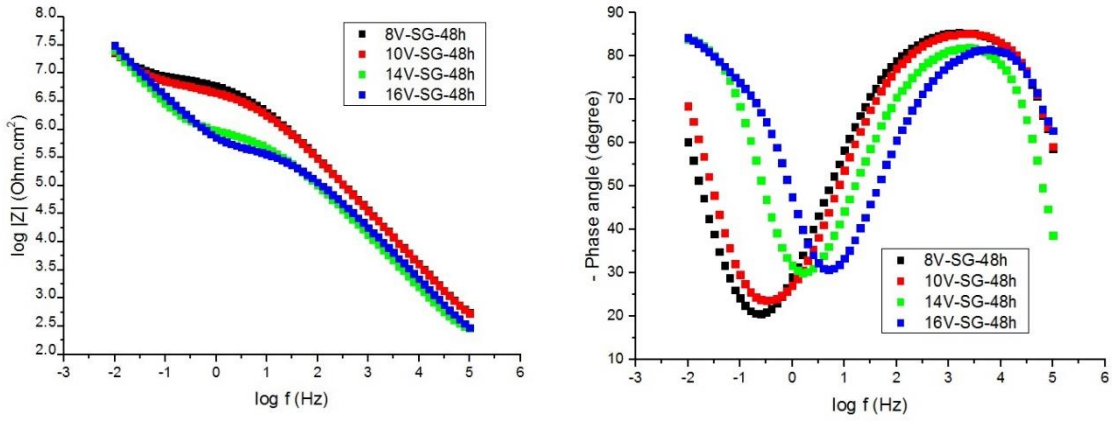

(a) 48 h of immersion

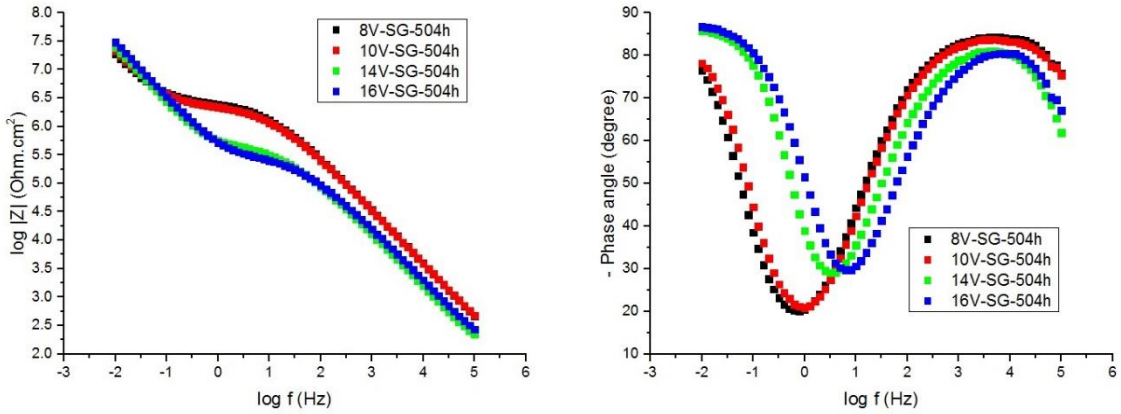

(b) 504 h of immersion

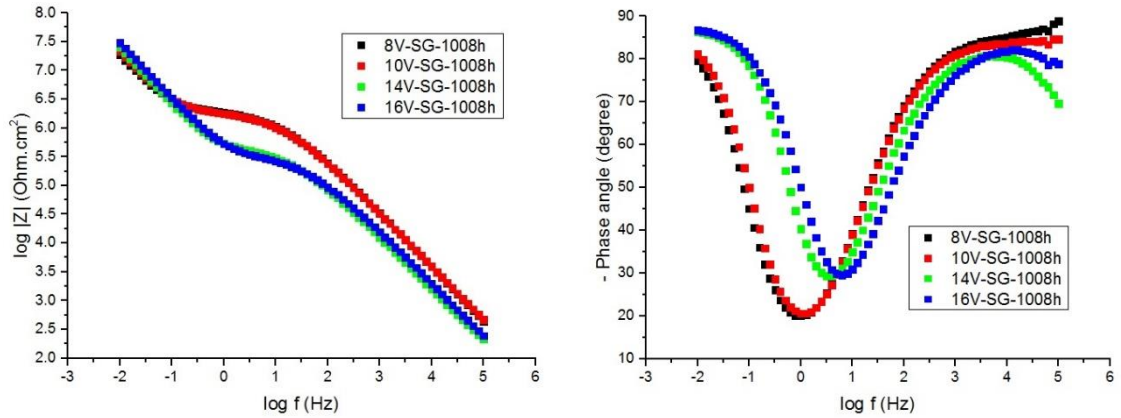

(c) 1008 h of immersion

Figure 5.38 displays the evolution with immersion time in the test electrolyte of the impedance modulus at 0.01 Hz for AA2524 anodized in TSA at different voltages and coated with the hybrid sol-gel. Regardless the immersion time, the LF impedance modulus increases

with anodizing voltage, indicating better overall impedance behaviour for the sample anodized at 16 V. However, the analysis of the LF frequency part of the impedance diagrams is severely impaired by the poor definition of the LF time constant, particularly for the samples anodized at lower voltages. Therefore, a more accurate analysis is necessary in order to determine which system presents the best anticorrosion performance.

Figure 5.38 - Evolution with immersion time in 0.1 mol.L^{-1} NaCl of the impedance modulus at 0.01 Hz for AA2524 anodized in TSA at different voltages and coated with sol-gel.

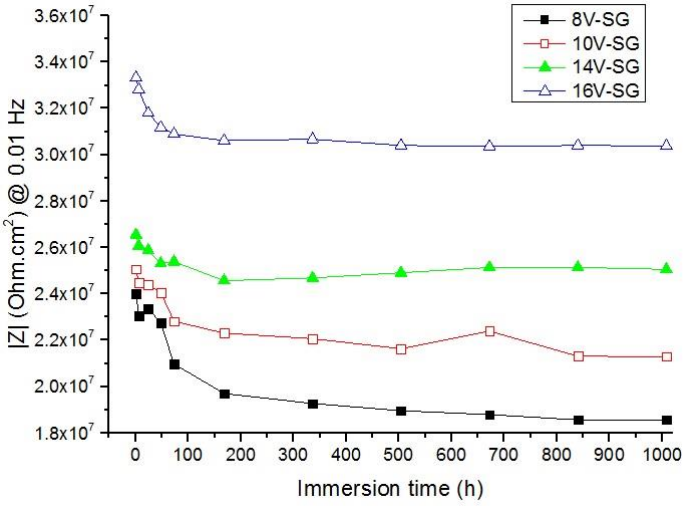

The impedance diagrams of Figure 5.36 were fitted with the EEC presented in Figure 5.39. In the physical model the electrolyte resistance is represented by R_{el} and CPE_{pw} accounts for the constant phase element response of the pore walls. $CPE_{sg}//R_{sg}$ is attributed to the response of the pores filled with the sol gel coating and CPE_b is assigned to the response of the barrier layer. R_b could not be estimated as the time constant of this process is below the lowest frequency used in this experiment, and only few points were available for its definition. Therefore, any tentative of fitting resulted in extremely high resistance values associated with elevated errors. As for the fitting of the HTSed samples, the exponent of the CPE_{SG} element, n_{SG}, was fixed at 0.5 in order to minimize the errors. The reason for this is possibly the inhomogeneous properties of the sol-gel coating with pore depth (HOAR, WOOD, 1962) requiring for a good fit the use of a transmission line. This procedure has already been used by Capelossi et al. (2014) to fit the impedance data of sol-gel coated TSA anodized clad AA2024.

Figure 5.39 - Electrical equivalent circuit used to fit the EIS data of the AA2524 anodized in TSA and coated with the hybrid sol-gel associated with the physical model of the interface

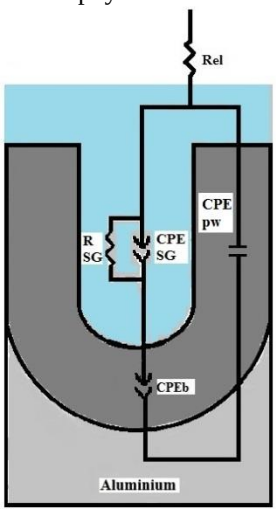

Tables 5.12 to 5.15 present the results of the fitting procedure of the EIS diagrams of Figure 5.36 with the EEC of Figure 5.39. For the four samples, CPE_{SG} gradually increases with immersion time pointing either to water uptake or to a thinning of the hybrid coating (DONLEY et al., 2003; WANG; AKID, 2007). As it had already been foreseen from the qualitative analysis of the EIS diagrams (Figure 5.36), the resistances of the hybrid sol-gel layer, R_{SG}, steadily decrease for the whole samples sets, indicating that electrolyte penetration becomes easier (DEFLORIAN; ROSSI; FEDRIZZI, 2006; CAPELOSSI et al., 2014). However, the R_{SG} values remain relatively high, in the order of $M\Omega.cm^2$, indicating that the electrolyte penetration through the sol-gel coating is really hindered. This helps to explain why R_b definition for these samples is below the frequency range investigated in the present work.

The CPE_b remained fairly constant during the whole experiment, indicating that the layer properties are not changed. The exponents of the CPE_b were close to one (n_b between 0.88 and 0.97), showing that it behaves almost like an ideal capacitor. Finally, the CPE_{pw} values are quite stable, and, for all the fittings, the CPE exponent (n_{pw}) varied between 0.93 and 0.99, indicating an almost capacitive behaviour. Interestingly, the presence of the sol-gel coating seems to contribute for the frequency dispersion of this element, that deviate from the ideal behaviour determined for the HTSed samples.

Table 5.12 - Fitted parameters values for the EIS diagrams of the AA2524 anodized in TSA at 8 V and coated with the hybrid sol-gel.

Immersion time (h)	**CPE_{pw} ($\mu F.cm^{-2}.s^{(n-1)}$)**	**n_{pw}**	**CPE_{SG} ($\mu F.cm^{-2}.s^{(n-1)}$)**	**CPE_b ($\mu F.cm^{-2}.s^{(n-1)}$)**	**n_b**	**R_{SG} ($M\Omega.cm^2$)**
1	$4.49x10^{-3}$	0.98	$2.13x10^{-2}$	0.78	0.97	13.98
6	$4.63x10^{-3}$	0.98	$2.22x10^{-2}$	0.74	0.95	11.88
24	$4.80x10^{-3}$	0.98	$2.32x10^{-2}$	0.64	0.92	10.82
48	$4.99x10^{-3}$	0.98	$2.52x10^{-2}$	0.60	0.90	9.07
72	$5.11x10^{-3}$	0.98	$2.89x10^{-2}$	0.62	0.90	6.66
168	$5.42x10^{-3}$	0.97	$3.41x10^{-2}$	0.65	0.91	4.32
336	$5.70x10^{-3}$	0.97	$3.58x10^{-2}$	0.68	0.92	3.66
504	$5.82x10^{-3}$	0.96	$3.94x10^{-2}$	0.70	0.93	3.01
672	$5.96x10^{-3}$	0.96	$4.15x10^{-2}$	0.71	0.93	2.67
840	$6.05x10^{-3}$	0.96	$4.60x10^{-2}$	0.73	0.94	2.22
1008	$4.97x10^{-3}$	0.98	$5.54x10^{-2}$	0.76	0.95	2.26

Table 5.13 - Fitted parameters values for the EIS diagrams of the AA2524 anodized in TSA at 10 V and coated with the hybrid sol-gel.

Immersion time (h)	**CPE_{pw} ($\mu F.cm^{-2}.s^{(n-1)}$)**	**n_{pw}**	**CPE_{SG} ($\mu F.cm^{-2}.s^{(n-1)}$)**	**CPE_b ($\mu F.cm^{-2}.s^{(n-1)}$)**	**n_b**	**R_{SG} ($M\Omega.cm^2$)**
1	$4.24x10^{-3}$	0.99	$2.76x10^{-2}$	0.59	0.92	9.91
6	$4.38x10^{-3}$	0.99	$2.84x10^{-2}$	0.59	0.92	8.80
24	$4.53x10^{-3}$	0.99	$3.06x10^{-2}$	0.55	0.91	7.79
48	$4.77x10^{-3}$	0.98	$3.21x10^{-2}$	0.55	0.90	6.66
72	$4.92x10^{-3}$	0.98	$3.62x10^{-2}$	0.57	0.91	4.98
168	$5.44x10^{-3}$	0.97	$3.99x10^{-2}$	0.59	0.92	3.43
336	$5.91x10^{-3}$	0.96	$3.96x10^{-2}$	0.61	0.93	3.04
504	$6.27x10^{-3}$	0.96	$4.09x10^{-2}$	0.61	0.93	2.57
672	$6.32x10^{-3}$	0.96	$3.50x10^{-2}$	0.61	0.94	3.52
840	$6.69x10^{-3}$	0.95	$4.49x10^{-2}$	0.65	0.95	2.10
1008	$6.71x10^{-3}$	0.95	$4.61x10^{-2}$	0.65	0.95	2.04

Table 5.14 - Fitted parameters values for the EIS diagrams of the AA2524 anodized in TSA at 14 V and coated with the hybrid sol-gel.

Immersion time (h)	CPE_{pw} ($\mu F.cm^{-2}.s^{(n-1)}$)	n_{pw}	CPE_{SG} ($\mu F.cm^{-2}.s^{(n-1)}$)	CPE_b ($\mu F.cm^{-2}.s^{(n-1)}$)	n_b	R_{SG} ($M\Omega.cm^2$)
1	$1.23x10^{-2}$	0.98	$6.14x10^{-2}$	0.55	0.96	3.89
6	$1.28x10^{-2}$	0.97	$7.85x10^{-2}$	0.55	0.96	2.77
24	$1.38x10^{-2}$	0.97	$9.48x10^{-2}$	0.55	0.96	1.72
48	$1.42x10^{-2}$	0.97	$1.16x10^{-1}$	0.57	0.96	1.09
72	$1.47x10^{-2}$	0.96	$1.26x10^{-1}$	0.57	0.97	0.87
168	$1.59x10^{-2}$	0.96	$1.36x10^{-1}$	0.58	0.96	0.64
336	$1.73x10^{-2}$	0.95	$1.50x10^{-1}$	0.58	0.97	0.46
504	$1.79x10^{-2}$	0.94	$1.38x10^{-1}$	0.57	0.97	0.52
672	$1.79x10^{-2}$	0.94	$1.37x10^{-1}$	0.57	0.97	0.55
840	$1.86x10^{-2}$	0.94	$1.33x10^{-1}$	0.57	0.97	0.56
1008	$1.96x10^{-2}$	0.93	$1.39x10^{-1}$	0.57	0.97	0.49

Table 5.15 - Fitted parameters values for the EIS diagrams of the AA2524 anodized in TSA at 16 V and coated with the hybrid sol-gel.

Immersion time (h)	CPE_{pw} ($\mu F.cm^{-2}.s^{(n-1)}$)	n_{pw}	CPE_{SG} ($\mu F.cm^{-2}.s^{(n-1)}$)	CPE_b ($\mu F.cm^{-2}.s^{(n-1)}$)	n_b	R_{SG} ($M\Omega.cm^2$)
1	$8.79x10^{-3}$	0.97	$6.80x10^{-2}$	0.34	0.89	1.47
6	$9.96x10^{-3}$	0.96	$7.74x10^{-2}$	0.34	0.88	0.91
24	$1.09x10^{-2}$	0.95	$9.37x10^{-2}$	0.35	0.88	0.63
48	$1.14x10^{-2}$	0.95	$1.18x10^{-1}$	0.39	0.91	0.52
72	$1.17x10^{-2}$	0.95	$1.36x10^{-1}$	0.41	0.92	0.45
168	$1.16x10^{-2}$	0.96	$1.63x10^{-1}$	0.45	0.95	0.40
336	$1.23x10^{-2}$	0.95	$1.51x10^{-1}$	0.45	0.95	0.44
504	$1.32x10^{-2}$	0.95	$1.63x10^{-1}$	0.46	0.96	0.36
672	$1.29x10^{-2}$	0.95	$1.66x10^{-1}$	0.46	0.96	0.36
840	$1.33x10^{-2}$	0.95	$1.54x10^{-1}$	0.46	0.96	0.40
1008	$1.35x10^{-2}$	0.95	$1.58x10^{-1}$	0.46	0.96	0.38

Figure 5.40 displays a comparison between the relevant fitted parameters for the AA2524 substrate anodized in TSA at the different voltages and coated with the hybrid sol-gel. Figure 5.40 (a) shows that the resistances of the hybrid sol-gel layer (R_{SG}) are higher for the samples anodized at 8 V or 10 V than for the samples anodized at 14 V or 16 V, indicating better anticorrosion performance for the formers. This is in agreement with the SEM micrographs

(Fig. 5.14), that show a more homogeneous sol-gel layer coverage for these two samples and with the GDOES (Figure 5.17) determinations that indicate more effective sol-gel penetration into the pores for the samples anodized at lower voltages. Moreover, the CPE associated with the hybrid sol-gel layer (CPE_{SG}) (Fig. 5.40 (b)) the samples anodized at 8 V or 10 V pointing that the properties of these coatings are different from those applied on the samples anodized at 14 V and 16 V. The interpretation of these results is difficult to clarify because they are influenced by many parameters: hybrid sol-gel coverage, thickness of the sealed porous layer, transmission line behaviour and water uptake.

Finally, CPE_b remained fairly constant during the whole experiment; nevertheless, a close correlation exists between their values and the anodizing voltage. The samples produced with the lower anodizing voltage present higher CPE_b values, indicating thinner barrier layer, conversely, increasing the anodizing voltage provokes a decrease in the layer capacity, which is a consequence of its higher thickness (LEE; PARK, 2014; WOOD; O'SULLIVAN, 1970).

As for the HTSed samples, the barrier layer thicknesses for the samples coated with the sol gel was estimated from the fitting procedure using equation 5.4. The calculated values are presented in Table 5.16. In accordance with the correlation of the barrier layer thickness and the anodizing voltage, the layer was thicker the higher the anodizing voltage. A good correlation exists between the calculated and the theoretical values (BOGDANOV et al., 1990; BREVNOV et al., 2004). Except for the sample anodized at 16 V, the estimated barrier layer thicknesses remain fairly constant, indicating that the sol-gel coating is efficient in its role of hindering aggressive species to reach the interface. Moreover, the estimated thicknesses were much higher than those calculated for the HTSed samples, Table 5.11. This indicates that, indeed, the dielectric constant of the barrier layer must be increased during the HTS process, as we do not believe in its thinning due to immersion of the sample in the boiling hot water.

Figure 5.40 - Variation with immersion time in NaCl 0.1 mol.L^{-1} of the relevant passive elements parameters obtained from the fitting of impedance diagrams of AA2524 anodized in TSA at different voltages and coated with the hybrid sol-gel with the EEC of Figure 5.39: (a) R_{SG}, (b) CPE_{SG}, (c) CPE_b.

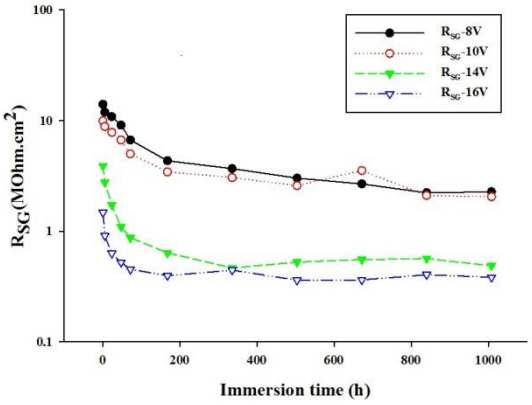

(a)

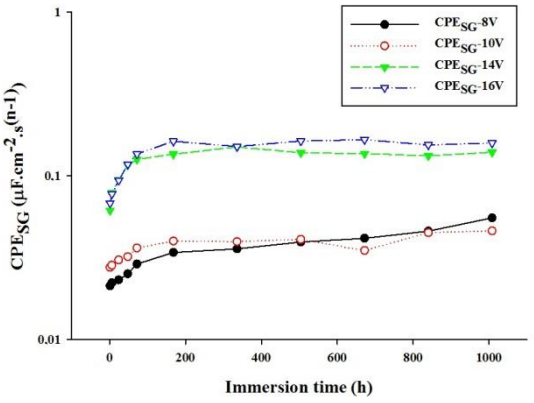

(b)

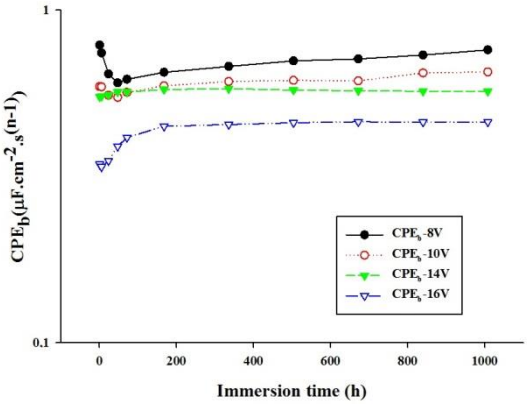

(c)

Table 5.16 - Barrier layer thicknesses determined with Eq. 5.4 using the CPE_b values from the fitting procedure presented in Tables 5-13 to 5-16.

	Thickness of the barrier layer (nm) Sealed with SG			
Immersion time (h)	**8 V**	**10 V**	**14 V**	**16 V**
1	11.29	15.05	16.14	25.77
6	11.93	15.08	16.09	26.24
24	13.78	15.98	15.95	25.15
48	14.68	16.23	15.62	22.76
72	14.30	15.67	15.64	21.41
168	13.64	14.98	15.36	19.82
336	13.09	14.53	15.27	19.58
504	12.60	14.42	15.42	19.33
672	12.43	14.47	15.49	19.21
840	12.10	13.70	15.55	19.26
1008	11.68	13.60	15.55	19.21

For the sol-gel coated samples, it is important to note that the samples anodized at 16 V and 14 V present better overall corrosion resistance. This is indicated by the LF impedance modulus in Figure 5.38 and by the lower CPE_b values in Figure 5.40 (c), even though the resistances of the hybrid sol-gel layer (R_{SG}) were higher for the samples anodized at 8 V or 10 V (Fig. 5.40 (a)). This indicates that the sol-gel present inside the pores is able to avoid aggressive species penetration protecting the barrier layer. The fitting results also highlighted that this latter effectively plays an important role against corrosion, as already stated by Mansfeld et al. (1988), thus, the best anticorrosion performance was found for the samples with the thicker barrier layer, even considering that pore sealing by the sol-gel hybrid coating did not presented the best results, as demonstrated both by the fitting procedure and by the microstructural characterization (SEM and GDOES).

5.6.5 Comparison between the EIS behaviour of AA2524 samples anodized in TSA and hydrothermally sealed or coated with the hybrid sol-gel

Figures 5.41 and 5.42 show, respectively, the comparison of the EIS behaviour after 48 h and 1008 h of immersion in 0.1 $mol.L^{-1}$ NaCl, for AA2524 anodized in TSA at 8 V (a), 10 V (b), 14 V (c) and 16 V (d) and then hydrothermally sealed or coated with the hybrid sol-gel.

Figure 5.41- Bode plots as impedance modulus and phase angle in 0.1 mol L^{-1} NaCl of AA2524 anodized in TSA and then hydrothermally sealed or coated with the hybrid sol-gel. Anodizing voltages: (a) 8 V, (b) 10 V, (c) 14 V, (d) 16 V. Immersion time 48 h.

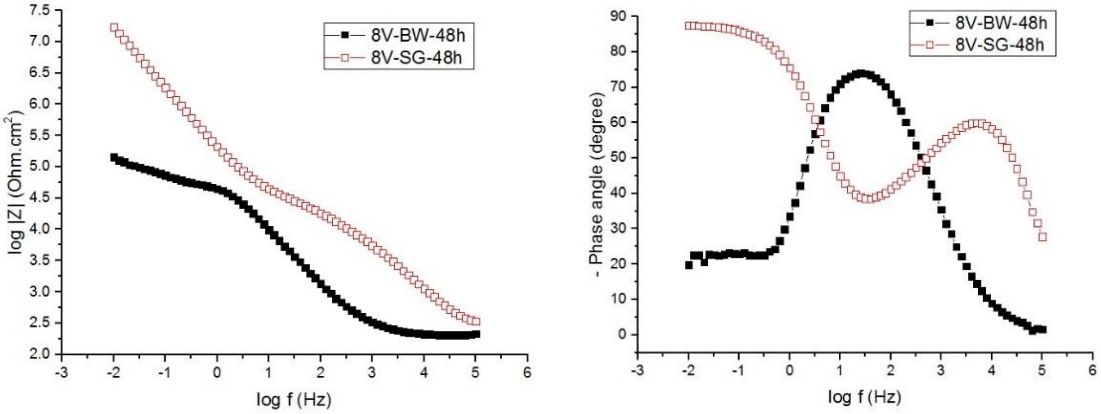

(a) 8 V

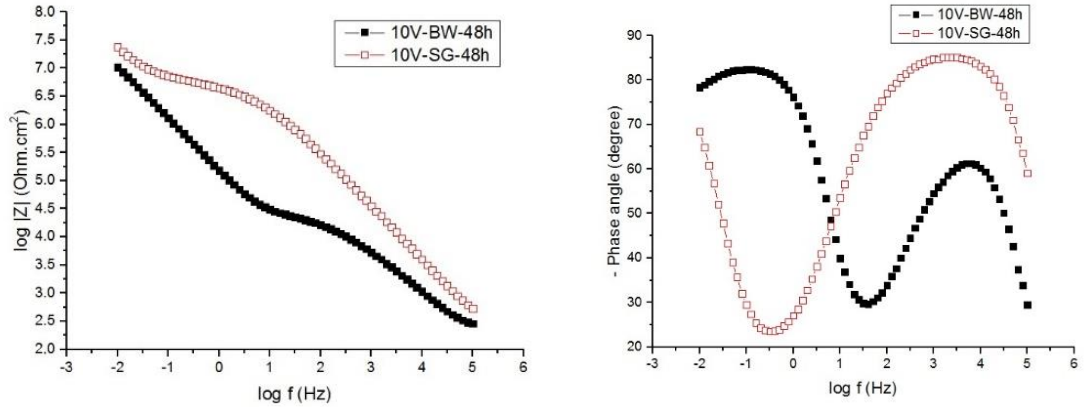

(b) 10 V

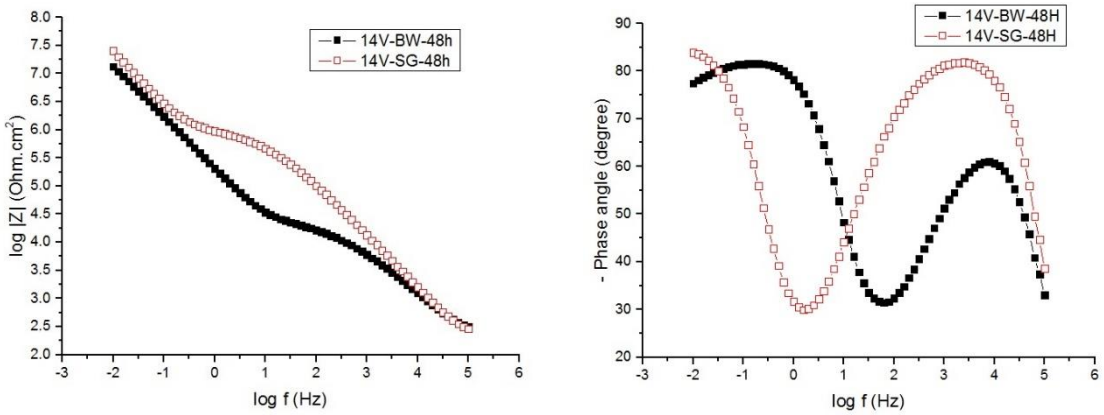

(c) 14 V

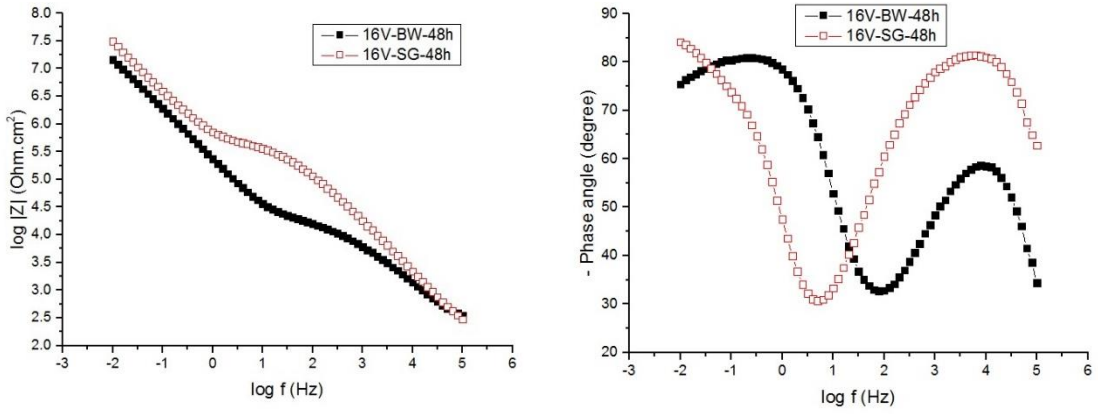

(d) 16 V

Figure 5.42 - Bode plots as impedance modulus and phase angle in 0.1 mol.L^{-1} NaCl of AA2524 samples anodized in TSA and then hydrothermally sealed or coated with the hybrid sol-gel. Anodizing voltages: (a) 10 V, (b) 14 V, (c) 16 V. Immersion time 1008 h.

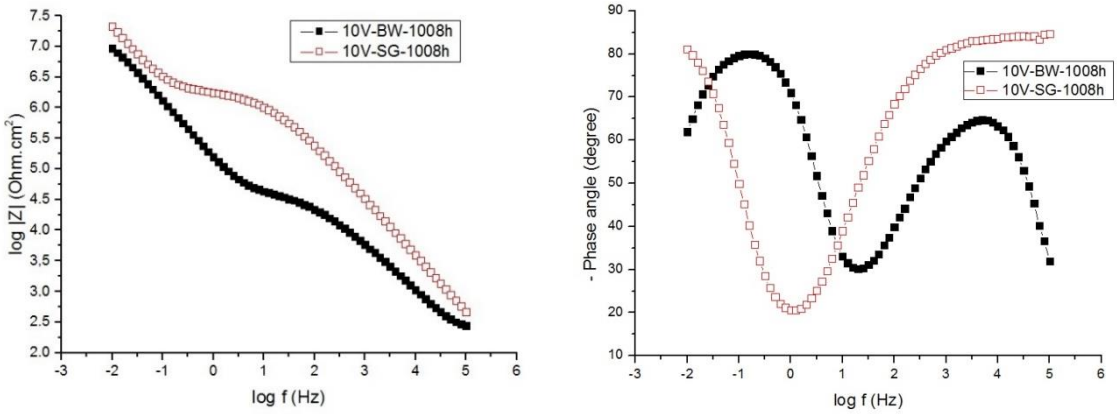

(a) 10 V

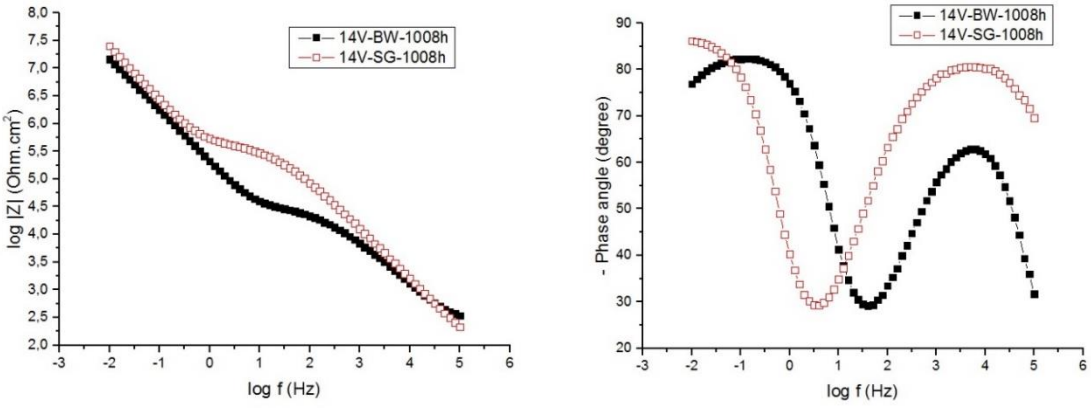

(b) 14 V

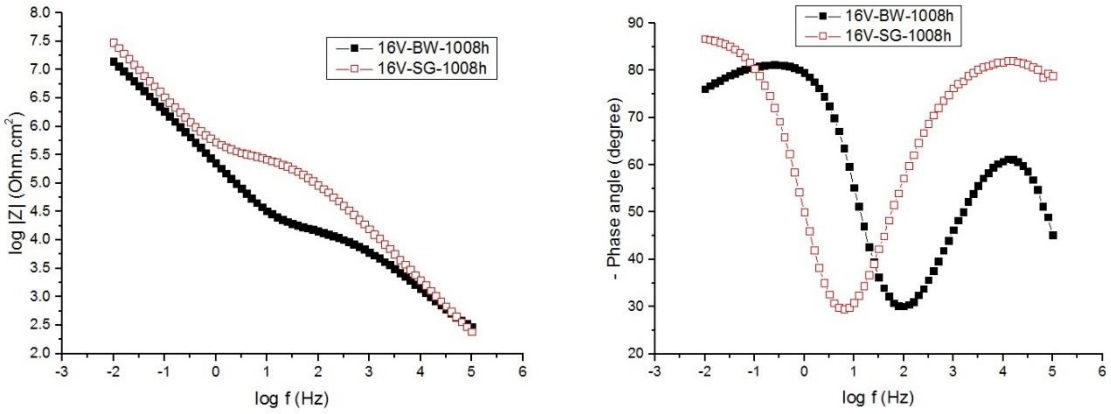

(c) 16 V

Except for the samples anodized at 8 V, for which the impedance modulus of the sol-gel coated sample was more than two orders of magnitude superior to the HTSed one (Figure 5.41 (a)), for all other conditions, the comparison of the LF impedance moduli suggests that the corrosion resistances of the sol-gel coated samples are slightly higher. This happens because the LF time constants of the samples protected with the sol-gel coating are not well defined and are displaced to very low frequencies. Therefore, it is expected a much better behaviour for the sol-gel coated samples. Moreover, the diagrams displayed in Figures 5.41 and 5.42 clearly show a wider and more capacitive HF time constant for the sol-gel coated anodized samples as well as higher impedance modulus in the MF range. Both these features indicate a better blockage against electrolyte penetration through the pores for the hybrid sol-gel coated samples, which will protect more effectively the barrier layer against aggressive species attack.

As the main difference between the two sets of samples is the post-treatment after the anodizing procedure: HTS or sol-gel, Figure 5.43 displays a comparison, for 10 V, 14 V and 16 V, between the parameters R_p and R_{SG} determined from the EEC fitting procedure of the EIS diagrams for each post-treatment. In all the cases, the pore resistance of the sol-gel coated samples were at least two orders of magnitude superior to the HTSed ones, pointing to an effective role of the sol-gel layer in blocking the corrosion activity at the interface.

Figure 5.43 - Comparison between R_p and R_{SG} with immersion time in NaCl 0.1 mol.L^{-1} for AA2524 samples anodized in TSA at (a)10 V, (b) 14 V and (c) 16 V.

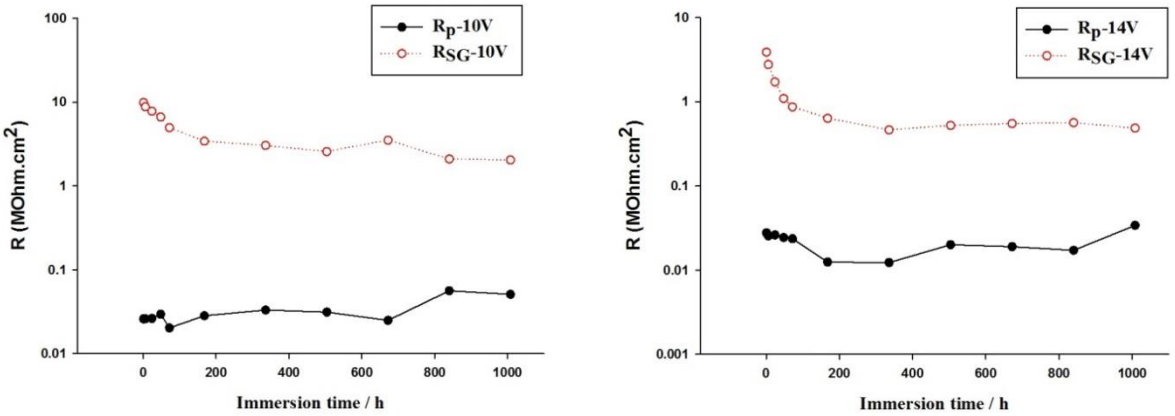

(a)

(b)

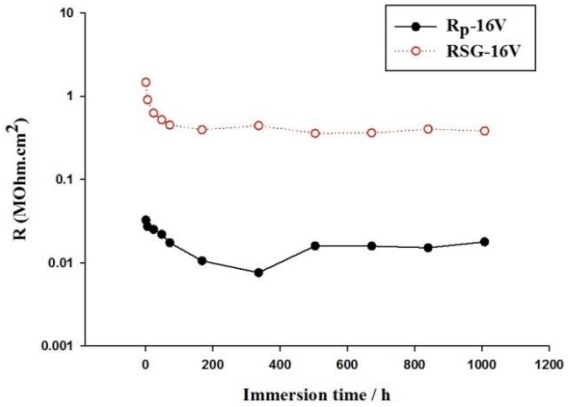

(c)

5.7 Salt spray test of the AA2524 samples anodized in TSA and then hydrothermally sealed or coated with the hybrid sol-gel

Salt spray tests were carried out in triplicate and according to ASTM B117-11 standard. The samples anodized and hydrothermally sealed or coated with the hybrid sol-gel were analysed after 6 h, 24 h , 48 h, 72 h, 168 h, 240 h, 336 h and 504 h of exposure.

Figures 5.44 to 5.47 display the comparative images acquired after 168 h (a), 336 h (b) and 504 h (c) of exposure to the salt spray chamber of samples anodized in TSA at 8 V, 10 V, 14 V and 16 V and then hydrothermally sealed (HTSed) or sol-gel coated.

Figure 5.44 - Photographs of the surface of AA2524 samples anodized in TSA and either hydrothermally sealed (BW) or sol-gel coated (SG) after: (a) 168 h, (b) 336 h and (c) 504 h exposure to the salt spray test. Anodizing voltage 8 V.

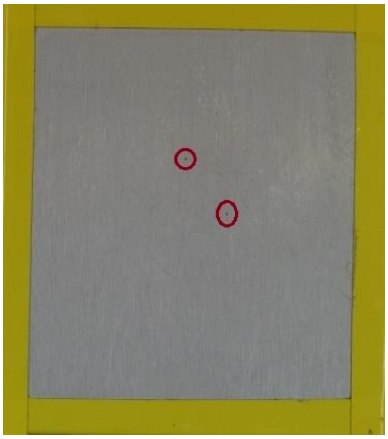

8 V - BW

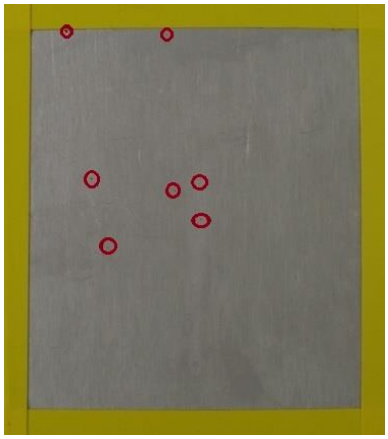

8 V - SG

(a) 168 h

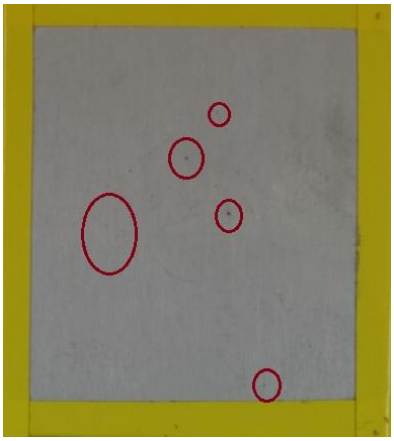

8 V - BW

8 V - SG

(b) 336 h

8 V - BW

8 V - SG

(c) 504 h

Figure 5.45 - Photographs of the surface of AA2524 samples anodized in TSA and either hydrothermally sealed (BW) or sol-gel coated (SG) after: (a) 168 h, (b) 336 h and (c) 504 h exposure to the salt spray test. Anodizing voltage 10 V.

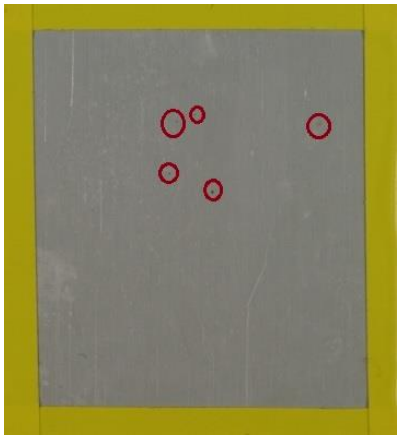

10 V - BW

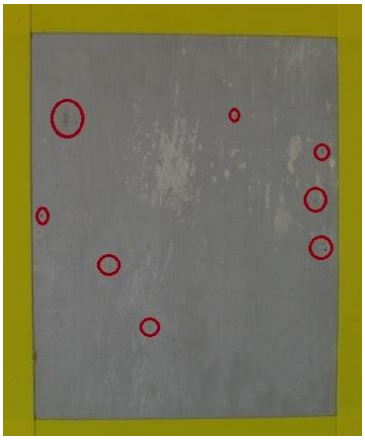

10 V - SG

(a) 168 h

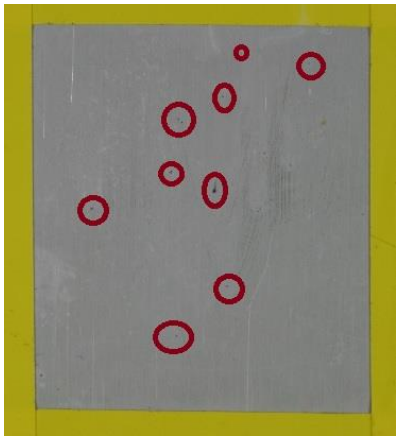

10 V - BW

10 V - SG

(b) 336 h

10 V - BW

10 V - SG

(c) 504 h

Figure 5.46 - Photographs of the surface of AA2524 samples anodized in TSA and either hydrothermally sealed (BW) or sol-gel coated (SG) after: (a) 168 h, (b) 336 h and (c) 504 h exposure to the salt spray test. Anodizing voltage 14 V.

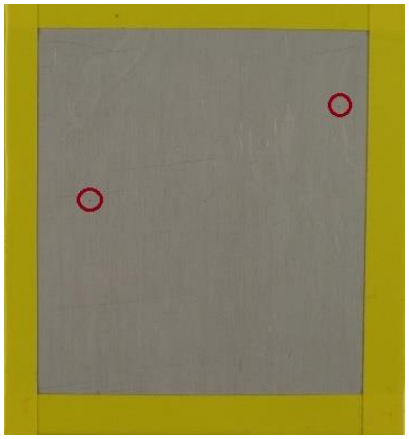

14 V - BW

14 V - SG

(a) 168 h

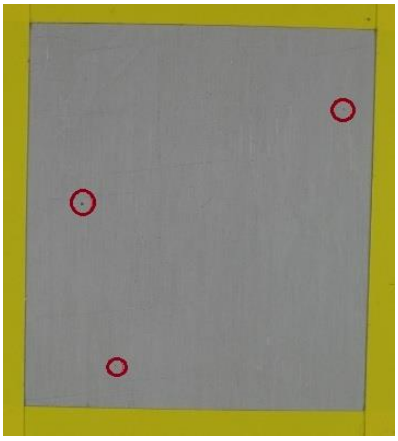

14 V - BW

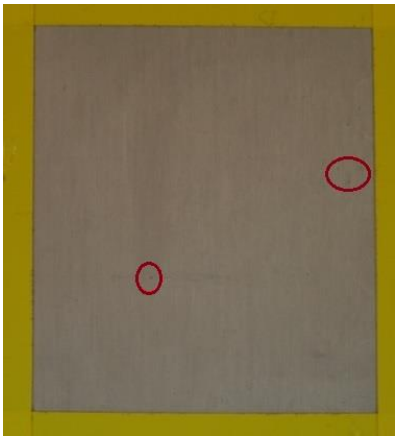

14 V - SG

(b) 336 h

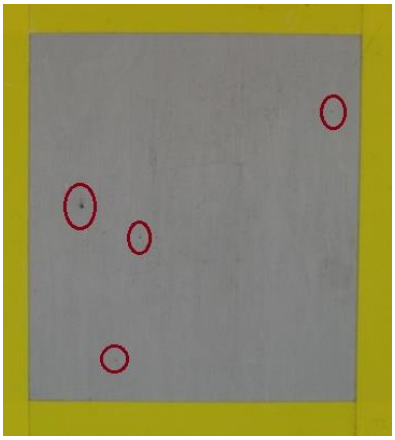

14 V - BW

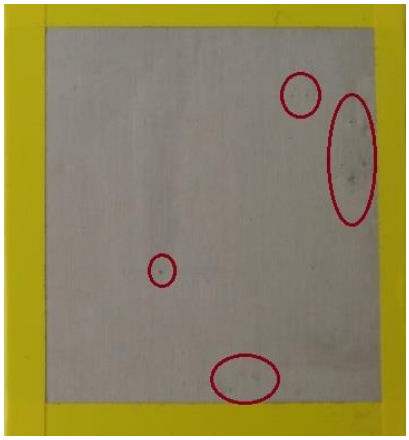

14 V - SG

(c) 504 h

Figure 5.47 - Photographs of the surface of AA2524 samples anodized in TSA and either hydrothermally sealed (BW) or sol-gel coated (SG) after: (a) 168 h, (b) 336 h and (c) 504 h exposure to the salt spray test. Anodizing voltage 16 V.

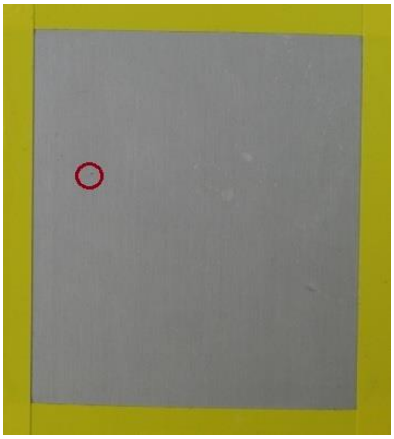

16V - BW

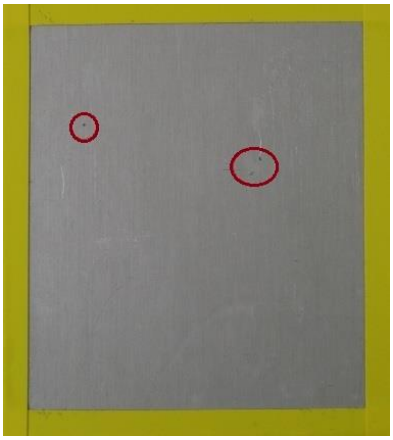

16V - SG

(a) 168 h

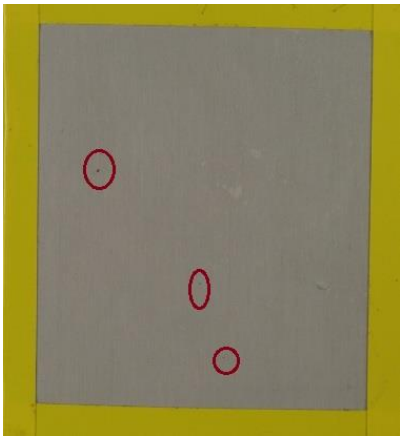

16V - BW

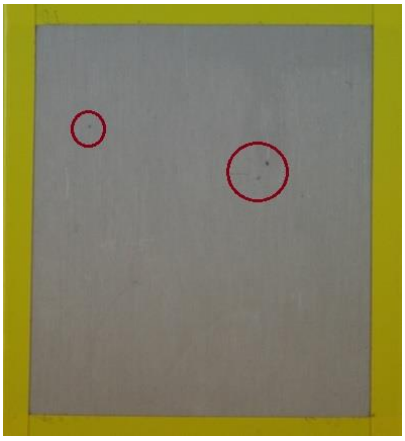

16V - SG

(b) 336 h

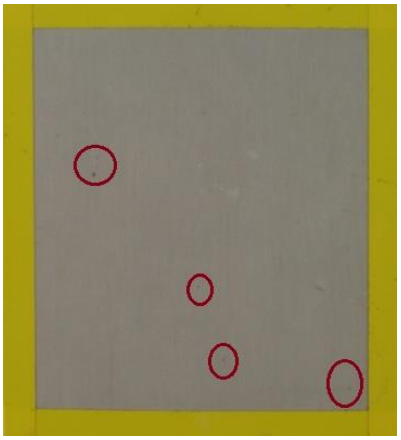

16V - BW

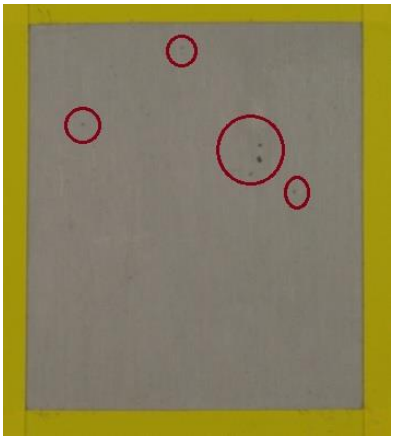

16V - SG

(c) 504 h

For both post-treatments, pits were observed after 72 h of exposure to the salt spray chamber. However, the samples coated with the sol-gel presented a larger number of pits at the beginning of the exposure period than the HTSed samples (images not shown). After 168 h pits increased in number and size for the hybrid sol-gel coated sample (not captured by the camera) while for the HTSed samples they remained almost the same as those observed at shorter exposure times (Fig. 5.44, 5.45, 5.46 and 5.47 (a)).

For longer exposure times (336 h – Fig. 5.44, 5.45, 5.46 and 5.47 (b) and 504 h – Fig. 5.44, 5.45, 5.46 and 5.47 (c)), pits increased in number and size and covered the whole surface of the HTSed samples. Most of them were very small and could not be detected by the camera. As expected, the samples anodized at 14 V or 16 V presented better results than the samples anodized at 8 V or 10 V, with good agreement with the EIS measurements.

The samples anodized at 8 V or 10 V coated with the sol-gel seem to have been submitted to a peeling phenomenon at the end of the 504 h exposure period, as can be seen in Figures 5.44 (c) and 5.45 (c). On the other hand, for samples anodized at 14 V and 16 V, the deep pits are greatly inferior in number than the HTSed samples, indicating that the hybrid sol-gel post-treatment avoid their growth.

From this point of the work only samples anodized at 14 V were produced to evaluate the influence of different parameters in the corrosion protection afforded by the sol-gel coating. This was done because at this anodizing voltage the corrosion tests previously reported indicated better protective properties. Moreover, this is the anodizing voltage applied by AirBus in its TSA anodizing procedure (MUSEUX; THEILMANN, 2009). Finally, last, but not least, the use of a lower voltage than 16 V, which presented slightly inferior corrosion behaviour, implies in money savings.

5.8 EIS characterization of AA2524 samples anodized in TSA at 14 V and protected with the hybrid sol-gel coating aged for different times (increasing hydrolysis time)

One of the main concerns about the industrial use of sol-gel coatings is the lifetime of the hydrolysis solution. Increasing the shelf life of the sol-gel bath will result in money saving and in less wastage generations. Some works are available where this parameter was investigated on the anticorrosion performance of this class of coatings (OOIJ et al., 2005;

GANDHI et al., 2006; CHEN et al., 2011). They show that the condensation reactions that occur concurrently with the hydrolysis lead to agglomeration of the precursor molecules in the solution, forming crosslinked films, which result in slow polymerization and eventual precipitation of these compounds (OOIJ et al., 2005; CHEN et al., 2011). This is critical for the anticorrosion protection afforded by the coating, as increasing the concentration of condensed species (Si-O-Si groups) decreases the efficiency of the interactions between the sol-gel and the metal surface. This results in more messy structures (OOIJ et al., 2005; GANDHI et al., 2006), increasing the number of conductive pathways to the interface and, ultimately, decreasing the protective properties of the coating (GANDHI et al., 2006).

Figure 5.48 shows the EIS responses with immersion time in the 0.1 mol.L^{-1} NaCl test solution of the AA2524 anodized in TSA at 14 V and then coated with the sol-gel applied after different ageing times of the hydrolysis solution.

Figure 5.48 - Bode plots as impedance modulus and phase angle after different immersion times in 0.1 mol.L^{-1} NaCl of the AA2524 anodized in TSA at 14 V and coated with the hybrid sol-gel applied after different ageing times of the hydrolysis solution: (a) 24 h (b) 72 h (c) 168 h and (d) 336 h.

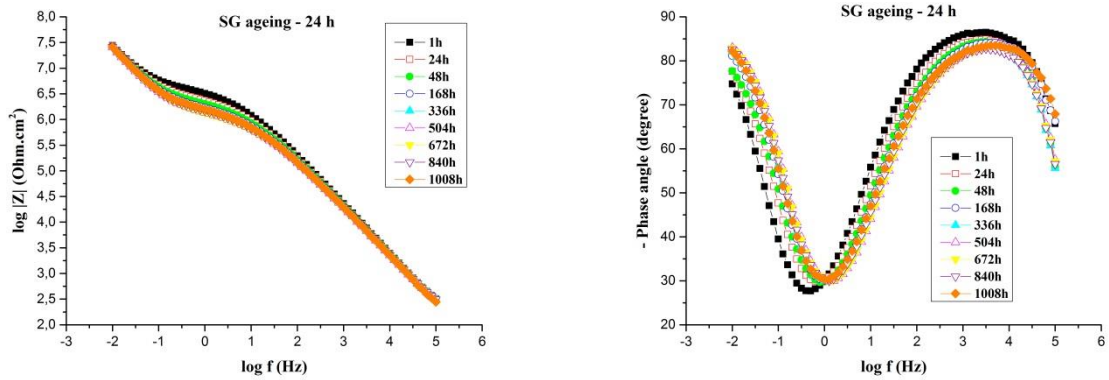

(a) SG ageing – 24 h

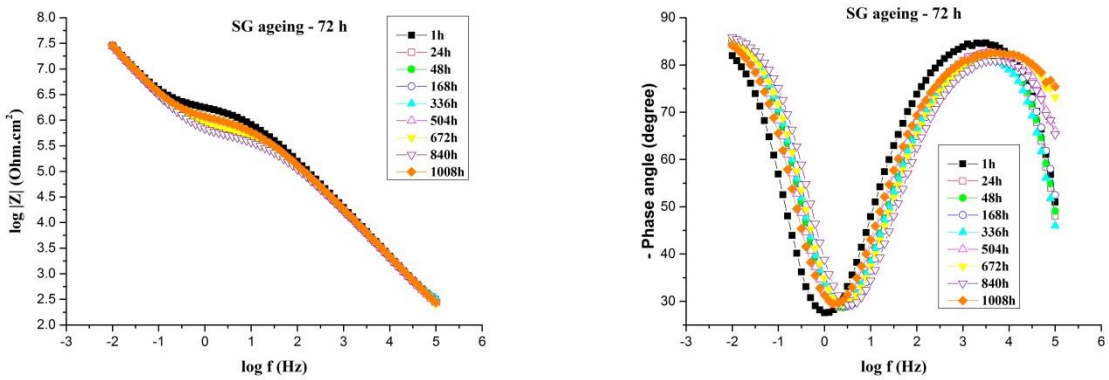

(b) SG ageing – 72 h

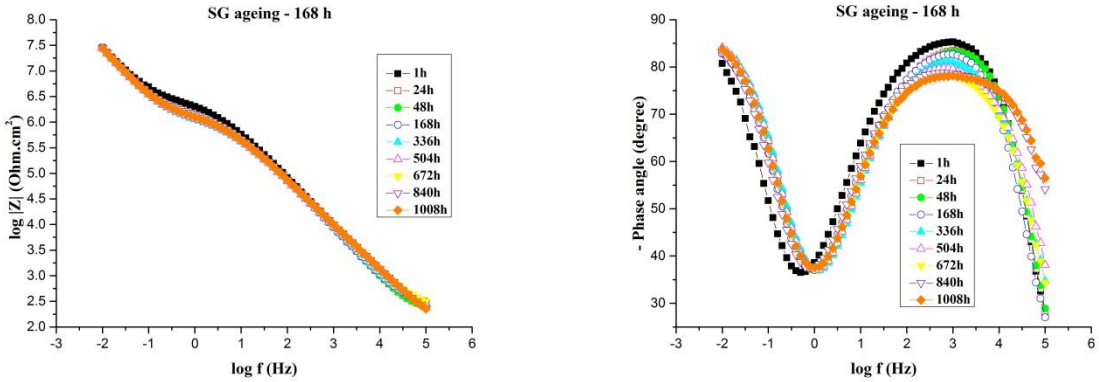

(c) SG ageing – 168 h

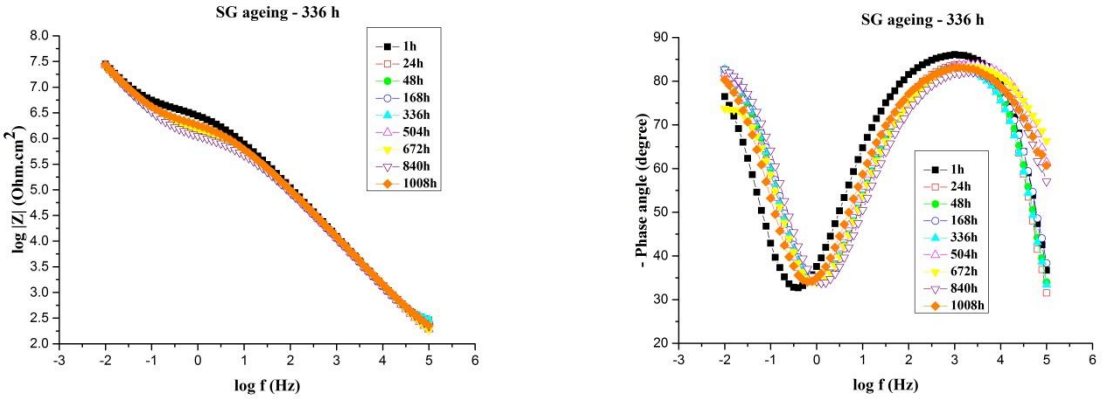

(d) SG ageing – 336 h

The EIS behaviours presented in Figure 5.48 were quite similar to those presented in Figure 5.36 for the samples anodized at 8 V, 10 V, 14 V, and 16 V coated with the sol-gel hydrolysed during 2 h. The phase angle plots presented two well-separated time constants, which origins were already discussed in the previous items. The impedance moduli slightly decrease in the MF, indicating penetration of electrolyte through the pores, while in the HF and LF domains they remained quite stable. Nevertheless, with immersion time, the phase angle plots show that the LF time constant shifts to higher frequencies accompanied by a decrease in the phase angle, whereas for the HF time constant there is a diminution in the phase angle maximum and a displacement to higher frequencies of the minimum separating the two time constants. As discussed before, the changes in the HF time constant is associated with the deterioration of the protective properties of the hybrid coating within the pores (the resistive pathways become easier due to coating deterioration), whereas the displacement to

higher frequencies of the LF time constant is associated to a decrease in the protective properties of the barrier layer, mainly decreased resistance.

Figure 5.49 shows a comparison between the EIS responses after selected immersion times: 48 h (a), 504 h (b) and 1008 h (c) in the NaCl 0.1 mol L^{-1} test solution for AA2524 samples anodized in TSA at 14 V and coated with the sol-gel aged (hydrolysed) for different times: 2 h, 24 h, 72 h, 168 h, 336 h. The diagrams show that, whatever the hydrolysis time, the EIS spectra are similar. For all immersion times, it seems evident that the MF impedance modulus plateau (representative of the resistive response within the sealed pores (GONZÁLEZ et al., 1997; LOPEZ et al., 2000) is lower for the lowest hydrolysis time. This behaviour is particularly evident for longer immersion times, and indicates an improvement of the protective properties of the sol-gel coating as hydrolysis proceeds.

Figure 5.49 - Comparison between the EIS responses of the AA2524 anodized in TSA at 14 V and coated with sol-gel after 2 h, 24 h, 72 h, 168 h and 336 h of ageing of the hydrolysis solution. Immersion time in NaCl 0.1 mol L^{-1}: (a) 48 h, (b) 504 h and (c) 1008 h.

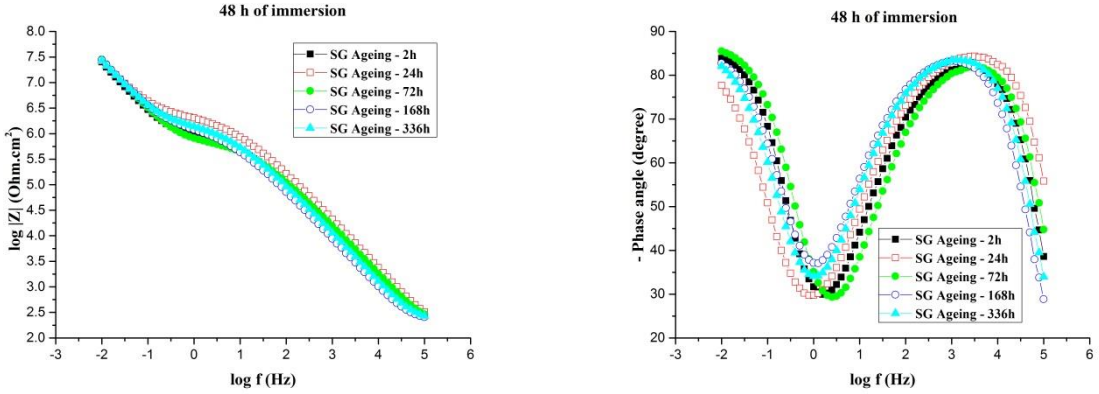

(a) 48 h of immersion

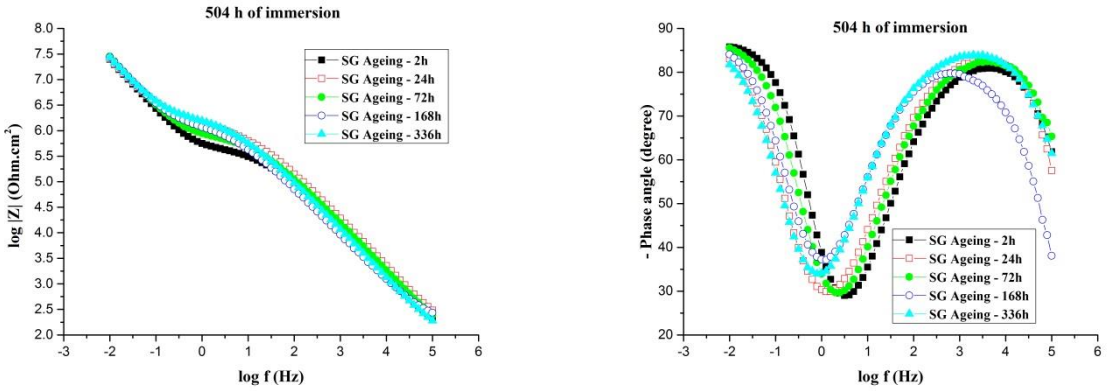

(b) 504 h of immersion

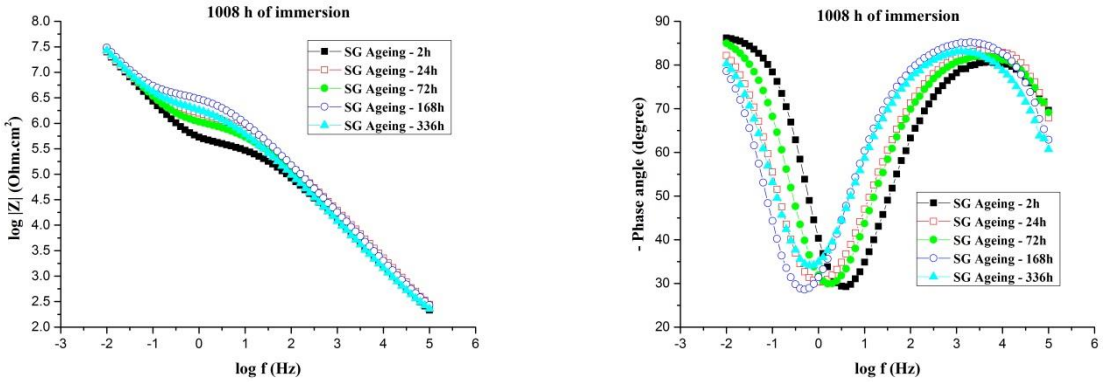

(c) 1008 h of immersion

Figure 5.50 displays the evolution with immersion time of the impedance modulus at 0.01 Hz of AA2524 samples anodized in TSA at 14 V and coated with the sol-gel aged for different times. This representation clearly shows a superior performance for the samples coated with the sol-gel hydrolysed during 72 h and 168 h. The former hydrolysis condition presented a more stable behaviour throughout the whole test period, whereas the latter, even though exhibiting impedance moduli slightly lower for most of the test period, suddenly increased for the experiment performed after 1008 h. Figure 5.50 also highlights the poorer performance of the sample coated with the sol-gel hydrolysed during 2 h.

Figure 5.50 - Evolution with immersion time in 0.1 mol.L^{-1} NaCl of the impedance modulus at 0.01 Hz of AA2524 samples anodized in TSA at 14 V and coated with sol-gel aged (hydrolysed) for different times.

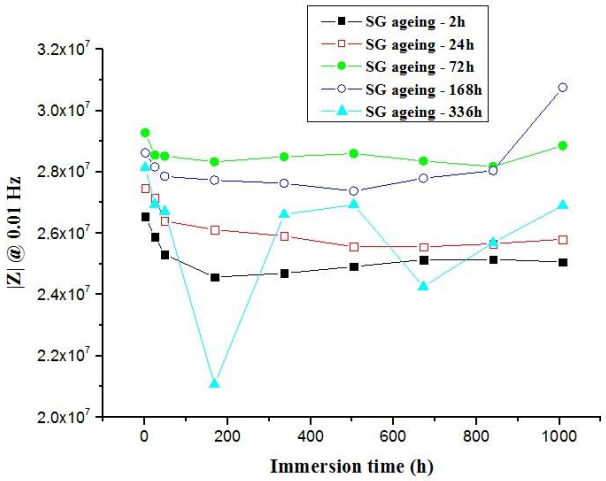

In order to obtain more information about the sol-gel solution stability, rheological characterizations of the hydrolysis solution were carried out up to 504 h of ageing. If any transition occurs, a strong increase in viscosity must be detected. As explained in the item 3.7.1, during the ageing of the sol-gel hydrolysis solution, the silanol groups can condensate

and form siloxane bonds (Si-O-Si) forming clusters. These grouped siloxanes clusters form a 3D-network in the hydrolysis solution leading to an increase in the viscosity. For all hydrolysis time, the rheological behaviour of the sol-gel solutions is Newtonian meaning that the viscosity is the same in the investigated shear rate range with a viscosity slightly higher than that of water (1 mPa.s at 20 °C). Increasing the shear rate does not change the apparent viscosity (NICOLAY et al., 2015).

Figure 5.51 shows the evolution of the Newtonian viscosity of the hybrid sol-gel solution after ageing for 2 h, 24 h, 72 h, 168 h, 336 h and 504 h. A decrease in viscosity is observed between 2 h and 24 h of hydrolysis. For longer hydrolysis time, the viscosity slightly rises likely due to the formation of siloxane groups within the solution but no significant change was detected. The sol-gel transition was not observed during the investigated ageing period, meaning that the condensation rate is very slow. The measured viscosities remain in the range between 0.003 Pa.s and 0.004 Pa.s. These results are in good agreement with the EIS behaviour. The ageing of the sol-gel solution does not induce strong modification in the viscosity and, therefore, the impregnation of the pores by capillarity is always possible during sol-gel application. The compatibility between the solution and the alumina matrix is conserved. These results are very promising from a practical point of view because they highlight that the condensation rate in solution is slow and, thus, the hydrolysis solution can be used even after few weeks of preparation without hindering the anticorrosion performance and the sealing properties of the hybrid coating.

Figure 5.51 - Variation of the viscosity of the hybrid sol-gel hydrolysis solution with ageing (hydrolysis) time.

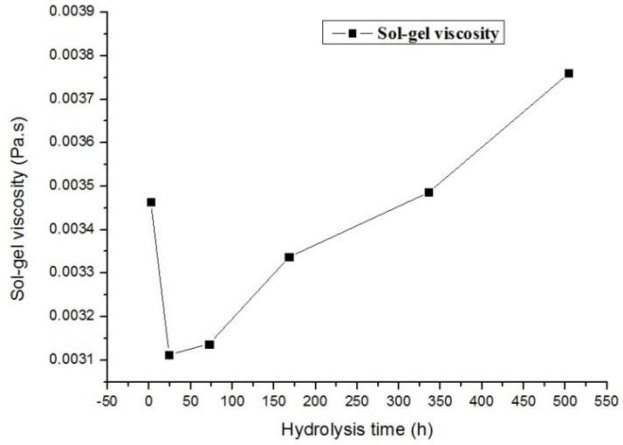

5.9 Corrosion behaviour of AA2524 non-anodized and anodized in TSA at 14 V and protected with an epoxy coating without or with the previous application of a sol-gel layer

The main objective of this research was to evaluate the anticorrosion properties of the AA2524 anodized in TSA and protected by a hybrid sol-gel coating compatible with a top-coating system that could be employed in the aircraft industry. The GPTMS precursor was chosen because its glycidoxyl functional group is compatible with epoxy coatings, which are widely used in aerospace industry (LIU et al., 2006; OSBORNE et al., 2001). Moreover, in order to limit the emission of volatile organic compounds (VOC), a free solvent bi-component epoxy coating was applied.

The coating was applied by spin coating on different substrates and the adopted hydrolysis time of the sol-gel solution was 2 h. Some difficulties arose during the application of the topcoat: the spin coating rotation speed needed to be tuned during each application because the cross-linking reaction occurred during the procedure, and even if the rate of coating application was uniform, thicknesses variations were not negligible from one sample to another. Thus, the epoxy coatings applied on the sol-gel treated samples (SG + OC and 14V + SG + OC) were about 20 to 30 µm thicker than those applied on the samples just pre-treated (OC) and pre-treated and anodized (14V + OC) (Table 4.2). This issue may have an important role in the results presented and discussed in the following pages. In some cases, the limitations of the EIS equipment were reached during the measurements because the obtained systems were very protective and the measured currents were lower than the equipment resolution, this led to strong dispersion in the LF range of the EIS diagrams. The presented results are, therefore, preliminary and the discussion will be mainly qualitative.

The coating was applied to the AA2524 in four different conditions, two without and two with anodizing:

a) Only pre-treated AA2524 coated with the epoxy topcoat (OC);
b) Only pre-treated AA2524 coated with the sol-gel and the epoxy topcoat (SG+OC);
c) Unsealed AA2524 anodized at 14 V in TSA and coated with the epoxy topcoat (14V+OC);
d) AA2524 anodized at 14 V in TSA and coated with the sol-gel and the epoxy topcoat (14V+SG+OC).

Figure 5.52 (a) shows the evolution of the EIS diagrams with immersion time in the 0.1 mol.L^{-1} NaCl test solution of the only pre-treated AA2524 sample coated with the epoxy top coating. For this sample, at least two time constants were observed since the beginning of the test. The HF time one is ascribed to the epoxy coating and that at LF is due to the reactions occurring at the substrate surface due to penetration of the aggressive electrolyte through the defects and pores of the coating (JIANG et al., 2015; DUONG et al., 2016). The impedance modulus diagram shows a general tendency of decrease with immersion time. The impedance oscillations can be explained both by increasing penetration of aggressive species through the coating due to its deterioration and to the precipitation of corrosion products that blocks the defects followed by their dissolution and desorption (BAJAT et al., 2008; CHEN et al., 2011; LAMAKA et al., 2015). The phase angle diagrams also show this oscillatory behaviour with decrease and increase e of the phase angle and the shift of the time constant to lower and higher frequencies.

For the three other conditions (Figure 5.52 (b) (c) and (d)), the EIS diagrams are characterized by a single time constant with phase angle close to -90°, presenting a resistive drift at the lowest frequencies, as shown by the LF plateau in the impedance modulus diagrams. The LF impedance modulus was at least superior to $10^{9.5}$ Ω.cm^2 and only a slight decrease was observed during the whole test duration (up to 1344 h, corresponding to 8 weeks). This indicates that the electrolyte starts to permeate through the different coating systems, however the high impedance values point to an efficient protection of the substrate against corrosion. The detected time constant can be ascribed to the mainly capacitive response of the epoxy coating. Therefore, the substrate response was not detected by the EIS experiments in the investigated frequency range.

Figure 5.52 - Bode plots as impedance modulus and phase angle after different immersion times in 0.1 mol.L^{-1} NaCl for AA2524 samples: (a) only pre-treated and coated with the epoxy top coating (**OC**), (b) only pre-treated and coated with the sol-gel and the epoxy topcoat (**SG+OC**), (c) anodized at 14 V in TSA and coated with the epoxy topcoat in the unsealed condition (**14V+OC**) and (d) anodized at 14 V in TSA and coated with the sol-gel and the epoxy topcoat (**14V+SG+OC**).

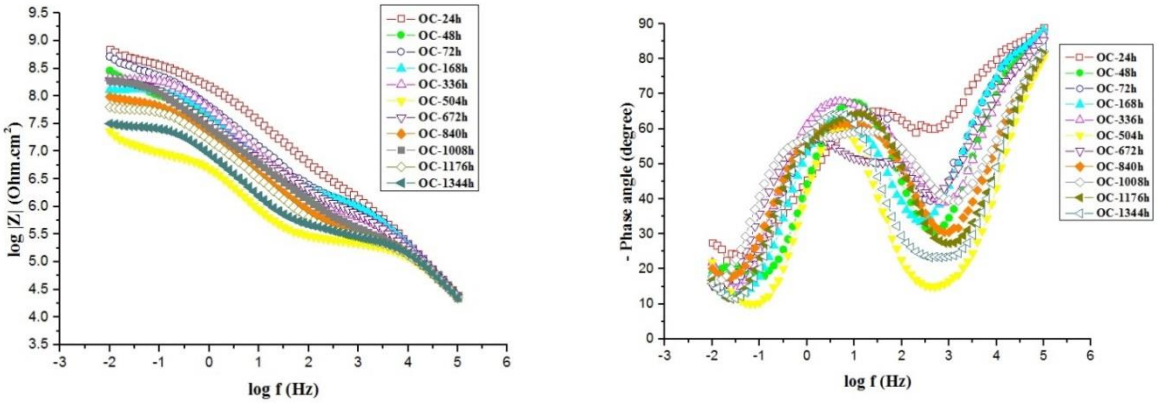

(a)

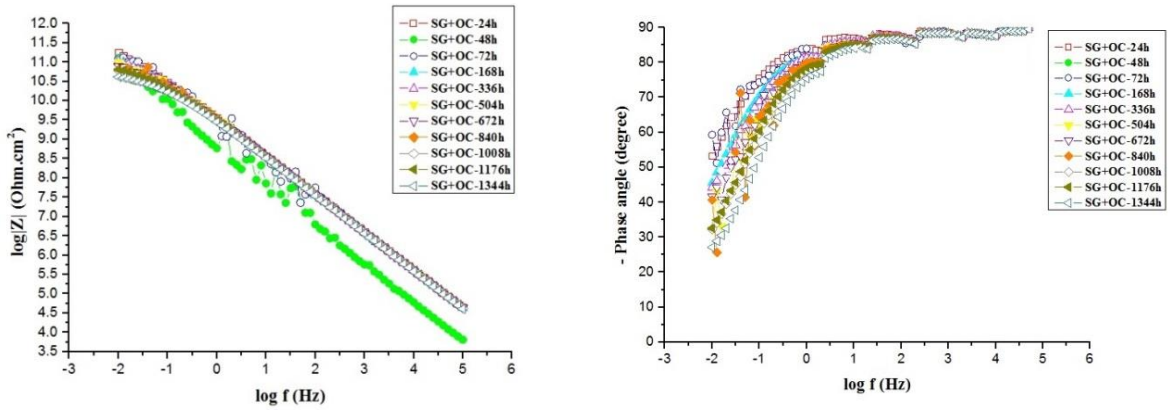

(b)

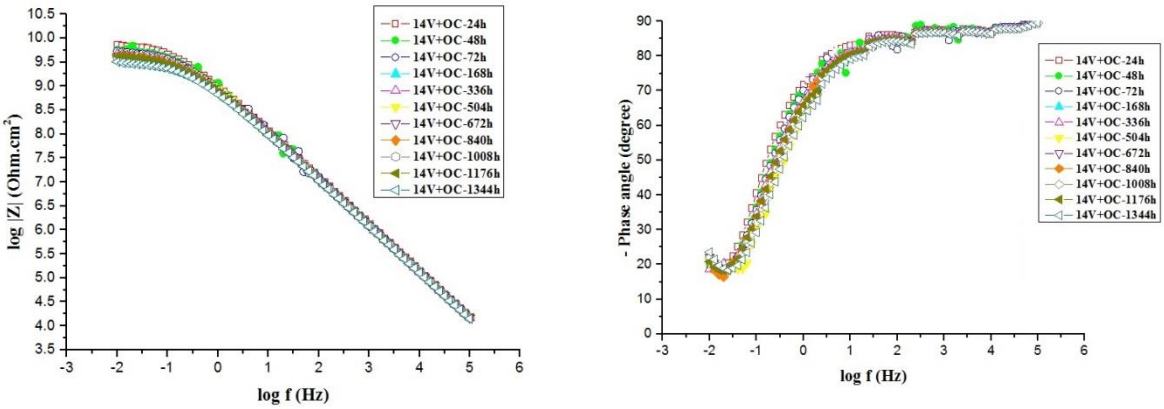

(c)

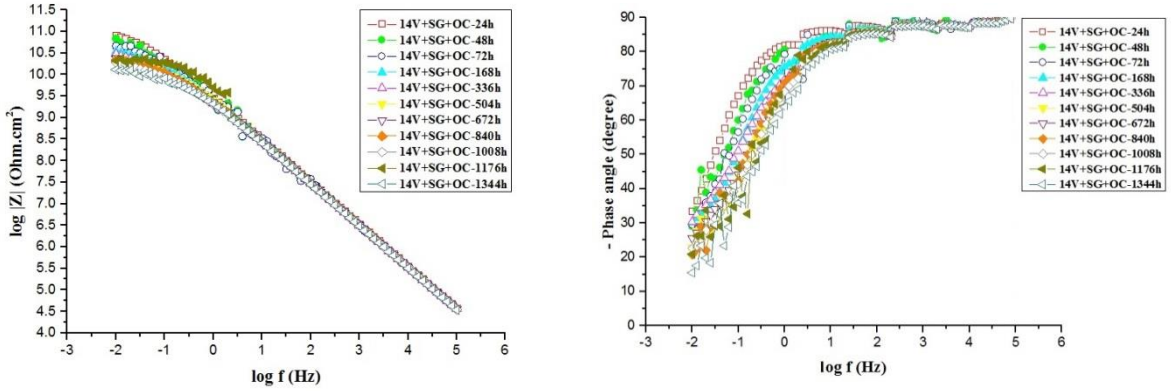

(d)

Figure 5.53 shows a comparison between the EIS responses of the samples coated with epoxy after 24 h, 672 h and 1344 h of test, whereas Figure 5.54 depicts the evolution of the LF impedance modulus (at 0.01 Hz) during the whole test period. Both representations show that the sample only pre-treated AA2524 and coated with the epoxy top coating (OC) presented the worst performance. On the other hand, the LF impedance modulus was higher and the phase angles more capacitive for the two samples protected with the sol-gel: only pre-treated AA2524 coated with the sol-gel and the epoxy topcoat (SG+OC) followed by the sample anodized at 14 V in TSA and coated with the sol-gel and the epoxy topcoat (14V+SG+OC). The better anticorrosion behaviour of these two samples can be assigned to a very good interaction between the hybrid sol-gel and the organic coating. Finally, the unsealed AA2524 anodized at 14 V in TSA and coated with the epoxy top coating (14V+OC) also showed a good corrosion resistance, but more than one order of magnitude lower than the samples treated with the sol-gel. However, the reader must bear in mind the reported difference in the coating thicknesses (Table 4.2), which may an important role in the results.

Regarding the response of the sample 14V+SG+OC, its anticorrosion behaviour could be affected by the non-uniformity of the sol-gel distribution on the top surface of the porous AAO layer, as demonstrated by the SEM characterization (Fig. 5.14 (c)) and GDOES measurements (Fig. 5.17). This would hinder the interaction between the sol-gel and the organic coating. These results indicate that the sol-gel indeed has a good interaction with the organic coating and that the surface condition before applying the organic coating plays an important role in the protection of the aluminium substrate, helping to optimize the barrier properties of the topcoat system. However, taking into account the complexity of this particular interface: composed of a porous AAO, the pores impregnated by the hybrid sol-gel

coating and the epoxy top coating, it cannot be ruled out that in the LF limit of the EIS diagrams, the response of the sol-gel coated anodized layer arises. Therefore, the LF impedance modulus would not indicate the onset of the corrosion process; instead, it would be the response of the other protective barriers (sol-gel and barrier layer of the porous AAO). Therefore, further experiments, with more controlled conditions or even with more aggressive solutions must be conducted prior to a definitive ranking of the different systems is established.

Figure 5.53- Comparison between the EIS responses for AA2524 samples: only pre-treated and coated with the epoxy topcoat (**OC**); only pre-treated and coated with the sol-gel and the epoxy topcoat (**SG+OC**); anodized at 14 V in TSA and coated with the epoxy topcoat in the unsealed condition (**14V+OC**); anodized at 14 V in TSA and coated with the sol-gel and the epoxy topcoat (**14V+SG+OC**) after: (a) 24 h. (b) 672 h and (c) 1344 h of immersion in NaCl 0.1 mol.L^{-1}.

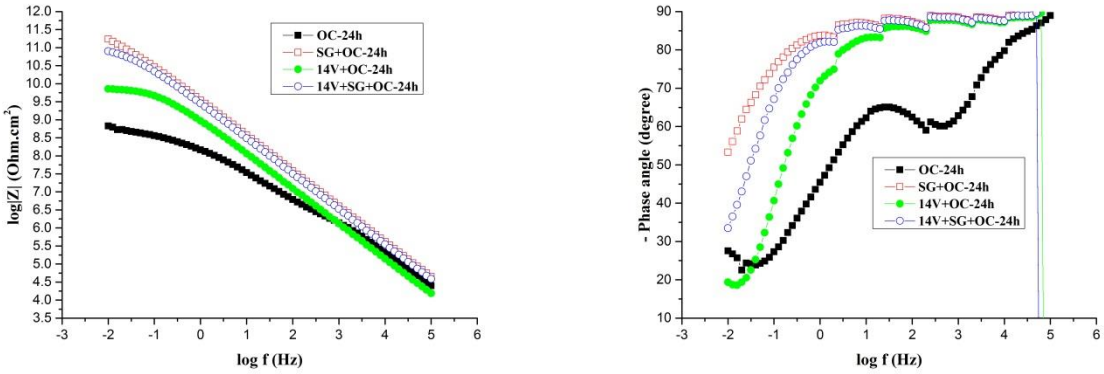

(a) 24 h of immersion

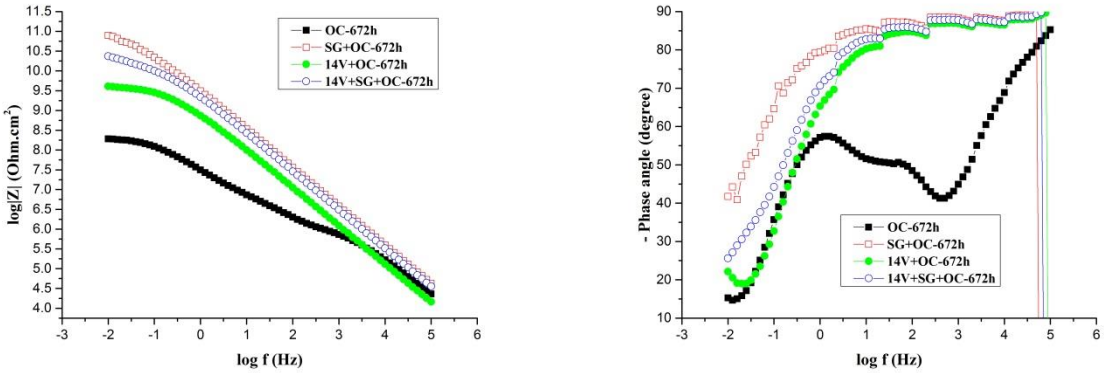

(b) 672 h of immersion

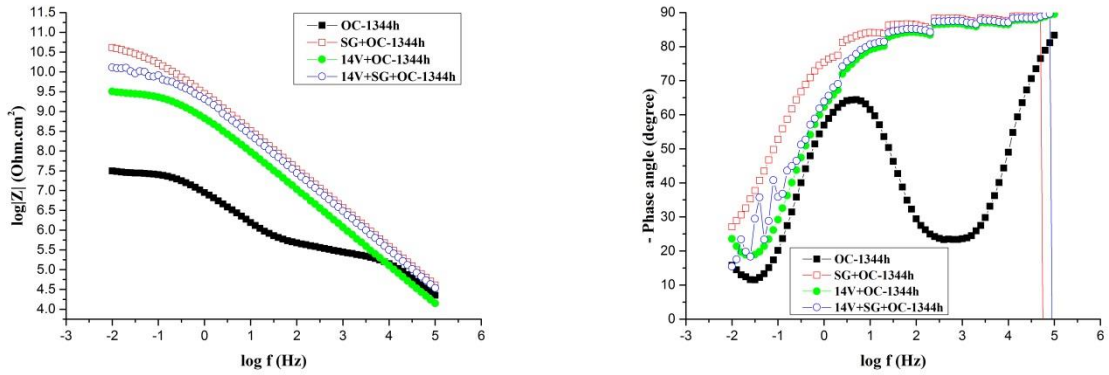

(c) 1344 h of immersion

Figure 5.54 - Evolution with immersion time in 0.1 mol.L^{-1} NaCl of the impedance modulus at 0.01 Hz for AA2524 samples: only pre-treated and coated with the epoxy topcoat (**OC**); only pre-treated and coated with the sol-gel and the epoxy topcoat (**SG+OC**); anodized at 14 V in TSA and coated with the epoxy topcoat in the unsealed condition (**14V+OC**); anodized at 14 V in TSA and coated with the sol-gel and the epoxy topcoat (**14V+SG+OC**).

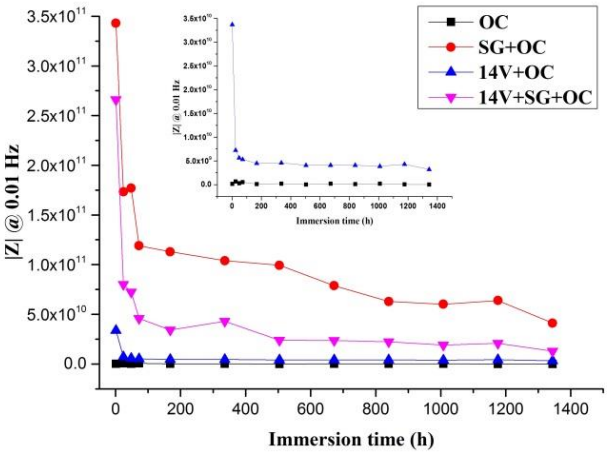

5.10 Salt spray tests of AA2524 samples non-anodized and anodized in TSA at 14 V and protected with an epoxy coating without and with the previous application of a sol-gel layer

Figure 5.55 displays comparative images of AA2524 samples protected with the epoxy top coating in the four previously described conditions: OC; SG+OC; 14V+OC and 14V+SG+OC after (a) 216 h, (b) 336 h, (c) 504 h, (d) 672 h and (e) 1008 h of exposure to the salt spray test.

Pits were observed after 72 h of exposure to the salt spray chamber of the OC sample (images not shown). For the other conditions, pits occurred from 168h of exposure (images not shown). However, the OC sample presented larger number of pits than the SG+OC. For this sample, many small pits were only observed in one specific region where the epoxy coating did not cover the surface.

The 14V+OC and 14V+SG+OC samples presented only one and two pits, respectively, after 168 h of exposure. From 168 h until 504 h of test, pits increased in number and size for the OC and for the 14V+OC samples, while for the SG+OC and 14V+SG+OC specimens they remained at the same condition as that observed after 168 h of test. From 672 h to the end of the test, three more pits were observed for the SG+OC, whereas for the 14V+SG+OC sample the same two pits remained. For the other two conditions (OC and 14V+OC), pits increased in number and size. The camera did not capture most of the pits, but it is possible to observe in Figure 5.55 (d) pronounced pits for these two last conditions.

It must be emphasized that, whatever the condition, pits were generally developed in the defects produced during the spin coating procedure, where some parts of the surface were not adequately covered by the epoxy top coating. The most important difference between them is that for OC and 14V+OC pits were formed at all defects and at a larger number, while for SG+OC and 14V+SG+OC just few and small pits were observed.

The results obtained by the salt spray test are in good agreement with the EIS measurements, showing that the samples previously protected with the sol-gel have the best corrosion resistance, confirming the good compatibility between the sol-gel and the epoxy top coating and the excellent barrier properties promoted by this layer. It must also be stressed that the best response (fewer pits) for the 14V+SG+OC sample at the end of the salt spray test (1008 h) strength the hypothesis that maybe the lower LF impedance verified for this sample in the EIS experiments when compared to the SG+OC sample is a result of the complex nature of this coating. Therefore, the response of the sol-gel impregnated porous layer is not really detected in the EIS tests.

Figure 5.55 - AA2524 samples coated with epoxy (OC), coated with sol-gel and epoxy (SG+OC), anodized at 14 V and coated with epoxy (14V+OC) and anodized at 14 V, coated with sol-gel and with epoxy (14V+SG+OC) after (a) 216 h, (b) 336 h, (c) 504 h, (d) 672 h and (e) 1008 h of exposure to salt spray test.

OC

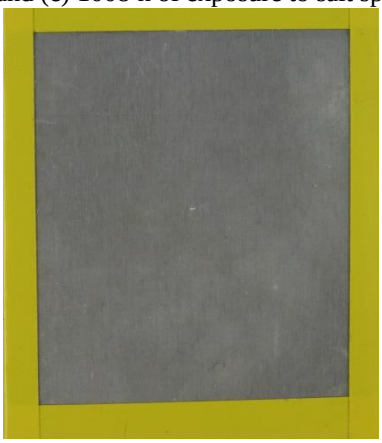

SG + OC

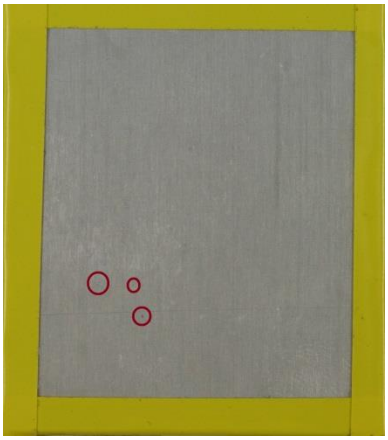

14 V + OC

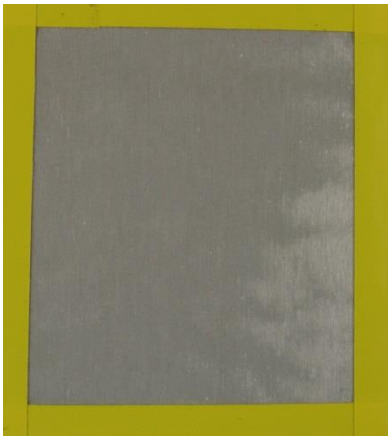

14 V + SG + OC

(a) 216 h (9 days)

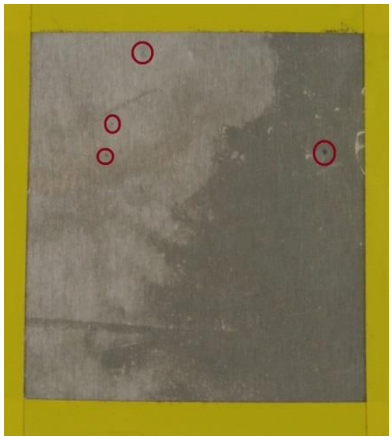

OC

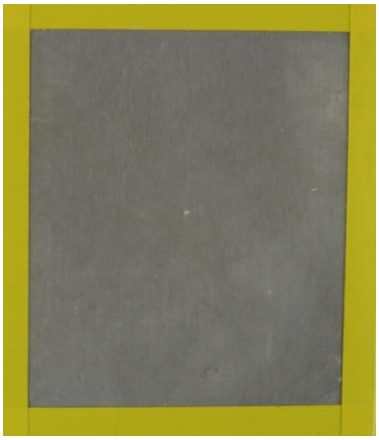

SG + OC

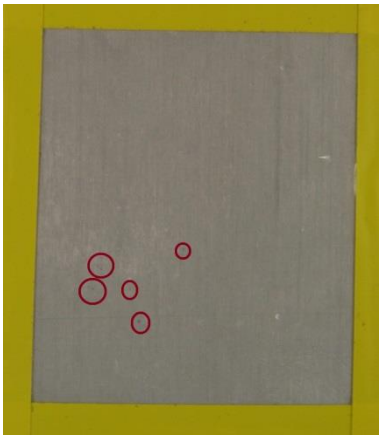

14 V + OC

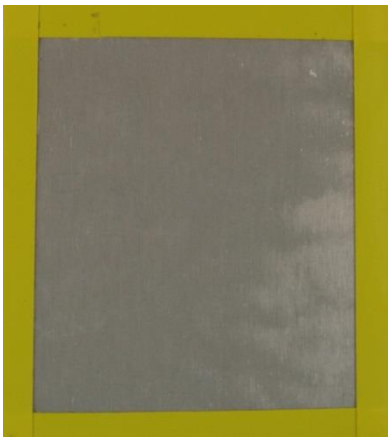

14 V + SG + OC

(b) 336 h (2 weeks)

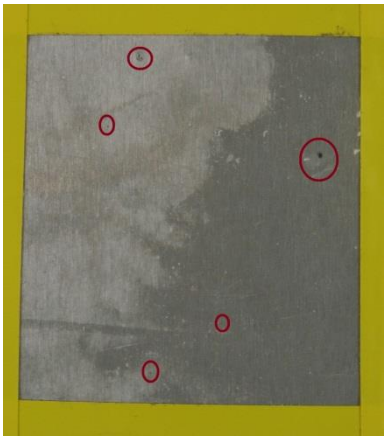

OC

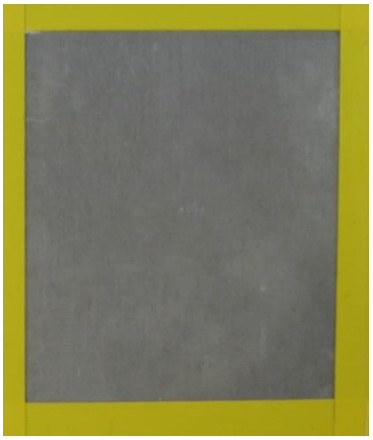

SG + OC

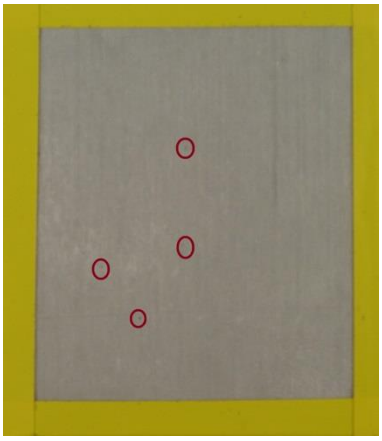

14 V + OC

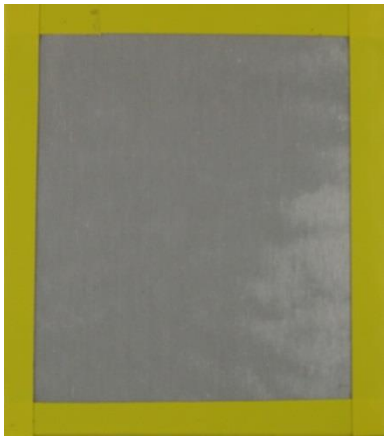

14 V + SG + OC

(c) 504 h (3 weeks)

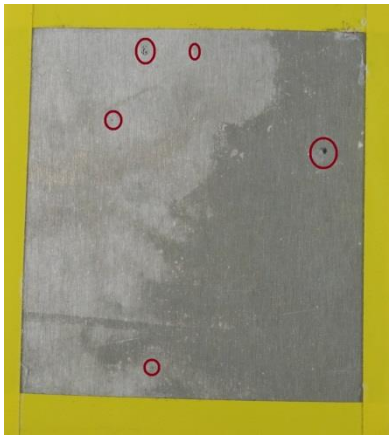

OC

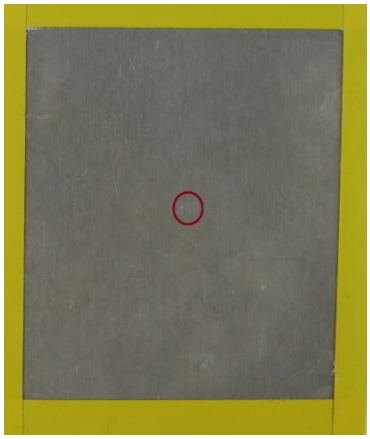

SG + OC

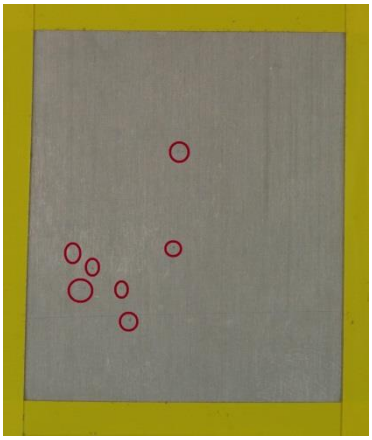

14 V + OC

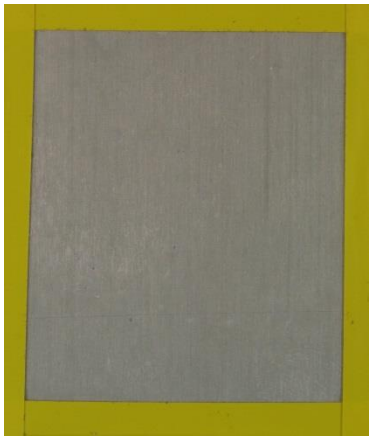

14 V + SG + OC

(d) 672 h (4 weeks)

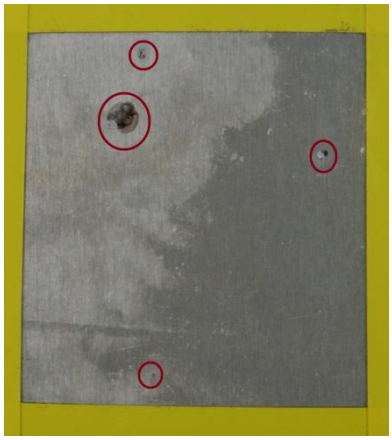

OC

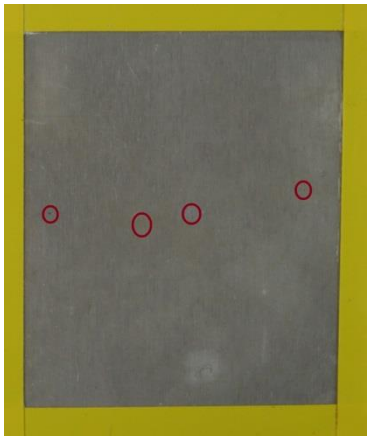

SG + OC

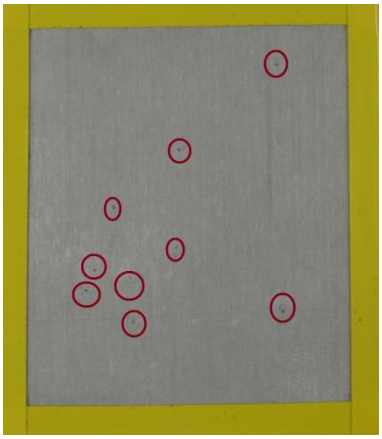

14 V + OC

14 V + SG + OC

(e) 1008 h (6 weeks)

6 CONCLUSIONS

In the present study the corrosion behaviour of AA2524 samples anodized at different voltages in TSA and protected with a hybrid sol-gel coating was investigated.

The results of the preliminary investigation showed that AA2524 has a similar behaviour to AA2024 when anodically polarized in sulphuric (SAA) or tartaric-sulphuric (TSA) acid baths. It was verified that the anodic potentiodynamic curves exhibit two current peaks located at similar potentials to those found for AA2024 in the literature, which are ascribed to the anodic dissolution of intermetallic (IM) particles. Similarly to AA2024-T3, the intensity of the peak at lower anodic potential, ascribed to the oxidation of Mg-rich IMs, was reduced when the experiments were performed in TSA. Moreover, anodic potentiostatic polarization experiments of AA2524 in SAA and TSA showed similar anodic behaviour, even though reduced current density were obtained in the TSA bath. These same features are reported in the literature for AA2024.

Potentiostatic anodizing experiments performed with AA2524 in TSA bath at different potentials confirmed the strong influence of the applied potential on the properties of the porous aluminium anodic oxide (AAO). In this way, pore diameter and the thicknesses of the porous and barrier layer increase with the applied voltage, whereas porosity decreases. The surface pore structure revealed to be irregular, whatever the applied anodizing potential, as a consequence of the complex microstructure of the substrate.

The application of the sol-gel coating directly to the only pre-treated AA2524 sample proved to be a poor corrosion protection methodology: impedance rapidly dropped after short immersion times in the test electrolyte and corrosion was quickly established on the sample surface. The anodized and non-sealed sample exhibited a similar corrosion behaviour to the other sample mentioned in this paragraph. Even though presenting higher impedance modulus at the beginning of the exposure period, its impedance rapidly dropped and after 72 h of test the impedances of both samples were of the same order of magnitude, and their surfaces were completely corroded. The presence of the anodized layer can explain the initial higher impedance of the non-sealed anodized sample; however, the results demonstrate that the unprotected open structure of the pores is unable to effectively hinder the corrosion process upon immersion in an aggressive medium.

Hydrothermal sealing treatment (HTS) confirmed to be an effective methodology to improve the corrosion resistance of the TSA anodized layer. Samples anodized at 16 V, 14 V and 10 V exhibited high and stable impedance modulus, and no corrosion could be seen at the samples surface after 1008 h (42 days) of immersion in the 0.1 $mol.L^{-1}$ NaCl solution. Nevertheless, the sample anodized at 8 V showed a relatively poor anticorrosion behaviour and failed after 168 h (7 days) of test, indicating that the HTS treatment must be applied to anodized samples with more opened pore structure.

The EIS investigation showed that the application of the GPTMS-TEOS sol-gel hybrid coating to AA2524 anodized in TSA is a very promising surface treatment. Irrespectively to the anodizing voltage, all samples showed a very good anticorrosion behaviour during the 1008 h (42 days) of test in 0.1 $mol.L^{-1}$ NaCl solution, and no corrosion could be detected at the samples surface. GDOES depth profiles obtained with those samples indicated complete penetration of the hybrid solution into the pores and evidenced that the distribution of the hybrid sol-gel within the pores is extremely dependent of the porous layer thickness. Samples produced at lower voltages, presented complete pore filling and, therefore, higher impedance behaviour of the porous layer.

EEC fitting of the EIS diagrams helped to interpret the overall corrosion results. It was evidenced that the resistance of the sol-gel layer to aggressive species penetration was much higher than that afforded by the pores sealed with HTS, helping to explain the better overall EIS response of this former treatment. In addition, the fitting results confirmed the prominent role played by the barrier layer on the corrosion protection of the porous AAO, irrespectively to the post-treatment. In this way, for each investigated post-treatment, AA2524 anodized at 14 V and 16 V showed the best impedance behaviour.

Salt-spray tests confirmed the best anticorrosion performance of the samples anodized at 14 V and 16 V, and highlighted that, for these particular anodizing conditions, the AA2524 samples anodized in TSA and coated with the sol-gel were less sensitive to pitting corrosion onset and growth than the HTS treated samples. Nevertheless, the results of these tests evidenced a surface peeling process of the sol-gel layer for the samples anodized at lower voltages (8 V and 10 V), which presented a complete sol-gel surface coverage, leading them to present a worst overall anticorrosion resistance than their HTS counterparts.

Rheological characterization showed good stability of the sol-gel solution after 336 h of hydrolysis. Anodized samples protected with the hybrid sol-gel which hydrolysis solution was

aged up to this time showed excellent EIS response up to 1008 h of immersion in the 0.1 mol.L^{-1} NaCl solution.

Preliminary EIS tests performed with non-anodized (only pre-treated) and TSA anodized (14 V) AA2524 samples protected with the hybrid sol-gel layer and with an epoxy based top coating indicated a good compatibility between the two protective layers. High and stable impedance modulus were obtained (superior to 10^{10} Ω.cm^2) up to 1344 h (8 weeks) of test in NaCl 0.1 mol.L^{-1}. Only one time constant was observed during the whole test period, indicating that the substrate was not reached. The salt spray test highlighted the good interaction between the sol-gel and the organic coating (epoxy) and, in very good agreement with the EIS results, the samples protected with the sol-gel and the epoxy coating presented only few pits after 1008 h of exposure to the chamber, independently of the anodizing procedure. This is a very promising result for future industrial use of the sol-gel technology in the aerospace industry.

7 RECOMMENDATIONS FOR FUTURE WORKS

Regarding the hybrid sol-gel solution - optimize the sol-gel hydrolysis solution composition by modifying the TEOS-GPTMS concentrations; optimize the sol-gel withdrawal rate in order to improve the sol-gel distribution on top of samples anodized at 14 V; investigate the effect of temperature and curing time on the protection afforded by the sol-gel layer. Increase the proportion of water in the hydrolysis solution and/or test completely water-soluble silane precursors. Consider sol-gel spray coating application, as used in the aerospace industry.

Increase the comprehension on the ageing of the hydrolysis solution by performing rheological studies up to the gelation point coupled to the analysis of the hydrolysis and condensation reactions by means of FT-IR.

Continue the investigation of the corrosion resistance of sol-gel coated samples protected with a top coating. In this regard, it is particularly important to control the thickness of the organic coating.

Test other coating systems of interest to the aerospace industry applied to the TSA anodized Al alloys protected with the hybrid sol-gel, tailoring this latter in order to improve their mutual compatibility.

Use the same methodology for other alloys of interest to the aerospace industry, specially Al-Li-Cu ones.

8 REFERENCES

AERTS, T.; DIMOGERONTAKIS, TH.; GRAEVE, I. DE.; FRANSAER, J.; TERRYN, H. **Influence of the anodizing temperature on the porosity and the mechanical properties of the porous anodic oxide film.** Surface and Coatings Technology, v. 201, p. 7310–7317, 2007.

AIROLDI, C.; FARIAS, R. F. de. **Alcóxidos como precursores na síntese de novos materiais através do processo sol-gel.** Quimica Nova, v. 27(1), p. 84-88, 2004

ARENAS, M. A.; CONDE, A.; DAMBORENEA, J. J. DE. **Effect of acid traces on hydrothermal sealing of anodising layers on 2024 aluminium alloy.** Electrochimica Acta, v. 55, p. 8704-8708, 2010.

ASSOCIAÇÃO BRASILEIRA DO ALUMÍNIO. **Tratamento de Superfície.** Guia técnico do alumínio. 1a ed. São Paulo: ABAL, 1996. p. 39-56

BAJAT, J. B.; MIŠKOVIC´-STANKOVIC, V. B.; KACAREVIC´-POPOVIC, Z.´ **Corrosion stability of epoxy coatings on aluminum pretreated by vinyltriethoxysilane.** Corrosion Science, v. 50, p. 2078–2084, 2008.

BALBYSHEV, V. N.; ANDERSON, K. L.; SINSAWAT, A.; FARMER, B. L.; DONLEY, M. S. **Modeling of nano-sized macromolecules in silane-based self-assembled nano-phase particle coatings.** Progress in Organic Coatings, v. 47, p. 337–341, 2003.

BARBUCCI, A.; CABOT, P. L.; BRUZZONE, G.; CERISOLA, G**. Role of intermetallics in the activation of Al–Mg–Zn alloys.** Journal of Alloys and Compounds, v. 268, p. 295–301, 1998.

BARON-WIECHÉC, A.; BURKE, M. G.; HASHIMOTO, T.; LIU, H.; SKELDON, P.; THOMPSON, G. E.; HABAZAKI, H.; GANEM J. -J.; VICKRIDGE, I. C. **Tracer study of pore initiation in anodic alumina formed in phosphoric acid.** Electrochimica Acta, v. 113, p. 302–312, 2013.

BIERWAGEN, G.; TALLMAN, D.; LI, J.; HE, L.; JEFFCOATE, C. **EIS studies of coated metals in accelerated exposure.** Progress in Organic Coatings, v. 46, p. 148-157, 2003.

BIRBILIS, N.; BUCHHEIT, R. G. **Electrochemical Characteristics of Intermetallic Phases in Aluminum Alloys.** Journal of The Electrochemical Society, v. 152(4), p. B140-B151, 2005.

BREVNOV, D. A.; RAO, G. V. R.; LÓPEZ, G. P.; ATANASSOV, P. B**. Dynamics and temperature dependence of etching processes of porous and barrier aluminum oxide layers.** Electrochimica Acta, v. 49, p. 2487–2494, 2004.

BOAG, A.; HUGHES, A. E.; GLENN, A. M.; MUSTER, T. H.; MCCULLOCH, D. **Corrosion of AA2024-T3 Part I: Localised corrosion of isolated IM particles.** Corrosion Science, v. 53, p. 17–26, 2011.

BOAG, A.; HUGHES, A. E.; WILSON, N. C.; TORPY, A.; MACRAE, C. M.; GLENN, A. M.; MUSTER, T. H. **How complex is the microstructure of AA2024-T3.** Corrosion Science, v. 51, p. 1565-1568, 2009.

BOAG, A.; TAYLOR, R. J.; MUSTER, T. H.; GOODMAN, N.; MCCULLOCH, D.; RYAN, C.; ROUT, B.; JAMIESON, D.; HUGHES, A. E. **Stable pit formation on AA2024-T3 in a NaCl environment.** Corrosion Science, v. 52 , p. 90–103, 2010.

BOGDANOV, Z.; POPOVIC, N.; MILIC, M.; NENADOVIC, T. **Investigation of the barrier layer of porous anodic coatings on aluminium.** Thin Solid Films, v. 193/194, p. 675- 682, 1990.

BOISIER, G.; PÉBÈRE, N.; DRUEZ, C.; VILLATTE, M.; SUEL, S. **FESEM and EIS Study of Sealed AA2024 T3 Anodized in Sulfuric Acid Electrolytes: Influence of Tartaric Acid.** Journal of The Electrochemical Society, v. 155, p. C521-C529, 2008.

BOISIER, G.; LAMURE, A.; PÉBÈRE, N.; PORTAIL, N.; VILLATTE, M. **Corrosion protection of AA2024 sealed anodic layers using the hydrophobic properties of carboxylicacids.** Surface and Coatings Technology, v. 203, p. 3420–3426, 2009.

BONORA, P. L.; DEFLORIAN, F.; FEDRIZZI, L. **Electrochemical impedance spectroscopy as a tool for investigating underpaint corrosion.** Electrochimica Acta, v. 41, n. l/8, p. 1073- 1082, 1996.

BOUSQUET, E. **Durabilité des Assemblages Soudès par Friction Stir Welding (FSW)**. L'Université de Bordeaux 1. Bordeaux, França, 21 de Julho de 2011, 254 p.

BROWN, G. M.; SHIMIZU, K.; KOBAYASHI, K.; SKELDON, P.; THOMPSON, G. E.; WOOD, G. C. **The growth of a porous oxide film of a unique morphology by anodic oxidation of an Al-0.5wt% Ni alloy.** Corrosion Science, v. 40, p. 1575-1586, 1988.

BUCHHEIT, R. G.; GRANT, R. P.; HLAVA P. F.; MCKENZIE, B.; ZENDER, G. L. **Local Dissolution Phenomena Associated with S Phase (Al_2CuMg) Particles in Aluminum Alloy 2024-T3.** Journal of the Electrochemical Society, v. 144(8), p. 2621-2628, 1997.

CAI, J.-P.; LI, B.; LIU, M. –H. ; XIONG, J.-J.; ZHENG, L**. Effect of anodizing on fatigue performance of aeronautic aluminum alloys.** Journal of Aeronautical Material, v. 27(2), p. 25-28, 2007.

CAMPESTRINI, P.; WESTING, E. P. M. VAN; WIT, J. H. W. DE. **Influence of surface preparation on performance of chromate conversion coatings on Alclad 2024 aluminium alloy Part I: Nucleation and growth.** Electrochimica Acta, v. 46, p. 2553–2571, 2001.

CAPELOSSI, V. R.; POELMANC, M.; RECLOUXA, I.; HERNANDEZ, R. P. B.; MELO, H. G. de.; OLIVIERA, M. G. **Corrosion protection of clad 2024 aluminum alloy anodized in tartaric-sulfuric acid bath and protected with hybrid sol–gel coating.** Electrochimica Acta, v. 124, pg. 69 - 79, 2014.

CARANGELO, A.; CURIONI, M.; ACQUESTA, A.; MONETTA, T.; BELLUCCI, F. **Application of EIS to In Situ Characterization of Hydrothermal Sealing of Anodized Aluminum Alloys: Comparison between Hexavalent Chromium-Based Sealing, Hot Water Sealing and Cerium-Based Sealing.** Journal of The Electrochemical Society, v. 163 (10), p. C619-C626, 2016.

CERVANTES, R. L.; MURR, L; EARROWOOD, R. M. **Copper nucleation and growth during the corrosion of aluminum alloy 2524 in sodium chloride solutions.** Journal of Material Science, v. 36, p. 4079 – 4088, 2001.

CHAHROUR, K. M.; AHMED, N. M.; HASHIM, M. R.; ELFADILL, N. G.; MARYAM, W.; AHMAD, M. A.; BOUOUDINA, M. **Effects of the voltage and time of anodization on modulation of the pore dimensions of AAO films for nanomaterials synthesis.** Superlattices and Microstructures, v. 88, p. 489-500, 2015.

CHEN, G., GAO, S., & WEI, R. **Microconstituent-induced pitting corrosion in aluminium alloy 2024-T3.** Corrosion, *v*. 52, n. 1, p. 8-15, 1996.

CHEN, M.; LU, X.; GUO, Z.; HUANG, R. **Influence of hydrolysis time on the structure and corrosion protective performance of (3-mercaptopropyl)triethoxysilane film on copper.** Corrosion Science, v. 53, p. 2793–2802, 2011.

CHEN, Y. Q.; PAN, S. P.; ZHOU, M. Z.; YI, D. Q.; XU, D. Z.; XU, Y. F. **Effects of inclusions, grain boundaries and grain orientations on the fatigue crack initiation and propagation behavior of 2524-T3 Al alloy.** Materials Science & Engineering, v. A 580, p. 150–158, 2013.

CHIDAMBARAM, D.; CLAYTON, C. R.; HALADA, G. P. **A Duplex Mechanism-Based Model for the Interaction between Chromate Ions and the Hydrated Oxide Film on Aluminum Alloys.** Journal of the Electrochemical Society, v. 150, n. 5, p. B224-B237, 2003.

CHOI, Y. C.; HYEON, J. Y.; BU, S. D. **Effects of Anodizing Voltages and Corresponding Current Densities on Self-ordering Process of Nanopores in Porous Anodic Aluminas Anodized in Oxalic and Sulfuric Acids.** Journal of the Korean Physical Society, v. 55, n. 2, p. 835-840, 2009.

CLAYDEN, J.; GEEVES, N.; WARREN, S. **Organic Chemistry.** Oxford University Press, 2. ed, p. 1234, 2012.

COSTA, T. S.; ORNELAS, D. L.; GUIMARÃES, P. I. C.; MERÇON, F. **Experimentos com alumínio.** Química Nova na Escola, v. 23, p. 38-40, 2006.

COTE, J.; HOWLETT, E. E.; WHEELER, M. J.; LAMB, H. J. **The Behavior of Intermetallic Compounds in Aluminum during Sulfuric Acid Anodizing, Part 1: AlMn, AlFe, $AlMg_2Si$, AlCr Alloys.** Plating, v. 56, n. 4, p. 386-394, 1969.

COTE, J.; HOWLETT, E. E.; LAMB, H. J. **The Behavior of Intermetallic Compounds in Aluminum during Sulfuric Acid Anodizing Part 2: AlCu, AlMg, AlSi, AlTi, AlFeSi, AlZnMg Alloys.** Plating, v. 57, n. 5, p. 484-496, 1970.

COTELL, C. M.; SPRAGUE, J. A.; SMIDT, F. A. **Anodizing.** ASM Handbook, 1994. v. 5: Surface Engineering, p. 482-493.

CREE, A. M.; DEVLIN, M.; CRITCHLOW, G.; HIRST, T. **Fatigue and fracture assessment of toxic metal replacement coatings for aerospace applications.** Transactions of the Institute of Metal Finishing, v. 88(6), p. 303-310, 2010.

CROSSLAND, A. C.; HABAZAKI, H.; SHIMIZU, K.; SKELDON, P.; THOMPSON, G. E.; WOOD, G. C.; ZHOU, X.; SMITH, C. J. E. **Residual flaws due to formation of oxygen bubbles in anodic alumina.** Corrosion Science, v. 41, p. 1945-1954, 1999.

CURIONI, M.; MIERA, M. S.; SKELDON, P.; THOMPSON, G. E.; FERGUSON, J. **Macroscopic and Local Filming Behavior of AA2024 T3 Aluminum Alloy during Anodizing in Sulfuric Acid Electrolyte.** Journal of The Electrochemical Society, v. 155(8), p. C387-C395, 2008a.

CURIONI, M.; ROETH, F.; GARCIA-VERGARA, S. J.; HASHIMOTO, T.; SKELDON, P.; THOMPSON, G. E.; FERGUSON, J. **Enrichment, incorporation and oxidation of copper during anodising of aluminium–copper alloys.** Surface and Interface Analysis, v. 42, p. 234-240, 2010.

CURIONI, M.; SKELDON, P.; KOROLEVA, E.; THOMPSON, G. E.; FERGUSON, J. **Role of Tartaric Acid on the Anodizing and Corrosion Behavior of AA 2024 T3 Aluminum Alloy.** Journal of The Electrochemical Society, v. 156(4), p.C147-C153, 2009.

CURIONI, M.; SKELDON, P.; THOMPSON, G. E.; FERGUSON, J. **Graded Anodic Film Morphologies for Sustainable Exploitation of Aluminium Alloys in Aerospace.** Advanced Materials Research, v.38, p.48-55, 2008b.

CURIONI, M.; ZULETA, A. A.; CORREA, E.; PAN X.; BARON-WIECHEC, A.; SKELDON, P.; CASTANO, J. G.; ECHEVERRIA, F.; THOMPSON, G. E. **Formation of protective anodic oxides on aluminium by low voltage anodising in sulphuric acid with cerium nitrate and tartaric acid additions.** Transactions of the Institute of Metal Finishing, v. 90(6), p. 290-297, 2012.

CRITCHLOW, G. W.; BREWIS, D. M. **Review of surface pretreatments for aluminium alloys.** J. Adhesion and Adhesives, v. 16, p. 255-275, 1996.

DALMORO, V.; ALEMÁN, C.; FERREIRA, C. A.; SANTOS, J. H. Z. DOS; AZAMBUJA, D. S., ARMELIN, E. T**he influence of organophosphonic acid and conducting polymer on the adhesion and protection of epoxy coating on aluminium alloy.** Progress in Organic Coatings, v. 88, p. 181–190, 2015.

DEBARTOLO E. A.; HILLBERRY, B. M. **A model of initial flaw sizes in aluminum alloys.** International Journal of Fatigue, v. 23, p. S79–S86, 2001.

DEBUYCK, F.; MOORS, M.; VAN PETEGHEM, A. P. **The influence of the anodization temperature and voltage porosity of the anodization layer on aluminium.** Materials Chemistry and Physics, v. 36, p. 146-149, 1993

DEFLORIAN, F.; ROSSI, S.; FEDRIZZI, L. **Silane pre-treatments on copper and aluminium.** Electrochimica Acta, v. 51, p. 6097–6103, 2006.

DIGGLE, J. W.; DOWNIE, T. C.; GOULDING, C. W. **Anodic oxide films on aluminum.** Chem. Rev., v. 69 (3), p. 365-405, 1969.

DOCHE, M. L.; RAMEAU, J. J.; DURAND, R.; NOVEL-CATTIN, F**. Electrochemical behaviour of aluminium in concentrated NaOH solutions.** Corrosion Science, v. 41, p. 805-826, 1999.

DOMINGUES, L.; FERNANDES, J. C. S.; DA CUNHA BELO, M.; FERREIRA, M. G. S.; GUERRA-ROSA, L. **Anodising of Al 2024-T3 in a modified sulphuric acid/boric acid bath for aeronautical applications.** Corrosion Science, v. 45, p. 149–160, 2003.

DONLEY, M. S.; MANTZ, R. A.; KHRAMOV, A. N.; BALBYSHEV, V. N.; KASTEN, L. S.; GASPAR, D. J. **The self-assembled nanophase particle (SNAP) process: a nanoscience approach to coatings.** Progress in Organic Coatings, v. 47, p.401–415, 2003.

DROMGOOL, M. B. **Moisture Issues with Solvent Free Epoxies.** Retrieved from*:* <http://www.epoxyproducts.com/solventfree.pdf>. Data: Date accessed: October 20th 2016.

DRUART, M. E.; RICHIR, J. B.; POIRIER, C.; MASERI, F.; GODEAU, N.; LANGER, L.; OLIVIER, M. **Influence of sol–gel application conditions on metallic substrate for optical applications**. Corrosion Engineering, Science and Technology, v. 46(6), p. 677-684, 2011.

DUONG, N. T.; HANG, T. T. X.; NICOLAY, A.; PAINT, Y.; OLIVIER, M. **Corrosion protection of carbon steel by solvent free epoxy coating containing hydrotalcites intercalated with different organic corrosion inhibitors.** Progress in Organic Coatings, v. 101, p. 331–341, 2016.

FARNAN, I.; DUPREE, R. **Structural Chemistry of Anodic Alumina.** Thin Solid Films, v. 173, p. 209-2 15, 1989.

FELIU, S. J.; BARTOLOME, M. J.; GONZÁLEZ, J. A. LOPEZ, V.; FELIU, S. **Passivating oxide film and growing characteristics of anodic coatings on aluminium alloys.** Applied Surface Science, v. 254, p. 2755–2762, 2008.

FENG, Z.; LIU, Y.; THOMPSON, G. E.; SKELDON, P. **Sol–gel coatings for corrosion protection of 1050 aluminium alloy.** Electrochimica Acta, v. 55, p. 3518–3527, 2010.

FIGUEIRA, R. B.; SILVA, C. J. R.; PEREIRA, E. V. **Organic–inorganic hybrid sol–gel coatings for metal corrosion protection: a review of recent progress.** J. Coat. Technol. Res., v. 12, n. 1, p. 1–35, 2015.

FRANQUET, A.; TERRYN, H.; VEREECKEN, J. **IRSE study on effect of thermal curing on the chemistry and thickness of organosilane films coated on aluminium.** Applied Surface Science, v. 11, p. 259–269, 2003.

FRATILA-APACHITEI, L. E.; DUSZCZYK, J.; KATGERMAN, L. **Voltage transients and morphology of AlSi(Cu) anodic oxide layers formed in H_2SO_4 at low temperature.** Surface and Coatings Technology, v. 157, p. 80-94, 2002.

FRATILA-APACHITEI, L. E.; TERRYN, H.; SKELDON, P.; THOMPSON, G. E.; DUSZCZYK, J.; KATGERMAN, L. **Influence of substrate microstructure on the growth of anodic oxide layers.** Eletrochimica Acta, v. 49, p. 1127-1140, 2004.

FUKUDA, Y.; FUKUSHIMA, T. **Behavior of Sulfate Ions during Formation of Anodic Film on Aluminium.** Bulletin of the Chemical Society of Japan, v. 53, p. 3125-3130, 1980.

GANDHI, S.; METROKE, T. L.; EASTMAN, M. A.; OOIJ, W. J. VAN, APBLETT, A. **Effect of the Degree of Hydrolysis and Condensation of Bis-[Triethoxysilylpropyl]Tetrasulfide on the Corrosion Protection of Coated Aluminum Alloy 2024-T3.** Corrosion, v. 62, n. 7, p. 612-623, 2006.

GARCÍA-RUBIO, M.; LARA, M. P. DE; OCÓN, P.; DIEKHOFF, S.; BENEKE, M.; LAVÍA, A.; GARCÍA, I. **Effect of postreatment on the corrosion behaviour of tartaric–sulphuric anodic films.** Electrochimica Acta, v.54, p.4789–4800, 2009a.

GARCÍA-RUBIO, M.; OCÓN, P.; CLIMENT-FONT, A.; SMITH, R. W.; CURIONI, M.; THOMPSON, G. E.; SKELDON, P.; LAVÍA, A.; GARCÍA, I. **Influence of molybdate species on the tartaric acid/sulphuric acid anodic films grown on AA2024 T3 aerospace alloy**. Corrosion Science, v.51, p.2034–2042, 2009b.

GARCÍA-RUBIO, M.; OCÓN, P.; CURIONI, M.; THOMPSON, G. E.; SKELDON, P.; LAVÍA, A.; GARCÍA, I. **Degradation of the corrosion resistance of anodic oxide films through immersion in the anodising electrolyte.** Corrosion Science, v.52, p.2219–2227, 2010.

GARCIA-VERGARA, S. J.; IGLESIAS-RUBIANES, L.; BLANCO-PINZON, C. E.; SKELDON, P.; THOMPSON, G. E.; CAMPESTRINI, P. **Mechanical instability and pore generation in anodic alumina.** Proceedings of the Royal Society, v. A 462, p. 2345–2358, 2006a.

GARCIA-VERGARA, S. J.; KHAZMI, K. EL; SKELDON, P.;THOMPSON, G. E. **Influence of copper on the morphology of porous anodic alumina.** Corrosion Science, v. 48, p. 2937–2946, 2006b.

GARCIA-VERGARA, S. J.; LE CLERE, D.; HASHIMOTO, T.; HABAZAKI, H.; SKELDON, P.; THOMPSON, G. E. **Optimized observation of tungsten tracers for investigation of formation of porous anodic alumina.** Electrochimica Acta, v. 54, p. 6403–6411, 2009.

GARCIA-VERGARA, S. J.; SKELDON, P.; THOMPSON, G. E.; HABAZAKI, H. **A flow model of porous anodic film growth on aluminium.** Electrochimica Acta, v. 52, p. 681–687, 2006c.

GARCIA-VERGARA S.J.; SKELDON, P.; THOMPSON G. E.; HABAZAKI, H. **A tracer investigation of chromic acid anodizing of aluminium.** Surface and Interface Analysis, v. 39, p. 860–864, 2007a.

GARCIA-VERGARA, S. J.; SKELDON, P.; THOMPSON, G. E.; HABAZAKI, H. **Pore development during anodizing of Al–3.5 at.%W alloy in phosphoric acid.** Surface and Coatings Technology, v. 201, p. 9506–9511, 2007b.

GARCIA-VERGARA, S. J.; SKELDON, P.; THOMPSON, G. E.; HABAKAKI. H**. Pore development in anodic alumina in sulphuric acid and borax electrolytes.** Corrosion Science, v. 49, p 3696–3704, 2007c.

GARCIA-VERGARA, S. J.; SKELDON, P.; THOMPSON, G. E.; HABAZAKI, H. **Stress generated porosity in anodic alumina formed in sulphuric acid electrolyte.** Corrosion Science, v. 49, p. 3772–3782, 2007d.

GARCIA-VERGARA, S. J.; SKELDON, P.; THOMPSON, G. E.; HABAKAKI, H. **Tracer studies of anodic films formed on aluminium in malonic and oxalic acids.** Applied Surface Science, v. 254, p. 1534–1542, 2007e.

GARCIA-VERGARA, S. J.; HABAZAKI, H.; SKELDON, P.; THOMPSON, G. E. **Tracer studies relating to alloying element behaviour in porous anodic alumina formed in phosphoric acid.** Electrochimica Acta, v. 55, p. 3175–3184, 2010.

GLENN, A. M.; MUSTER, T. H.; LUO, C.; ZHOU, X.; THOMPSON, G. E.; BOAG, A.; HUGHES, A. E. **Corrosion of AA2024-T3 Part III: Propagation.** Corrosion Science, v. 53, p. 40–50, 2011.

GONZÁLEZ, J. A.; LOPEZ, V.; OTERO, E.; BAUTISTA, A.; LIZARBE, R.; BARBAT, C.; BALDONEDOT, J. L. **Overaging of sealed and unsealed aluminium oxide films.** Corrosion Science, v. 39 (6), p. 1109-1118, 1997.

GONZÁLEZ, J.; MORCILLO, M.; ESCUDERO, E.; LÓPEZ, V.; OTERO, E. **Atmospheric corrosion of bare and anodized aluminium in a wide range of environmental conditions. Part I: Visual observations and gravimetric results.** Surface and Coatings Technology, v. 153, p. 225–234, 2002.

GONZÁLEZ, J. A.; LOPEZ, V.; BAUTISTA, A.; OTERO, E. **Characterization of porous aluminium oxide films from a.c. impedance measurements.** Journal of applied electrochemistry, v. 29, p. 229-238, 1999.

GOROKH, G.; MOZALEV, A.; SOLOVEI, D.; KHATKO, V.; LLOBET, E.; CORREIG, X. **Anodic formation of low-aspeio porous alumina films for metal-oxide sensor application.** Electrochimica Acta, v. 52, p. 1771–1780, 2006.

GRIESHOP, S.; BUCHHEIT, R. **Comparison of the Corrosion Behavior of High Strength Aluminum Alloys after Exposure to ASTM B117 Environment.** Retrieved from:<https://kb.osu.edu/dspace/handle/1811/60362>. Date accessed: March 1st, 2015.

GUMINSKI, R. D.; SHEASBY, P. G.; LAMB, H. J. **Reaction rates of second-phase constituents in aluminium during etching, brightening and oxalic acid anodizing processes.** Transactions of the Institute of Metal Finishing, v. 46, p. 44–48, 1968.

HABAZAKI, H.; SHIMIZU, K.; PAEZ, M. A.; SKELDON, P.; THOMPSON, G. E.; WOOD, G. C.; XHOU, X. **Oxidation of Copper and Mobility of Copper Ions During Anodizing of an A1-1.5 wt.% Cu Alloy.** Surface and Interface Analysis, .v. 23, p. 892-898, 1995.

HABAZAKI, H.; SHIMIZU, K.; SKELDON, P.; THOMPSON, G. E.; WOOD, G. C. **Inter-relationships between ionic transport and composition in amorphous anodic oxides.** Proceedings of the Royal Society A, v. 453, p. 1593-1609, 1997a.

HABAZAKI, H.; ZHOU, X.; SHIMIZUT, K.; SKELDON, P.; THOMPSON, G. E.; WOOD, G. C. **Mobility of copper ions in anodic alumina films.** Electrochimica Acta, v. 42, n. 17, p. 2621-2635, 1997.

HAN, H.; PARK, S. J.; JANG, J. S.; RYU, H.; KIM, K. J.; BAIK, S.; LEE, W. **In situ determination of the pore opening point during wet-chemical etching of the barrier layer of porous anodic aluminum oxide: nonuniform impurity distribution in anodic oxide.** A*CS* Applied Materials and Interfaces, v. 5, p. 3441–3448, 2013.

HAO, L.; CHENG, B. R. **Sealing Processes of Anodic Coatings-Past, Present and Future.** Metal Finishing, v. 98, p. 8-18, 2000.

HITZIG, J.; JÜTTNER, K.; LORENZ, W. J.; PAATSCH, **W.** AC-Impedance Measurements on Corroded Porous Aluminum Oxide Films. Journal of Electrochemical Society, v. 133, p. **887-892, 1986.**

HITZIG, J.; JUTTNER, K.; LORENZ, W. J.; PAATSCH, W. **Ac-impedance measurements on porous aluminium oxide films.** Corrosion Science, v. 24, b. 11/12, p. 945-952, 1984.

HIRAI, S.; SHIMAKAGE, K.; AIZAWA, S.; WADA, K. **Alkaline corrosion resistance of anodized aluminum coated with zirconium oxide by a sol-gel process.** Journal of the American Ceramic Society, v. 81, p. 3087-3092, 1998.

HIRAI, S.; SHIMAKAGE, K.; SEKIGUCHI, M.; WADA, K.; NUKUI, A. **Zirconium Oxide Coating on Anodized Aluminum by the Sol–Gel Process Combined with Ultraviolet Irradiation at Ambient Temperature.** Journal of the American Ceramic Society, v. 82, n. 8, p. 2011–2016, 1999.

HOAR, T. P.; MOTT, N. F. **A Mechanism for the formation of porous anodic oxide filmes on aluminium.** Journal of Physics and Chemistry of Solids, v. 9, p. 97-99, 1959.

HOAR, T. P.; WOOD, G. C. **The sealing of porous anodic oxide films on aluminium.** Electrochimica Acta, v. 7, p. 333-353, 1962.

HUGHES, A. E.; BOAG, A.; GLENN, A. M.; MCCULLOCH, D.; MUSTER, T. H.; RYAN, C.; LUO, C.; ZHOU, X.; THOMPSON, G. E. **Corrosion of AA2024-T3 Part II: Co-operative corrosion.** Corrosion Science, v. 53, p. 27–39, 2011.

HUGHES, A. E.; MACRAE, C.; WILSON, N.; TORPY, A.; MUSTER, T. H.; GLENN, A. M. **Sheet AA2024-T3: a new investigation of microstructure and composition.** Surface and Interface Analysis, v. 42, p. 334-338, 2010.

IGLESIAS-RUBIANES, L.; GARCIA-VERGARA, S. J.; SKELDON, P.; THOMPSON, G. E.; FERGUSON, J.; BENEKE, M. **Cyclic oxidation processes during anodizing of Al–Cu alloys.** Electrochimica Acta, v. 52, p. 7148–7157, 2007.

JESSENSKY, O.; MÜLLER, F.; GÖSELE, U. **Self-Organized Formation of Hexagonal Pore Structures in Anodic Alumina.** Journal of the Electrochemical Society, Volume 145(11), p. 3735-3740, 1998.

JI, W.; HU, J.; LIU, L.; ZHANG, J.; CAO, C. **Improving the corrosion performance of epoxy coatings by chemical modification with silane monomers**. Surface & Coatings Technology, v.201, p.4789–4795, 2007.

JIANG, M.; WU, L.; HU, J.; ZHANG, J. **Silane-incorporated epoxy coatings on aluminum alloy (AA2024). Part 1: Improved corrosion performance**. Corrosion Science, v. 92, p. 118–126, 2015.

KAKDE, V.; MANNARI, V. **Advanced chrome-free organic–inorganic hybrid pretreatments for aerospace aluminum alloy 2024-T3—application of novel bis-ureasil sol–gel precursors**. J. Coat. Technol. Res., v. 6(2), p. 201–211, 2009.

KELLER, F.; HUNTER, M. S.; ROBINSON, D. L**. Structural Features of Oxide Coatings on Aluminum.** Journal of the Electrochemical Society, v.100(9), p. 411-419, 1953.

KENDIG, M.; JEANJAQUET, S.; ADDISON, R.; WALDROP, J. **Role of hexavalent chromium in the inhibition of corrosion of aluminum alloys.** Surface and Coatings Technology, v. 140, p. 58-66, 2001.

KHRAMOV, A. N.; BALBYSHEV, V. N.; VOEVODIN, N. N.; DONLEY, M. S. **Nanostructured sol–gel derived conversion coatings based on epoxy- and amino-silanes.** Progress in Organic Coatings, v. 47, p. 207–213, 2003.

KITTEL, J.; CELATI, N.; KEDDAM, M.; TAKENOUTI, H. **Influence of the coating–substrate interactions on the corrosion protection: characterisation by impedance spectroscopy of the inner and outer parts of a coating.** Progress in Organic Coatings, v. 46, p. 135–147, 2003.

KOSMULSKI, M. **Isoelectric points and points of zero charge of metal (hydr)oxides: 50 years after Parks'review.** Advances in colloid and Interface Science, v. 238, p. 1-61, 2016.

LAMAKA, S.V.; XUE, H. B.; MEIS, N. N. A. H.; ESTEVES, A. C. C.; FERREIRA, M. G. S. **Fault-tolerant hybrid epoxy-silane coating for corrosion protection of magnesium alloy AZ31.** Progress in Organic Coatings, v. 80, p. 98–105, 2015.

LAMPKE, T.; DARWICH, S.; NICKEL, D.; WIELAGE, B. **Development and characterization of sol-gel composite coatings on aluminum alloys for corrosion protection.** Mat.-wiss. u. Werkstofftech, v. 39(12), p. 914-919, 2008.

LE COZ, F.; ARURAULT, L.; DATAS, L. **Chemical analysis of a single basic cell of porous anodic aluminium oxide templates.** Material Characterization, v. 61, p. 283 – 288, 2010.

LEE, E.; JEONG, Y.; KIM S. **S-N Fatigue Behavior of Anodized 7050-T7451 Produced in Different Electrolytes.** Metallurg. Mat. Transact., v. 43A, p. 2012-2011, 2012.

LEE, W.; PARK, S. **Porous Anodic Aluminum Oxide: Anodization and Templated Synthesis of Functional Nanostructures.** Chemical Reviews, v. 114, p.7487−7556, 2014.

LI, F., ZHANG, L., METZGER, R.M. **On the Growth of Highly Ordered Pores in Anodized Aluminum Oxide.** Chemistry of Materials, v.10, p. 2470-2480, 1998.

LIU, J.; CHAUDHURY, M. K.; BERRY, D. H.; SEEBERGH, J. E.; OSBORNE, J. H.; BLOHOWIAK, K. Y. **Effect of Surface Morphology on Crack Growth at a Sol-Gel Reinforced Epoxy/Aluminum Interface.** The Journal of Adhesion, v. 82, p. 487–516, 2006.

LIU, T.; ZHANG, F.; XUE, C.; LI, L.; YIN, Y. **Structure stability and corrosion resistance of nano-TiO_2 coatings on aluminum in seawater by a vacuum dip-coating method.** Surface and Coatings Technology, v. 205, p. 2335-2339, 2010.

LIU, Y.; ARENAS, M. A.; FRUTOS, A. DE; DAMBORENEA, J. DE, CONDE, A.; SKELDON, P.; THOMPSON, G. E.; BAILEY, P.; NOAKES, T. C. Q. **Influence of nitric acid pre-treatment on Al–Cu alloys.** Electrochimica Acta, v. 53, p. 4454–4460, 2008.

LOHRENGEL, M. M. **Thin anodic oxide layers on aluminium and other valve metals: high field regime.** Materials Science and Engineering, v. R11, p. 243-294, 1993.

LÓPEZ, V.; BARTOLOMÉ, M. J.; ESCUDERO, E.; OTERO, E.; GONZÁLEZ, J. A. **Comparison by SEM, TEM, and EIS of Hydrothermally Sealed and Cold Sealed Aluminum Anodic Oxides.** Journal of The Electrochemical Society, v. 153 (3), p. B75-B82, 2006.

LÓPEZ, V.; OTERO, E.; BAUTISTA, A.; GONZÁLEZ, J. A. **Sealing of anodic films obtained in oxalic acid baths.** Surface and Coatings Technology, v. 124, p. 76–84, 2000.

LUNDER, O.; NISANCIOGLU, K. **The Effect of Alkaline-Etch Pretreatment on the Pitting Corrosion of Wrought Aluminum.** Corrosion, v. 44(7), p. 414-422, 1988.

MA, Y.; ZHOU, X.; THOMPSON, G. E.; CURIONI, M.; HASHIMOTO, T.; SKELDON, P.; THOMSON P.; FOWLES, M. **Anodic Film Formation on AA 2099-T8 Aluminum Alloy in Tartaric–Sulfuric Acid.** Journal of The Electrochemical Society, v. 158, n. (2), p. C17-C22, 2011a.

MA, Y.; ZHOU, X.; THOMPSON, G. E.; CURIONI, M.; ZHONG, X.; KOROLEVA, E.; SKELDON, P.; THOMSON, P.; FOWLES, M. **Discontinuities in the porous anodic film formed on AA2099-T8 aluminium alloy.** Corrosion Science, v. 53, p. 4141–4151, 2011b.

MANSFELD F.; KENDIG, M. W**. Evaluation of Anodized Aluminum Surfaces with Electrochemical Impedance Spectroscopy**. Journal of the Electrochemical Society, v. 135, p. 828-833, 1988.

MATA-ZAMORA, M. E.; SANIGER, J. M. **Thermal evolution of porous anodic aluminas: a comparative study.** Revista Mexicana de Física, v. 51, n. 5, p. 502-509, 2005.

MÍNGUEZ-BACHO, I.; RODRÍGUEZ-LÓPEZ, S.; CLIMENT, A.; FICHOU, D.; VÁZQUEZ, M.; HERNÁNDEZ-VÉLEZ, M. **Influence of sulfur incorporation into nanoporous anodic alumina on the volume expansion and self-ordering degree.** The Journal of Physical Chemistry C, V. 119, p. 27392-27400, 2015.

MOLCHAN, I. S.; MOLCHAN, T. V.; GAPONENKO, N. V.; SKELDON, P.; THOMPSON, G. E. **Impurity-driven defect generation in porous anodic alumina**. Electrochemistry Communications, v. 12, p. 693–696, 2010.

MOLENA DE ASSIS, C. **Estudo do comportamento de corrosão de ligas de alumínio soldadas por fricção (FSW) utilizando técnicas eletroquímicas globais e locais.** São Paulo: Escola Politécnica da Universidade de São Paulo. Departamento de Engenharia Química, 2017, 164 p.

MORETO, J. A.; GAMBONI, O.; RUCHERT, C. O. F. T.; ROMAGNOLI, F.; MOREIRA, M. F.; BENEDUCE, F.; BOSE FILHO, W. W. **Corrosion and fatigue behavior of new Al alloys.** Procedia Engineering, v. 10, p. 1521-1526, 2011.

MUBAROK, M. Z.; WAHAB, SUTARNO, WAHYUDI, S. **Effects of Anodizing Parameters in Tartaric-Sulphuric Acid on Coating Thickness and Corrosion Resistance of Al 2024 T3 Alloy.** Journal of Minerals and Materials Characterization and Engineering, v. 3, p. 154-163, 2015.

MUSEUX, F.; THEILMANN, R. **Introducing more eco-efficient chemical treatments for aircraft structure.** Towards a chromate-free Airbus. Flight air worthiness support technology (FAST), n. 45, 2009. Retrieved from*:* http:<//www.airbus.com/support/publications/>. Date accessed: January, 26th, 2017.

NAGAYAMA, M.; TAMURA, K. **On the mechanism of dissolution of porous oxide films on aluminium during anodizing.** Electrochimica Acta, v. 13, p. 1773-1783, 1969.

NICOLAY, A.; LANZUTTI, A.; POELMAN, M.; RUELLE, B.; FEDRIZZI, L.; DUBOIS, PH.; OLIVIER, M.-G. **Elaboration and characterization of a multifunctional silane/ZnOhybrid nanocomposite coating.** Applied Surface Science, v. 327, p. 379–388, 2015.

OKA, Y.; TAKAHASHI, T. **Structural analysis of anodic alumina films. Journal of Non-Crystalline Solids**, v. 30, p. 349-357, 1979.

ONO, S.; MASUKO, N. **Evaluation of pore diameter of anodic porous films formed on aluminum.** Surface and Coatings Technology, v. 169, p. 139–142, 2003.

ONO, S.; SAITO, M.; ASOH, H. **Self-ordering of anodic porous alumina formed in organic acid electrolytes.** Electrochimica Acta, v. 51, p. 827–833, 2005.

OOIJ, W. J. VAN; ZHU, D.; STACY, M.; SETH, A.; MUGADA, T.; GANDHI, J.; PUOMI, P. **Corrosion Protection Properties of Organofunctional Silanes —An Overview.** Tsinghua Science and Technology, v. 10, n. 6, p. 639-664, 2005.

OOIJ W. J. VAN; ZHU, D.; PALANIVEL, V.; LAMAR, J. A.; STACY, M. Overview: **The Potential of silanes for chromate replacement in metal finishing industries.** Silicon Chemistry, v. 3, p. 11–30, 2006.

OSBORNE, J. H.; BLOHOWIAK, K. Y.; TAYLOR, S. R.; HUNTER, C.; BIERWAGON, G.; CARLSON, B.; BERNARD, D.; DONLEY, M. S. **Testing and evaluation of nonchromated coating systems for aerospace applications.** Progress in Organic Coatings, v. 41, p. 217–225, 2001.

O'SULLIVAN, J. P.; WOOD, G. C. **The Morphology and Mechanism of Formation of Porous Anodic Films on Aluminium.** Retrieved from: <http://rspa.royalsocietypublishing.org/subscriptions>. Date accessed: November, 2nd, 2014.

PAEZ, M. A.; BUSTOS, O.; THOMPSON, G. E.; SKELDON, P.; SHIMIZU, K.; WOOD, G. C. **Porous Anodic Film Formation on an Al-3.5 wt % Cu Alloy.** Journal of The Electrochemical Society, v. 147, n. 3, p. 1015-1020, 2000.

PAEZ, M. A.; FOONG, T. M.; NI, C.T.; THOMPSON, G. E.; SHIMIZU, K.; HABAZAKI, H.; SKELDON, P.; WOOD, G. C. **Barrier-type Anodic Film formation film on an Al-3.5 wt% Cu alloy.** Corrosion Science, v. 38, n. 1, p. 59-72, 1996.

PALOMINO, L.E. M. **Caracterização microestrutural e eletroquímica de revestimentos ambientalmente amigáveis aplicados sobre a liga de Al 2024-T3**. 2007.265 p. Universidade de São Paulo. São Paulo, 14 de novembro de 2007. Retrieved from*:* <http://www.teses.usp.br/teses/disponiveis/3/3137/tde-14012008-093144/pt-br.php>. >. Date accessed: April, 25th, 2015.

PAREL, T. S.; WANG, S. C.; STARINK, M. J. **Hardening of an Al–Cu–Mg alloy containing Types I and II S phase precipitates.** Materials and Design, v. 31, p. S2–S5, 2010.

PATERMARAKIS, G.; PLYTAS, J. **A novel theory interpreting the extremes of current during potentiostatic anodising of Al and the mechanisms of normal and abnormal growth of porous anodic alumina films.** Journal of Electroanalytical Chemistry,v. 769, p. 97-117, 2016.

PATERMARAKIS, G.; CHANDRINOS, J.; MOUSSOUTZANIS, K. **Interface physicochemical processes controlling sulphate anion incorporation in porous anodic alumina and their dependence on the thermodynamic and transport properties of cations.** Journal of Electroanalytical Chemistry, v. 510, p. 59-66, 2001.

POURBAIX, M. **Atlas of electrochemical equilibria in aqueous solutions.** Houston: NACE, 2. ed., , p.173, 1974.

QUEIROZ, F. M. **Estudo do comportamento de corrosão dos intermetálicos presentes na liga AA 2024-T3, por meio de técnicas de microscopia associada a técnicas**

eletroquímicas. Universidade de São Paulo. Instituto de Pesquisas Energéticas e Nucleares. São Paulo, 2 de setembro de 2008. Retrieved from: http://www.teses.usp.br/teses/disponiveis/85/85134/tde-17082009-152449/pt-br.php. Date accessed: December 2nd, 2016.

QUEIROZ, F. M.; MAGNANI, M.; COSTA, I. MELO, H. G. de. **Investigation of the corrosion behaviour of AA 2024-T3 in low concentrated chloride media.** Corrosion Science,v. 50, p. 2646–2657, 2008.

QUEIROZ, F. M.; TERADA, M.; BUGARIN, A.F.S.; MELO, H. G.; COSTA, I. **Study of corrosion behavior of the AA2524-T3 alloy by electrochemical impedance spectroscopy.** In: XX SIBEE - Simpósio Brasileiro de Eletroquímica e Eletroanalítica, Uberlândia, 2015.

RAMANATHAN, L. V. **Corrosão e seu Controle.** São Paulo: Hemus, p.82-84, 1988.

RATEICK JR, R. G.; GRIFFITH, R. J.; HALL, D. A.; THOMPSON, K. A. **Relationship of microstructure to fatigue strength loss in anodised aluminium–copper alloys.** Materials Science and Technology, v. 21, p. 1227-1235, 2005.

REIS, F. M. dos. **Investigação do tratamento com moléculas auto-organizáveis para substituição da cromatização da liga AA5052H32 no preparo da superfície prévio a pintura.** 2005. 203 p. Retrieved from: http://pelicano.ipen.br/PosG30/TextoCompleto/Fernando%20Morais%20dos%20Reis_M.pdf >. Date accessed: April, 29th, 2015.

SAENZ DE MIERA, M.; CURIONI, M.; SKELDON, P.; THOMPSON, G.E. **Modelling the anodizing behaviour of aluminium alloys in sulphuric acid through alloy analogues**. Corrosion Science, v. 50, p. 3410–3415, 2008.

SAENZ DE MIERA, M.; CURIONI, M.; SKELDON, P.; THOMPSON, G. E. **Preferential anodic oxidation of second phase constituents during anodizing of AA2024-T3 and AA7075-T6 alloys.** Surface and Interface Analysis, v. 42, p. 241–246, 2010a.

SAENZ DE MIERA, M.; CURIONI, M.; SKELDON, P.; THOMPSON, G. E. **The behaviour of second phase particles during anodizing of aluminium alloys.** Corrosion Science, v. 52, p. 2489–2497, 2010b.

SAFRANY, J-S. **Anodisation de l'aluminium et de ses alliages. Techniques de l'ingénieur,** Réf. M1630, v. 5, M1 630 v2-4, 2008.

SHEN, F.; WANG, B.; YI, D.; LIU, H.; TANG, C.; SHOU, W. **Effects of heating rate during solid-solution treatment on microstructure and fatigue properties of AA2524 T3 Al–Cu–Mg sheet.** Materials and Design, v. 104, p. 116–125, 2016.

SHEN, Z.; LIU, C.; DING, Q.; WANG, S.; WEI, X.; CHEN, L.; LI, J.; ZHANG, Z. **The structure determination of $Al_{20}Cu_2Mn_3$ by near atomic resolution chemical mapping.** Journal of Alloys and Compounds, v. 601, p. 25–30, 2014.

SHI, Z.; SONG, G.; ATRENS, A. **The corrosion performance of anodized magnesium alloys.** Corrosion Science, v. 48, p. 3531–3546, 2006.

SHIMIZU, K.; FURNEAUX, R. C.; THOMPSON, G. E.; WOOD, G. C.; GOTOH, A.; KOBAYASHIT, K. **On the Nature of "Easy Paths" for the Diffusion of Oxygen in Thermal Oxide Films on Aluminum.** Oxidation of Metals, v. 35, n. 5/6, p. 427-43 9, 1991.

SKELDON, P.; SHIMIZU, K.; THOMPSON, G. E.; WOOD, G. C. **Selective interfacial processes and the incorporation of electrolyte species into anodic films on aluminium.** Philosophical Magazine Part B, v. 72, n. 4, p. 391-400, 1995.

SRIVATSAN, T. S.; KOLAR, D.; MAGNUSEN, P. **The cyclic fatigue and final fracture behavior of aluminum alloy 2524.** Materials and Design, v. 23, p. 129-139, 2002.

STALEY, J. T.; LEGE, D. J. **Advances in aluminum alloy products for structural applications in transportation.** 3rd European Conference on Advanced Materials and Processes. Paris, jun 08-10, 1993.

STARKE, E. A.; STALEY, J. T. **Application of modern aluminum alloys to aircraft.** Prog. Aerospace Sci., v. 32, p. 131-172, 1996.

SULKA, G. D.; STEPNIOWSKI, W. J. **Structural features of self-organized nanopore arrays formed by anodization of aluminum in oxalic acid at relatively high temperatures.** Electrochimica Acta, v. 54, p. 3683–3691, 2009.

TAKAHASHI, H.; NAGAYAMA, M. **The determination of the porosity of anodic oxide films on aluminium by the pore-filling method.** Corrosion Science, v. 18, p. 911-925, 1978.

THEOHARI, S.; KONTOGEORGOU, CH. **Effect of temperature on the anodizing process of aluminum alloy AA 5052.** Applied Surface Science, v. 284, p. 611– 618, 2013.

THOMPSON, G. E.; HABAZAKI, H.; SHIMIZU, K.; SAKAIRI, M.; SKELDON, P.; ZHOU, X.; WOOD, G. C**. Anodizing of aluminium alloys**. Aircraft Engineering and Aerospace Technology, v. 71, p. 228 – 238, 1999.

THOMPSON, G.E. **Porous anodic alumina: fabrication, characterization and applications.** Thin solid films, v. 297, p. 192-201, 1997.

TROMPETTE, J. L.; ARURAULT, L.; FONTORBES, S.; MASSOT, L. **Influence of the anion specificity on the electrochemical corrosion of anodized aluminum substrates.** Electrochimica Acta, v. 55, p. 2901–2910, 2010.

TWITE, R. L.; BIERWAGEN, G. P**. Review of alternatives to chromate for corrosion protection of aluminum aerospace alloys.** Progress in Organic Coatings, v. 33, p. 91–100, 1998.

VAKILI, H.; RAMEZANZADEH, B.; AMINI, R. **The corrosion performance and adhesion properties of the epoxy coating applied on the steel substrates treated by cerium-based conversion coatings.** Corrosion Science, v. 94, p.466–475, 2015.

VAN DER LINDEN, B.; TERRYN, H.; VEREECKEN, J. **Investigation of anodic aluminium oxide layers by electrochemical impedance spectroscopy.** Journal of Applied Electrochemistry, v. 20, p. 798-803, 1990.

VARGEL, C. **Corrosion of Aluminium.** Elsevier Science, 1st ed., p. 190, 2004.

VIEJO, F.; ABURAS, Z.; COY, A. E.; GARCIA-GARCIA, F. J.; LIU, Z.; SKELDON, P.; THOMPSON, G. E**. Performance of Al alloys following excimer LSM—anodising approaches.** Surface and Interface Analysis, v. 42, p. 252-257, 2010.

VOEVODIN, N. N.; BALBYSHEV, V. N.; KHOBAIB, M.; DONLEY, M. S. **Nanostructured coatings approach for corrosion protection.** Progress in Organic Coatings, v.47, p. 416–423, 2003.

VOON, C. H.; DERMAN, M. N.; HASHIM, U.; FOO, K. L.; ADAM, T. **Effect of Anodizing Voltage on the Morphology and Growth Kinetics of Porous Anodic Alumina on Al-0.5 wt% Mn Alloys.** Advanced Materials Research, v. 832, p. 101-106, 2014.

WANG, D.; BIERWAGEN, G. P. **Sol–gel coatings on metals for corrosion protection.** Progress in Organic Coatings, v. 64, p. 327–338, 2009.

WANG, H.; AKID, R. **A room temperature cured sol–gel anticorrosion pre-treatment for Al 2024-T3 alloys.** Corrosion Science, v. 49, p. 4491–4503, 2007.

WANG, S. C.; STARINK, M. J. **Two types of S phase precipitates in Al–Cu–Mg alloys.** Acta Materialia, v. 55, p. 933–941, 2007.

WHELAN, M.; CASSIDY, J.; DUFFY, B. **Sol–gel sealing characteristics for corrosion resistance of anodised aluminium.** Surface and Coatings Technology, v. 235, p. 86–96, 2013.

WOLYNEC, S. **Técnicas Eletroquímicas em Corrosão**. São Paulo: Editora da Universidade de São Paulo, p. 73-146, 2003.

WOOD, G. C.; O'SULLIVAN, J. P. **The Anodizing of Aluminium in Sulphate Solutions.** Electrochimica Acta, v. 15, p. 1865 -1876, 1970.

WOOD, G. C.; COLE., M.; HOAR, T. P. **An a.c. bridge for measurements in electrochemical systems.** Electrochimica Acta, v. 3, p. 179-185, 1960.

WOJCIECHOWSKI, J.; SZUBERT, K.; PEIPMANN, R.; FRITZ, M.; SCHMIDT, U.; BUND, A.; LOTA, G. **Anti-corrosive properties of silane coatings deposited on anodised aluminium**. Electrochimica Acta, v. 220, p. 1–10, 2016.

XU, D.; YU, Y.; ZHENG, M.; GUO, G.; TANG, Y. **Electrochemical fabrication of one-dimensional silica nanostructures.** Electrochemistry Communications, v. 5, p. 673–676, 2003.

XU, S.; WANG, Y. **Estimating the effects of corrosion pits on the fatigue life of steel plate based on the 3D profile.** International Journal of Fatigue, v. 72, p. 27–41, 2015.

YANG, Y.; ZHAN, L.; LI, J. **Constitutive modeling and springback simulation for 2524 aluminum alloy in creep age forming.** Trans. Nonferrous Met. Soc. China, v. 25, p. 3048−3055, 2015.

ZEMANOVÁ, M.; CHOVANCOVÁ, M.; FELLNER, P.; PREKOPP, K. **Corrosion Resistance and Quality of Sealed Porous Alumina Coatings.** Chem. Papers, v. 52 (3), p. 152—155, 1998.

ZEMANOVA, M.; CHOVANCOVA, M. **Sol gel methodology for sealing anodized aluminum.** Metal Finishing, v. 101, n. 12, p. 14-16, 2003.

ZHAO, J.; XIA, L.; SEHGAL, A.; LU, D., MCCREERY, R. L.; FRANKEL, G. S. **Effects of chromate and chromate conversion coatings on corrosion of aluminum alloy 2024-T3.** Surface and Coatings Technology, v. 140, p. 51-57, 2001.

ZHAO, X.; ZUO, Y.; ZHAO, J.; XIONG, J.; TANG, Y. **A study on the self-sealing process of anodic films on aluminum by EIS.** Surface & Coatings Technology, v. 200, p. 6846–6853, 2006.

ZHAO, Y. L.; YANG, Z. Q.; ZHANG, Z.; SU, G. Y.; MA, X. L. **Double-peak age strengthening of cold-worked 2024 aluminum alloy.** Acta Materialia, v. 61, p. 1624–1638, 2013.

ZHAO, X.; WEI, G.; YU, Y.; GUO, Y.; ZHANG, A. An analysis of mechanical properties of anodized aluminum film at high stress. **Surface Review and Letters**, v. 22, n. 1, p. 1550002 (7 pages), 2015.

ZHENG, Z. Q.; CAI, B.; ZHAI, T.; LI, S. C. **The behavior of fatigue crack initiation and propagation in AA2524-T34 alloy.** Materials Science and Engineering, v. A 528, p. 2017–2022, 2011.

ZHOU, F.; MOHAMED AL-ZENATI, A. K.; BARON-WIECHEĆ, A.; CURIONI, M.; GARCIA-VERGARA, S. J.; HABAZAKI, H.; SKELDON, P.; THOMPSON, G. E. **Volume expansion factor and growth efficiency of anodic alumina formed in sulphuric acid.** Journal of The Electrochemical Society, v.158, p. C202-C214, 2011.

ZHOU, F.; BARON-WIECHÉC, A.; GARCIA-VERGARA, S. J.; CURIONI, M.; HABAZAKI, H.; SKELDON, P.; THOMPSON, G. E. **Effects of current density and electrolyte temperature on the volume expansion factor of anodic alumina formed in oxalic acid.** Electrochimica Acta, v. 59, p. 186-195, 2012a.

ZHOU, X.; LUO, C.; HASHIMOTO, T.; HUGHES, A. E.; THOMPSON, G. E. **Study of localized corrosion in AA2024 aluminium alloy using electron tomography.** Corrosion Science, v. 58, p. 299–306, 2012b.

ZHU, D.; OOIJ, W. J. VAN. **Corrosion protection of AA 2024-T3 by bis-[3-(triethoxysilyl)propyl]tetrasulfide in sodiumchloride solution. Part 2: mechanism for corrosion protection.** Corrosion Science, v. 45, p. 2177–2197, 2003.

ZHU, X.; SONG, Y.; LIU, L.; WANG, C.; ZHENG, J.; JIA, H.; WANG X**. Electronic currents and the formation of nanopores in porous anodic alumina.** Nanotechnology, v. 20, 2009.

ZOLTOWSKI, P. **On the electrical capacitance of interfaces exhibiting constant phase element behaviour.** Journal of Electroanalytical Chemistry, v. 443, p. 149–154, 1998.

ZUO, Y.; ZHAO, P.; ZHAO, J. **The influences of sealing methods on corrosion behavior of anodized aluminum alloys in NaCl solutions.** Surface and Coatings Technology, v. 166, p. 237–242, 2003.